The resolution performance of two and three dimensional electrical impedance mammography

James Laurence Wheeler

Supervisor: Dr Wei Wang

A thesis submitted in partial fulfilment of the requirements for the degree of Doctor of Philosophy

De Montfort University

April 2003

SUMMARY

Electrical Impedance Mammography (EIM) offers the potential for early detection of breast cancer in ways that conventional methods such as x-ray mammography and ultrasound mammography fail. EIM involves passing low level alternating currents through the breast tissues via a number of surface electrodes placed on the skin, and monitoring the surface voltages produced as a result. Images of the complex impedance of the internal tissues are formed by solving the mathematical equations governing the relationships between current, voltage and impedance in a volume conductor. However, due to inherent ill-conditioning within these equations the image formation process is inefficient and leads to poor resolution images. The work presented here is a simulation study aimed at investigating the factors that affect the conditioning of the underlying equations in order to gain a better understanding of how the image resolution might be maximised. The first part of the investigation focuses on 2-dimensional EIM, and in particular the effect of increasing the number of electrodes used. The second part explores 3-dimensional imaging and concentrates on the interrelated effects on image quality of breast shape, electrode placement and the current and voltage patterns applied to the electrodes. In doing so an algorithm for modelling breast imaging in 3-dimensions is developed and a number of original approaches to data collection strategies are proposed and tested. As well as optimising image performance, one of the key considerations throughout the study is the spatial variance of the resolution, since it is desirable to have an imaging modality which is not biased to any particular region of the breast. In conclusion, a new electrode placement methodology is proposed which promises an improvement in resolution over any of the existing EIM systems, and has the added benefit of easily adapting to a wide range of breast shapes and sizes.

ACKNOWLEDGMENTS

There are certain individuals who have contributed in many different ways to the work presented in this thesis, and I would like to acknowledge them here.

Firstly I thank my supervisors, Dr Wei Wang and Prof Malcolm McCormick who have both given helpful advice throughout the course of the PhD, and in particular Dr Brian Bramer who has made himself available on numerous occasions to discuss a great many issues.

I am privileged to have been in the company of fellow research students; Ben Tunstall, Mengxing Tang, Jieque Yang and Fraser MacAndrew, who often stopped what they were doing to entertain my questions.

During times of mental overload I have found great encouragement from the company of Nikki and Mark, whose enthusiasm for their many interests has often inspired a broader panorama of thought. I am also grateful to Andy for offering musical distraction when I have needed it, and to Marie for making me tasty coffee.

Finally I would like to thank my parents who have endured my frustrated complaints and muddled discoveries with equal sincerity during the ups and downs of the research.

DECLARATION

The work presented within this thesis is the exclusive work of the author, James Wheeler, except where otherwise acknowledged. Furthermore the work presented has not been published or otherwise distributed by any person other than the author.

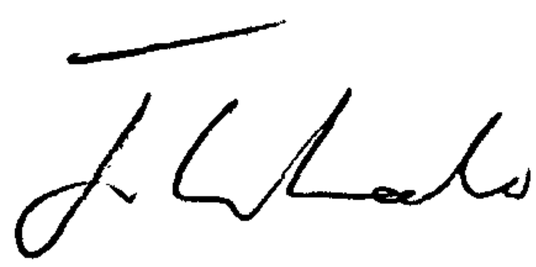

James Wheeler

April 2003

TABLE OF CONTENTS

CHAPTER ONE

WHAT IS BREAST CANCER AND HOW IS IT DETECTED?

1.1 Introduction

The work presented here, although technical in nature, refers to the detection of cancers of the breast. Initially the nature of the anatomical and physiological processes involved in both the healthy breast and the diseased are outlined. Subsequently imaging techniques used for the detection of breast cancer are presented, one of which; Electrical Impedance Mammography, forms the central theme of the remaining chapters.

1.2 Breast Anatomy

The breast is a modified sweat gland consisting of fat, fibrous and glandular tissue. The bulk of a non-lactating breast is predominantly fatty tissue, which determines the breast size (Moffat, 1993). On the surface there is a nipple which is surrounded by a ring of pigmented skin known as the areola. The breast overlies the pectoralis major and serratus anterior muscles, but is separated from them by the deep fascia. (See figure 1.1).

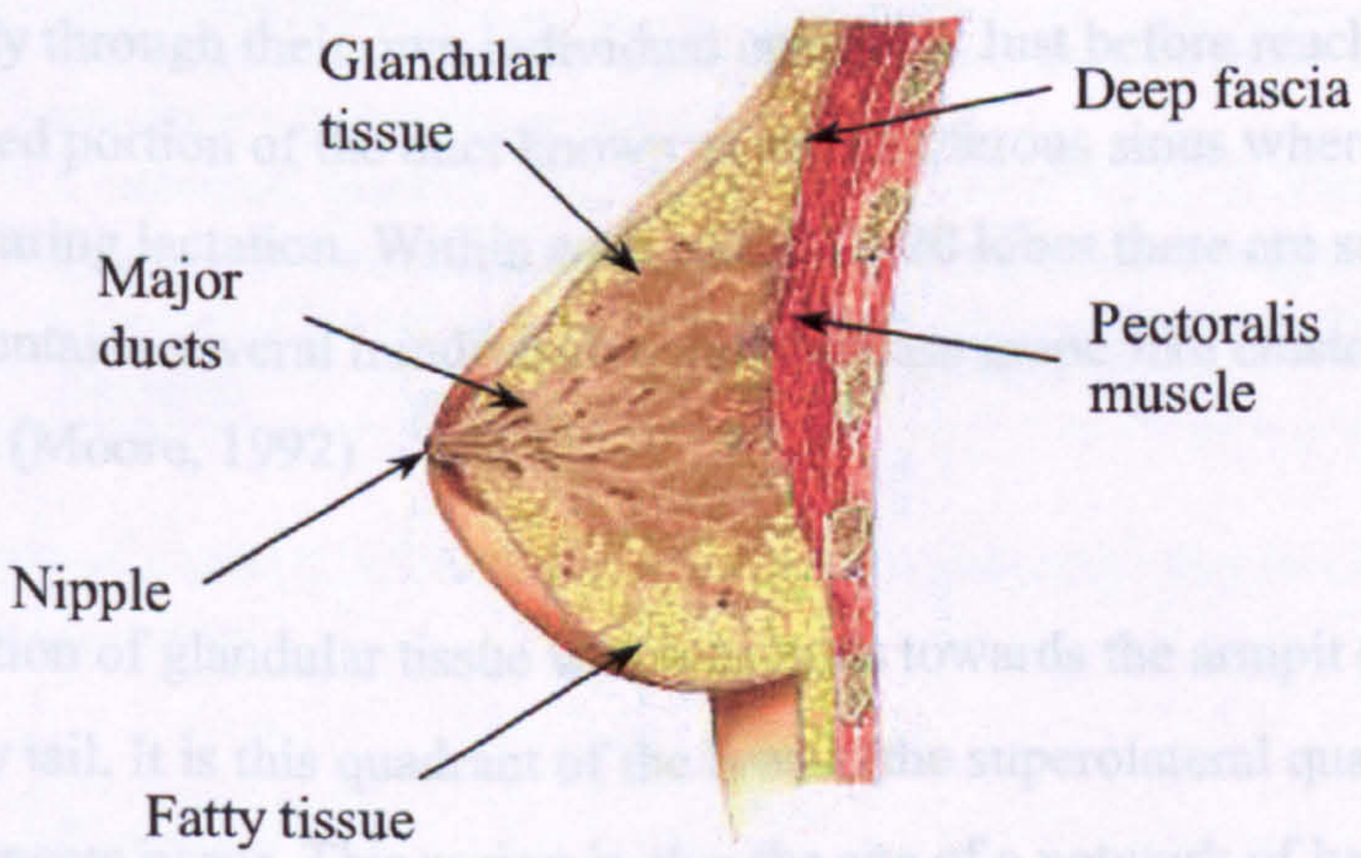

Figure 1.1 – Sagittal cross-section of the human breast, indicating location and structure of the glandular tissue.

The breast is loosely connected to the deep fascia by a layer of loose connective tissue (known as the retromammary space) and as a consequence is usually fairly mobile over the deep fascia. In contrast to this, the skin around the surface of the breast and the nipple is intricately connected to the glandular tissue by fibrous suspensory ligaments (also known as Cooper's ligaments) which play a role in supporting the breast (Tortora and Grabowski, 1993).

1.2.1 Breast size and position

Breast size can vary greatly between women; in multiparous women (those who have borne several children) they may become large and pendulous, whereas in elderly women they become small and wrinkled due to a decrease in fatty and glandular tissue (Moore, 1992). Despite the large size range, the base of the breast is usually well defined as being circular and extending between the 2^{nd} and 6^{th} ribs in the vertical direction and from the edge of the sternum to the midaxilliary line in the lateral direction. On the same woman the breasts are usually equal in size, although if one is larger it is normally the right breast (Tortora and Grabowski, 1993)

1.2.2 Structure of glandular tissue

The glandular tissue consists of 15-20 lobes each of which drains into a lactiferous duct. These ducts converge towards the nipple where they open out onto the skin surface, usually through their own individual openings. Just before reaching the nipple, there is a dilated portion of the duct known as the lactiferous sinus where milk accumulates during lactation. Within each of the 15-20 lobes there are several lobules. Each lobule contains several hundred alveoli which are grape-like clusters of milk-secreting cells (Moore, 1992)

There is a portion of glandular tissue which extends towards the armpit (axilla) known as the axilliary tail. It is this quadrant of the breast (the superolateral quadrant) where most breast cancers occur. This region is also the site of a network of lymph nodes through which about 75% of the lymph produced in the breast drains. Since the lymphatic system is one of the primary routes for spreading of secondary cancers (metastases) the axilliary area requires careful examination when screening for breast cancer (Tortora and Grabowski, 1993)

1.3 Cancer and the breast

Cancer is a generic term for abnormal or uncontrolled cell division within the body (see figure 1.2). This usually results in growths which are known as tumours or neoplasms.

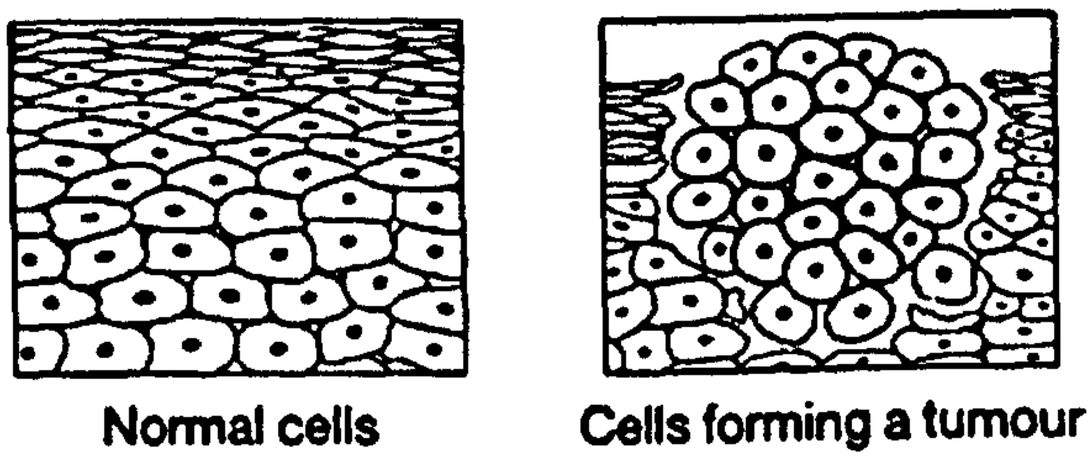

Figure 1.2 – Illustration of the typical cell structures observed in normal tissue and those in a carcinoma. Cancerous cells are often densely packed due to their rapid growth.

Tumours are loosely classified as being benign when they do not invade healthy tissue or malignant when they invade and destroy surrounding healthy tissue. Another term for a malignant tumour is a carcinoma (sometimes abbreviated to 'CA'). The more detailed classification of tumours comes from their microscopic appearance and the site from which they originated (Tortora and Grabowski, 1993). Table 1.1 lists some examples of these.

Classification	Description
Melanoma	Cancerous growth originating from melanocytes (skin cells which produce pigment) e.g. moles
Sarcoma	Cancerous growth originating from muscle cells or connective tissue
Leukemia	Cancer of blood forming organs and leukocytes (white blood cells)
Lymphoma	Cancer of lymphatic tissue, i.e. the lymph nodes (e.g. Hodgkin's disease)

Table 1.1 – Examples of Cancer classification based on the cells from which they originate (from Tortora and Grabowski, 1993)

1.3.1 Causes of cancer

There are currently three major known causes of cancer; environmental, viruses and genetic factors. Environmental agents (carcinogens) which enter the body via food, water or air include hydrocarbons in cigarette tar, radon gas from the earth, ultraviolet radiation from the sun and fatty foods. It is thought that these chemicals are

responsible for 60-90% of all human cancers. There are viruses which can infect the genetic information in cells and convert them into virus producers. Also there are genes which can transform normal cells into cancer cells. They originate from normal growth regulation genes known as proto-oncogenes and undergo a transformation into the cancer-causing oncogenes (Tortora and Grabowski, 1993).

1.3.2 The stages of breast cancer

In order to provide a common measure for the degree of breast cancer severity, a staging scheme has been developed by the American Joint Committee on Cancer (AJCC). The scheme (sometimes referred to as the TNM system) involves an assessment of tumour size, lymph node involvement and metastases status. Based on the combined results of these three areas, one of four stage levels is assigned. Table 1.2 summarises the TNM codes with their associated meanings, and Table 1.3 shows how the cancer stage is deduced.

Code	Meaning
TX	Tumour cannot be assessed
T0	No evidence of primary tumour
Tis	Carcinoma in situ, or Paget's disease of the nipple, without an associated tumour mass
T1	Tumour <2cm in greatest dimension
T2	Tumour >2cm but <5cm
T3	Tumour >5cm in greatest dimension
T4	Any size with direct spread to chest wall or skin; includes inflammatory carcinoma or ulceration of the skin
N0	Regional lymph nodes contain no metastases
N1	Metastasis to movable, same side, axillary lymph node(s)
N2	Metastasis to movable, same side, lymph node(s) fixed to one another or to other structures
N3	Metastasis to same side lymph node(s) beneath the sternum
MX	The presence of distant metastasis cannot be assessed
M0	No distant metastases are found
M1	Distant metastases are present

Table 1.2 – Summary of the TNM staging scheme in which the tumour, node and metastases status is assessed.

Stage 0	In situ breast cancer – Tis, N0, M0
Stage 1	T1, N0, M0
Stage 2a	T0-1, N1, M0 or T2, N0, M0
Stage 2b	T2, N1, M0 or T3, N0, M0
Stage 3a	T0-2, N2, M0 or T3, N1-2, M0
Stage 3b	T4, N(any), M0 or T(any), N3, M0
Stage 4	T(any), N(any), M1

Table 1.3 – Summary of the overall breast cancer stage in terms of the TNM codes.

1.3.3 Breast cancer statistics

Breast cancer affects 1 in 9 UK women (Cancer Research UK). Not all women, however, have an equal risk of developing breast cancer. Factors which have an effect are (Tortora and Grabowski, 1993);

- Family history (especially mother or sister)
- Never having children, or having the first child after the age of 34
- Previous cancer in one breast
- Exposure to ionising radiation
- Excessive fat and alcohol intake, or smoking

The likelihood of developing breast cancer also increases with age. Table 1.4 shows the age-related probability for a woman born in the UK of being diagnosed with breast cancer.

Age:	Probability:
Up to 25	1 in 15,000
Up to 30	1 in 1,900
Up to 40	1 in 200
Up to 50	1 in 50
Up to 60	1 in 23
Up to 70	1 in 15
Up to 80	1 in 11
Up to 85	1 in 10
Lifetime risk (all ages)	1 in 9

Table 1.4 – Summary of the age-related probability of a UK -born woman being diagnosed with cancer (From Cancer Research UK)

The chances of survival having been diagnosed with breast cancer is strongly linked to the stage at which the cancer was first discovered. Table 1.5 summarises the 5 year survival rate based on stage.

TNM stage	5 year survival %
1	92
2a	77
2b	69
3	64
4	27
Unknown	81

Table 1.5 – The 5 year survival rate depending on the TNM stage at the time of diagnosis, (from Cancer Research UK).

1.4 Types of breast cancer

As with most cancers, cancers of the breast divide into benign and malignant. The benign cancers do not present any particular health risk to the patient but may cause discomfort due to increased pressure at the tumour site. The malignant cancers present a major health hazard since they have the ability to invade and destroy healthy tissue, and can form metastases which are able to relocate in other more crucial organs in the body. The classifications and statistics that follow are all taken from Underwood (2000).

1.4.1 Benign cancers of the breast

There are four main categories of benign breast cancers:

1. *Fibroadenomas* – the commonest of the benign tumours which arise from lobular tissue. Their size is typically 10-40mm and they are not tethered, hence can move around under the skin, but will not metastasise.
2. *Duct papillomas* – form from ductal tissue and usually form a solid lesion within a large duct. They often cause nipple discharge and can be up to 40mm long.
3. *Adenomas* – consist of tubular structures and measure 10-40mm diameter
4. *Connective tissue tumours* – form on connective tissues such as Cooper's ligaments or the nipple

1.4.2 Malignant cancers of the breast

The malignant cancers further divide into two categories; non-invasive and invasive. The non-invasive cancers (sometimes referred to as *in situ*) attack healthy tissue, but will not break through the basement membrane surrounding the structure in which they originate. Invasive cancers (sometimes called *infiltrating* cancer), can break through the basement membrane and therefore can spread much more easily.

1.4.3 Non-invasive breast carcinomas

1. *Intraduct carcinoma* – originate in and are confined to a duct. They account for 5% of all breast carcinomas and measure 10-80mm
2. *Intralobular carcinoma* – confined to a lobule but can replace ductal tissue. They account for 6% of all breast carcinomas and are not palpable.

1.4.4 Invasive breast carcinomas

1. *Infiltrating ductal* – account for 85% of invasive carcinomas. Their size varies between patients
2. *Infiltrating lobular* – accounts for 10% of invasive carcinomas. They can occur all over the breast. Cells infiltrate around existing ducts and alveoli rather than destroying them
3. *Mucinous carcinoma* – forms 2% of invasive carcinomas. They measure 10-50mm diameter and have smooth, well defined edges
4. *Tubular carcinoma* – account for <1% of invasive carcinomas and have a firm, irregular shape
5. *Medullary carcinoma* - <1% of invasive carcinomas and have well defined edges
6. *Papillary carcinoma* - <1% of invasive carcinomas and usually have well defined edges

A graphical representation of the statistics of the different malignant breast cancer types is shown in figure 1.3.

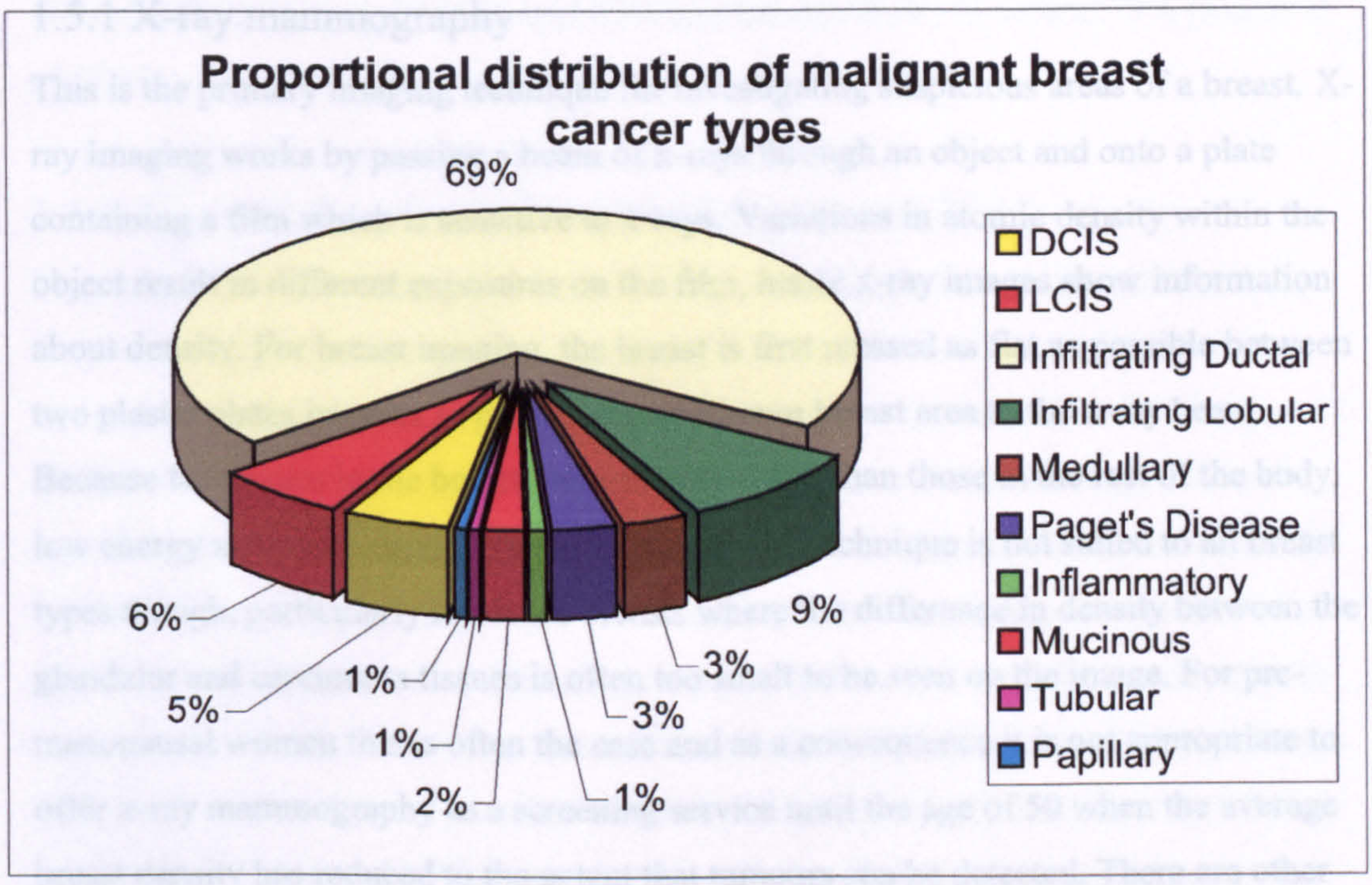

Figure 1.3 – Graphical illustration of the relative proportions of malignant cancer types. (From Underwood, 2000)

1.5 Detection of breast cancer

Some breast cancers cause changes which may be observed on the surface of the breast, examples of this include one breast lifting upwards, a discharge from the nipple and a thickening or dimpling of the skin (*peau d'orange*). The majority of cancers can be felt through the skin by manual palpation of the breast. These effects provide one route of detection of breast cancer, and usually begin as a suspicion of the patient that is referred to a physician. Indeed women are encouraged to check their breasts regularly since this provides an effective route for early detection. A different route for detecting breast cancer is through a routine breast cancer screening programme. In the UK, women between the ages of 50 and 64 are invited to have an X-ray mammogram once every three years. Suspicious areas are then further investigated using ultrasound imaging or by histological examination of cells removed from the breast. The various detection and diagnostic methods currently in use are outlined below.

1.5.1 X-ray mammography

This is the primary imaging technique for investigating suspicious areas of a breast. X-ray imaging works by passing a beam of x-rays through an object and onto a plate containing a film which is sensitive to x-rays. Variations in atomic density within the object result in different exposures on the film, hence x-ray images show information about density. For breast imaging, the breast is first pressed as flat as possible between two plastic plates in order to present the maximum breast area to the x-ray beam. Because the tissues in the breast are generally softer than those in the rest of the body, low energy x-rays are used to form the image. The technique is not suited to all breast types though, particularly for dense breasts where the difference in density between the glandular and carcinoma tissues is often too small to be seen on the image. For pre-menopausal women this is often the case and as a consequence it is not appropriate to offer x-ray mammography as a screening service until the age of 50 when the average breast density has reduced to the extent that tumours can be detected. There are other factors as well which effect whether or not mammography can detect breast cancers, the most significant of which are patient weight and number of pregnancies (Tartter *et al*, 1999). The sensitivity of x-ray mammography is in the region of 84% whilst the specificity is around 69% (Malur *et al*, 2001).

1.5.2 Ultrasound mammography

Ultrasound imaging works by transmitting high frequency acoustic energy into the body via an ultrasound transmitter and recording the reflected wave-fronts. Reflections occur wherever there is a change in density of the imaged tissues. More abrupt changes in density give rise to stronger reflections, and the depth of the density change is calculated from the time taken between the pulse being transmitted and the recorded echo. Ultrasound mammography (Entrekin *et al*, 1999) is the application of ultrasound imaging for the detection of breast cancer. It is usually used as an adjunct to x-ray mammography and clinical examination to evaluate suspicious regions for which a conclusive diagnosis cannot be reached (Durfee *et al*, 2000). One of the benefits of ultrasound imaging is its ability to diagnose whether a lump is solid or fluid-filled (i.e. a cyst). For cases where there is fluid, the images may be used to direct a needle into the site of the cyst so that fluid may be drawn off and analysed. The sensitivity of

ultrasound mammography is around 89% and the specificity is around 79% (Malur *et al*, 2001).

1.5.3 Magnetic Resonance Imaging of the breasts (MRI)

Magnetic Resonance Imaging is a non-invasive imaging technique which uses radio-frequency signals in the presence of a strong magnetic field to extract information about the atomic properties of the part of the body under investigation. The image quality is very clear, although the cost of performing an MRI scan is high due to the need for expensive cryogens involved in generating the magnetic field. Research into MRI of the breast has been going on for a number of years, and has revealed it to be useful for studying augmented breasts (i.e. those with a silicone implant) and also for mapping the extent of known tumours. The sensitivity for MR mammography is very high with typical values in the region of 95%, whilst specificity is around 69% (Malur *et al*, 2001). The use of MRI for screening purposes, however, is regarded as inappropriate (Editorial, The Breast Journal, 1999).

1.5.4 Scintimammography

Scintimammography is the use of gamma cameras to investigate breast disease. The general procedure for this is to inject a radiopharmaceutical 'tracer' into the patient's bloodstream which subsequently distributes itself around the body. The radioactive part of the tracer is a gamma emitter and is commonly Tc-99m. The gamma camera then forms images of the gamma radiation being emitted from the patient, and thus can give an indication of regions of abnormal blood flow, which is a common feature of breast lesions associated with the increased vascularisation. Although gamma cameras are well established as a medical imaging modality, the application to breast cancer detection is very much in its infancy. Preliminary investigations have revealed that whilst it may be useful for imaging patients with radiographically dense breasts (Cutrone *et al*, 1999) other infections of the breast such as mastitis can mask the effect of a tumour (Pappo *et al*, 2000). In addition, the use of a radioactive material to collect the image presents a small health risk in itself.

1.5.5 Electrical Impedance Mammography (EIM)

An area of more recent interest in detecting breast cancers is that of Electrical Impedance Tomography (EIT) often referred to as Electrical Impedance Mammography (EIM) when used for breast imaging. A number of different approaches have been used to date, but they are all based on the concept that living tissues present a variety of impedances to the passage of electrical currents. Furthermore, the effect is frequency dependent and appears to provide an indication of the cell structure. Unlike x-ray mammography it is not sensitive to the density of the breast tissues, hence may be able to offer routine breast imaging for pre-menopausal women. Reconstructing images of electrical impedance, however, is problematic due to difficulties in modelling the precise behaviour of currents in the unknown tissue distribution. As a consequence the image resolution is poor. One technique, which has been licensed as an adjunct to x-ray mammography by the Food and Drug Administration (FDA, 1999) is the 'TranScan T-Scan 2000'. It passes low frequency currents between a hand-held probe and a number of points on the breast, and builds a planar map of relative impedance (Assenheimer *et al*, 2001). Variations in the impedance map may indicate a possible lesion. Another technique involves the patient lying prone, with the breast pendant inside a ring of 16 electrodes. Current at frequencies from 10-950kHz is passed between the electrodes in various patterns and an image is formed using a mathematical reconstruction algorithm (Osterman *et al*, 2000). A similar system has been developed in DeMontfort University, Leicester, UK (Wang *et al*, 1998). Although no in-vivo data has been gathered from it to date, there has been substantial software development for the analysis and diagnosis of breast images (Tunstall 2000). The subject of Electrical Impedance Tomography and its image resolution limitations are expanded in detail in Chapters 2 and 3.

1.6 Diagnosing the breast cancer type

Whilst providing a useful tool to the detection of breast cancer, the results from the imaging methods described above are only regarded as an indicator. For a conclusive diagnosis of any suspicious areas it is necessary to remove a sample of the tissue and to examine the cells under a microscope. There are three principle methods for removing the cells (Underwood, 2000):

1. *Fine needle aspiration cytology* – removal of a sample of cells using a fine needle. No anaesthetic is required.
2. *Tru-Cut biopsy* – removal of a core of tissue using a biopsy needle. A local anaesthetic is required and the tissue needs processing prior to histological examination. A development of this is the *Mammotome* (Joshi *et al*, 2001) in which the tissue samples are removed through the needle using a vacuum, allowing several samples to be taken without needing to remove the needle from the breast.
3. *Frozen section examination* – a small breast sample is removed by surgery after which it is frozen, sliced and examined. This method is less popular since it requires a general anaesthetic.

For the first two methods it is common to use x-ray or ultrasound imaging to aid positioning of the needle at the site of the suspected tumour.

1.7 Aims and objectives

The primary aim of this thesis is to assess the key factors which influence the image resolution in Electrical Impedance Mammography with a view to steering the design of the De Montfort Mk2b EIM system towards its performance goals. One particular feature peculiar to breast imaging is that the shape of the human breast is not rigid, and thus offers an extra degree of freedom not available when imaging other parts of the body. Most EIM systems, however, tend to regard the breast as having a fixed shape. This thesis explores the effect that breast shape has on image resolution, and endeavours to establish whether there is an optimum data collection strategy that offers good image quality over a wide range of breast shapes. There are a number of distinct subjects that are examined and reported, as outlined below.

Initially the issue of image quality is considered. A literature review of the factors known to contribute to image degradation is presented. In addition the methods commonly used for quantifying resolution are outlined and a new method suitable for use with 3-dimensional images is developed.

The assessment of factors affecting image quality begins by considering the breast as a 2-dimensional object. At this stage the breast shape is not taken into consideration and

it is assumed that it can be imaged as a set of circular transaxial slices. The influence of the number of electrodes and the measurement strategies is assessed.

In the next stage, the breast is considered as a 3-dimensional object which can take on a range of different shapes. This involves the development of an algorithm to model the breast shape and software to simulate EIM in three dimensions. Key factors learned from the 2-dimensional investigation are applied where appropriate. The analysis of the image quality favours those measurement strategies which are least sensitive to breast shape and tumour position, since these are important requirements for a breast cancer screening service.

1.8 Outline of the thesis

The overall aim is to evaluate the image resolution performance of EIM systems with a view to finding an optimum imaging technique. As such it can be broken down into a number of distinct areas which are grouped into separate chapters.

Following the introduction, Chapter 2 provides an overview of the background to Electrical Impedance Tomography with an emphasis on its use for breast imaging. In Chapter 3, the issue of image quality is addressed both in terms of the factors which influence it and the methods used to quantify it. Chapter 4 describes the development of a simulation for evaluating the performance of 2-dimensional EIT systems in which the number of electrodes and the measurement strategy are varied. The results from the 2-dimensional simulation are presented at the end of Chapter 4 along with a detailed discussion. In Chapter 5 the development of a 3D breast model for simulating various breast shapes is given. In addition a technique for simulating 3D EIM imaging and forming images is presented. Chapter 6 contains the results of the 3-dimensional investigation along with a detailed discussion. In Chapter 7 the conclusions from the 2D and 3D simulations are presented along with suggestions for further work.

CHAPTER TWO

OVERVIEW OF ELECTRICAL IMPEDANCE TOMOGRAPHY

2.1 Introduction

In the previous chapter, the anatomical and physiological processes of the healthy and diseased breast were introduced. Various imaging modalities used for the detection of breast cancers were outlined, including Electrical Impedance Mammography (EIM). This chapter provides a background to the subject of Electrical Impedance Tomography (EIT) on which EIM is based. It begins by addressing the electrical properties of biological tissues and shows how these are related to cell structure. The factors involved in making impedance measurements from isolated tissue samples are then considered. Finally the concept of collecting multiple impedance measurements and forming images from them is explored.

2.2 Impedance characteristics of biological tissues

Biological tissues are known to present a complex impedance (i.e. having both resistance and reactance) which varies with frequency, temperature and tissue type. The conventional unit for quoting the resistivity (ρ) of a substance is [Ωm] (ohm-metres). This relates to the resistance R via the relationship:

$$R = \rho(l/A) \qquad 2.1$$

where l and A are the length and area of the conductor respectively. Sometimes it is convenient to quote the conductivity (the reciprocal of resistivity) which has units [S/m] where S is the conductance in Siemens.

The human body is composed of a number of different types of tissue ranging from fluid substances such as blood, lymph and cerebrospinal fluid to hard solids like bone and teeth. Each of these has its own electrical properties, and over the last few decades there has been great interest in determining the numerical values of resistivity and permittivity. From work carried out by Geddes and Baker (1967), it appears that there is a wide range of resistivities for human tissues, ranging from ~1.5Ωm for blood up to

~150Ωm for bone (when measured along the length of the bone). Table 2.1 lists some of the tissues along with their resistivities and, where known, the frequency and temperature at which the measurements were made.

Tissue	Resistivity (Ωm)	Frequency	Temperature /°C
Blood	1.65	1 kHz	37
Plasma	0.63	1 kHz	37
CSF	0.64	1 kHz	24.5
Fat	21.8	1 MHz	Room – 37
Skeletal muscle	Longitudinal – 2.4	1 kHz	37
	Transverse – 6.8	1 kHz	37
Kidney	1.26	1 MHz	Room
Liver	2.98	1 MHz	Room
Grey matter	2.8		
White matter	6.8		
Spleen	2.56	1 MHz	Room
Lung	1.61	500 MHz	27
Bone – axial	170	1 kHz	Room
Radial	540	1 kHz	Room
Circumferential	360	1 kHz	Room

Table 2.1 – Some human tissues along with their electrical resistivities. (From Geddes and Baker, 1967)

2.2.1 The frequency dependence of impedance measurements

All biological tissue is based on a cell structure, which on a simple level consists of a cell membrane that contains the intracellular fluid and nucleus, around which is the extracellular fluid. A simple electrical model of this is to represent the intra- and extracellular fluids by resistances and the cell membrane by a capacitance. Based on this idea, the biological cell can be modelled electrically as a resistor (S) representing the intracellular fluid connected in series with a capacitor (C) representing the cell membrane. The extracellular fluid is represented using a resistor (R) in parallel with both S and C (see figure 2.1). Griffiths (1995) developed a more comprehensive electrical model with several RSC networks. At lower frequencies, the resistive (or real) part of the impedance is dominant. However, as the measuring frequency is increased above ~50kHz, the charging and discharging of the cell membranes allows some of the current to be shunted through the intracellular fluid, thereby reducing the overall impedance of the tissue (see figure 2.2). For this reason, frequency effects are important and must be taken into consideration. Indeed, the very nature of this

frequency dependence may be used to help characterise tissue type, particularly between normal and cancerous tissues (Surowiec *et al*, 1988).

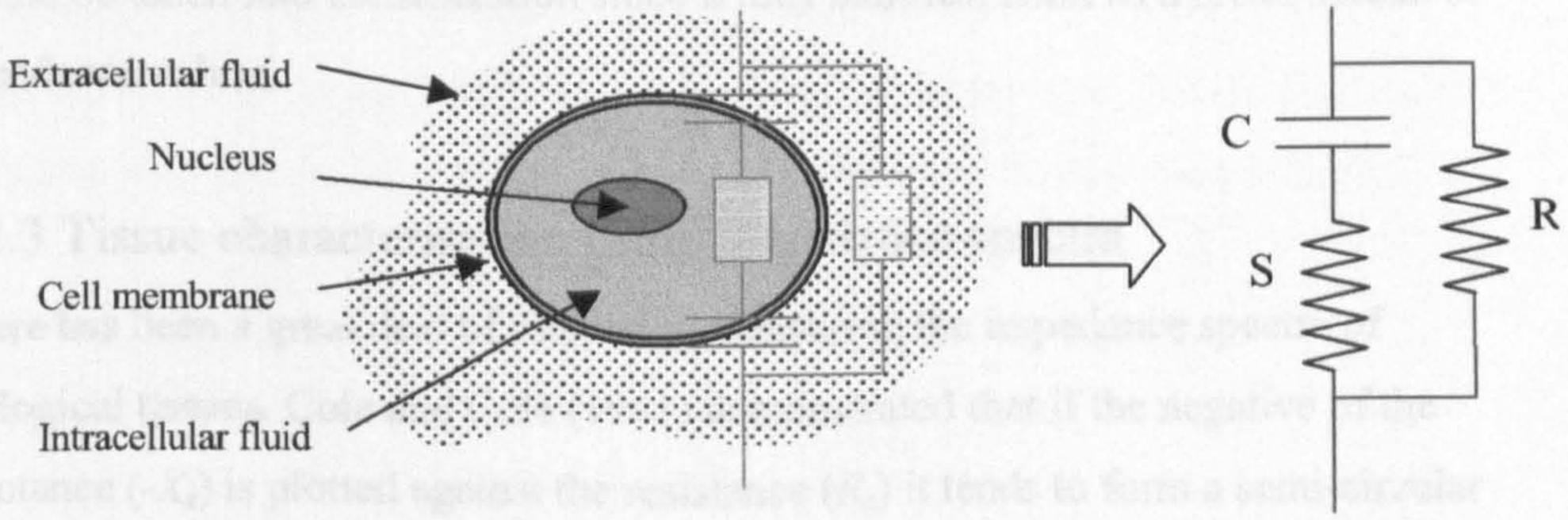

Figure 2.1 – A basic electrical model of the biological cell structure which can be broken down into three components, namely: R – a resistor representing the extracellular fluid, S – a resistor representing the intracellular fluid and C – a capacitor representing the cell membrane.

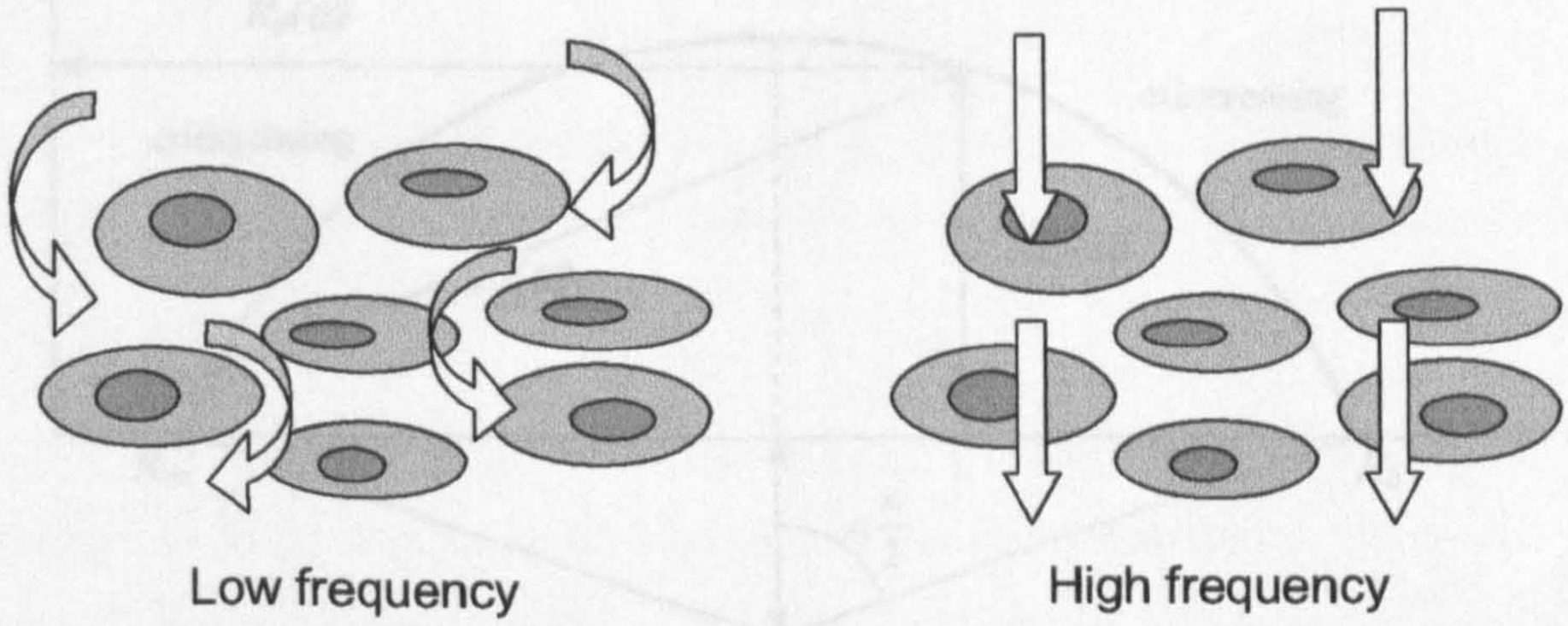

Figure 2.2 – Illustration of the electrical current paths in a cell structure. The left-hand diagram indicates the low frequency current paths around the insulating cell membranes. At higher frequencies (right hand diagram) the impedance of the capacitive cell membranes drops, allowing current to be shunted through the cells.

2.2.2 Anisotropy of the impedance of biological tissues

In addition to the microscopic cell structure, another property of biological tissues which can affect their impedance is their macroscopic structure. Some biological tissues are organised into bundles of fibres which the body uses to transport various fluids (e.g. blood) or in some cases electric charge (e.g. nerves). Such tissues usually present a range of electrical impedances depending on their orientation. For example, skeletal muscle conducts electric current roughly three times more easily along the

direction of the fibres than across them. This effect may also occur with breast tissue which has bundles of ducts which all flow towards the nipple. It is not so clear how this could be applied at the imaging level for tissue identification purposes, but it should be taken into consideration since it may manifest itself as a broad spread of impedance values.

2.2.3 Tissue characterisation using impedance spectra

There has been a great deal of interest in measuring the impedance spectra of biological tissues. Cole and Cole (1941) demonstrated that if the negative of the reactance ($-X_s$) is plotted against the resistance (R_s) it tends to form a semi-circular locus, usually with its centre located somewhere beneath the real axis (see figure 2.3). This type of plot is now generally referred to as a Cole-Cole plot after the authors.

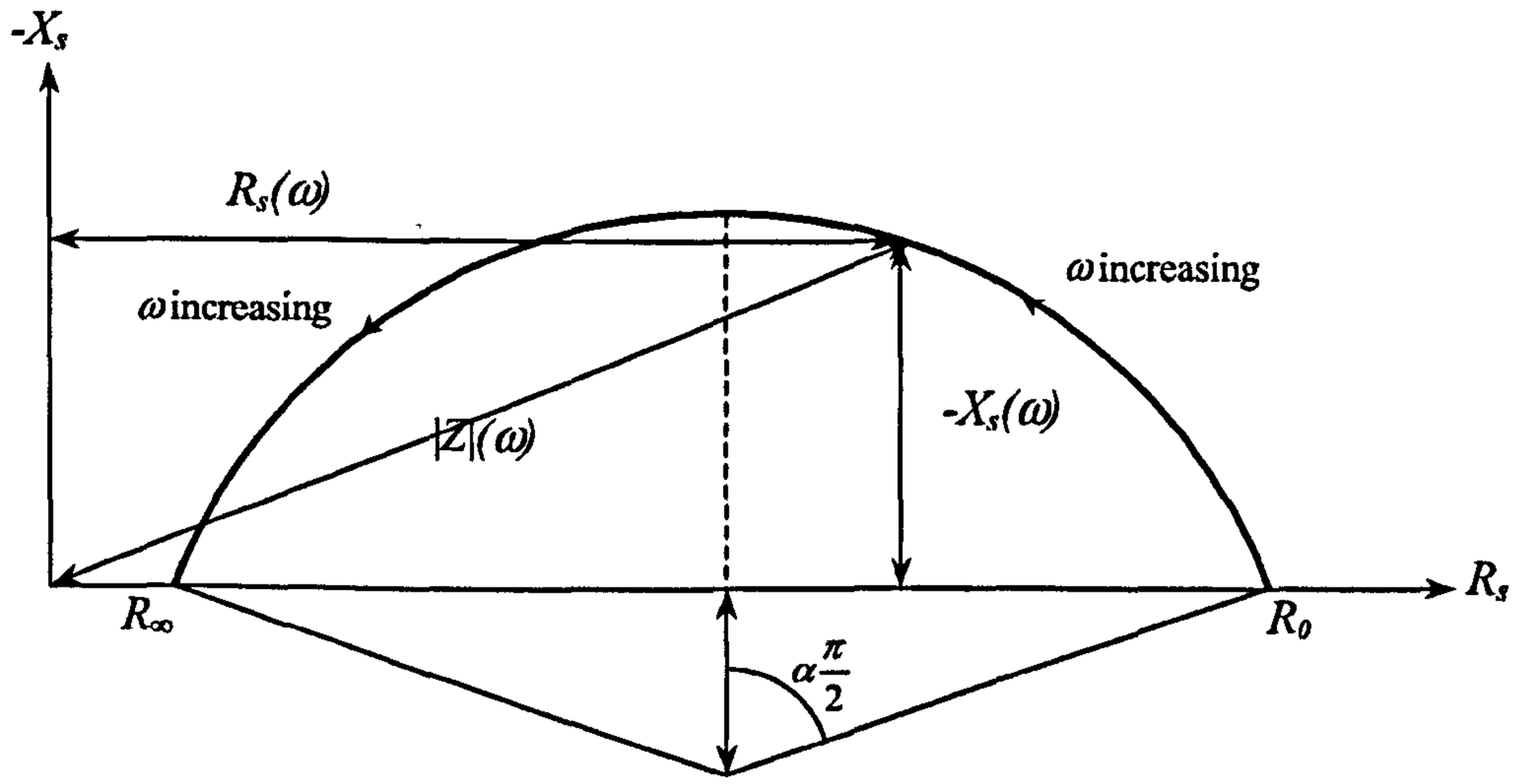

Figure 2.3 – An illustration of the Cole-Cole plot in which the negative reactance ($-X_s$) is plotted against the resistance (R_s) at various frequencies to form a semi-circular arc. The angular frequency of the applied signal is ω and α is a dimensionless constant in the range 0-1 which controls the position of the centre of the arc beneath the real axis. R_0 and R_∞ are the respective low-frequency and high-frequency intercepts on the real axis.

Cole (1940) proposed the following formula to model this behaviour, which has become termed the Cole equation:

$$Z = R_\infty + (R_0 - R_\infty)/\left[1 + (j\omega/\omega_0)^\alpha\right] \qquad 2.2$$

R_0 is the measured DC resistance and R_∞ is the measured high-frequency resistance of the tissue sample. ω_0 is the angular 'turnover frequency' at which the measured reactance is at a maximum and may be expressed as $\omega_0 = 1/T_0$ where T_0 is a time constant. α (which has valid values between 0 and 1) controls the position of the centre of the arc beneath the real axis and is chosen such that the curve fits the measured data as closely as possible. This model relates to the RSC model as shown in figure 2.4.

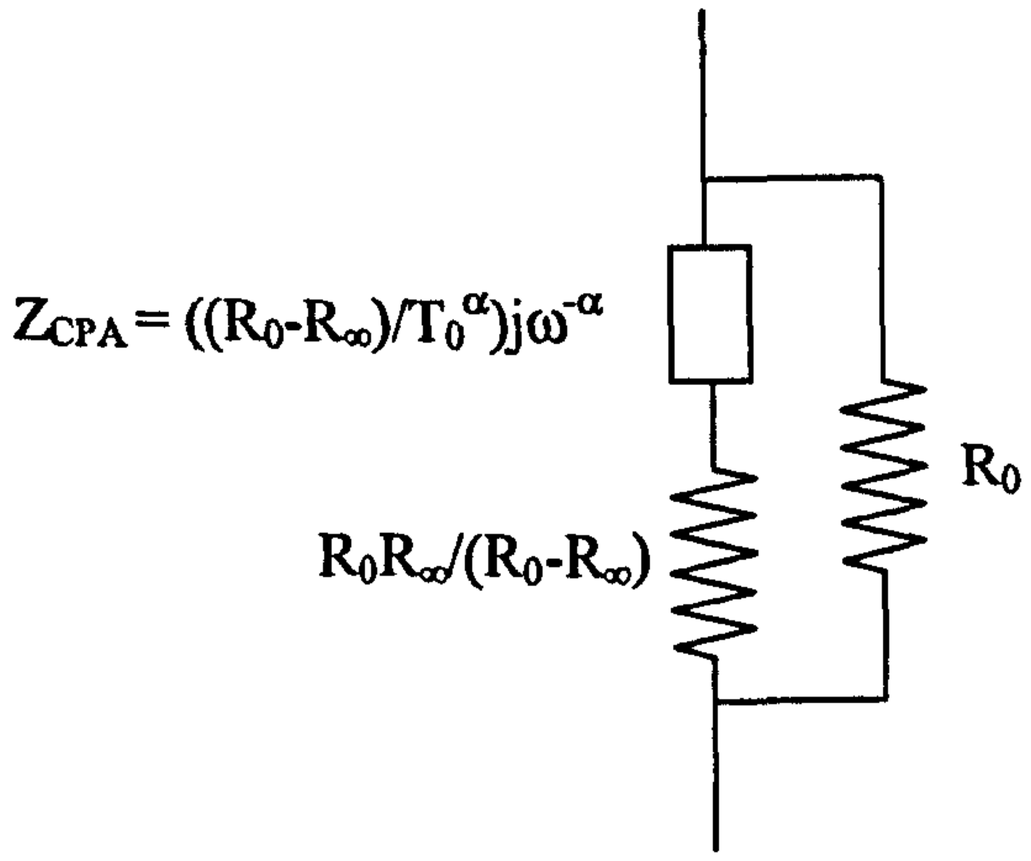

Figure 2.4 – A modified version of the RSC model (see fig 2.1) which is based on the Cole equation (Equation 2.2). Instead of using a pure capacitance for C, a constant phase angle impedance (Z_{CPA}) is used.

The capacitive element (C) in the RSC model (fig. 2.1) has been replaced with a constant phase angle impedance (Z_{CPA}) rather than a pure capacitance. Using the Cole equation (2.2) and the above model, a given tissue sample can be assigned parameters that produce a best fit to its Cole-Cole plot. These parameters can then be used as a means of characterising the tissue sample (Rigaud *et al*, 1995).

Surowiec *et al* (1988) presented some limited data for the Cole parameters of seven different breast tumours. They showed that conductivity as a function of frequency increases more significantly in tumours than healthy tissue for frequencies in the MHz region. For DC measurements (obtained using curve fitting software), the conductivity within a tumour was found to be between 2 and 20 times greater than the surrounding healthy tissue. They remarked that their results seem to indicate that radio frequency impedance imaging can potentially be used as a diagnostic modality for early breast cancer detection.

2.2.4 Methods used for measurement of tissue impedance

To understand how tissue impedance is measured it is helpful to first consider a tissue sample in isolation that is removed from the body. Essentially there are two approaches to measuring the impedance of the sample; either observing current for a given voltage or observing voltage for a given current. In general it is preferred to supply a constant current and to measure the subsequent voltage(s) produced across the tissue surface. The surface voltage can be measured with the same electrodes used to supply the current, but this introduces errors when the electrode-to-tissue contact impedance is significant and/or unknown (see figure 2.5a). This is known as a 2-terminal impedance measurement. A better way is to use separate pairs of electrodes for current injection and voltage measurement, and to ensure the voltmeter has a high input impedance. This ensures that virtually no current flows through the voltage measuring leads, hence keeping any potential drop across the unknown contact impedance to a minimum. This is known as a 4-terminal impedance measurement (figure 2.5b) and is also the method used in this work.

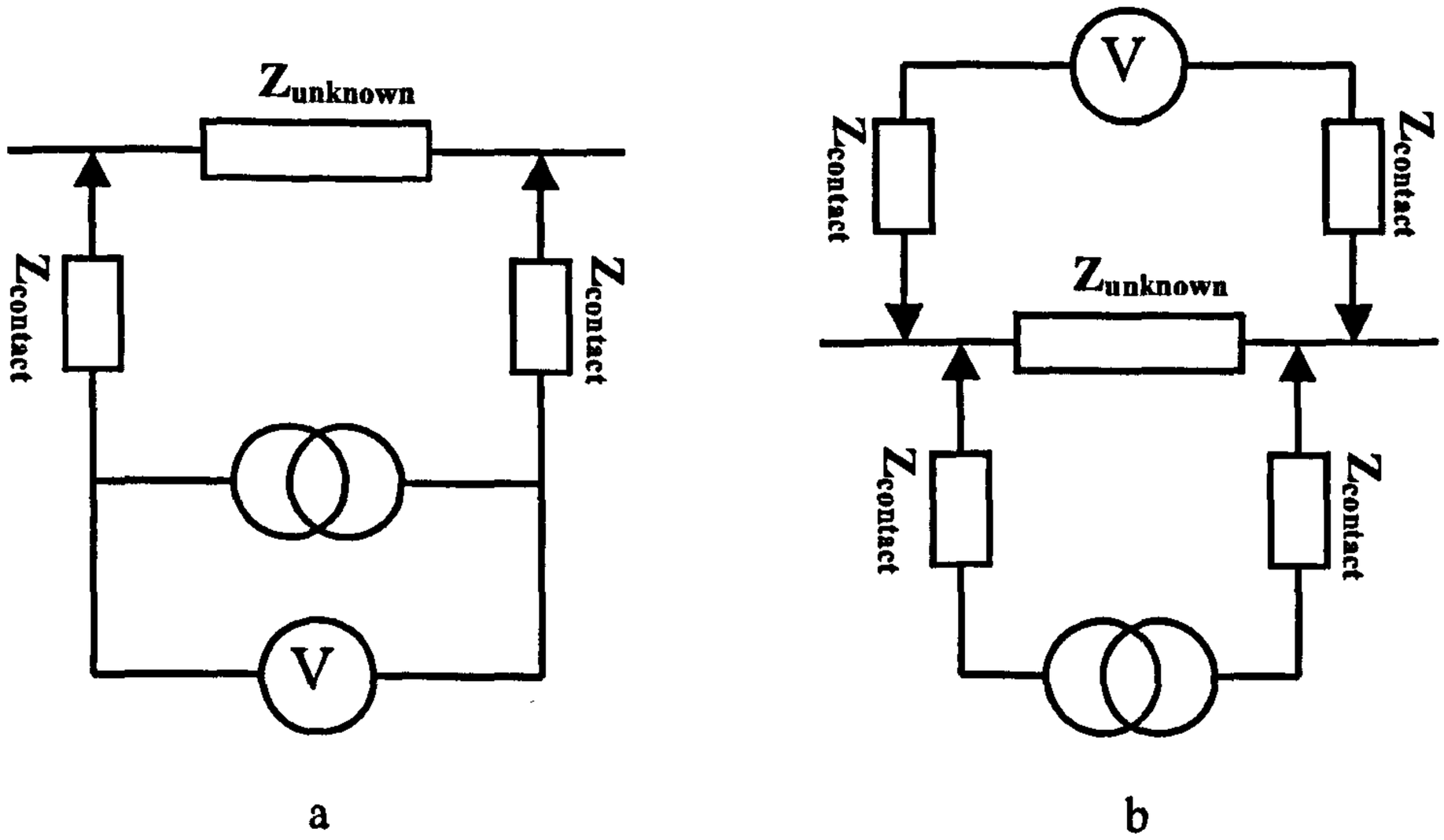

Figure 2.5 – Circuit diagrams of a) the two-terminal technique and b) the four-terminal technique as used for making impedance measurements in EIT.

2.2.5 Electrodes used for bio-impedance measurements

The electrodes perform the task of both supplying current to, and measuring surface voltage potentials on the part of the body in question, although usually not at the same

time. They are a vital link between the impedance measuring circuitry and the patient, and must fulfil several important requirements. Ideally they should have a low impedance so as not to interfere with the measurement of biological impedances. They should also represent as closely as possible the true voltages occurring at the surface of the skin.

A problem that arises when measuring *in-vivo* bio-potentials is that the area of contact between the electrode and the skin can become accumulated with ions, leading to what is known as interfacial polarisation. Thus the measured voltage differs from the actual surface potential that would have occurred in the absence of an electrode. For *in-vitro* work, however, where there is no skin between the electrodes and the tissue being tested, the problem of polarisation does not occur.

The most commonly used skin electrode is the silver-silver chloride electrode, (or Ag-AgCl). This is routinely used in electrocardiography. It comprises a silver electrode with a chlorided surface in conjunction with a silver chloride gel. Care must be taken when applying the chloride gel to avoid short-circuiting adjacent electrodes.

An additional problem associated with *in-vivo* electrodes is that physiological changes in the body (e.g. perspiration) can cause the surface potentials to vary in an unpredictable way. This leads to problems of noise in the measurement data which is hard, if not impossible to remove.

2.3 The concept of impedance imaging

Electrical Impedance Tomography involves imaging the variations in electrical impedances within an object by injecting currents and measuring voltages using electrodes placed on the surface of the object. Many measurements are collected, each of which represents the bulk impedance of all tissues through which current flows. Analysis of the data involves the use of mathematical relationships to establish the conductivity distribution from which an image can be formed. A background to the equations commonly used and principles on which the imaging is based now follows.

2.3.1 Equations governing the electrical behaviour in a volume conductor

In EIT the aim is to solve for the conductivity distribution of the imaging target based on a knowledge of the surface voltage potentials and the surface current density. An expression is therefore required for the relationship:

$$\sigma = f(\phi_s, J_s) \tag{2.3}$$

where σ is the conductivity distribution, ϕ_s represents the sampled surface potential measurements, J_s is the surface current density and f represents the function to be found. At the frequencies used for EIT imaging it is reasonable to assume that the electric field and current density can be described by Maxwell's equations of electrostatics (De Wolf, 2001):

$$\nabla \times E = 0 \tag{2.4a}$$

$$\nabla \cdot J = \rho \tag{2.4b}$$

where E is electric field, J is current density, ρ is charge density and ∇ is the gradient operator. Since the human body has no sources of free charges at the frequencies used in EIT, ρ can be considered as zero, and equation 2.4b becomes:

$$\nabla \cdot J = 0 \tag{2.5}$$

From Ohm's law the relationship between current density, electric field and conductivity is given as:

$$J = \sigma E \tag{2.6}$$

Substituting 2.6 into 2.5 yields:

$$\nabla \cdot \sigma E = 0 \tag{2.7}$$

The electric field E is defined as:

$$E = -\nabla\phi \tag{2.8}$$

where ϕ is the voltage potential field. Substituting 2.8 into 2.7 gives:

$$\nabla \cdot (\sigma \nabla \phi) = 0 \tag{2.9}$$

which describes the general relationship between conductivity and voltage potential distribution for any small region within the conducting volume. There are many solutions to 2.9 depending on the applied surface currents, therefore constraints must be applied in the form of boundary conditions. For this type of problem the boundary conditions fall into three categories; known surface voltages (Dirichlet conditions), known surface current densities (Neumann conditions) or a mixture of the two (Cauchy conditions).

2.3.2 The forward problem

Solving equation 2.9 to obtain ϕ based on a known conductivity distribution and specified boundary conditions (usually Neumann conditions) is known as the forward problem. Analytical solutions to this are only possible for simple shapes and boundary conditions. In general the forward problem is solved using numerical techniques such as the Finite Element Method (FEM) in which the conducting region is discretised into a number of small elements, each having uniform conductivity. Solving the forward problem for each element is then a trivial linear operation, and is performed whilst ensuring a consistency between the voltages and currents of adjacent elements (Murai and Kagawa, 1985).

Image reconstruction involves solving equation 2.9 to recover σ for a given surface voltage distribution (ϕ_s) and specified boundary conditions and is an inverse problem. The forward solver forms an important component of solving the inverse problem; iterative methods involve repeated calculations of the forward problem based on the latest update of σ, each time allowing increasingly accurate estimates of σ to be calculated until the surface potentials calculated by the forward solver converge with the actual measurements (see section 2.5.1). Other methods involve calculation of the sensitivity matrix (detailed in section 2.3.3) for which the forward solver is also

required. Section 2.5 outlines a number of different approaches to image reconstruction.

2.3.3 The sensitivity theory

For a given data measurement strategy, the sensitivity matrix describes the relationship between changes in small conducting regions, or pixels, within an object and the corresponding changes in the measured voltages. It is based on the sensitivity theory which is now discussed. Consider a conducting region Ω to which four electrodes (A,B,C and D) are connected. Let ϕ be the potential field associated with current I_ϕ flowing in electrode pair AB and let ψ be the potential field associated with current I_ψ flowing in electrode pair CD (See figure 2.6).

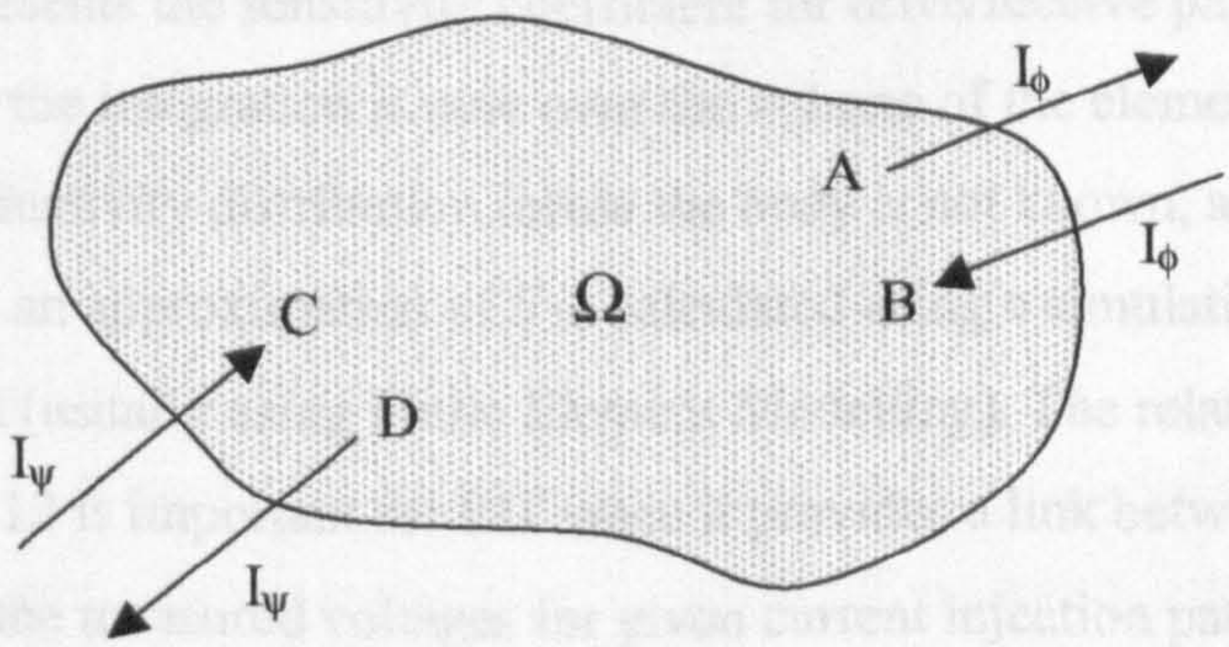

Figure 2.6 – An illustration showing the terms used to represent current and electrodes associated with a conducting region Ω.

Geselowitz (1971) showed that the mutual impedance Z is given by:

$$Z = \frac{\phi_{CD}}{I_\phi} = \frac{\psi_{AB}}{I_\psi} \qquad 2.10$$

In other words there is a reciprocity between 4-terminal impedance measurements such that if the current source and voltmeter connections are exchanged, the same voltage would be obtained. Geselowitz (1971) further developed the theory to arrive at an expression for the sensitivity relationship between a change in impedance of a small region within the conducting volume and the change in mutual impedance:

$$\Delta Z = -\Delta g \int \frac{\nabla \phi}{I_\phi} \cdot \frac{\nabla \psi^t}{I_\psi} dv \qquad 2.11$$

where ΔZ is the change in mutual impedance, Δg is the change in impedance of a small region enclosed by volume v and the superscript t refers to the potential field measured after the impedance change inside volume v. If it is assumed that Δg is small then ψ^t tends towards ψ. With the additional assumption that currents I_ϕ and I_ψ are unit, the sensitivity relationship becomes:

$$S_{i,j} = -\int \nabla \phi \cdot \nabla \psi dv \qquad 2.12$$

where $S_{i,j}$ represents the sensitivity coefficient for drive/receive pair i and image element j, and the integration is now over the volume of the element (Kotre, 1994). Since the conductivity distribution inside the body is not known, a true solution to S is not known, so an approximation of S is calculated using a simulation of the intended imaging target (usually using Finite Element Modelling). The relationship described by equation 2.12 is important for EIT since it provides a link between the image elements and the measured voltages for given current injection patterns. It is more conveniently expressed in matrix form as:

$$v_i = S_{i,j} c_j \qquad 2.13$$

where v is a vector containing all the voltage changes as a result of the conductivity changes in contained vector c. The image reconstruction process can be thought of as recovering c from a knowledge of v, for which the inverse of S is required:

$$c = S^{-1} v \qquad 2.14$$

Indeed this is the basis of some of the image reconstruction methods used in EIT.

2.4 Strategies used for multiple impedance measurements

The data collection strategy has three important elements; electrode positions, current injection patterns and voltage measurement patterns. The electrode positions are important since they define the points at which current is injected and voltages measured. For 2-dimensional imaging there has been an almost universal choice to place the electrodes in rings of 16 or 32 electrodes, spaced evenly around the circumference of the object to be imaged. Other variations are now more common, however, especially as the concept of 3-dimensional EIT is being explored, and they are outlined in greater detail in Chapter 3 where issues relating specifically to mammography are addressed. The patterns of injected current applied to the electrodes are important since this defines the electric potential field within the object to be measured. The voltage measurement patterns are important since this represents the way in which the electric potential field is sampled.

2.4.1 Current injection

2.4.1.1 Bipolar current injection

The most common current injection method uses only two electrodes at any one time for passing current into the body. For a 16-electrode system this allows a total of 8 unique current injection 'modes', each of which may be rotated through 16 different positions. In practise, only 3 of the 8 modes tend to be used. The most common is termed the 'adjacent drive' method, where the current is injected only through adjacent electrodes. The 'polar drive' method involves injecting current through diametrically opposite electrodes. Less common is the 'cross' method, where electrodes separated by 90° are used to carry the current (see figure 2.7).

In general, the adjacent drive method has been found to produce the best images in terms of resolution, although the polar drive method has been found to work more favourably when the data is noisy or if the conductivity changes tend to be towards the centre of the object (Avis and Barber, 1994).

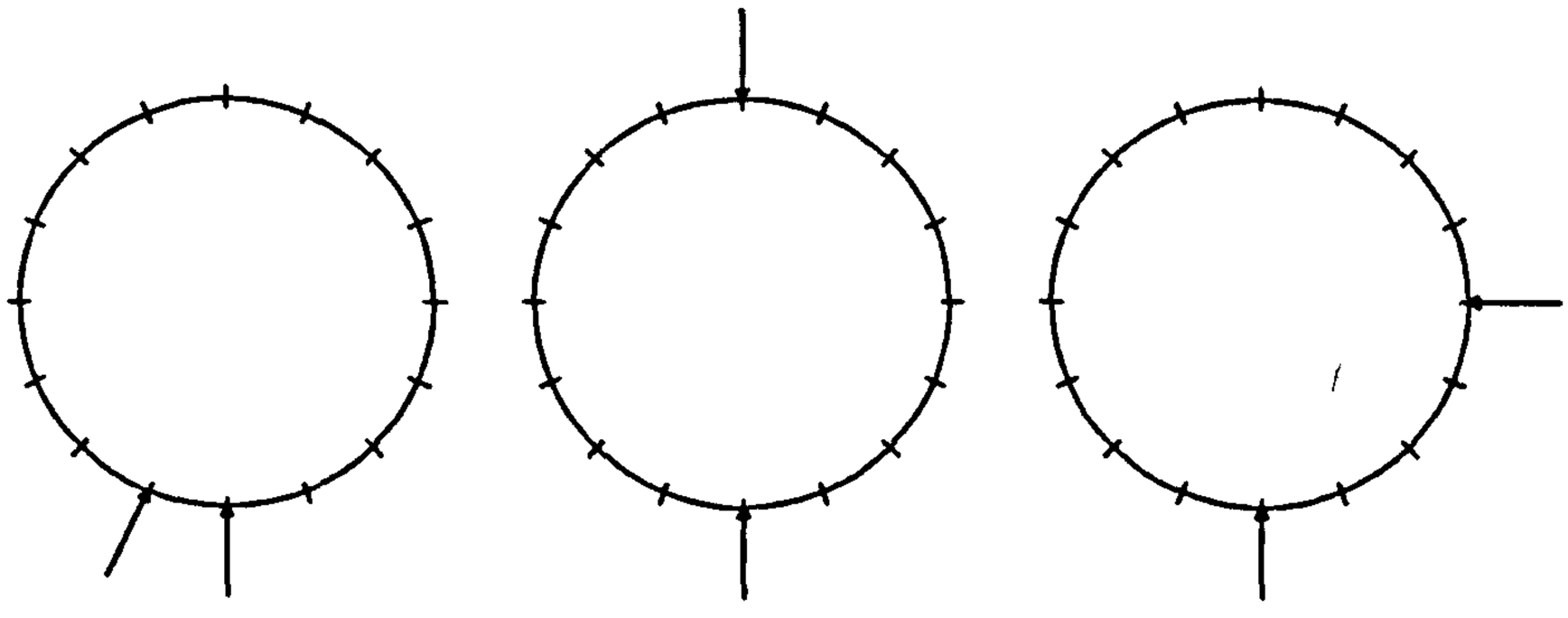

Figure 2.7 – An illustration of the three common bipolar drive methods used. The arrows indicate the positions of the drive pair for each case (not the flow of current).

2.4.1.2 Optimal current injection

It has been shown mathematically that to achieve the maximum distinguishability of one conductivity distribution against another, current should be simultaneously injected through all electrodes. The mathematics involved in selecting the optimum current injection patterns is shown by Isaacson (1986) to be related to the eigenfunctions of the difference in voltage fields for the two conductivity distributions to be distinguished between. An EIT imaging system and image reconstruction algorithm employing this optimal currents technique is described by Woo *et al*, (1993). The problem with this approach, however, is that if all electrodes are carrying current, then the 4-terminal principle is violated. Since the work presented here is concerned with the De Montfort Mk2b system which uses bipolar current injection, optimal current injection patterns will not be considered further.

2.4.2 Measuring the surface voltage potentials

Voltage measurements are generally made between all adjacent pairs of electrodes which are not used for carrying current, thus maintaining the advantages of the 4-terminal principle. This is clearly not always possible with the multiple currents method for which the 2-terminal method is often used. The number of voltage measurements made depends on the overall number of electrodes used. For a 16-electrode system with bipolar current injection, there are a total of 14 voltage electrodes available for voltage measuring at any one time, from which 13 potential differences can be measured, producing a total of 208 measurements. In practise,

however, only half of these will be unique impedance observations due to reciprocity of 4-terminal impedance measurements. One method sometimes used for increasing the number of independent measurements slightly is to have the voltage measuring electrodes interleaved between the current electrodes (requiring a total of 32 electrodes), thus allowing 16 voltage measurements for each current pattern and hence a total of 256 measurements per frame of which 128 are unique (again due to reciprocity).

2.5 Image reconstruction methods used in EIT

Image reconstruction algorithms in EIT tend to fall into one of two categories; those which aim to reconstruct the absolute conductivity through the use of iterative methods, and those which perform a single-step linearised reconstruction. The iterative methods are, by their nature, time consuming, but can if set up properly arrive at impressively accurate conductivity maps. Conversely, the single-step methods are faster but less accurate and tend to be used for reconstructing the difference in conductivity between two sets of measured data rather than the absolute conductivity. Some of the more commonly used image reconstruction algorithms are briefly reviewed here. The method chosen for use in this work is the sensitivity method (section 2.5.4) and is described in detail in section 4.2.2.

2.5.1 Modified Newton Raphson method

This method uses a FEM forward voltage solver in conjunction with a modified Newton-Raphson iterative procedure to minimise the error between the measured voltages and those predicted by the forward solver (Yorkey *et al*, 1987). If the forward transform F to predict the boundary voltages V from a known conductivity distribution c is given by:

$$V = F(c) \tag{2.15}$$

then the squared error $e(c)$ of the reconstruction is:

$$e(c) = \tfrac{1}{2}(F(c) - V_0)^T (F(c) - V_0) \tag{2.16}$$

where V_0 is the measured surface voltages and ^{T} represents the matrix transpose. The idea of the reconstruction method is to minimise the error function, and this is achieved by differentiating it and setting the result to zero:

$$e'(c) = [F'(c)]^T [F(c) - V_0] = 0 \qquad 2.17$$

where F'(c) is known as the Jacobian matrix. Yorkey *et al* (1987) solved this and found an expression for the k^{th} conductivity update to be:

$$\Delta c^k = -\left\{[F'(c^k)]^T [F'(c^k)]\right\}^{-1} \left\{[F'(c^k)][F(c^k) - V_0]\right\} \qquad 2.18$$

This image reconstruction method was compared against many other methods by Yorkey *et al* (1987) and, of the iterative techniques, is shown to have the fastest and most reliable convergence.

In order to overcome lengthy image reconstruction times associated with the iterative nature and also the time taken in re-computing the Jacobian matrix, a single step version of the Newton-Raphson method has been developed (Cheyney and Isaacson, 1995). The so-called NOSER algorithm (Newton One Step Error Reconstruction) uses a pre-computed Jacobian matrix, and calculates only the first iteration of the full iterative procedure. The algorithm is claimed to be able to handle 60 image reconstructions per second based on a 32-electrode system (Cheyney and Isaacson, 1995), thus making real-time imaging possible.

2.5.2 Double constraint method

This finite element based method proposed by Wexler *et al* (1985), utilises a twofold iterative process in which the first part involves calculating the internal voltage distribution based on the known boundary currents (Neumann conditions) and the most recent estimate of conductivity distribution. In the second stage, the internal voltage distribution is recalculated based on the measured boundary voltages combined with the known boundary currents (Cauchy conditions). The second distribution is regarded as more accurate since it is based on measured voltages, and is used to arrive at new

conductivity estimates which bring the internal voltage distribution closer to the best calculation. These two procedures are repeated iteratively.

Although the double constraint method does not involve an inversion of the sensitivity matrix, and is hence immune to the ill-conditioning problems normally associated with sensitivity matrices, in practise it takes a long time to converge (Yorkey *et al*, 1987).

2.5.3 Back projection

The back projection method is a single step image reconstruction algorithm, and was developed at Sheffield University by Barber *et al* (1983). Rather than using the differences in measured voltages, they chose to use normalised perturbed data, thus cancelling out errors caused by poor electrode positioning. They also adopted a reconstruction approach based on the x-ray CT concept of backprojecting boundary data into the image for several different angular positions. Since the current paths in EIT do not flow in straight lines as x-rays do, it involves projecting along the curved equipotentials. The action of backprojection is linear and can be performed in a single matrix multiplication of the form:

$$c_m = Bg_n \qquad 2.19$$

where c_m is a normalised conductivity vector of m pixel values, g_n is the vector of n normalised perturbed boundary voltages and B is an (m x n) matrix containing the backprojection coefficients.

The equipotential lines are calculated using a dipole approximation for the current sources. As a consequence they tend to introduce spoke-like artefacts in the reconstructed images. To overcome this a filter has been developed to map the normalised measured voltages into a form which when backprojected using the method described above would result in the true image. The improved reconstruction algorithm has the form:

$$c_m = B(FB)^{-1} g_n \qquad 2.20$$

where the first B is the back-projection matrix which will form the image, F is a forward solving matrix which maps conductivity to voltages and the second B is a back-projection matrix designed for the conductivity distribution from which F was derived. The filtering operation is formed by the $(FB)^{-1}$ matrix. A comprehensive description of the development of this method is given by Avis (1993).

2.5.4 Sensitivity method

Many image reconstruction methods are based on the sensitivity theorem presented by Geselowitz (1971) (See section 2.3.3). The basic operation is initially to generate the sensitivity matrix which contains the sensitivity relationships between conductivity perturbations at each point in the image space and the subsequent changes observed in the measured voltages. A simple method for this is to measure the changes in simulated surface voltage measurements in response to small conductivity perturbations in a simulated conductivity distribution. This is known as the perturbation technique and is described in more detail in section 4.2.3. By its nature the sensitivity matrix contains information about the current injection patterns, voltage measurement positions and image element structure. Since the matrix effectively maps conductivity distributions to differential measured voltages, its inverse does the opposite, providing differential conductivity values for a given set of measured voltages. Inversion of the sensitivity matrix presents an interesting problem since it is ill-conditioned. A common technique is to use the singular value decomposition method, and to truncate any particularly ill-conditioned measurements (Avis 1993). Since the sensitivity method was chosen as the most appropriate algorithm for the work presented here, it is described in more detail in Section 4.2.2.

2.6 Overview of Electrical Impedance Mammography systems

Electrical Impedance Tomography has been applied to breast imaging in a number of cases, where the term Electrical Impedance Mammography (or EIM) is used. Some of these are described below:

2.6.1 De Montfort Mk2b EIM system

The DeMontfort Mk2b EIM imaging system (developed at De Montfort University, Leicester, UK) is currently based on 32 electrodes arranged in a 2-dimensional circular

array. Although no literature has been published on the proposed positioning of a breast within the electrode ring, it is assumed that the preferred orientation of the patient would be prone such that the breast is pendant, therefore presenting its smallest natural diameter to the electrode ring. The data collection strategy comprises 16 current-carrying electrodes interleaved between 16 voltage electrodes with which an adjacent drive – adjacent receive measurement strategy is used. The current drive circuitry is designed to supply 1mA over a frequency range of 10kHz to 5MHz and is applied differentially through 2 electrodes at a time via a pair of fully programmable 16-channel multiplexers. The waveform generators are fully programmable in frequency, phase and amplitude from the host PC. The surface voltages are switched serially via a pair of 16-channel multiplexers to the detection circuitry in which a programmable gain amplifier (PGA) automatically selects the most appropriate gain to fill the ADC's 5V input range. An analogue multiplier is used to demodulate the carrier frequency, after which the DC signal is sampled using a 16-bit, 100kHz ADC. Real and imaginary voltages are measured by using in-phase and quadrature demodulation waveforms. The system has the capacity to compensate for known phase-shifts in the circuitry and cables by storing a phase calibration look-up-table and applying this to the demodulation waveforms.

The acquisition time for one frame of data is approximately 1 second per frequency. The system noise level at the ADC input is ~2mV, producing a signal to noise ratio performance of between 44-60dB which is improved to 50-60dB when the PGA is enabled. Image reconstruction is computed as the impedance update vector calculated from the first iteration of the modified Newton-Raphson method. This is similar to the NOSER algorithm, except that the image is presented as the difference in conductivity from a predefined background level rather than the absolute conductivity.

No in-vivo images have been acquired for breast work at this stage, although some 2-dimensional simulation work has been carried out to assess the expected tumour detectability based on modelling known breast tissue conductivities (Wang *et al*, 2001). In-vivo images of the thorax have been acquired successfully, with the ability to observe lung ventilation and a high conductivity region associated with cardiac perfusion.

2.6.2 Dartmouth College EIM system

The EIM imaging system at Dartmouth College uses an annular ring of 32 electrodes in which a pendant breast is positioned with the aid of a purpose built patient bed. A specialised mounting system allows the electrodes to translate radially and vertically in order to accommodate a wide range of breast shapes (Kerner *et al*, 2001a). The electrode driving circuitry can operate as either a voltage or a current source, and there is a dedicated drive channel for each electrode. The input to each drive channel is supplied by a waveform generator operating in the range 1kHz to 1MHz and the input amplitude to each channel can be individually programmed. Thus it is possible to drive current through all electrodes simultaneously with fully programmable patterns. The boundary voltages are switched via a switching matrix to a 16-bit ADC which samples the waveform at 200kHz. A multiperiod undersampling technique is used to capture the waveform at an effective sampling rate greater than the 200kHz conversion speed. The amplitude of the sampled signal is recovered using a digital phase-sensitive detection technique, and allows both real and imaginary components to be measured (Hartov *et al*, 2000). Although their system can apply currents to all electrodes simultaneously, it is found that voltages measured from current carrying electrodes are subject to errors caused by unknown skin contact impedance (Kerner *et al*, 2001b). To overcome this the desired current patterns (in this case trigonometric patterns) are decomposed into currents applied sequentially through 1 electrode at a time and a fixed ground, whilst making voltage measurements on all the remaining electrodes. By combining weighted sums of the measured voltages, trigonometric current patterns can be synthesized.

The Dartmouth system is quoted to have a frame rate of 0.22 images/s suggesting an acquisition time of 4.5s, although it is not clear if this includes a range of frequencies or one single frequency. The signal to noise ratio performance is 75dB (Hartov *et al*, 2000). Image reconstruction is performed using the Newton-Raphson method to optimise a conductivity distribution modelled by a pair of finite element meshes.

In a preliminary in-vivo breast imaging trial, 16 electrodes were used to supply currents at 10 different frequencies from 10kHz to 950kHz. Out of 13 patients

examined, all 4 documented abnormalities were detected as regions of increased permittivity (Osterman *et al*, 2000).

2.6.3 Moscow EIM system

A 256-electrode 3D EIM system developed at the Institute of Radio-Engineering and Electronics within the Russian Academy of Sciences in Moscow is described by Cherepenin *et al* (2001). It comprises a flat bed of 256 electrodes, arranged in a grid format on a hand-held probe which is pressed onto the breast parallel to the chest wall. In addition, two remote electrodes are attached to both of the patient's wrists, one used for supplying current to the patient and the other as a voltage reference point. The alternating current source of 0.5mA is driven by a waveform generated from a digital-to-analogue converter. A frequency range of up to 110kHz is possible, although it is claimed that 50kHz produces better quality results (Korjenevsky *et al*, 2001). One of the current source outputs is connected permanently to one of the wrist electrodes, whilst the other is selected sequentially from the 256 breast electrodes via a multiplexer. For the voltage detection circuitry the remaining 255 electrodes are selected in sequence by a multiplexer and referenced to the second wrist electrode. The output voltage is sampled using a 14-bit ADC (13 effective bits) and the amplitude is obtained using digital demodulation. Using this method a total of 65280 voltage measurements are made in a time of less than 20 seconds.

Although only one acquisition is made, the image reconstruction algorithm generates a set of seven image slices, allowing depth information to be obtained down to 5cm beneath the array (Cherepenin *et al*, 2001). Image reconstruction is based on a modification of the backprojection technique (see section 2.5.3) in which the 3D equipotential field distribution is assumed to conform to spherical surfaces.

In-vivo experiments using this device include monitoring changes in the breast throughout the menstrual cycle (Trokhanova *et al*, 2001), and some examples of images from patients with known carcinomas and lactating breasts (Korjenevsky *et al*, 2001).

2.6.4 TranScan T-Scan™ 2000

The T-Scan breast imaging system, developed in Migdal Ha'Emek, Israel, has many similarities with the Moscow EIM system. It uses a flat grid of either 64 or 256 electrodes housed in a hand-held probe which is pressed onto the breast. Alternating currents in the frequency range 100Hz-100kHz are supplied via a large probe held in the patient's hand. Each of the breast electrodes is sequentially switched to a voltage measuring circuit whilst holding the remaining breast electrodes at ground potential. The received voltages are digitised and filtered to recover the in-phase and quadrature components at a range of different frequencies. If only 64 electrodes are used, the system is claimed to have a frame rate of 17 frames/s. The signal to noise ratio of the detection circuitry is just under 70dB at 100Hz but falls to 40dB at 100kHz (Assenheimer *et al*, 2001).

Image reconstruction is not attempted in the conventional way associated with EIT, but from the surface measurements, an admittance map of the area under the breast electrodes is formed. Based on modelling the tumour as a spherical region of increased conductivity, it is argued that distortions in the measured surface voltage field will reflect the tumour's effect on current density, and can be used to estimate the depth, size, conductance and dielectric constant of the tumour (Assenheimer *et al*, 2001).

2.7 Discussion

In this chapter, the behaviour of the electrical impedance of biological tissue has been presented, and shown to be potentially useful as a tool for distinguishing between different tissue types; in particular between healthy and cancerous tissues. The mathematical equations underpinning the relationship between conductivity, current density and electric fields have been explained. These provide the mechanisms behind which impedance imaging works, and various techniques for computing the conductivity distribution have been outlined. Since these methods are all attempting to solve an ill-posed, inverse problem, they are prone to large errors caused by only the slightest inaccuracies in measurement. The practical consequence of this is poor spatial resolution of the reconstructed images.

Of the recently documented Electrical Impedance Mammography systems, only the Dartmouth group have presented imaging results from in-vivo breast cancer trials. Their system is successful in detecting tumours down to 3-4cm in size. For smaller tumours (down to 0.8cm) the images become ambiguous. For EIM to be considered a useful adjunct to x-ray and ultrasound imaging, it should be proven to have the capability of imaging the smaller tumours.

The purpose of the following chapter is therefore to establish the key factors which directly affect image resolution and to develop a suitable method for quantifying spatial resolution.

CHAPTER THREE

IMAGE RESOLUTION IN ELECTRICAL IMPEDANCE TOMOGRAPHY

3.1 Introduction

This chapter aims to identify the origins of the characteristically poor image quality in EIT. In doing so, key factors which influence the image quality are explored, and in particular, the issue of data collection strategies. In addition some of the methods reported in literature for measurement of spatial resolution are reviewed since quantitative analysis of spatial resolution forms an important part in the experimental work undertaken.

3.2 Factors which affect image resolution

In an image, spatial resolution is related to information. A poor resolution image gives little information to the person viewing it, whereas a high-resolution image presents much information. The spatial resolution of an imaging system can be thought of as the efficiency with which it collects information from and forms images of the original object. The factors that affect this can be broken down into three categories:

- Limited quantity of measured data
- Limited signal-to-noise ratio of measured data
- Ill-conditioning of the detection system

Each is now separately addressed.

3.2.1 Limited quantity of measured data

It has already been stated in section 2.4.2 that for a 16-electrode system (such as described by Smith *et al*, 1995) there are only 104 independent (4-terminal) measurements which can be made. This implies that there can only be enough fully independent information for 104 pixels (or approximately a 10x10 pixel image). This can be contrasted with MRI for example, where collecting 65536 independent measurements to form a 256x256 image would be regarded as commonplace (Webb, 1988). It has been suggested that to obtain enough information for a 100x100 EIT

image would require 448 electrodes (Brown and Seagar, 1985). For 2-dimensional imaging the common electrode formats are a ring of 16 electrodes (e.g. Smith *et al*, 1995) or a ring of 32 electrodes (e.g. Cook *et al*, 1994). For 3-dimensional imaging the available surface area is increased with the consequence that more electrodes can be used. Common electrode numbers are: 32 electrodes (Newell *et al*, 2001), 64 electrodes (Metherall *et al*, 1996) and 256 electrodes (Korjenevsky *et al*, 2001). Using more electrodes, however, comes with a cost; firstly if the electrodes are manually positioned on the skin their positions are subject to human error, and secondly the circuit complexity is increased, thus introducing a greater scope for errors arising from parasitic capacitances associated with the signal carrying cables and components. While increased numbers of electrodes may help to improve the resolution at the periphery of the image, it is generally the case that regions furthest from the surface still suffer from poor resolution. The problem is that the depth of penetration of current into the object (and hence the depth at which impedance changes can be detected by external measurements) depends on the distance between the driving electrodes. If they are spaced far apart the current penetrates deeper, but then the current density is low since the current is spread out over a large volume. Since the current density in the deeper structures is small, the resulting surface measurements in response to deeply located impedance changes are also very small. Conversely the current penetration for closely spaced driving electrodes is shallow, resulting in a high current density in the surface regions. Impedance changes close to the surface therefore result in a higher level of surface voltage change. A further problem is that when more electrodes are added, the distance between the measuring electrode pairs is reduced, hence the differential voltage magnitude and measurement accuracy is reduced since the system noise is unchanged. The result is that the overall SNR is reduced.

3.2.2 System noise and measurement accuracy

In the precision sense, the resolution of a measurement system is ultimately limited by a) its ability to cope with noise and b) the precision of the device used for recording measurements (in this case the analogue to digital converter). For imaging at a spatial resolution of 100x100 and a pixel accuracy of 1%, Brown and Seagar (1985) calculated that a noise-to-signal ratio of 1e-7 (or a SNR of 140 dB) would be required. (Compare this with a practical example of the Dartmouth system which has a SNR in

the region of 75dB, Hartov *et al*, 2000). A simple way of improving the SNR is to increase the injected current so that the resulting surface potentials are increased, thus raising them further above the noise. In practise this is not possible for clinical investigations due to legal limitations on the permitted current (BS5724). Therefore improvement in SNR by this route is prevented.

The issue of measurement precision is addressed by Isaacson (1986) who presents a mathematical analysis for the distinguishability of conductivities by electrical impedance tomography. In this work, a circular conductor having a relative radius R at the centre of an otherwise constant background conductivity (as shown in figure 3.1) is considered.

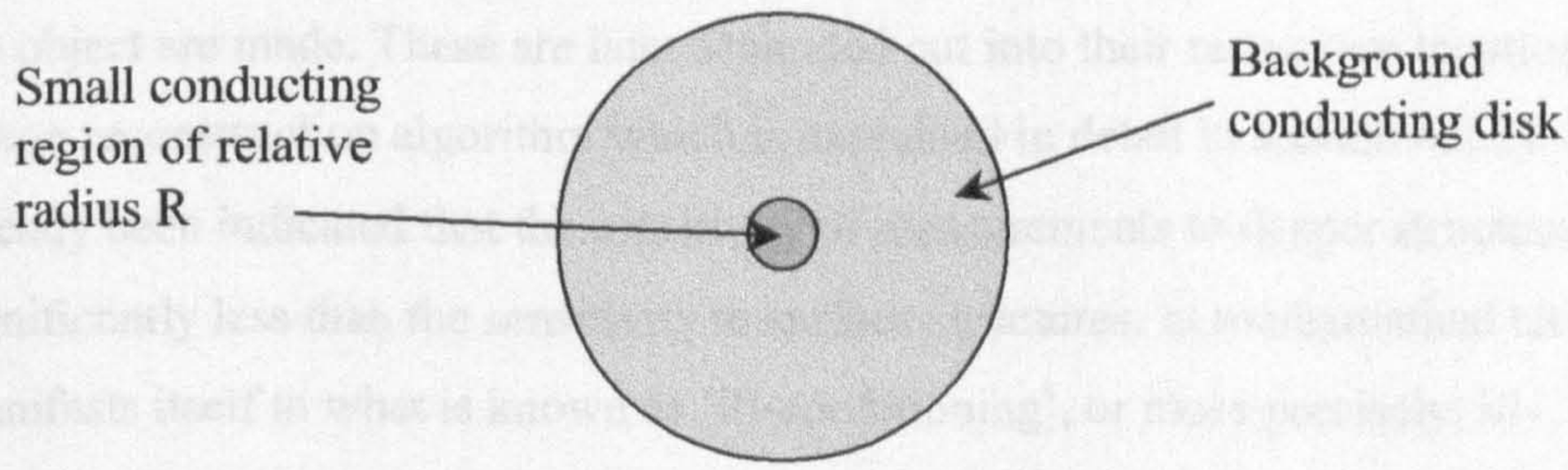

Figure 3.1 – Illustration of the conducting region analysed by Isaacson (1986).

If the norm of the applied currents is taken to be unity, then the required measurement precision ε to detect the small conducting region is given by:

$$\varepsilon < \frac{2R^2}{(1-R^2)} \quad \text{measured in Volts} \qquad 3.1$$

where R is the relative radius of the small region. For example, to achieve a spatial resolution of 1% (R = 0.01) would require that the noise performance and ADC resolution must be better than 0.2mV. For EIT systems where fast data acquisition is not an issue (i.e. breast imaging) signal averaging is often used as a way of reducing the noise, thereby improving the precision of the system. In considering the precision of data capture (i.e. the analogue to digital converter), EIT imaging presents another problem in that the dynamic range of the measured voltages can be as high as 200. Therefore if the circuit is calibrated so that the maximum expected signals just fill the

ADC input range, then the smallest size signals will be sampled with less accuracy. As an example, if the ADC uses 16 bits, then the maximum possible signal (65535) is subject to a quantization SNR of 102dB, but if the dynamic range is 200 then the minimum signal (328) has a quantization SNR of 56dB. Some EIT systems (such as the DeMontfort Mk2b system) overcome this by the use of a programmable gain amplifier (PGA) stage that has the effect of boosting the smaller signals by a known gain so that they fill the input range of the ADC. The true size of the signal is later recovered by dividing the signal by the known gain value.

3.2.3 Ill-conditioning of the detection system

At the data collection stage, rather than making impedance measurements of the object on a 'pixel-by-pixel' basis, observations of bulk impedance covering large portions of the object are made. These are later separated out into their respective locations by the image reconstruction algorithm which is explained in detail in section 4.2.2). It has already been indicated that the sensitivity of measurements to deeper structures is significantly less than the sensitivity to surface structures. In mathematical terms this manifests itself in what is known as 'ill-conditioning', or more precisely, ill-conditioning of the sensitivity matrix which contains the relationships between injected current, impedance distribution and measured voltages. At the image reconstruction stage some form of inversion of the sensitivity matrix is usually required in order to solve for the impedance distribution. Inverting an ill-conditioned matrix is mathematically troublesome, and in extreme cases impossible. It often requires careful manipulation of the matrix (a process known as regularisation) in order to prevent an unstable result. Regularisation techniques always seek to suppress the influence of the less sensitive parts of a matrix since it is these, which when inverted, cause instability (in a similar way that dividing any number by a very small number produces a large result). As a consequence the regions within the object that correspond to the low sensitivity measurements (i.e. those far from the electrodes) are poorly represented, resulting in degraded resolution in those areas (Dobson and Santosa, 1994).

3.3 The data measurement strategies

The degree of ill-conditioning is intricately bound up in the strategy used for driving current and measuring voltages since they both play an important part in defining the

sensitivity matrix. There are, however, three distinct components that together define the measurement strategy for EIT. These are:

- Electrode placement
- Current drive patterns
- Voltage measurement patterns

The current and voltage patterns are clearly dependent on the positioning of the electrodes since they determine the available points for injecting current and measuring voltage. Electrode positioning is therefore an important part of the measurement strategy and is considered in detail in Chapter 6 where the effect of electrode positioning on image quality is assessed. A review of the common electrode placement schemes found in literature follows.

3.3.1 Two-dimensional measurement strategies

Mueller *et al* (1999) stated that for an n-electrode system there are n(n-1)/2 independent measurements since at most n-1 independent current patterns can be applied, and there is a reciprocity between the applied currents and measured voltages. This suggests a maximum of 120 independent measurements from a 16-electrode system. Assuming a 2-dimensional ring of electrodes is used with bipolar current injection, then there are in fact n(n-3)/2 independent measurements if the 4-terminal impedance measurement principle is upheld (or 104 from a 16-electrode system).

For 2-dimensional imaging based on a circular electrode array and bipolar current drive, the Current-Voltage patterns tend to be grouped into a few different 'modes' based on the separation between the current driving pair. For a 16 electrode system there are a total of 8 of these current injection modes. By far the most common is the so-called *adjacent* or *neighbouring* method, where the source and sink electrodes are always adjacent to each other. The *polar* drive method, where the source and sink electrodes are diametrically opposite one another has received some attention, as has the *cross* method where the current electrodes are separated by 90°. Avis and Barber (1994) showed that of these three, the *adjacent* method performs better in terms of

image resolution, but that the *polar* method can produce better images under certain circumstances when the noise is a dominating factor.

Hua *et al* (1987) compared these three methods along with another approach known as *optimal* current injection where all of the available electrodes are used for injecting current in such a way as to produce the best signal-to-noise ratio. The optimum currents are calculated as the eigenfunctions having the largest eigenvalue of the impedance matrix, which for a centrally located conductivity perturbation turn out to have a trigonometric distribution (Isaacson, 1986). They (Hua *et al*, 1987) concluded that the *optimum* current method is the best at handling noise, followed by the *cross* and *polar* drive methods, but that the *neighbouring* (or *adjacent*) method is the worst in terms of noise-handling ability. This is in agreement with the work published by Avis and Barber (1994) in terms of the noise performance. The spatial resolution achieved by the *optimum* current method has also been found to be superior to other methods (Hua *et al*, 1991). 2-dimensional in-vivo imaging using the trigonometric current patterns is reported by Osterman *et al* (2000) and Newell *et al* (2001).

Another electrode placement method that has received limited attention in 2D EIT is the linear array where 16 electrodes are spaced evenly along a straight line. Powell *et al* (1987) reports results from a preliminary investigation which uses current drive methods based on a linearised version of the adjacent method used in circular imaging. This is similar to techniques used for geological imaging of the earth's strata (Tsourlos *et al*, 1999). For medical purposes, linear arrays have been shown to be potentially useful for imaging the repair of long bone fractures (Wheeler, 1996).

3.3.2 Three-dimensional measurement strategies

In 3D EIT the concept of image planes is discarded and instead, image volumes are considered. Since the available surface area is generally larger when dealing with volume imaging, the issue of electrode placement opens up considerably. This in turn allows for many more angles from which current can be injected, hence the consideration of 3D measurement strategies results in a broader spread of ideas. A review of some of these now follows.

3.3.2.1 Imaging a cylindrical volume

In a pilot investigation into 3D EIT image reconstruction algorithms, Kleinerman *et al* (1996) compare the sensitivity matrix for a conventional circular 2D conducting region with that of a circular plane within a 3D cylindrical conductor. They show that the sensitivity matrix for the 3D case is better conditioned than that of the 2D case and that more information about the central part of the image is available in the 3D case.

Taking this a stage further, Metherall *et al* (1996) describe a 3D cylindrical EIT system in which 64 electrodes are arranged in 4 rings of 16 electrodes at equally spaced heights. They demonstrate three different bipolar data collection methods using semi-adjacent electrodes (spaced 2 electrodes apart). These patterns are chosen such that current can either be injected parallel to the circular planes of the electrodes, or along the axial direction or both. They show that the best image resolution is achieved when current is injected in both directions. Newell *et al* (2001) describe a cylindrical system having 32 electrodes arranged in 4 rings of 8 electrodes. They apply multiple current patterns with a trigonometric distribution via all electrodes simultaneously, thus current is not restricted to any particular direction.

3.3.2.2 Imaging the volume beneath a flat surface

Another electrode geometry used for 3D EIT is a flat grid of evenly spaced electrodes. Several examples of this have been developed with breast imaging in mind.

Assenheimer *et al* (2001) describe a grid array used in conjunction with a hand held probe. In their system, 2-terminal impedance measurements are made by driving current between the hand-probe and each of the breast electrodes, and measuring the voltage. In this way current is driven directly through the breast and along the patient's arm. A slightly different approach to this is reported by Korjenevsky *et al* (2001) in which current is driven between one of the patient's wrists and one of the breast electrodes, whilst the voltage is measured between the patient's other wrist and another of the breast electrodes. By making selections from all of the breast electrodes, 4-terminal impedance measurements are made which are used to reconstruct 3-dimensional information about the breast impedance. Kotre (1996) applies currents to a grid array by stepping through all adjacent pairs in one direction, and afterwards repeating the procedure for the orthogonal pairs. Voltages are measured in a similar manner from electrodes not in use for driving current. He demonstrates *in-vivo* images

of gastric activity. Mueller *et al* (1999) also report use of a flat grid array, but they simultaneously apply currents through all electrodes.

Results from all the methods described are mainly qualitative rather than quantitative so it is hard to arrive at a conclusion as to which data collection method performs the best.

3.3.2.3 Imaging the head

A different approach to electrode placement and current / voltage patterns is required for EIT imaging of the head. Gibson *et al* (2001) suggest that optimum electrode placement is achieved by ensuring an even inter-electrode spacing over the surface of the head rather than applying grid or ring symmetry. For the current-source electrodes they claim that the best sensitivity to changes in brain impedance requires current to be driven through opposing electrodes. To achieve this a 'travelling salesman' algorithm is used to list pairs of electrodes with the maximum distance between them. For the voltage measuring electrodes adjacent pairs are reported to give the best performance in terms of spatial resolution. Although this does not apply directly to breast imaging since the breast is not surrounded by a low conductivity skull, it is an important result because both the head and the breast are approximately hemispherical objects.

3.3.3 Is there an optimum measurement strategy?

The recent interest in 3D EIT imaging has spawned a much broader approach to measurement strategy. In some cases such as imaging cylindrical volumes or regions beneath a flat surface, the choice of electrode positions is perhaps intuitive. For imaging of irregular surfaces such as the head or the breast, it is not clear as to what arrangement of electrodes would be most useful. The general trend from published work on 3D imaging tends to suggest that whatever shape the object happens to be it is best to aim for an even distribution of electrodes over the surface. However, for breast imaging a slightly different problem arises in that breast size and shape can vary significantly between different patients. In this case it is not obvious as to how the electrodes can be evenly spaced in a repeatable manner. In addition, it is not clear as to how the choice of electrode positioning will affect the final image quality.

Whatever scheme is used to arrive at the positions of the electrodes, the next step is to choose the strategy for driving currents. At this point there are two routes to the choice depending on whether the EIT hardware uses bipolar current drive or multiple current drive. Since the DeMontfort Mk2b system has been developed for bipolar current drive, this thesis is concerned with optimising the selection of bipolar current electrodes. From the literature (Methererall, 1998) there is evidence to suggest that in order to achieve improved resolution throughout the entire volume of interest, it is important to ensure that the various applied currents are not constrained to any one axis or plane, but rather are encouraged to intersect one another at different angles. Regarding the preferred proximity of the driving electrodes there appears to be two opposing views. One is to ensure the drive pair are adjacent and the other is to ensure they are as far apart as possible. This is a confusing conflict of ideas, and one that needs investigating. The issue of voltage measurement appears to be less contentious, with the general consensus that the measuring electrodes should be adjacent. This is not always adhered to however.

In light of the great diversity in measurement strategy methods, particularly for breast imaging, it is clear that an investigation is required to establish the most appropriate approach. This is the main objective of this work and is considered in depth for both 2D and 3D imaging in Chapters 4 and 5 respectively.

3.4 Methods used for measuring spatial resolution

In order to quantify the effect of the data acquisition strategy on image quality, a means for measuring system performance is required. One technique that is sometimes used is to analyse the singular values of the sensitivity matrix (Kleinerman *et al*, 1996; Avis, 1993), since this provides a direct indication of the conditioning of the image reconstruction process. While this enables a comparison of one method against another, it does not provide any information about the final image quality that can be expected.

A more common technique is to analyse the image quality directly. In broad terms, an image can be thought of as representing information about an object under observation, and the resolution of that image relates to how much information has been successfully

gathered from the object. It is because the measurement system is imperfect that the concept of resolution is considered. The imperfections arise because of inefficiencies in the underlying physical laws governing the image formation process, therefore it may be concluded that spatial resolution is closely related to the accuracy (or conditioning) of the image formation process (Webb, 1988). However, the way in which the inefficiencies of an imaging system usually manifest themselves are usually by either a smearing of the image or quantizaton or both, and it is often these effects that are used to quantify the spatial resolution performance of an imaging system. For this reason it has been decided that the performance criterion for the simulations are best measured from the image resolution. A brief review of resolution quantification methods appropriate to EIT now follows. The method used in this work is developed in section 4.3.1

3.4.1 Size of the finite element mesh

In their paper, Woo *et al* (1993) define the term 'spatial resolution' to mean the width of each (FEM) image element relative to the diameter of the whole image for which the value of resistivity can be correctly calculated within a specified tolerance. They use three different image meshes having 5%, 7% and 10% spatial resolution for image reconstruction, and the finest mesh which reconstructs the image to within a predefined tolerance is deemed to represent the spatial resolution for that particular case. This idea is limited by the number meshes used for image reconstruction and the result is therefore a closest match rather than an explicit calculation.

3.4.2 Width of the point spread function

A more quantitative measure of spatial resolution is given by Kotre (1994) as the reciprocal of the full width at half maximum (FWHM) of the point-spread function (PSF). Quoting the reciprocal of the FWHM differs from all other methods found in literature, and is presumably suggested so that higher numbers correspond to better resolution, rather than the conventional method in which higher values indicate more spreading of the point source. In addition the spatial variance of the resolution is investigated by measuring the resolution at a number of radial positions in the circular imaging plane. It is confirmed that the variation of spatial resolution with radial position follows the relationship:

$$W \propto \frac{1}{1-c^2} \qquad 3.2$$

where W is a measure of spatial resolution according to the aforementioned definition and c is the radial position within the image, normalised for a circular region of unit radius. This measurement of FWHM is based on the assumption that the PSF is circularly symmetric. This assumption is reasonable at the centre of the image but towards the periphery it breaks down; in particular when using the standard back-projection image reconstruction method with no filtering (section 2.5.3). This method is therefore not sufficient for measuring the spatial resolution across the full range of image reconstruction methods.

3.4.3 Area of the point spread function

Another alternative measure of spatial resolution used by Avis and Barber (1994) is to form images of the PSF and to count the number of pixels within 50% of the image peak, expressing this as a percentage of the total number of image pixels. This can be thought of as the Full Area at Half Maximum. The resulting ratio is notably small since it corresponds to an area measurement rather than a linear measure. A development of this idea is used as part of a figure of merit (Adler and Guardo, 1996) whereby the square root of the relative area of the PSF is expressed. In addition, the threshold above which pixels are deemed to be within the PSF is calculated for each case such that the sum of pixel intensities within the PSF is half the total sum of pixel intensities in the entire image.

3.4.4 Resolution profiles

Wheeler *et al* (2002) present a comparison of all of these methods and include a novel technique for measuring the spatial variance of the resolution. By making several resolution measurements along the radius of the image in a similar way to Kotre (1994) a resolution profile is produced. A curve fitting algorithm is then used to model the behaviour of the profile using the equation:

$$R_{fit} = R_c\left(1-\alpha.r^2\right) \qquad 3.3$$

where R_{fit} is the curve which is fitted to the measured resolution profile and r is the normalised radial position of the resolution measurements. The R_c and α parameters are iteratively adjusted until the curve is considered a best fit, after which they are deemed to represent the central resolution and spatial variance respectively. Based on a comparison using three different image reconstruction methods, it is shown that the technique is valuable in providing a quantitative measure of spatial variance for 2D circular images. In addition, by comparing a number of techniques for measuring resolution, it is concluded that the square-root relative area of the PSF produces the most reliable results. The primary reason for this is that it is not overly sensitive to the shape of the PSF as is the case with the FWHM approach. This approach is described in more detail in section 4.3.1.3

One of the major flaws of using resolution profiles to obtain spatial resolution information is that it requires the image to have rotational symmetry, since one profile is assumed to be representative of the entire image. In 2-dimensional EIT the images are nearly always circular so it is not a problem. For 3-dimensional imaging, the only image volume with a single centre of rotation is a sphere (or part of a sphere), hence the resolution profile technique becomes less useful when attempting to apply it to non-spherical objects such as a cylinder for example. This issue is explored further in Chapter 5 where analysis of 3-dimensional breast images is considered.

3.5 Discussion

The key causes of the poor spatial resolution in EIT have been identified as

1. A lack of independent data
2. Low SNR of the measured data
3. Ill-conditioning of the sensitivity problem

The amount of independent data and the degree of ill-conditioning are related to the electrode positioning and the current-voltage pattern. At present there are two approaches to electrode placement for EIM (see sections 2.6.1-4); one involving a ring of electrodes into which a pendant breast is placed and the other involving a flat grid of

electrodes which requires the breast to be pressed flat against the chest wall. For driving currents and measuring voltages there appear to be two schools of thought. One prefers a large distance between the drive and receive pair and the other prefers a small distance between the drive and receive pair. There is clearly a need for investigating other electrode placement strategies, breast shapes and current/voltage patterns, since these all have an influence on the ill-conditioning of the problem and may open up techniques for improving the spatial resolution. Since spatial resolution and the conditioning of the image forming process are linked, image resolution can be regarded as a useful indicator for quantifying the efficiency and accuracy of the image forming process. For EIT there have been a number of techniques used for quantifying spatial resolution, but these have been primarily aimed at 2-dimensional images and have often assumed that the image is circular. If the resolution of 3-dimensional irregularly shaped images (such as the breast) is to be studied then an improved technique for its quantification must be developed. This is further explored in Chapter 5.

In the next chapter, a detailed investigation into the resolution of 2-dimensional EIT images is presented. This is carried out using a simulation framework in which the number of electrodes and the data collection strategy can be varied in order to assess their effect on the resolution performance. The results of the simulation are presented and discussed at the end of the chapter.

CHAPTER FOUR

A COMPARISON OF RESOLUTION PERFORMANCE IN 2-DIMENSIONAL EIT SYSTEMS

4.1 Introduction

In the previous chapter, three key areas that contribute to the final image resolution were outlined. The first is the problem of limited independent data due to a limited number of electrodes used for data collection. This chapter addresses the issue through the development of a simulation study for various electrode configurations ranging from 16 to 128 electrodes. In order to maintain simplicity the simulation is based on 2-dimensional circular images. A technique for quantitative measurement of the resolution and its spatial variance is described. The results of these experiments are presented and discussed at the end of this chapter.

The aim of this Chapter is to investigate the question:

"If it were possible to have an unlimited number of surface electrodes would this help improve the image resolution, and if so what would be the best way to go about driving current and measuring voltages with them?"

This is considered in the context of robustness of the reconstructed image to noise present in the measured data and the prime focus is to achieve improved image resolution.

4.2 Software for simulating 2D EIT systems

Since the De Montfort Mk2b EIM imaging system was designed to use 16 current-driving electrodes interleaved with 16 voltage-measuring electrodes it is not capable of generating current-drive patterns requiring more than 16 electrodes. In order to investigate the resolution performance of a wide range of EIT configurations it is therefore necessary to implement a simulation framework in software. This section addresses the various components which form such a framework.

4.2.1 Simulating the currents and voltages; the forward solver

The most widely used technique for simulating surface potentials within a given conductivity distribution is to use the Finite Element Method (FEM). This involves discretising the conducting region into a number of small elements which are treated as having uniform conductivity. For 2-dimensional simulations the elements are usually triangular, and the final structure formed by them is termed the 'mesh'. Since a 2-dimensional FEM solver has already been developed for use with the De Montfort imaging system, this is used both for simulating the measured voltages and also for calculation of the image reconstruction matrices (See Appendix A). The design of the mesh is important since the number of edge nodes defines the maximum number of peripheral electrodes which can be simulated, and the element size governs the smallest simulated conductivity change. Since this work is primarily concerned with using up to 128 electrodes it is necessary to have at least the same number of edge nodes. In addition, because it is the resolution performance which is to be measured, it is necessary to have elements which are small enough to be regarded as a point source. One solution is to choose an extremely fine mesh having many more edge nodes than required and very small elements, however the time taken to solve the finite element problem increases exponentially with the number of elements used, so a compromise is required. The final design chosen is to have 128 peripheral nodes and 2048 triangular elements (see figure 4.1). This produces an element size corresponding to a resolution of 2.21%, which is better than the typical resolution values for EIT and is therefore small enough to be considered as a point source. The software for applying the currents and recording the surface potentials uses a Finite Element approach and has been adapted from software designed to operate with 16 adjacent drive pairs interlaced with 16 adjacent receive pairs. It is written as a MATLAB script file in conjunction with a C++ routine (see Appendix A for a complete listing). With the adapted software, each current drive pattern is defined as a vector whose entries represent the currents at each electrode, thus enabling full control over the current patterns. By combining all required current drive vectors for a given data collection strategy, a current drive matrix is formed. For the voltage measurement a similar approach allows full flexibility over which two electrodes are to be used for any given measuring pair. Using this system, any data collection strategy can be fully defined with a pair of matrices (one for current and one for voltage) and stored on the hard disk for future

retrieval. The conductivity distribution is supplied as a vector containing the individual conductivity values for each element within the mesh.

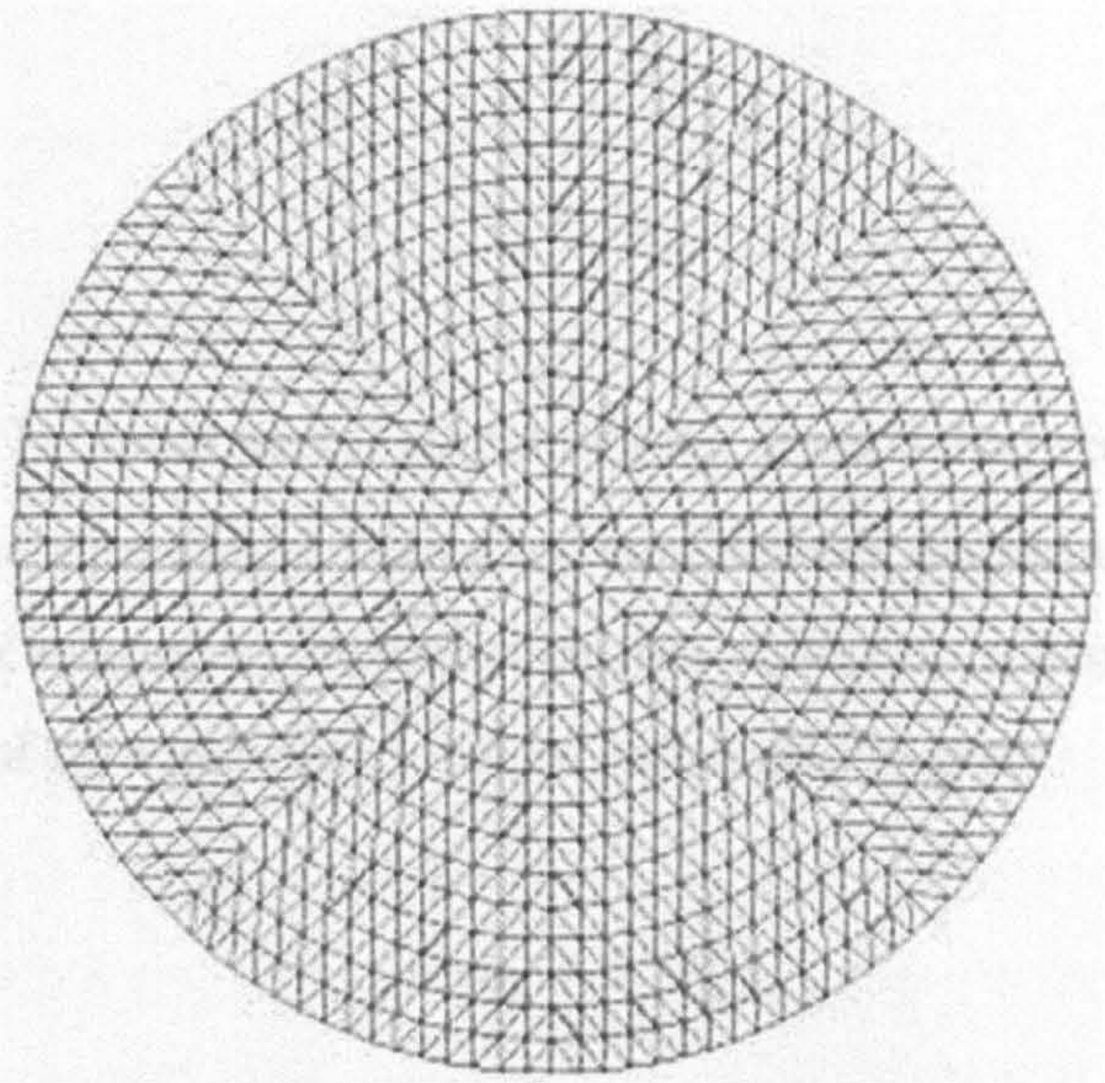

Figure 4.1 – Illustration of the finite element mesh used for solving the forward problem. The mesh has 128 peripheral nodes and 2048 triangular elements.

Since the mesh geometry is fixed for the entire simulation, the node co-ordinates and the list of nodes which make up each element are pre-calculated and stored on the hard disk. Once these three input variables have been defined, the forward solver is called and returns a vector of the simulated voltage measurements. To simulate system noise, a vector of random numbers is generated at a predefined amplitude (V_n) and added to the simulated voltage vector. A full listing of the forward solver code can be found in appendix A.

4.2.2 The image reconstruction algorithm

Since this simulation requires the reconstruction of many images a single step (non-iterative) image reconstruction algorithm is desired. It was decided that the sensitivity method in conjunction with the generalised matrix inversion (GMI) is the most appropriate method (see Metherall, 1998). An outline of the derivation and operation of this algorithm is now given:

The relationship between the perturbed conductivity distribution and the subsequent perturbations in surface voltages for a given measurement strategy is represented in the equation:

$$v_p = Sc_p \tag{4.1}$$

where v_p is a $[m \times 1]$ column vector containing the m perturbed voltages, c_p is a $[n \times 1]$ column vector of the n perturbed discretised conductivity distribution and S is the $[m \times n]$ sensitivity matrix relating to the particular data collection scheme. To recover c_p from a knowledge of v_p, equation 4.1 can be rearranged to give:

$$c_p = S^{-1}v_p \tag{4.2}$$

Since S is rarely square and is inherently ill-conditioned, finding a solution to S^{-1} for which equation 4.2 produces useful results is non trivial. A useful solution, often used in EIT, is to employ the generalised matrix inverse (or GMI) in which S is firstly decomposed using the singular value decomposition (SVD) to give:

$$S = UDV^T \tag{4.3}$$

where U is a $[m \times n]$ unitary matrix, D is a $[n \times n]$ diagonal matrix and V^T is a transposed $[n \times n]$ unitary matrix. The diagonal elements of D are known as the singular values of the sensitivity matrix and by convention are arranged to be in descending order. The rank of the matrix is defined as the number of non-zero singular values, hence a full-rank matrix would have n non-zero singular values. In practise, computer induced numerical rounding errors prevent absolute zero singular values from occurring, however if plotted on a log-scaled graph they can be identified as having a significantly reduced magnitude. The condition number of the matrix is defined as the ratio of the largest to the smallest non-zero singular value. A poorly conditioned matrix (such as S generally is in the case of EIT) has a large condition number. Based on the U, D and V matrices defined in equation 4.3, a minimum least-squares approximation of the inverse of S can be obtained using the equation:

$$S^{+} = VD^{!}U^{T} \qquad 4.4$$

where S^{+} is the pseudo-inverse of S and has dimensions $[n \times m]$, $D^{!}$ is a diagonal matrix formed from the reciprocals of the diagonal entries in the D matrix. Based on this approximate inverse of S, equation 4.2 now becomes:

$$c_p \approx S^{+} v_p \qquad 4.5$$

For matrices of less than full rank, the reciprocals of the (effectively) zero singular values dominate the $D^{!}$ matrix and thus prevent a stable solution to S^{+}. A common solution to this problem is to truncate the D matrix at some predefined threshold, thus removing the influence of the meaningless zero singular values. This process is known as truncated singular value decomposition (TSVD). An additional benefit of this is that if the noise level in the measured data is known, then it is possible to set a truncation threshold at a level which prevents the pseudo-inverse matrix (S^{+}) from being unduly affected by the noise. This issue is addressed more fully in section 4.4.2 where input parameters for the simulation are discussed. Implementation of the Singular Value Decomposition, image reconstruction and subsequent image display is accomplished using MATLAB, which has its own built in function for evaluating the SVD. The relevant functions are listed in Appendix B.

4.2.3 Calculation of the sensitivity matrix

Since the sensitivity method has been chosen for image reconstruction it is necessary to calculate the sensitivity matrix. There are a number of ways to achieve this but the method adopted here is similar to the perturbation method reported by Kim *et al* (1983). This is accomplished by recording the changes in measured voltages for a small change (in this case 1% from the background value) in each of the conducting elements within the mesh. This process is shown in figure 4.2. The result of this operation is a $[m \times n]$ matrix where m is the number of measured voltages and n is the number of mesh elements. Since the chosen mesh contains 2048 elements, the process involves solving the forward problem 2048 times. This is a time consuming task but since the sensitivity matrix for each measurement strategy need only be calculated

once, it is possible to pre-calculate and store them on the hard disk. The function listing for this operation is listed in Appendix B.

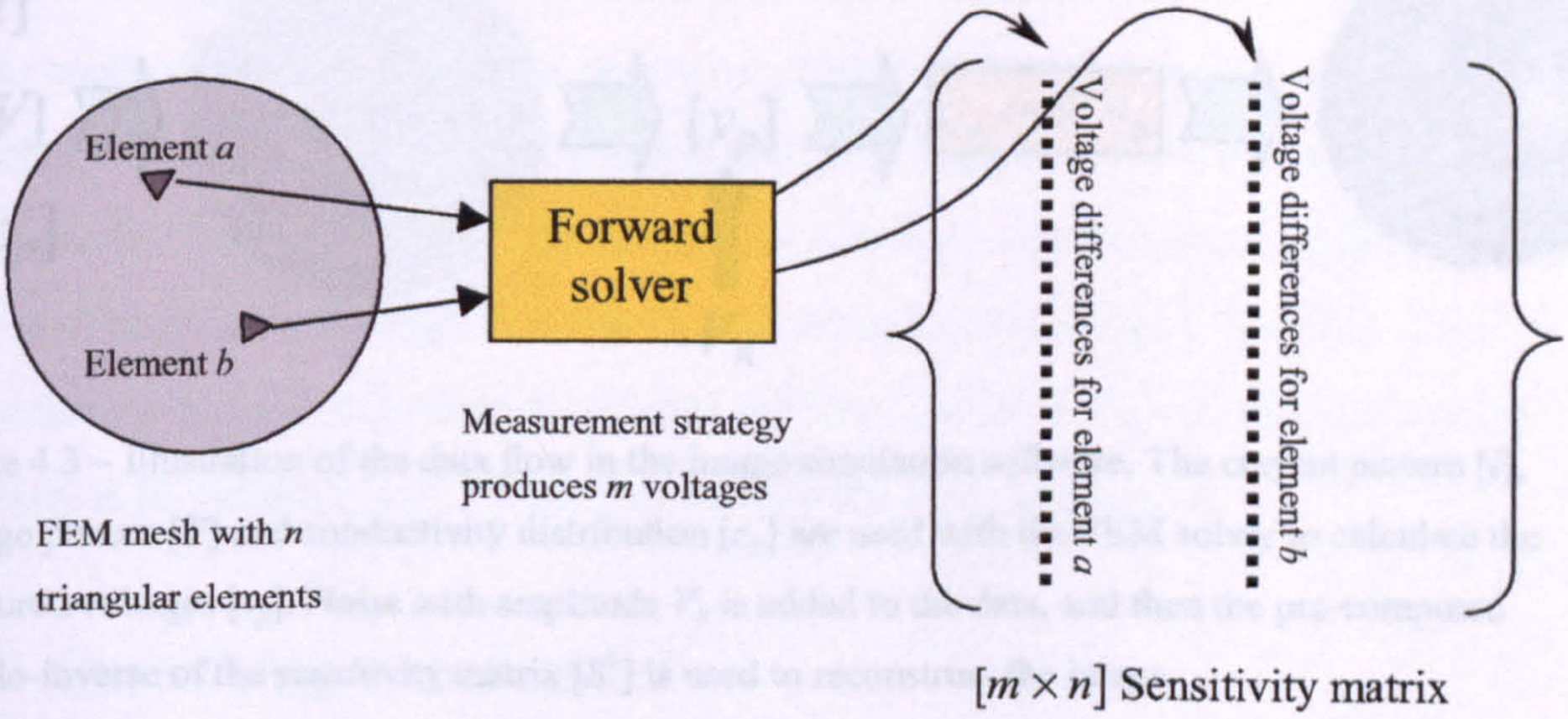

Figure 4.2 – Illustration of how the sensitivity matrix is formed using the perturbation method. In this case, two example elements (*a* and *b*) are indicated, and the corresponding columns in the sensitivity matrix are where the perturbed voltage values are stored.

4.2.4 Summary and verification of the software simulation

The full imaging simulation process involves four input parameters, namely the current drive strategy [I], voltage measurement strategy [V], conductivity distribution within the mesh [c_p] and the RMS noise level (V_n). These are all supplied as matrices except for V_n which is a scalar. The foreground and background voltage profiles are calculated using a finite element forward solver, and the background profile is subtracted from the foreground profile to produce a vector of perturbed voltages V_p. Noise is added at this stage using a Normally distributed random number generator. At this point the data are ready for image reconstruction, which is performed using the sensitivity method in conjunction with the generalised matrix inversion. The sensitivity matrix (S) is pre-calculated using the perturbation technique. The entire procedure is represented diagrammatically in figure 4.3 and the relevant functions are listed in full in Appendix B. In order to verify that the simulation software is correctly functioning, an image was collected from the De Montfort Mk2b system of a bundle of 4 pieces of spaghetti located at the 3 o'clock position. (The total area of the spaghetti is similar to the equivalent area of a single element within the mesh). A similar image was formed using the simulation software with a SNR equivalent to that of the Mk2b system (63dB). The two images are shown in figure 4.4.

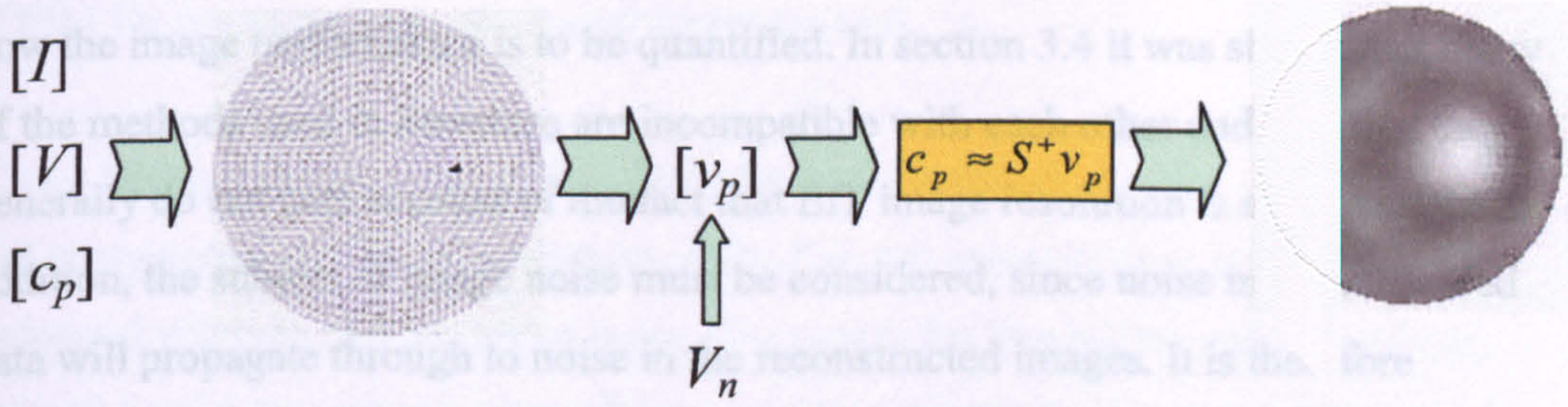

Figure 4.3 – Illustration of the data flow in the image simulation software. The current pattern [I], voltage pattern [V] and conductivity distribution [c_p] are used with the FEM solver to calculate the measured voltages [v_p]. Noise with amplitude V_n is added to the data, and then the pre-computed pseudo-inverse of the sensitivity matrix [S^+] is used to reconstruct the image.

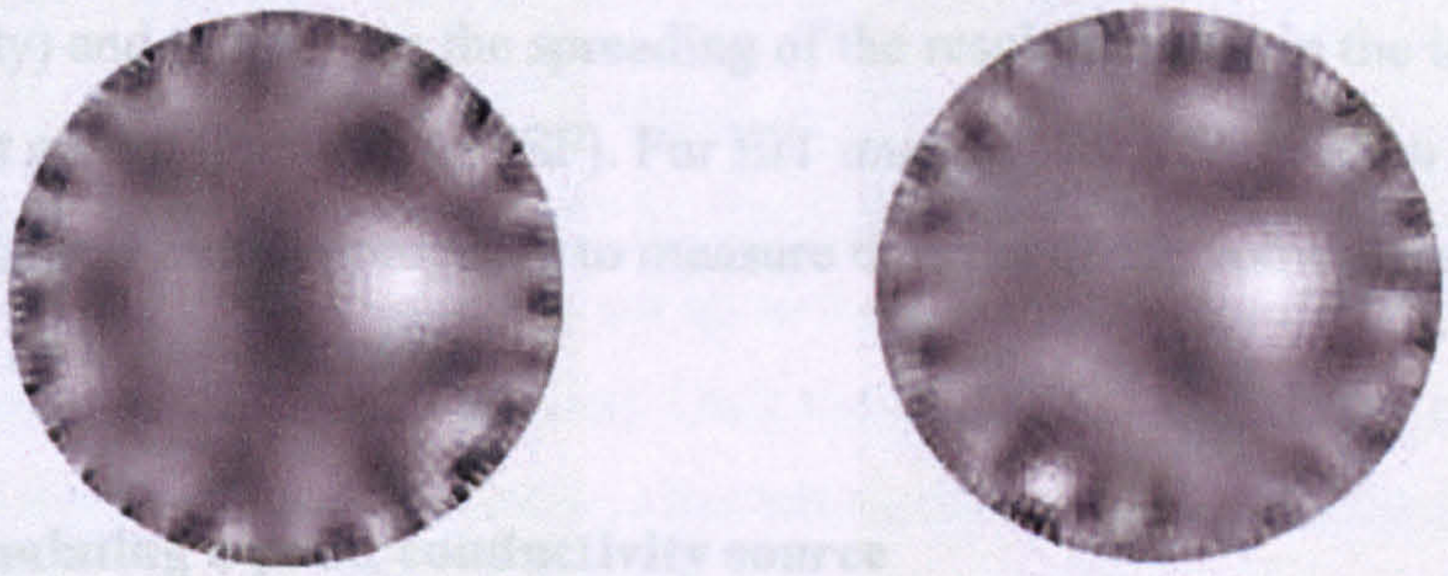

Real image – PSF: 19.4% Simulated image – PSF: 18.6%

Figure 4.4 – Images used for verification of the software simulation. The left image was collected from the De Montfort Mk2b system using spaghetti suspended within the saline tank. The right image was formed using the simulation software with a 10% conductivity change at the same position as the spaghetti, and artificial noise giving a SNR of 63dB.

Although the images are not identical, they demonstrate that the simulation software is realistic. The important factor is the size of the point spread function since this is what is used to quantify the resolution. In this case the spaghetti image has a resolution value of 19.4% and the simulated image has a resolution value of 18.6%. The error of 4% is considered acceptable.

4.3 Methods for analysing image performance

With the EIT simulation software established, it is necessary to address the issue of how the image performance is to be quantified. In section 3.4 it was shown that many of the methods used in literature are incompatible with each other and also that they generally do not take account of the fact that EIT image resolution is space variant. In addition, the subject of image noise must be considered, since noise in the measured data will propagate through to noise in the reconstructed images. It is therefore important to have a quantitative measure of how sensitive a given data collection strategy is to system noise. These two factors are now considered.

4.3.1 Quantifying spatial resolution

The most commonly used method for quantifying spatial resolution of any imaging system is to form an image of a point source (in this case a point change in conductivity) and to measure the spreading of the resultant point in the image (known as the point spread function, or PSF). For EIT imaging, the PSF is often irregular in shape, hence it is more appropriate to measure the area of the point spread function rather than its linear dimensions.

4.3.1.1 Simulating a point conductivity source

To simulate point responses using the software simulation described in section 4.2, the background conductivity of the finite element mesh is set to 1mS. This value is chosen since it is the same as the saline solution used in the De Montfort Mk2b saline phantom, for which the simulated voltages and noise levels are well documented. For the point source, a single element within the mesh is given a tenfold conductivity perturbation to 11mS. The choice of this value is important; if it is too small then the changes in surface voltages are easily corrupted by noise, if too large then the surface voltage changes become unrealistically large, giving the false impression of good noise robustness. In practice the relative change in conductivity between tumour and healthy breast tissue has been reported to be a factor of 2-20 (Surowiec *et al*, 1988), hence the chosen factor of 10 for the point source is in keeping with the intended imaging target. Based on the geometry of the FEM mesh, the point source described corresponds to a tumour size of 3% of the breast diameter (3mm for a 10cm diameter breast). Tumours of this size are classified as T1, which corresponds to stage 1 cancer for which the

survival rate is 92% (See tables 1.2, 1.3 and 1.4), hence the ability to reconstruct images of these point sources can be regarded as a direct indication of the suitability of EIM for use as a diagnostic breast screening tool.

4.3.1.2 Measuring the area of the Point Spread Function

The images used for the measurement of the PSF are reconstructed from 'pure' simulated voltages with no added noise. The reason for this is that adding artificial noise gives rise to a spread of possible point response images thus requiring several image reconstructions in order to arrive at a reasonable estimate of the resolution. The effects of system noise are therefore handled separately and are described in section 4.3.2. The method used for calculating the PSF area is to sum the areas of all the image elements whose amplitude is greater than half the maximum PSF amplitude (to maintain compatibility with the Full-Width-at-Half-Maximum [FWHM] approach). For some data collection strategies, artefacts can occur which give rise to large amplitudes in pixels outside the PSF region. In this case, calculation of the PSF area would include the artefacts and hence be incorrect. To prevent this happening, a search radius of 25% of the image radius is set up around the expected PSF centre (which is known from the point source location). Only the elements within this search radius are used to find the maximum amplitude, after which the area is calculated as described. This concept is shown in figure 4.5.

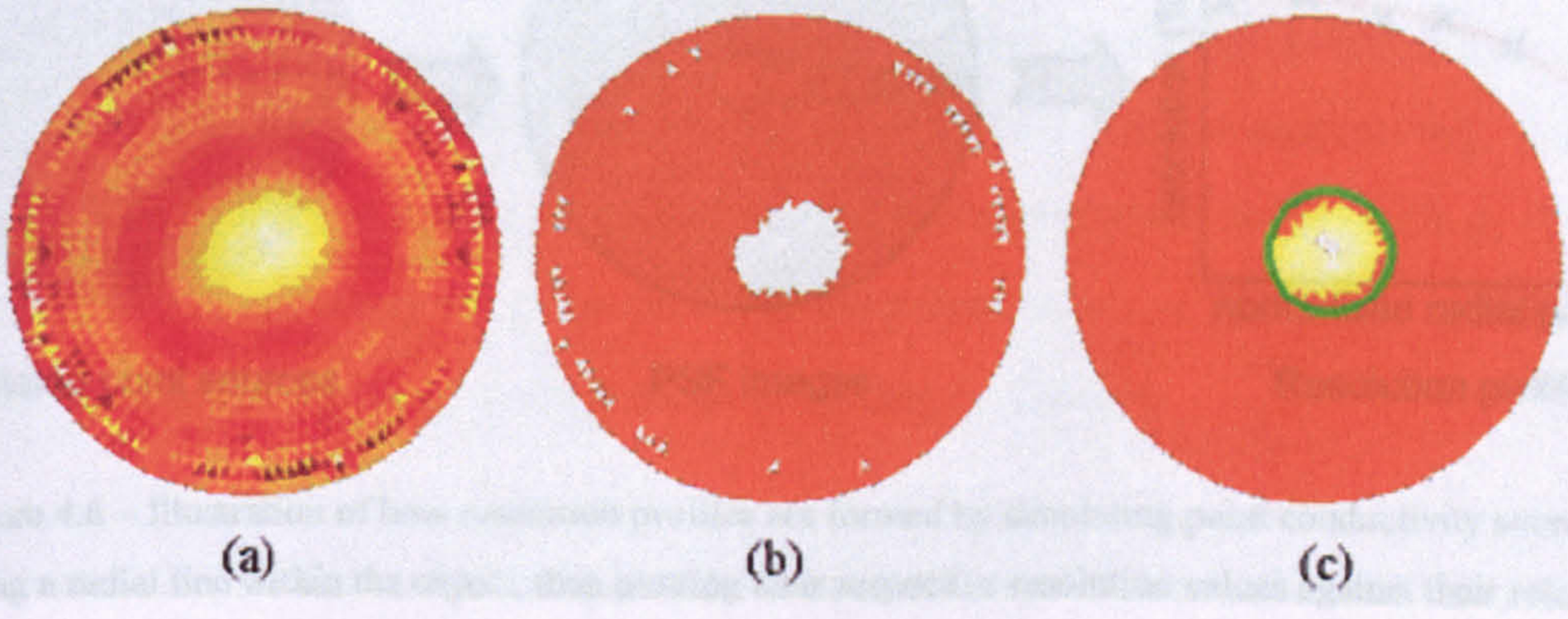

Figure 4.5 – Illustration of how the PSF area is calculated. Image (a) is the original PSF image which in this case has edge artefacts with amplitudes exceeding the PSF. Images (b) and (c) show those elements whose amplitude is greater than half the maximum. For image (b) the maximum was taken from all elements hence some of the artefact elements are included, whereas in image (c) the maximum was taken from elements within the green circle which has ¼ the radius of the image and is centred around the element used for the point source..

The resolution value is then calculated as the square root of the relative area of the PSF as shown in equation 4.6

$$R = \sqrt{\frac{\sum A_P}{\sum A_T}} \qquad 4.6$$

where R is the resolution, A_P represents the areas of only the elements within the PSF and A_T represents the areas of all the image elements. The function for implementing the algorithm is listed in Appendix C.

4.3.1.3 Quantifying the spatial variance

Since the images produced by EIT typically suffer from a large spatial variance in the resolution it is often not appropriate to quantify the resolution performance by quoting a single value. It has been shown by Wheeler *et al* (2002) that a more comprehensive approach is to make a series of resolution measurements along a radial line within the imaged object and to plot these as a resolution profile as shown in figure 4.6.

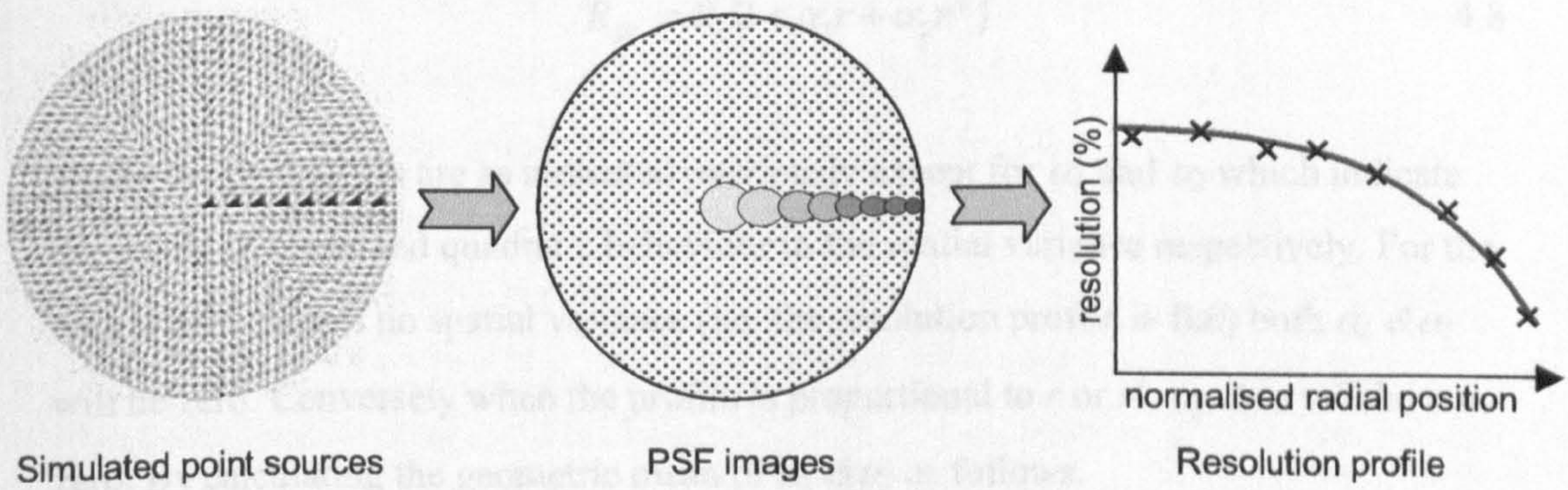

Figure 4.6 – Illustration of how resolution profiles are formed by simulating point conductivity sources along a radial line within the object, then plotting their respective resolution values against their relative radial positions. (NB although the point sources are all shown here in the same mesh, they are simulated separately).

The resolution profile is subsequently modelled using a curve of the form:

$$R_{fit} = R_c\left(1-\alpha.r^2\right) \qquad 4.7$$

where R_{fit} is the best-fit model of the measured resolution profile and r is the normalised radial position within the imaged object. By using this model, the parameters R_c and α (which are adjusted iteratively until a best-fit is achieved) represent the resolution at the centre of the image ($r = 0$) and the spatial variance respectively. The evaluation reported by Wheeler *et al* (2002) is performed using the adjacent drive technique for a number of different electrode spacings and reconstruction algorithms. It is found to fit the measured data reasonably well (mean $R^2 = 0.943$). For the data collection strategies proposed in this simulation (namely *adjacent*, *polar* and *cross*), preliminary tests using the technique described have revealed that the curve fitting model (hereafter referred to as the *r-squared* model) does not always correlate well with the measured data. An improvement is therefore proposed whereby the measured resolution profile is fitted to a second-order quadratic equation of the form:

$$R_{fit} = R_c\left(1+\alpha_1 r+\alpha_2 r^2\right) \qquad 4.8$$

where the parameters are as indicated previously except for α_1 and α_2 which indicate the levels of linear and quadratic behaviour in the spatial variance respectively. For the case where there is no spatial variance (i.e. the resolution profile is flat) both α_1 &α_2 will be zero. Conversely when the profile is proportional to r or r^2, α_1 &α_2 will be non-zero. By calculating the geometric mean of α_1 &α_2 as follows:

$$\alpha = \sqrt{\alpha_1^{\,2} + \alpha_2^{\,2}} \qquad 4.9$$

a single measure of the spatial variance is obtained. In addition, the regression coefficient (R^2) is quoted to indicate how well the data has been fitted to the curve. Typical values of α using both the methods described are in the range $0 < \alpha < 1$, where α=0 signifies zero spatial variance (the ideal case) and α=1 signifies the maximum

spatial variance. Since the *r-squared* and *quadratic* models are only approximations to what is observed in practise, there are occasions (particularly when the resolution profile is irregular) where the calculated value of α is greater than 1. In the case of the *r-squared* model (equation 4.6) this is meaningless, since it implies that the resolution at the periphery of the image is negative. For the rare instances where $\alpha > 1$, it is therefore interpreted to mean that the measured resolution profile is particularly irregular and that the spatial variance is poor. Although the *quadratic* model is proposed as an improvement upon the *r-squared* model, they both represent an original technique for the quantification of spatial variance in EIT images and will both be used to evaluate the images produced by the 2D resolution simulation. For a full listing of the functions used to implement the two models, see Appendix D.

4.3.2 Quantifying sensitivity to noise

The resolution measurements described in section 4.3.1 are performed in the absence of noise. Since it is already known that the various data collection strategies behave differently in terms of how much the final image is affected by signal noise (Avis and Barber, 1994) it is necessary to quantify the sensitivity of each measurement strategy to noise. The method chosen here is to generate two images; one from *pure data* (noise-free) and the other from *noisy data* (added noise). By subtracting the *pure data* image from the *noisy data* image, a third '*pure noise*' image is obtained, which represents only the contributions resulting from the noise. The nature of the *pure noise* image is essentially random, although the amplitude distribution is in part related to the point source location and the data collection strategy used. Since it is random in nature and since there are a statistically significant number of pixels in each image, it is reasonable to use the standard deviation of the pixel amplitudes to quantify the amount of noise in the image. The process is shown graphically in the diagrams of figure 4.7. The amplitude of the artificial noise is carefully chosen to reflect the expected SNR of the hardware and the typical base levels of system noise. This issue is considered in section 4.4.2 where the input parameters of the simulation are discussed.

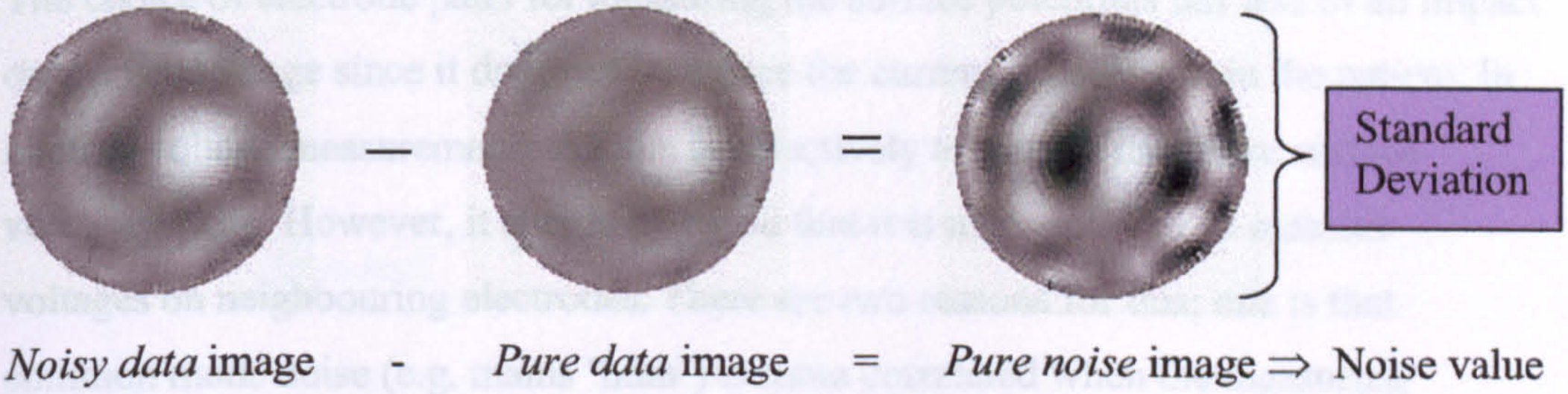

Figure 4.7 – The process of forming an image exclusively of noise contributions by subtracting the noiseless image from a noise-contaminated image. (NB To help visualise the noise effect, the greyscales are not the same for all three images).

4.4 Choosing parameters for the simulation

Although no hardware is used for the 2D resolution investigation it is important to ensure that the simulation is sensible in the way that it handles parameters such as noise levels, injected current and measured voltage levels. For this reason the role of the hardware is now considered in order to highlight the key influences on the measured data.

4.4.1 Current injection and voltage measurement patterns

The purpose of the hardware in an EIT system is to generate a current source from a predefined waveform, apply this to the body through a predefined pattern of electrodes and finally to measure the surface potentials which are produced as a result. The key limitation imposed on the hardware is the maximum allowed current which may be injected into the body for the purposes of medical imaging. This is presently set by BS5724 at 1mA(RMS) and is therefore the value used throughout the entire simulation.

Although the primary aim of this chapter is to observe the effect of increasing the number of surface electrodes on image performance, it is necessary to realise that the current drive patterns have an influence. Since the *adjacent*, *polar* and *cross* current drive methods have often been compared in literature they are simulated here to allow cross referencing to other work, thereby providing a validation source for the simulation.

The choice of electrode pairs for measuring the surface potentials has less of an impact on the final image since it does not influence the current density within the patient. In making voltage measurements the aim is effectively to sample the entire surface voltage profile. However, it should be noted that it is more sensible to measure voltages on neighbouring electrodes. There are two reasons for this; one is that common mode noise (e.g. mains 'hum') is more correlated when the measuring electrodes are closer together and hence can be rejected more easily; the second is that the aim is to collect an accurate sample of the surface voltage potentials. Consequently a closer electrode spacing can be considered as having a higher spatial sampling rate. A slight variation, adopted by some groups, is to interleave the measurement electrodes between the current driving electrodes. One of the primary purposes of this is to increase the number of independent measurements since the current drive and voltage measuring circuitry never share an electrode (thus preventing violation of the 4-terminal principal). It is not clear in the literature as to what effect this actually has on the final image quality, so this situation is also included for the simulation.

4.4.1.1 Interpolated receive positions

There are a number of problems encountered when increasing the number of electrodes. One limitation arises due to the finite size of the electrodes but there is also a noise-induced limit in that the closer the electrodes become, the smaller the differential voltages measured. If placed too close, the resulting signal becomes buried in noise, hence the system is limited by the signal-to-noise ratio.

A new method proposed here for overcoming this problem is to fix the minimum electrode separation such that the spacing between the measuring pair is maintained at $1/16^{th}$ of the circumference. If there are 128 electrodes then 128 voltage measurements can be made for each current pattern since the angular step from one measurement to the next is $1/128^{th}$ of the circumference. This concept has been termed '*interpolated receive*'. Figure 4.8 shows an example of how it is implemented in practise.

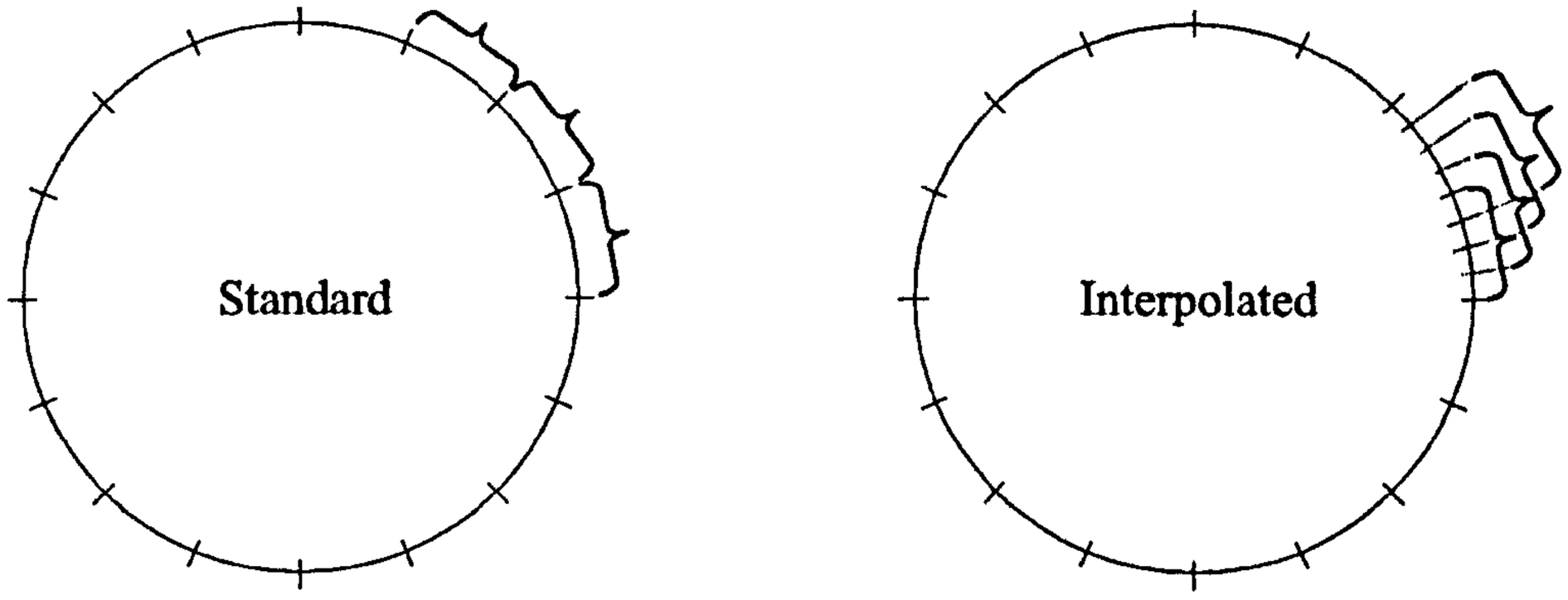

Figure 4.8 – Illustration of the interpolated receive principle. The image on the left shows the standard adjacent receive method based on a 16 electrode array. The image on the right shows the interpolated receive method based on a 128 electrode array, whereby a $1/16^{th}$ spacing is maintained between the receive pair so as to preserve the signal to noise ratio.

4.4.2 Simulating system noise

The noise levels within a real EIT hardware system depend on the quality and layout of the analogue circuitry, the use of appropriate screening on signal-carrying cables and the accuracy of the analogue to digital converter(s). For the De Montfort Mk2b EIT system the SNR is typically in the range 50-60dB. This is usually improved through the use of signal averaging so that by taking the mean of 20 frames a 13dB increase in SNR to 63-73dB is seen. For the purposes of simulating noise, quoting values of SNR can be misleading since the system noise level does not depend on the signal size and will typically have a fixed level. In addition, the minimum signal level in the measured voltage profiles depends upon the data collection strategy used. Hence if the noise is specified as a baseline SNR, then separate values for each data collection method are required. The important parameter is therefore the equivalent RMS noise level (taking into account any data averaging) which would be measured at the electrodes. This can be found by using the forward solver to simulate the voltages measured on the De Montfort imaging system, and to then choose a level of noise which would produce a minimum SNR of 63dB. Using this concept, the minimum signal size predicted by the forward solver is 6.2mV, hence the noise level should be 63dB below this level, that is: 4.4μV RMS.

In order to provide a range of noise performance values, it was decided that three different levels of simulated noise would be applied, namely 1μV, 3μV and 5μV. The larger value corresponds to the present SNR performance of the Mk2b system, and the smaller values are included to give an indication of the image noise performance possible if the hardware should be improved. The equivalent minimum SNRs of the three noise levels are; 76dB, 66dB and 62dB respectively. The random number generator is MATLAB's RANDN function which has a Normal amplitude distribution, hence the RMS noise amplitudes specified above can be handed directly to the noise generator.

It was mentioned in section 4.2.2 that when performing the generalised matrix inverse it is possible to truncate any singular values below a chosen threshold. Since the noise levels are explicitly defined it is possible to arrive at a sensible truncation level. Although it is theoretically possible to develop a system for choosing the optimum truncation level based on the quality of the measured data, it was decided that for this work it is more appropriate to fix the truncation level, thereby preventing it from obscuring the results. Since the best-case scenario for the simulated noise levels (i.e. 1μV) produces a minimum SNR of 76dB, it is sensible to set the truncation level at 76dB. At 66dB and 62dB the noise levels correspond to 3μV and 5μV respectively for which the image quality is more significantly affected. However, if the truncation level was optimised for the 5μV noise level (SNR = 62dB), it becomes harder to see the benefits possible through reducing the noise levels in the hardware to the 1μV level.

4.4.3 Electrode positions

The electrode positions used in the simulation are predefined by the peripheral nodes of the FEM mesh. Since there are 128 peripheral nodes a maximum of 128 evenly spaced electrodes is possible. The choice of electrodes used by each data collection strategy is made by the current drive and voltage vectors supplied to the forward solver (See section 4.2.1). Other than this, there are no further parameters required to specify the electrode positions.

4.4.4 Point conductivity source positions

For the point conductivity sources, single elements within the FEM mesh are perturbed one at a time along the radius of the mesh. The mesh geometry is such that there are 16 concentric layers of triangular elements that form 8 rotationally symmetric segments. The elements lying closest to the x-axis are all evenly spaced and have consistent areas, so these are chosen to represent the point source positions. Thus there are a total of 16 point sources simulated for each data collection strategy. The precise elements used are shown in figure 4.9.

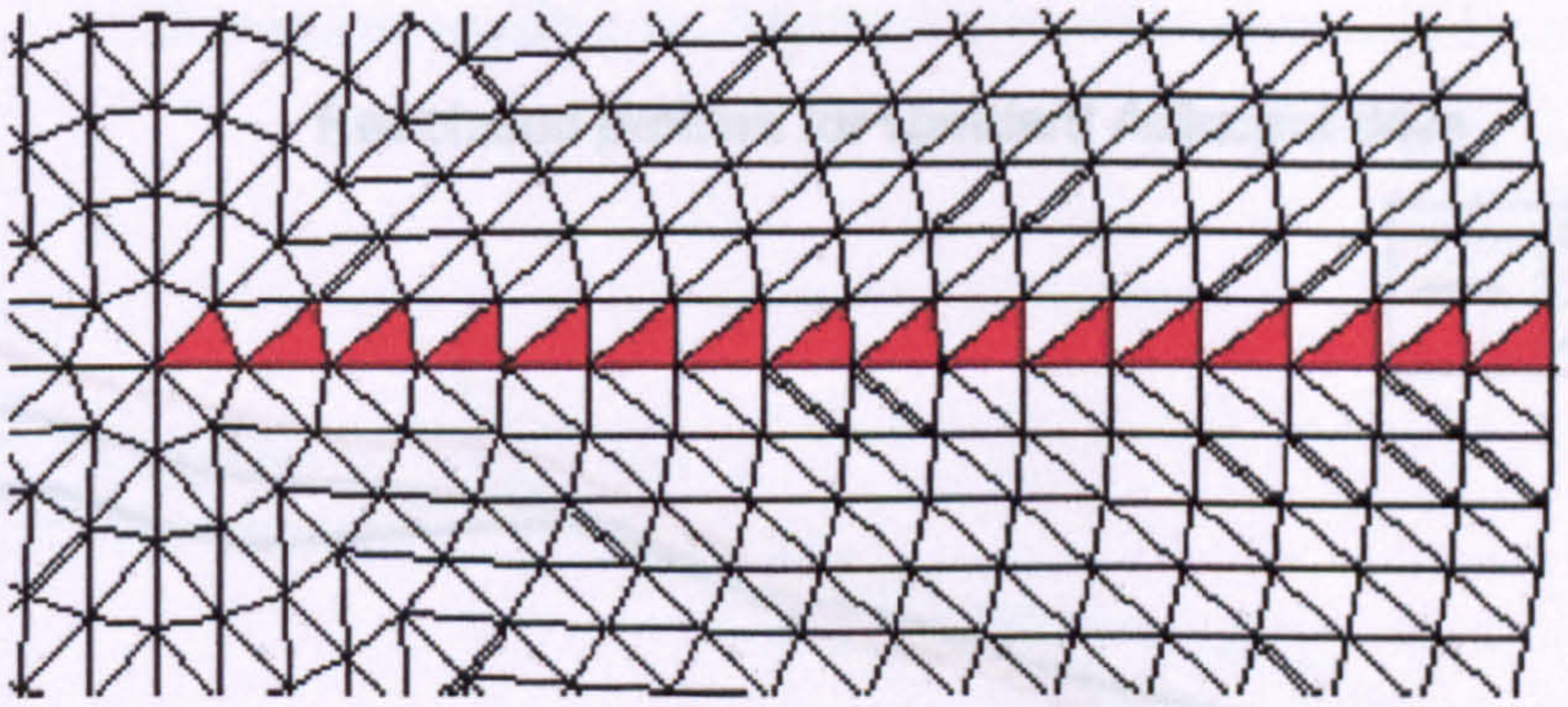

Figure 4.9 – A portion of the FEM mesh indicating the 16 elements (in red) used to form the point sources for the resolution simulation. (NB, the elements are simulated one at a time and not all together as illustrated here).

4.5 Results of the 2-dimensional simulation study

In this section the results of the resolution performance of 2-dimensional EIT images produced by several different electrode configurations are presented. To summarise, the resolution measurement involves reconstructing separate images of a series of point conductivity changes located in a radial line from the centre to the periphery of the FEM mesh. The relative areas of the resulting PSF images are plotted to form a profile from which two important parameters are extracted, namely central resolution and spatial variance. Since the simulation process requires the reconstruction of several hundred images they are not shown in this section but are grouped together in Appendix E, however, the resolution profiles are presented here. In addition, the noise robustness of each electrode configuration is tested by adding Normally distributed noise at RMS amplitudes of 0, 1, 3, and 5μV to the simulated voltages prior to image

reconstruction. The effects of the noise are numerically quantified as described in section 4.3.2 and are tabulated at the end of the results section (table 4.2) along with the resolution parameters that are obtained from the resolution profiles (table 4.1).

The data collection method used to produce the results in figure 4.10 is the standard *adjacent* drive method with *non-interleaved* voltage measurement. This method has been widely adopted in EIT for 16-electrode arrays, but the results presented here include 32- and 64-electrode arrays. From the resolution profiles it can be seen that the central resolution is significantly poorer than the peripheral resolution in all cases.

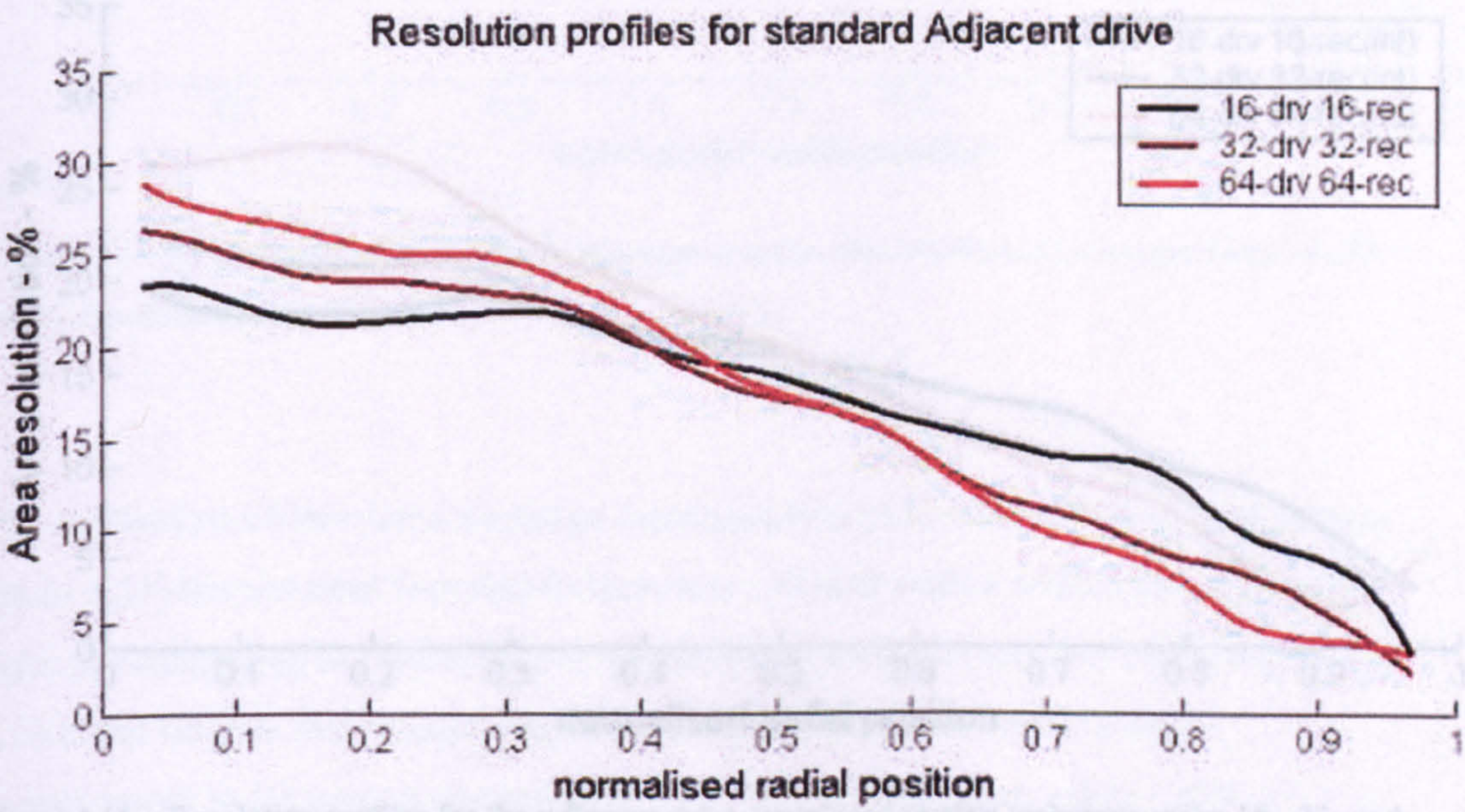

Figure 4.10 – Resolution profiles for the standard *adjacent* drive, *non-interlaced* method using 16-, 32- and 64-electrode arrays.

Increasing the number of electrodes has the effect of improving the peripheral resolution whilst worsening the central resolution. This can be seen from the red curve (representing 64 electrodes) compared with the black curve (representing 16 electrodes). Midway along the radius it can be seen that changing the number of electrodes has no effect on the spatial resolution. The effect of using *interleaved* voltage measurement with *adjacent drive* can be seen from the results in figure 4.11. Although less widely adopted than the *standard adjacent drive* method, this approach has been used as a means of increasing the amount of independent data and is the

method adopted by the De Montfort Mk2b system. By comparing the black curves of figures 4.10 and 4.11 (i.e. the 16-electrode arrays) it can be seen that the interleaved method offers an overall improvement in resolution. This is particularly notable at the centre of the image where the resolution is 20% for the *interleaved* method and 25% for the *non-interleaved* method. By increasing the number of electrodes used for the *interleaved* method, the central resolution becomes significantly worse whereas there are only marginal gains to the peripheral resolution. This can be seen by comparing the red curve (64-electrodes) with the black curve (16-electrodes) in figure 4.11.

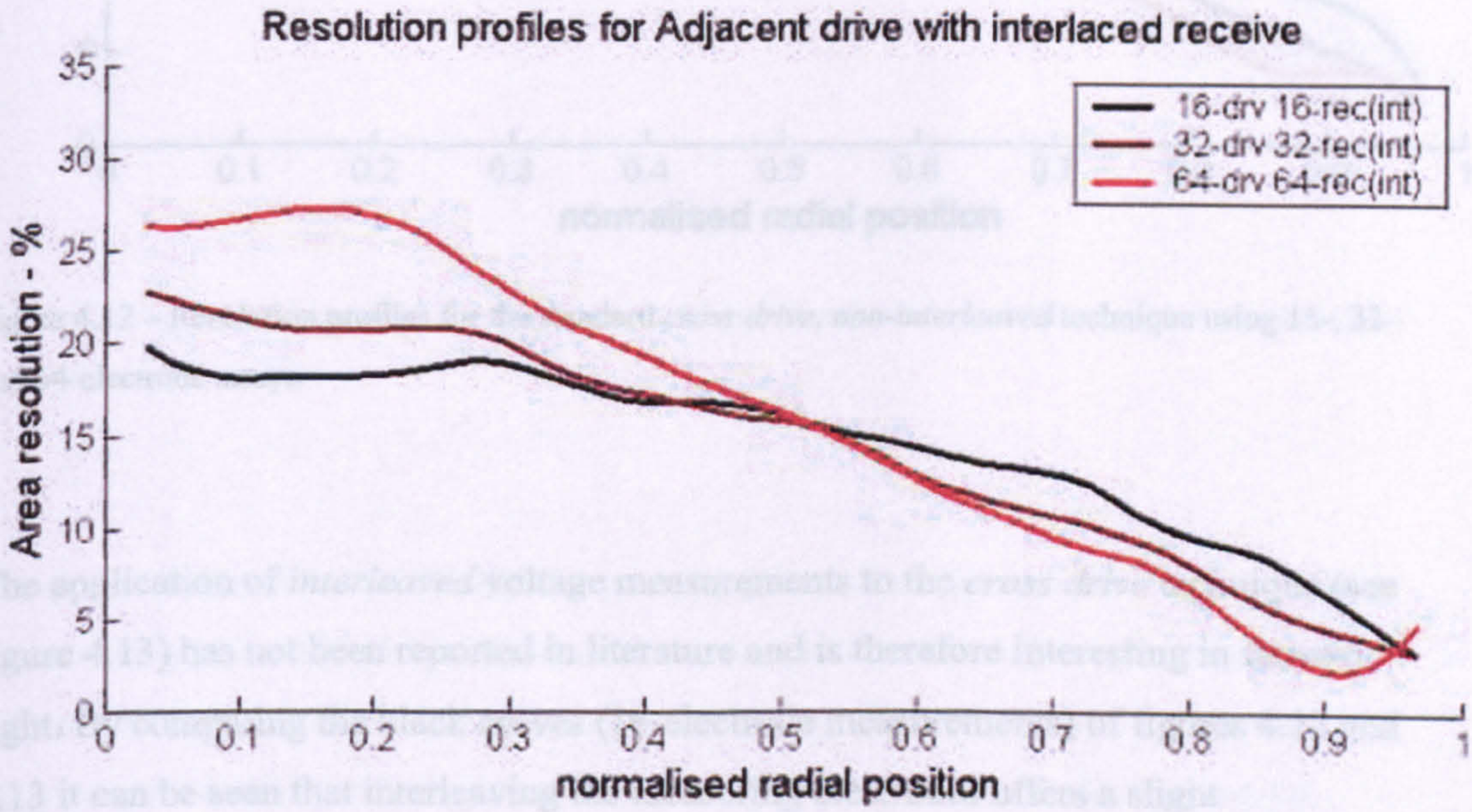

Figure 4.11 – Resolution profiles for the *adjacent drive*, *interlaced* receive technique using 16-, 32- and 64-electrode arrays.

The *cross drive* technique where drive electrodes are separated by 90° has received little attention in literature but is reported here for completeness. The results shown in figure 4.12 are for the *cross drive non-interleaved* method. It is interesting to note that whilst increasing the number of electrodes improves the peripheral resolution, the central resolution is barely affected. This is likely to be because the wider separation of the drive electrodes enforces a deeper current penetration into the object, thereby aiding imaging of the central structures. In addition, unlike the *adjacent drive* method, the electrode separation using the *cross drive* method does not vary with the number of electrodes.

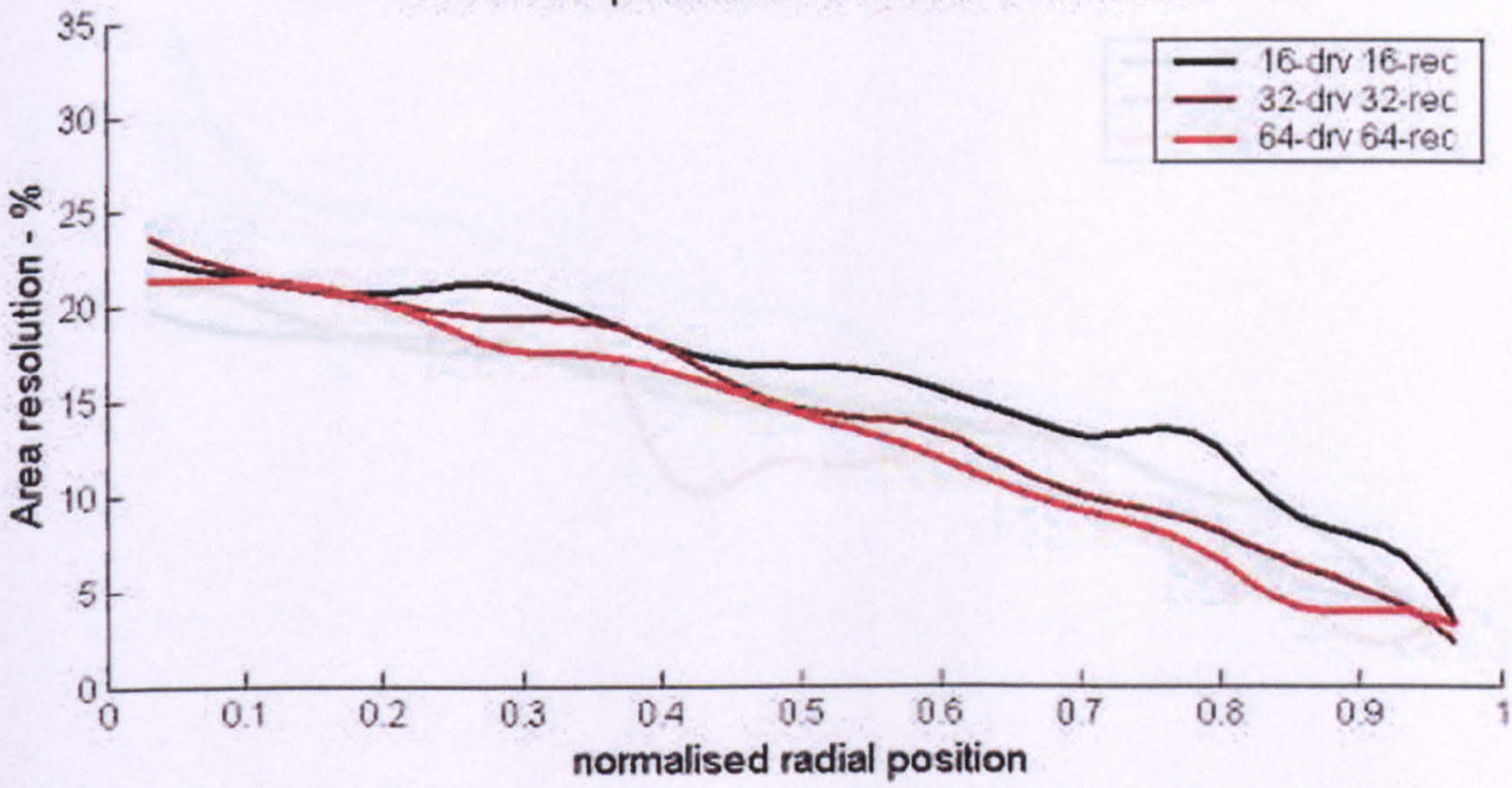

Figure 4.12 – Resolution profiles for the standard *cross drive, non-interleaved* technique using 16-, 32- and 64-electrode arrays.

The application of *interleaved* voltage measurements to the *cross drive* technique (see figure 4.13) has not been reported in literature and is therefore interesting in its own right. By comparing the black curves (16-electrode measurements) of figures 4.12 and 4.13 it can be seen that interleaving the measuring electrodes offers a slight improvement in the central resolution from ~22% (*non-interleaved*) to ~20% (*interleaved*). From the brown curve of figure 4.13 (32-electrodes) it can be seen that increasing the electrodes does improve the peripheral resolution. However, with 64 electrodes (red curve) the resolution profile appears erratic. By observing the images for this profile it can be seen that they do not reflect the expected point spread functions, but instead are dominated by structured ripple patterns (refer to figure E4 in Appendix E). It is only when the point source has a radial position greater than 0.8 that the reconstructed images resemble the expected point spread functions. The reason for this effect is not clearly understood, but is commented on in section 4.6 where the results are discussed.

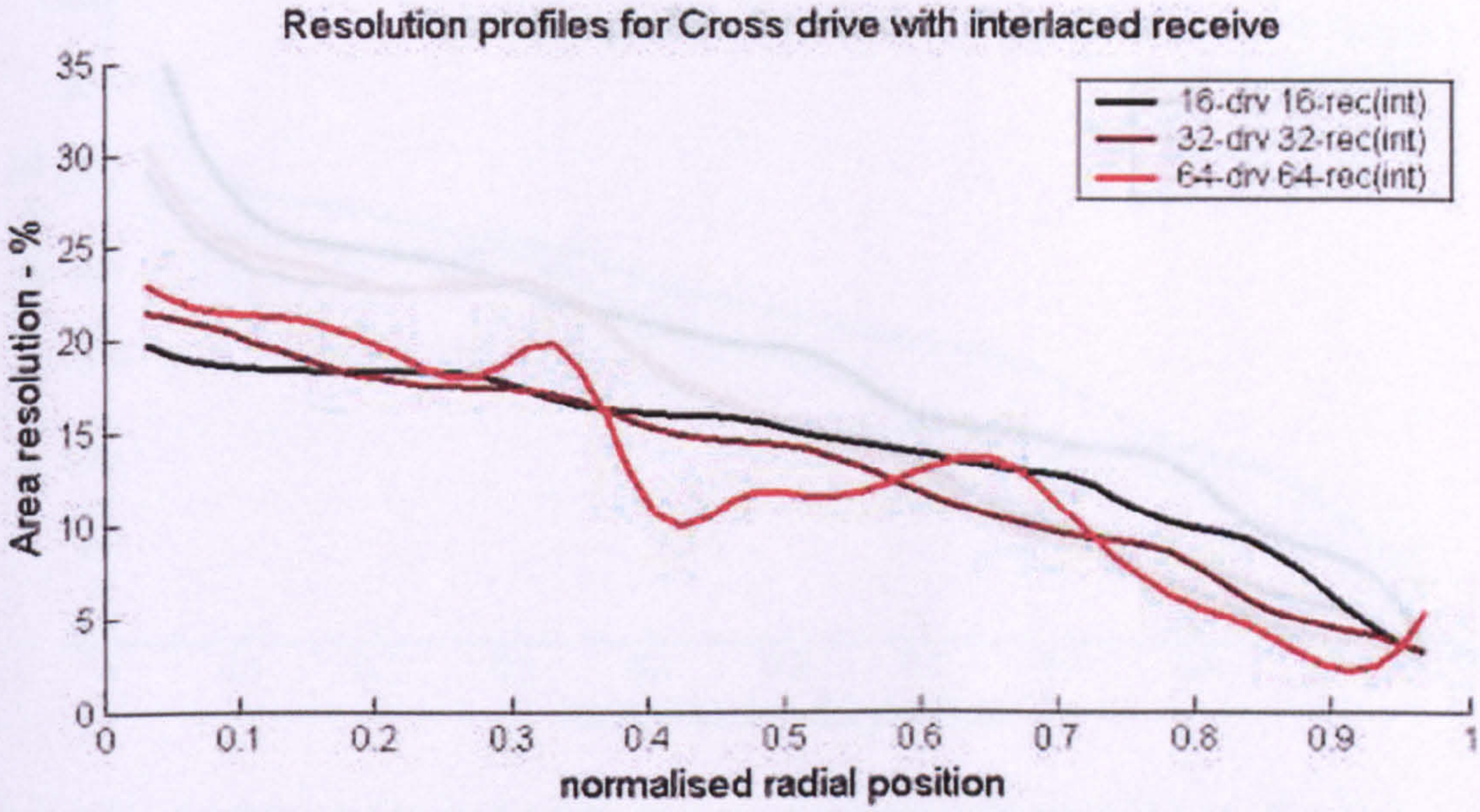

Figure 4.13 – Resolution profiles for the *cross drive*, *interlaced* receive technique using 16-, 32- and 64-electrode arrays.

The *polar drive* method, although less common than the *adjacent drive* method, is more widely reported in literature than the *cross drive* method. It is of particular interest for imaging of the head where it is necessary for the applied currents to penetrate the skull in order to successfully image the brain tissues. In figure 4.14, results are shown for the *polar drive, non-interleaved* technique. From the resolution profiles it can be seen that the resolution performance for the *polar drive* method is on the whole worse than for the *adjacent* or *cross drive* methods. In particular the central resolution is very poor at 30-35% compared with 20-30% for the *adjacent* and *cross* methods. Due to the maximum drive pair separation, the current is spread out over most of the object rather than being concentrated nearer the drive electrodes. As a result the sensitivity towards the central regions is increased, but the specificity is reduced. Increasing the number of electrodes from 16 (black curve) to 32 (brown curve) does improve the overall resolution, however, there is no further benefit from increasing to 64 electrodes (red curve).

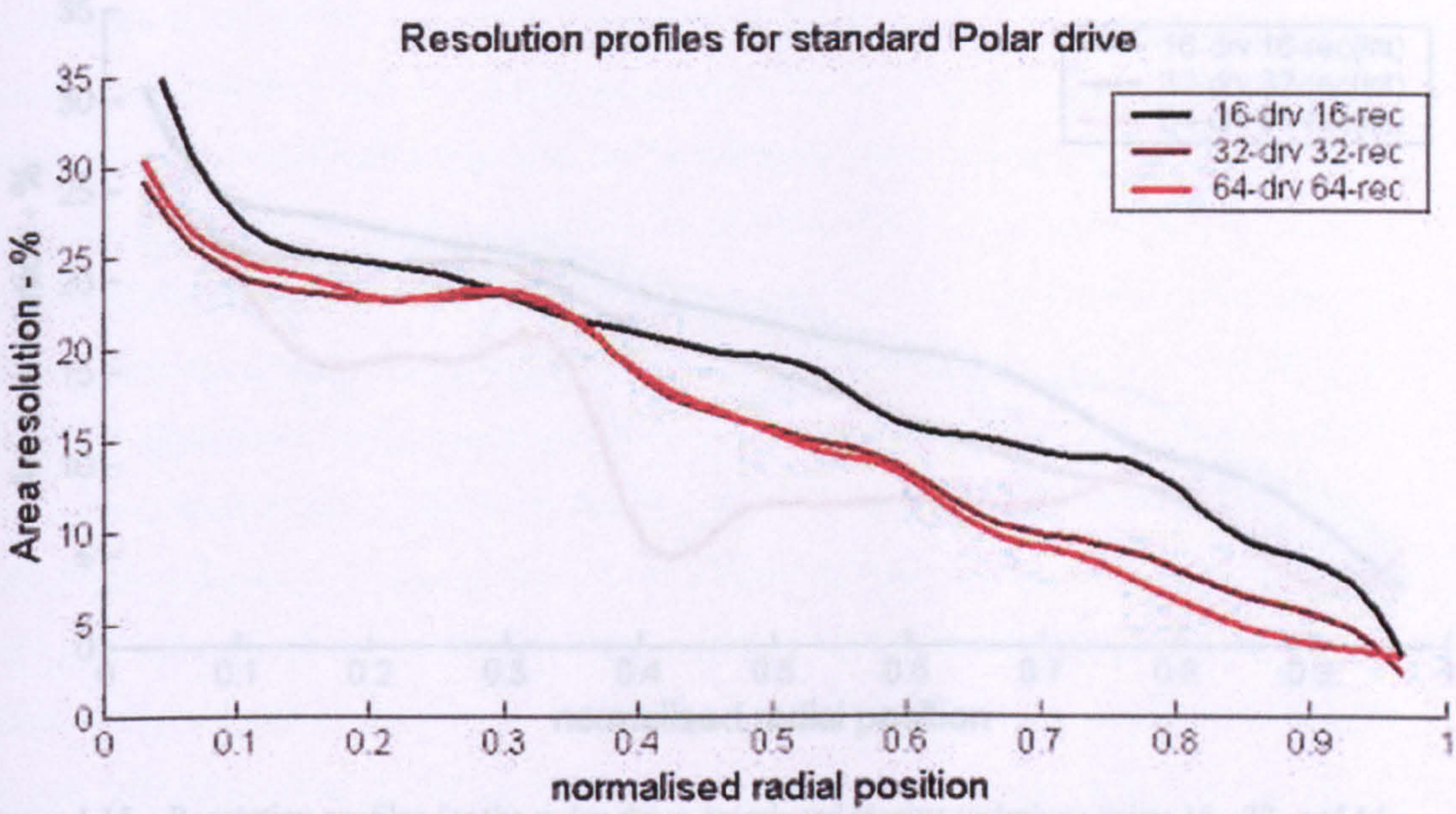

Figure 4.14 – Resolution profiles for the standard polar drive non-interleaved technique using 16-, 32- and 64-electrode arrays.

Results obtained from using *interleaved* voltage measurements with the *polar drive* method are shown in figure 4.15. By comparing these results with those in figure 4.14 it can be seen that interleaving the measuring electrodes improves the resolution performance for the 16- and 32-electrode arrays (black and brown curves respectively). However, for the 64-electrode case (red curve) the resolution profile appears erratic in a similar way to the 64-electrode *cross drive, interlaced receive* method (figure 4.13). Indeed, on inspection of the reconstructed images (figure E6 in Appendix E) it can be seen that the same structured ripple patterns are present for point sources at radial positions less than 0.8. This is an interesting result as it suggests that there is a problem when using interleaved measurements on large electrode arrays. In general it can be seen that the resolution performance of the *polar drive* method is significantly worse than for the other drive methods.

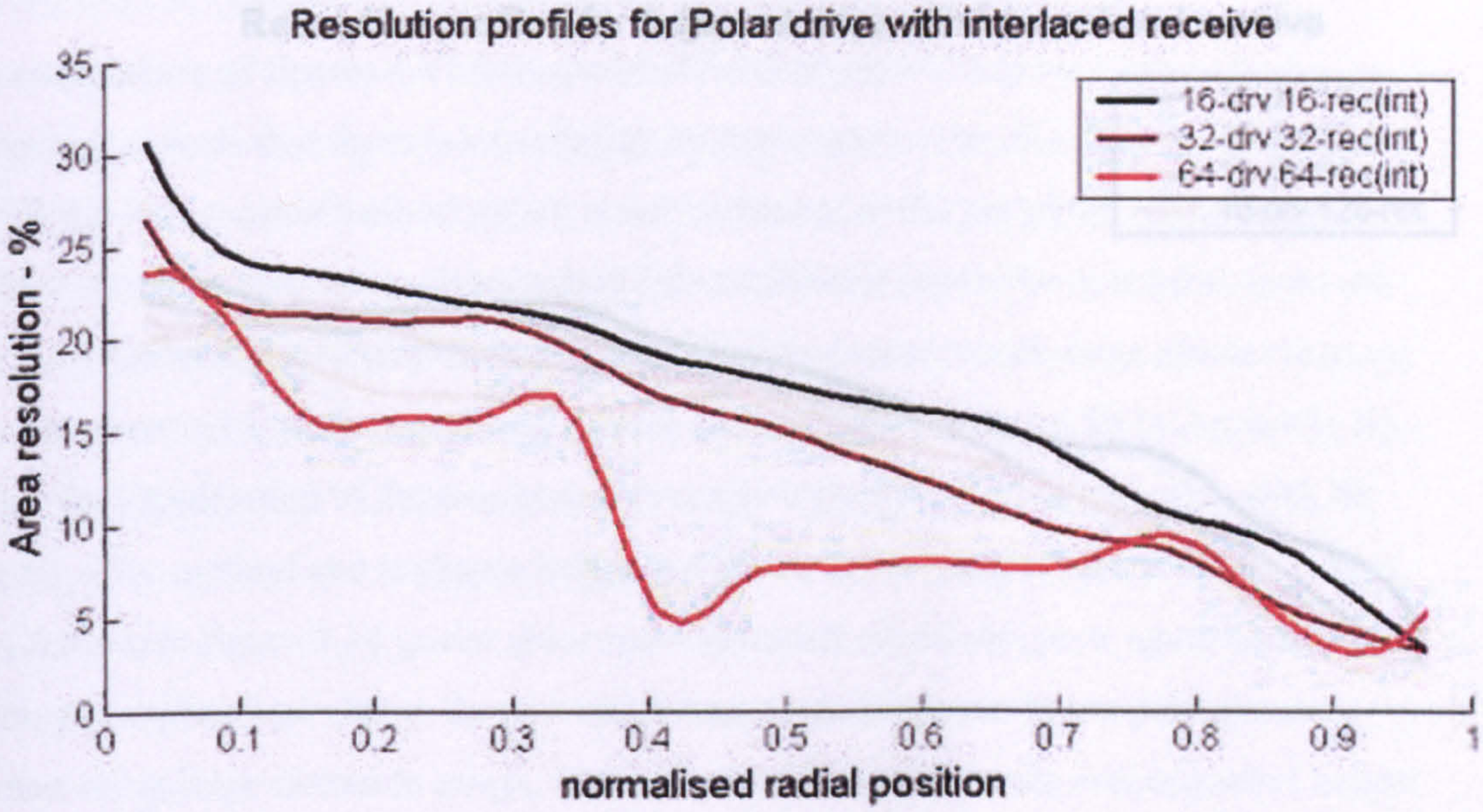

Figure 4.15 – Resolution profiles for the *polar drive, interlaced* receive technique using 16-, 32- and 64-electrode arrays.

In order to increase the quantity of measured data whilst preventing the separation between the measuring electrodes from becoming small the *interpolated receive* method was proposed in section 4.4.1.1. This is an original approach to data collection in that it allows voltages to be measured on large electrode arrays without the usual problems of poor signal to noise ratio. Simulations were carried out using the *interpolated receive* technique in conjunction with the *adjacent*, *cross* and *polar drive* methods on electrode arrays containing 16, 32 64 and 128 electrodes. The results in figure 4.16 are produced by the *adjacent drive, interpolated receive* method. From the resolution profiles it can be seen that there is an incremental improvement in overall resolution performance as the electrode array size is increased from 16 to 128 electrodes (black, brown, red and orange curves respectively). It should be noted that the 16-electrode curve (in black) is synonymous with the 16-electrode *adjacent drive* curve in figure 4.10. By comparing the *interpolated receive* method (figure 4.16) with the *standard receive* method (figure 4.10) it is clear that the *interpolated* method makes better use of larger electrode arrays in that it produces a resolution improvement across the whole of the image rather than improving the peripheral resolution at the expense of the central resolution.

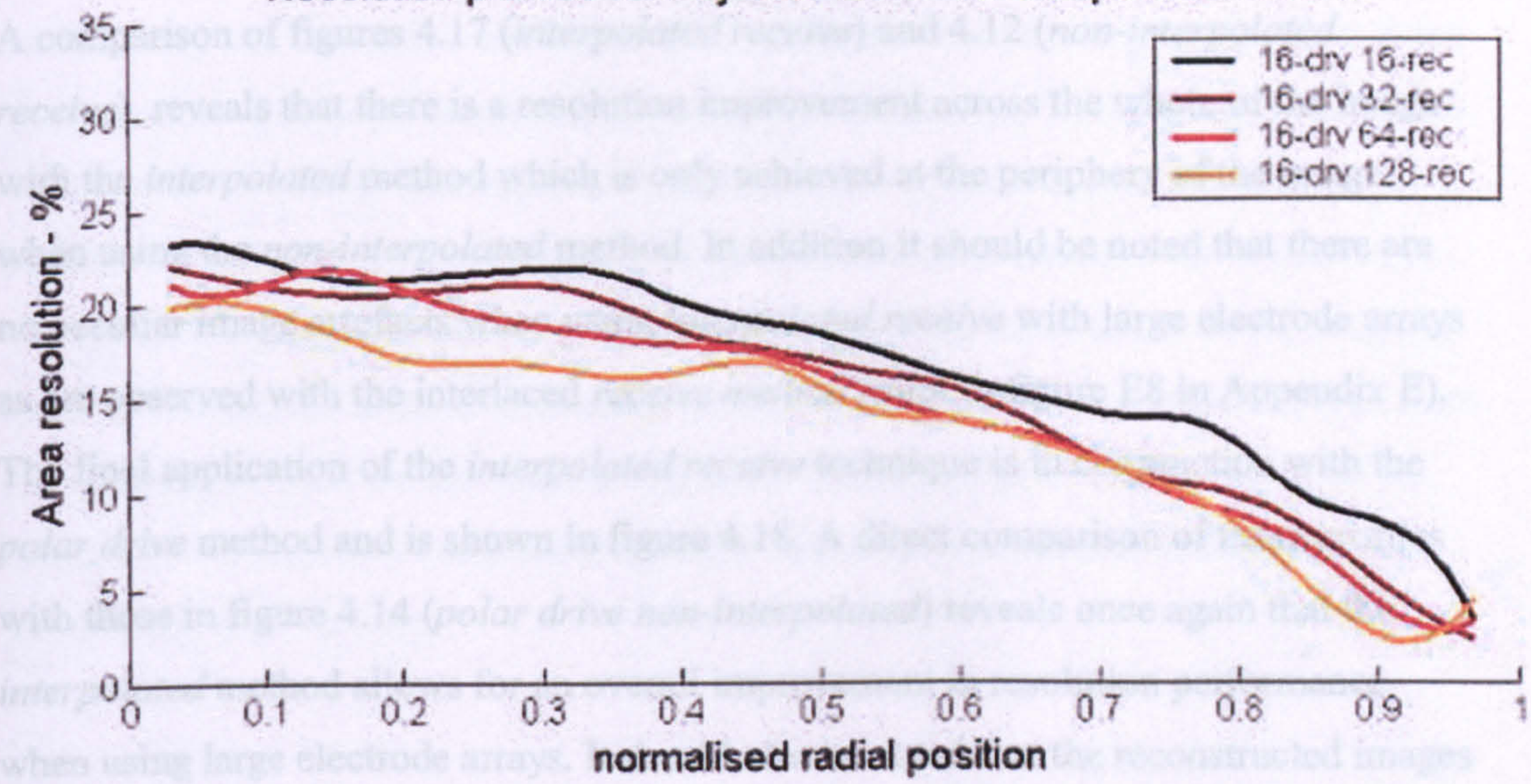

Figure 4.16 – Resolution profiles for the *adjacent drive, interpolated receive* technique using 16-, 32-, 64- and 128-electrode arrays.

In Figure 4.17, the results of the *cross drive, interpolated receive* method are shown. Once again it should be noted that the 16-electrode (black curve) corresponds exactly with the 16-electrode *cross drive* profile in figure 4.12.

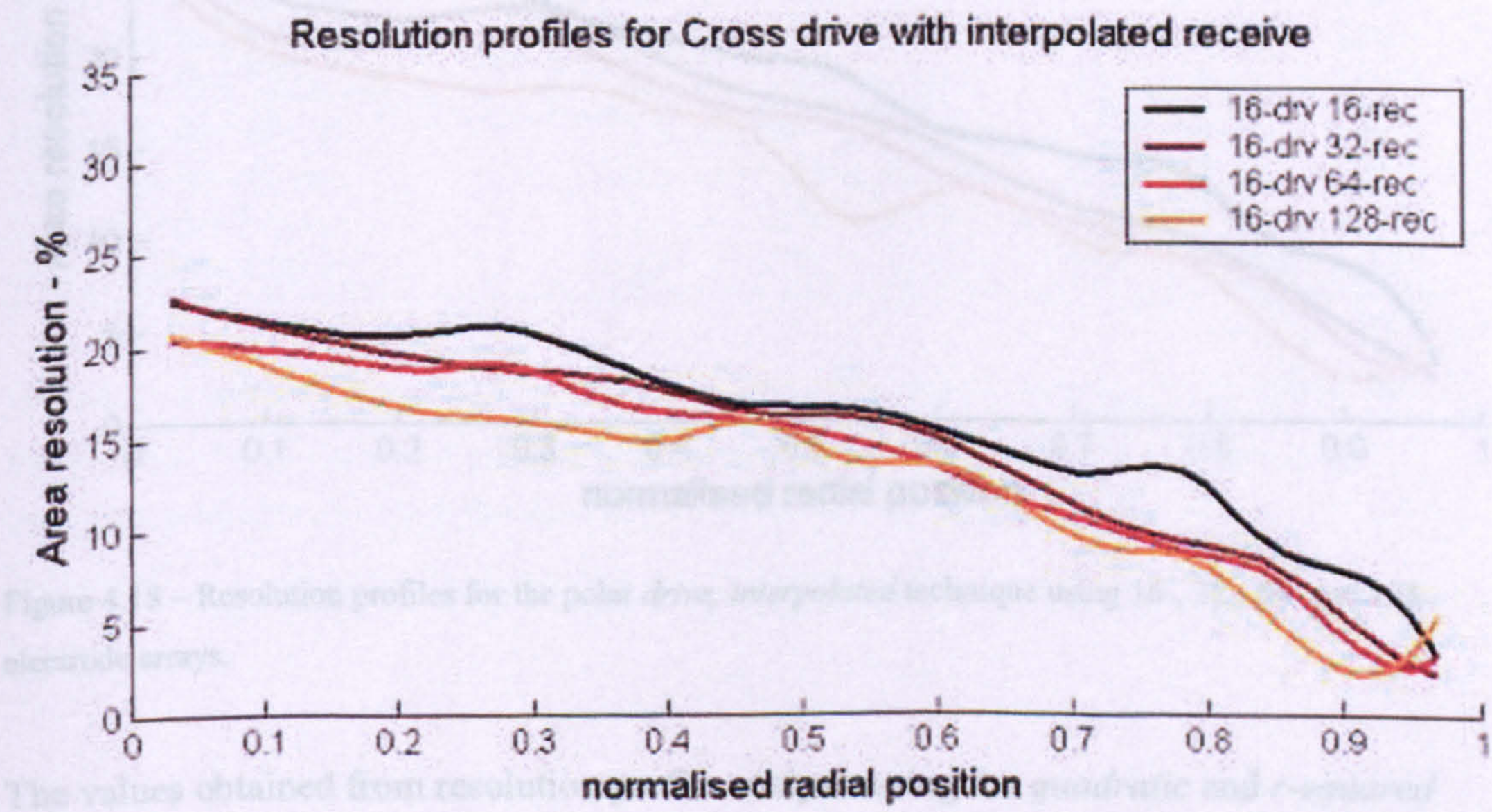

Figure 4.17 – Resolution profiles for the *cross drive, interpolated* technique using 16-, 32-, 64- and 128-electrode arrays.

A comparison of figures 4.17 (*interpolated receive*) and 4.12 (*non-interpolated receive*), reveals that there is a resolution improvement across the whole of the image with the *interpolated* method which is only achieved at the periphery of the image when using the *non-interpolated* method. In addition it should be noted that there are no peculiar image artefacts when using *interpolated receive* with large electrode arrays as are observed with the interlaced *receive method* (refer to figure E8 in Appendix E). The final application of the *interpolated receive* technique is in conjunction with the *polar drive* method and is shown in figure 4.18. A direct comparison of these profiles with those in figure 4.14 (*polar drive non-interpolated*) reveals once again that the *interpolated* method allows for an overall improvement in resolution performance when using large electrode arrays. It should also be noted that the reconstructed images do not suffer from strange artefacts when using large electrode arrays as is the case with the *polar drive interleaved receive* method (refer to figure E9 in Appendix E).

Figure 4.18 – Resolution profiles for the polar *drive, interpolated* technique using 16-, 32-, 64- and 128-electrode arrays.

The values obtained from resolution profile analysis using the *quadratic* and *r-squared* curve fitting methods are tabulated in table 4.1. For each data collection method there are there two columns representing the *quadratic* and *r-squared* curve fitting

techniques respectively. Within each column the central resolution (R_c), spatial variance (α) and regression coefficient (R^2) values for that particular method are listed. A discussion of these parameters is given in the next section. Table 4.2 lists the results of the noise sensitivity tests applied to all of the data collection methods used in the simulation. For each method, Normally distributed noise is added to the simulated voltage data at RMS amplitudes of 1,3 and 5μV and the overall effect on the image is quantified using the method outlined in section 4.3.2. Since the noise is measured from the images, the units are the same as that used to express the conductivity, which in this case is mSiemens. A detailed discussion of the noise sensitivity performance is given in the next section.

	Quadratic curve fitting			*r-squared* curve fitting		
Data collection method	R_c	α	R^2	R_c	α	R^2
Adjacent: 16-drv 16-rec	22.2	1.03	0.977	23.2	0.83	0.973
Adjacent: 32-drv 32-rec	26.5	0.68	0.994	26.2	1.13	0.942
Adjacent: 64-drv 64-rec	29.7	0.73	0.988	28.7	1.25	0.899
Adjacent: 16-drv 16-rec(int)	18.3	1.28	0.986	19.6	0.80	0.975
Adjacent: 32-drv 32-rec(int)	22.7	0.68	0.995	22.6	1.08	0.953
Adjacent: 64-drv 64-rec(int)	29.5	0.83	0.972	26.2	1.17	0.918
Cross: 16-drv 16-rec	21.6	0.84	0.971	22.4	0.87	0.961
Cross: 32-drv 32-rec	23.3	0.66	0.994	23.5	1.18	0.877
Cross: 64-drv 64-rec	22.3	0.68	0.992	21.1	1.10	0.958
Cross: 16-drv 16-rec(int)	18.7	0.95	0.980	19.6	0.86	0.972
Cross: 32-drv 32-rec(int)	21.1	0.64	0.994	21.2	1.15	0.866
Cross: 64-drv 64-rec(int)	23.7	0.93	0.899	22.8	1.28	0.632
Polar: 16-drv 16-rec	33.1	0.95	0.923	38.3	1.53	0.571
Polar: 32-drv 32-rec	28.2	0.81	0.982	29.2	1.39	0.584
Polar: 64-drv 64-rec	29.7	0.94	0.983	30.3	1.46	0.529
Polar: 16-drv 16-rec(int)	27.8	0.66	0.966	30.6	1.33	0.358
Polar: 32-drv 32-rec(int)	25.4	0.75	0.986	26.4	1.34	0.609
Polar: 64-drv 64-rec(int)	23.9	2.06	0.846	23.4	1.60	0.709
Adjacent: 16-drv 16-rec	22.2	1.03	0.977	23.2	0.83	0.973
Adjacent: 16-drv 32-rec	21.2	1.12	0.993	21.9	0.92	0.992
Adjacent: 16-drv 64-rec	21.3	0.88	0.993	20.9	0.91	0.991
Adjacent: 16-drv 128-rec	19.0	0.97	0.952	19.7	0.96	0.945
Cross: 16-drv 16-rec	21.6	0.84	0.971	22.4	0.87	0.961
Cross: 16-drv 32-rec	21.5	0.83	0.987	22.6	1.05	0.940
Cross: 16-drv 64-rec	20.2	0.85	0.994	20.3	0.95	0.991
Cross: 16-drv 128-rec	19.6	0.65	0.941	20.5	1.11	0.815
Polar: 16-drv 16-rec	33.1	0.95	0.923	38.3	1.53	0.571
Polar: 16-drv 32-rec	26.3	0.66	0.981	28.3	1.29	0.694
Polar: 16-drv 64-rec	23.8	0.67	0.982	25.3	1.23	0.789
Polar: 16-drv 128-rec	22.9	0.72	0.955	23.8	1.30	0.621

Table 4.1 – Results from analysis of the 2-dimensional resolution profiles using the *quadratic* and *r-squared* curve fitting methods. For each method the central resolution (R_c), spatial variance (α) and regression coefficient (R^2) are presented.

	Image noise (in mSiemens)		
Data collection method	1μV	3μV	5μV
Adjacent: 16-drv 16-rec	0.065	0.211	0.325
Adjacent: 32-drv 32-rec	0.112	0.334	0.549
Adjacent: 64-drv 64-rec	0.196	0.573	0.932
Adjacent: 16-drv 16-rec(int)	0.401	1.210	1.997
Adjacent: 32-drv 32-rec(int)	0.364	1.065	1.809
Adjacent: 64-drv 64-rec(int)	0.309	0.944	1.581
Cross: 16-drv 16-rec	0.101	0.281	0.478
Cross: 32-drv 32-rec	0.155	0.472	0.781
Cross: 64-drv 64-rec	0.211	0.647	1.061
Cross: 16-drv 16-rec(int)	0.554	1.392	2.591
Cross: 32-drv 32-rec(int)	0.391	1.140	1.942
Cross: 64-drv 64-rec(int)	0.375	1.097	1.903
Polar: 16-drv 16-rec	0.064	0.186	0.311
Polar: 32-drv 32-rec	0.151	0.399	0.615
Polar: 64-drv 64-rec	0.182	0.522	0.856
Polar: 16-drv 16-rec(int)	0.243	0.734	1.264
Polar: 32-drv 32-rec(int)	0.354	1.114	1.629
Polar: 64-drv 64-rec(int)	0.362	1.079	1.754
Adjacent: 16-drv 16-rec	0.064	0.188	0.353
Adjacent: 16-drv 32-rec	0.107	0.312	0.564
Adjacent: 16-drv 64-rec	0.152	0.447	0.766
Adjacent: 16-drv 128-rec	0.211	0.622	1.054
Cross: 16-drv 16-rec	0.083	0.300	0.502
Cross: 16-drv 32-rec	0.146	0.473	0.783
Cross: 16-drv 64-rec	0.183	0.504	0.826
Cross: 16-drv 128-rec	0.229	0.649	1.142
Polar: 16-drv 16-rec	0.070	0.187	0.348
Polar: 16-drv 32-rec	0.124	0.380	0.553
Polar: 16-drv 64-rec	0.151	0.462	0.805
Polar: 16-drv 128-rec	0.211	0.616	1.091

Table 4.2 – Results from analysis of the noise sensitivity of all of the 2-dimensional resolution results for all the electrode configurations. Artificial Normally distributed noise is added to each of the simulated voltage profiles at RMS amplitudes of 1,3 and 5μV. The noise sensitivity values quoted refer to the overall levels of noise contributed to the reconstructed images.

4.6 Discussion of the 2D EIT resolution performance results

4.6.1 Comparison of the resolution analysis methods

Analysis of the resolution profiles shown in the previous section is made using both the *r-squared* curve-fitting method (previously outlined by Wheeler *et al*, 2002) and the *quadratic* curve fitting method which was proposed in section 4.3.1.3 as an improvement. The results of both analytical methods are presented in table 4.1. By comparing the values predicted by these two methods for central resolution (R_c) and spatial variance (α) it can be seen that there is a significant discrepancy between them, thus it can be concluded that they do not agree. To investigate this discrepancy further it is helpful to know the closeness of fit of the curves predicted by the two models. This can be determined from the regression coefficients (R^2 values). The mean R^2 value for the *r-squared* method is 0.819 and the mean R^2 value achieved by the *quadratic* method is 0.969, suggesting that the *quadratic* method offers a better fit to the measured data. This result tends to undermine the hypothesis of Kotre (1994) which states that the resolution is related only to the square of the radius. However, it should be remembered that the measurements on which this hypothesis is based were made using only one data collection strategy (*adjacent drive / adjacent receive*) for which the *r-squared* model does in fact hold well ($R^2 = 0.973$).

By examining the central resolution values (R_c) predicted by the two curve-fitting methods and comparing these with central resolution values read from the resolution profiles (figures 4.10 to 4.18) it is observed that the *quadratic* method is sometimes in error by as much as 5% whereas the *r-squared* method predicts R_c to within 0.1% of the true value. This can be seen clearly in figure 4.19 in which the difference between the predicted R_c values and the measured values is shown. It is interesting to note that the *r-squared* method always slightly underestimates the central resolution. It is possible that the underestimation is introduced from the iterative method used for finding the closest match to the R_c and α parameters (see Appendix D for a full listing of the function).

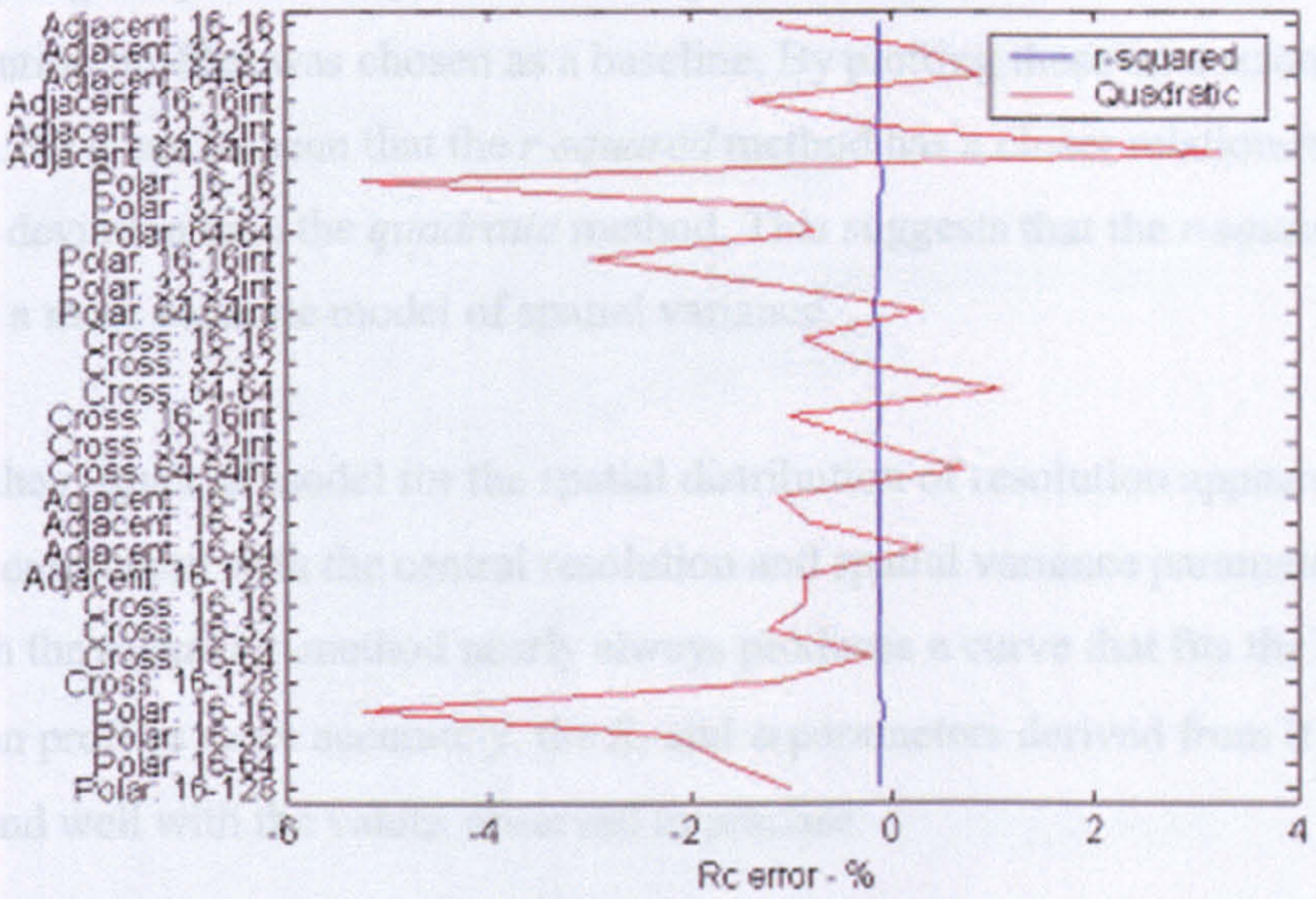

Figure 4.19 – Graph showing the errors in calculation of the central resolution (R_c) using the *r-squared* curve fitting model (blue graph) and the *quadratic* curve fitting model (red graph).

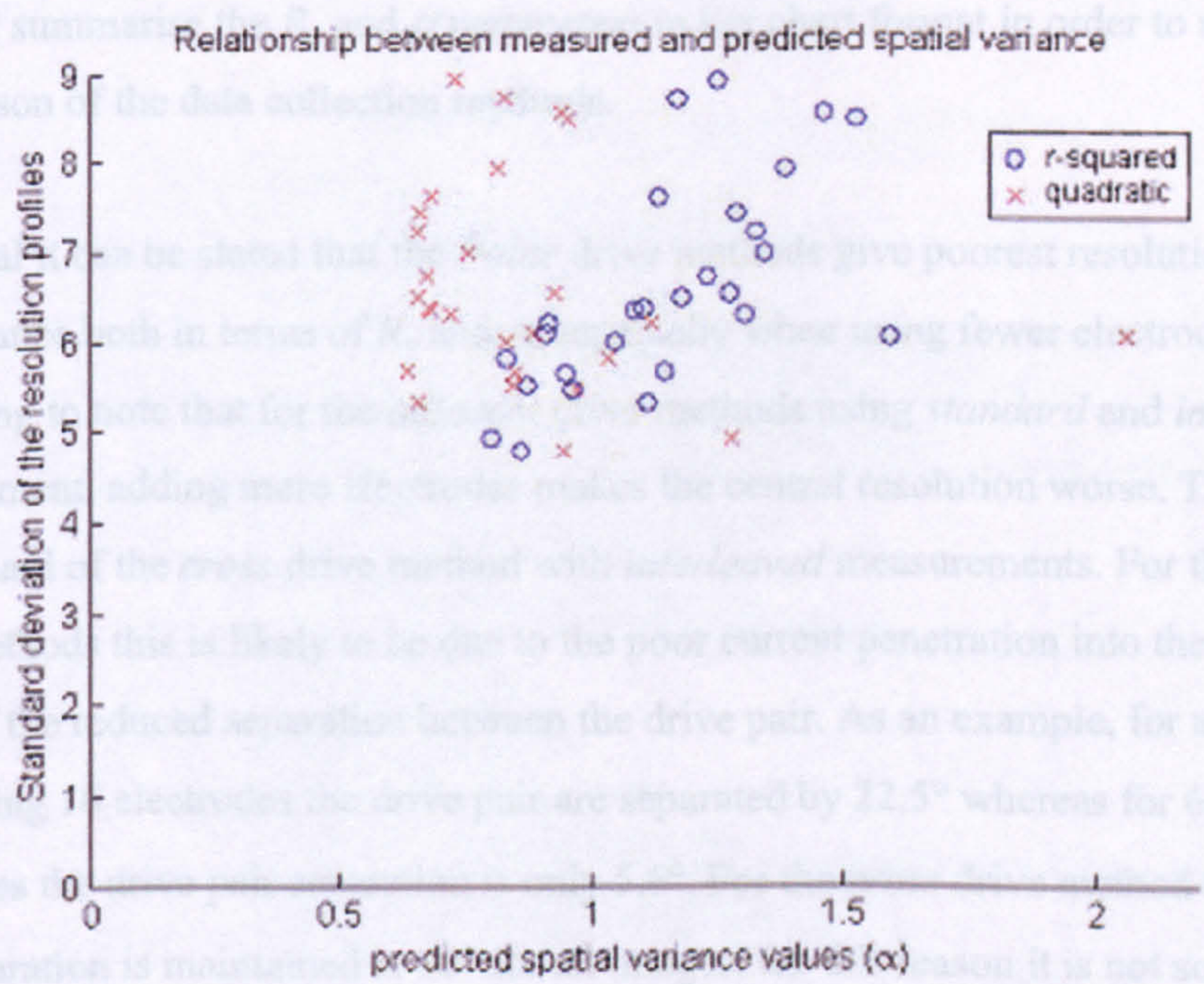

Figure 4.20 – Scatter graph showing the relationship between the predicted spatial variance values (α) from the two resolution models and the standard deviation of the resolution profiles.

For analysing the predicted spatial variance parameters (α), the standard deviation of the resolution profiles was chosen as a baseline. By plotting these on a scatter graph (figure 4.20) it can be seen that the *r-squared* method has a closer relationship to the standard deviation than the *quadratic* method. This suggests that the *r-squared* method provides a more accurate model of spatial variance.

Overall the *r-squared* model for the spatial distribution of resolution appears to have a stronger correlation with the central resolution and spatial variance parameters. Although the *quadratic* method nearly always produces a curve that fits the measured resolution profiles more accurately, the R_c and α parameters derived from it do not correspond well with the values observed in practise.

4.6.2 Comparison of the resolution performance

Having established that the *r-squared* model of resolution distribution is the most realistic, the performance of the different data collection strategies are now considered in terms of the central resolution and spatial variance calculated from it. Figures 4.21 and 4.22 summarise the R_c and α parameters in bar chart format in order to aid comparison of the data collection methods.

In general it can be stated that the *Polar* drive methods give poorest resolution performance both in terms of R_c and α, especially when using fewer electrodes. It is interesting to note that for the *adjacent* drive methods using *standard* and *interleaved* measurement, adding more electrodes makes the central resolution worse. This can also be said of the *cross* drive method with *interleaved* measurements. For the *adjacent* drive methods this is likely to be due to the poor current penetration into the object as a result of the reduced separation between the drive pair. As an example, for adjacent drive using 16 electrodes the drive pair are separated by 22.5° whereas for 64 electrodes the drive pair separation is only 5.6°. For the *cross* drive method the drive pair separation is maintained at 90° for all images; for this reason it is not so clear why adding extra electrodes should reduce the image quality. For the remainder of the data collection strategies, adding more electrodes improves R_c whilst α becomes worse.

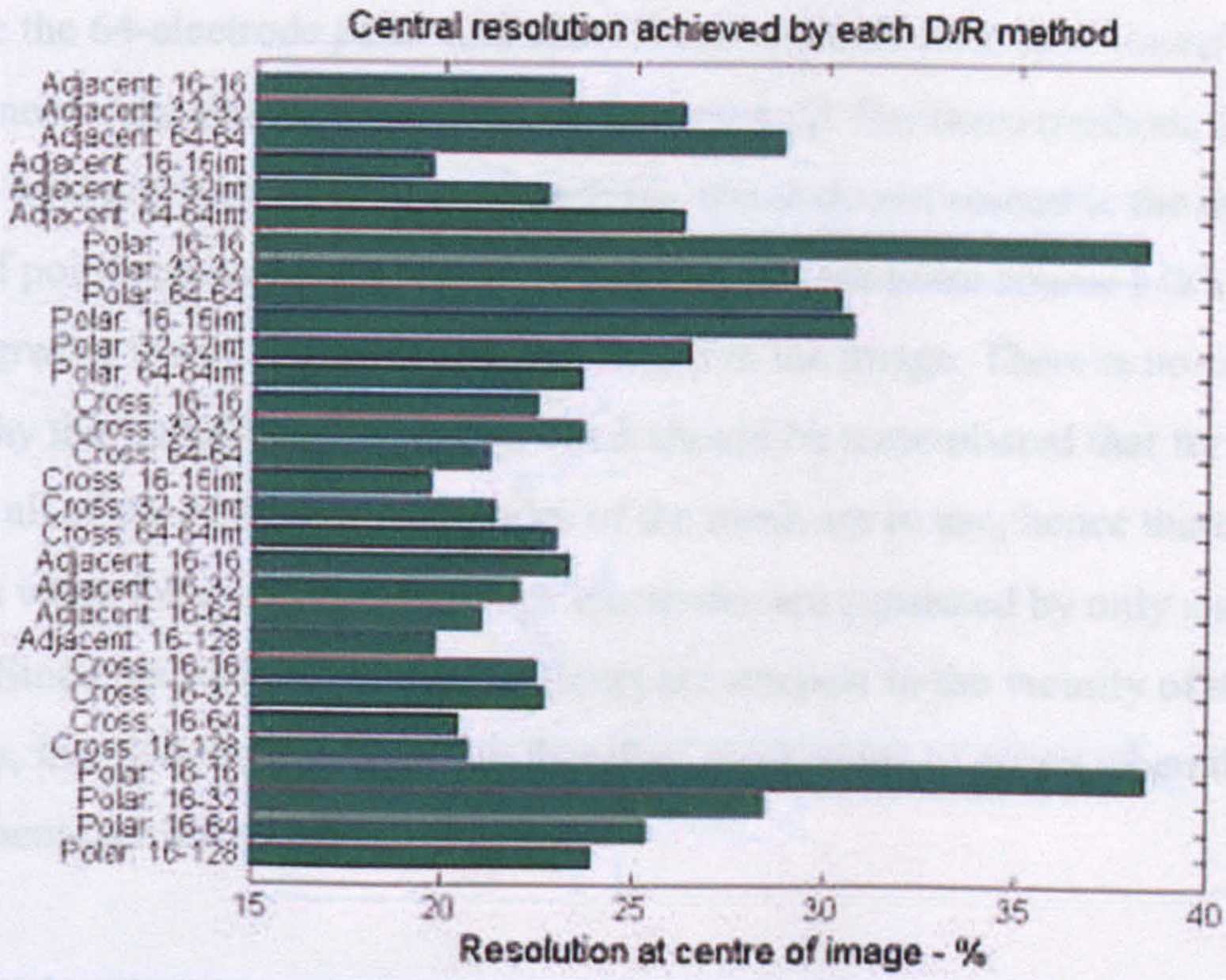

Figure 4.21 – Bar chart showing the central resolution values obtained for each of the different measurement strategies (values obtained using the *r-squared* model).

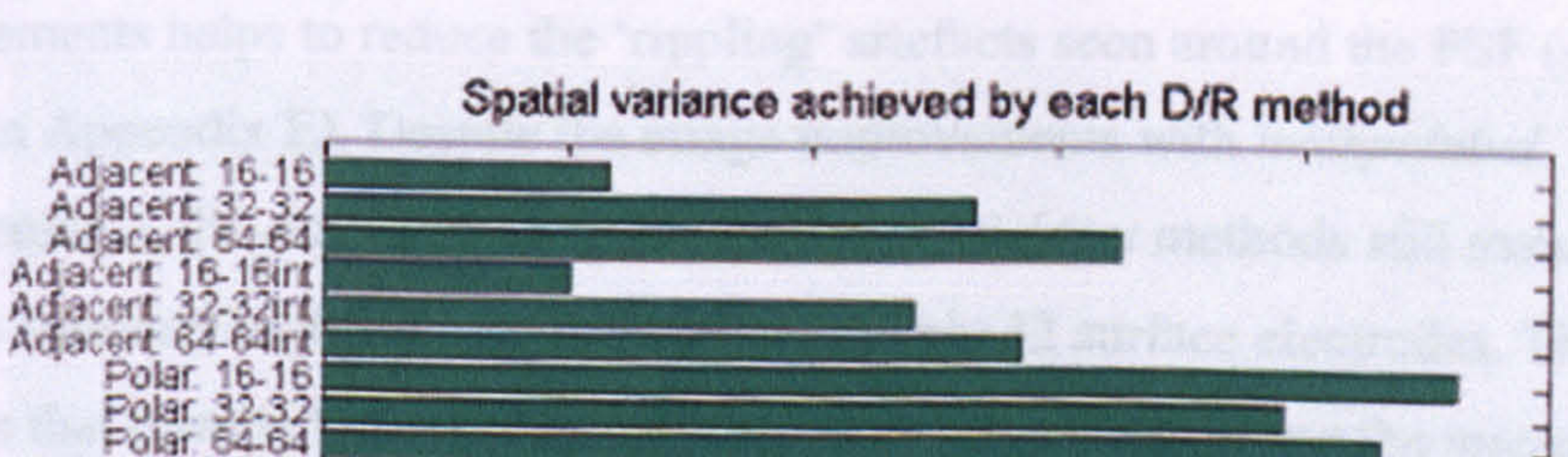

Figure 4.22 – Bar chart showing the spatial variance values obtained for each of the different measurement strategies (values obtained using the *r-squared* model).

There are two data collection strategies which produce severely distorted images. These are the 64-electrode *polar* and *cross* drive methods with *interleaved* measurements (see figures E4 and E6 in Appendix E). For these methods the images appear to be dominated by structured patterns which do not resemble the expected images of point conductivity change. It is only when the point source has a radial position greater than 0.8 that it becomes visible in the image. There is no obvious reason why this should be happening, but it should be remembered that for these two methods, all of the 128 peripheral nodes of the mesh are in use, hence there are occasions when the current and voltage electrodes are separated by only a single mesh element. Since the surface voltage gradients are steepest in the vicinity of the electrodes, the modelled voltages are therefore most prone to errors when the measurement pair are so close.

The *interpolated* measurement technique improves the image resolution in all cases, but most notably with the *polar* drive method, for which the resolution performance using 64 and 128 electrodes is comparable with the *adjacent* and *cross* methods. It can also be seen that increasing the number of electrodes when making *interpolated* measurements helps to reduce the 'rippling' artefacts seen around the PSF (see figures E7-E9 in Appendix E). Despite the image improvements with *interpolated* measurements, the *Adjacent:16-16int* and *Cross:16-16int* methods still manage to produce similarly high resolution images with only 32 surface electrodes. This suggests that there is little benefit to be gained from implementing the *interpolated* measurement concept since many more surface electrodes (and hence circuit components associated with driving them) are required.

4.6.3 Noise sensitivity

In order to assess the overall sensitivity of each data collection strategy to measurement noise, the noise sensitivity values have been plotted as a 'stacked' bar chart (see figure 4.23). Note: the end of each bar rather than its length corresponds to the actual noise value, which can be read off from the horizontal axis. The various data collection strategies are indicated by their names along the vertical axis.

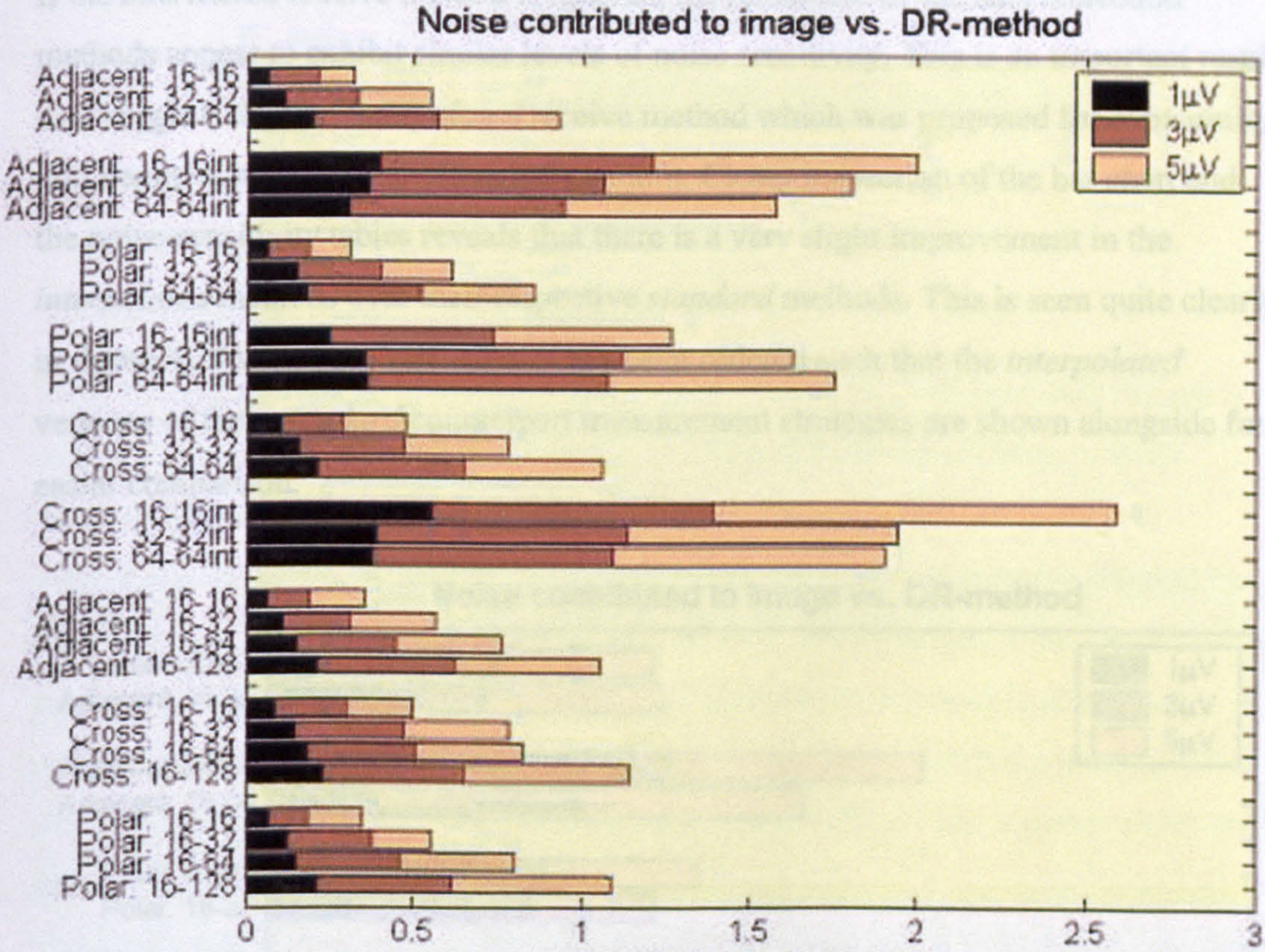

Figure 4.23 – Bar chart showing the noise sensitivity values (in mSiemens) as a result of simulated noise at 1,3 and 5μV for each of the different measurement strategies

It can be seen quite clearly that the *interleaved* receive methods generally suffer more from noise than the *non-interleaved* receive methods, but it is interesting to note that as the number of electrodes is increased, the noise sensitivity is decreased for the *adjacent* and *cross interleaved* methods. In all other cases, the noise sensitivity increases with the number of electrodes used. This would be expected with the *standard* (non-*interpolated*) methods since increasing the number of electrodes means that the voltage measurements are made closer together and are hence smaller and more noise-sensitive. For the *interpolated* methods, however, the actual signal-to-noise ratio should not change as the number of electrodes is increased. One possible explanation why the image noise still increases is that more measurements are used to reconstruct the images, hence more noise is being included in the image reconstruction process.

If the *interleaved* receive method is ignored, the remainder of the data collection methods appear to exhibit similar levels of noise sensitivity. This is an important result as it suggests that the *interpolated* receive method which was proposed for overcoming noise-sensitivity problems offers little benefit. Closer inspection of the bar chart and the noise-sensitivity tables reveals that there is a very slight improvement in the *interpolated* methods over their respective *standard* methods. This is seen quite clearly in figure 4.24 where the vertical axis has been ordered such that the *interpolated* versions of their *standard* counterpart measurement strategies are shown alongside for easier comparison.

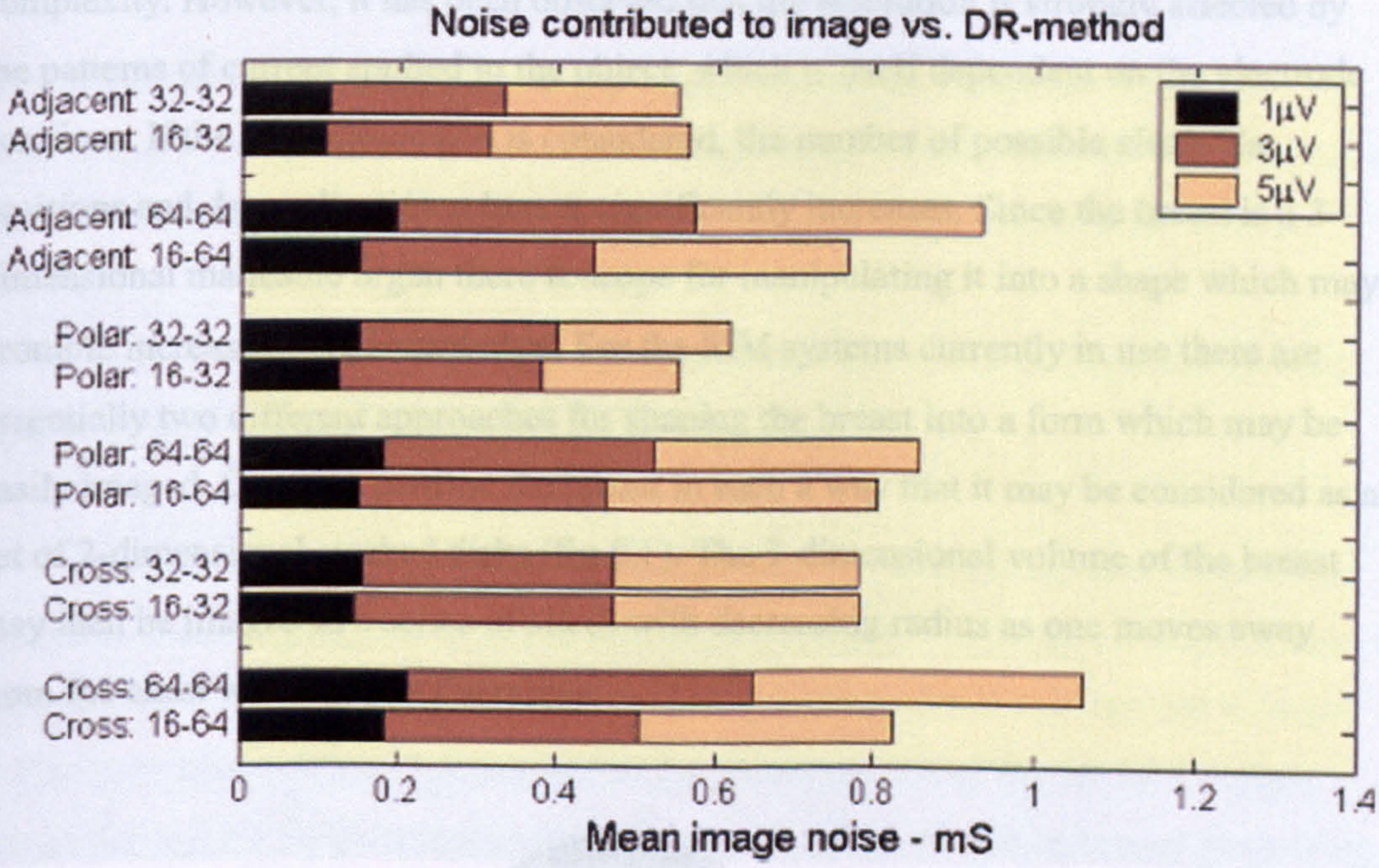

Figure 4.24 – Bar chart showing a comparison of noise sensitivity for various measurement strategies as a result of using the interpolated receive method. In each group, the upper bar corresponds to the standard measurement technique and the lower bar corresponds to the equivalent interpolated technique.

It is clear that in all but the 32 electrode *adjacent* method there is a slight benefit in terms of noise performance in using the *interpolated* method rather than the *standard* method, however, this benefit cannot be justified by the added circuit complexity necessary to accommodate the extra electrodes.

CHAPTER FIVE

DEVELOPMENT OF A SOFTWARE SIMULATION FOR 3D BREAST IMAGING USING EIM

5.1 Introduction

It has been shown in Chapter 4 that the image resolution for 2-dimensional images is inherently poor (central resolution is at best ~20%) and that the addition of extra electrodes does not offer a significant improvement to justify the added circuit complexity. However, it has been observed that the resolution is strongly affected by the patterns of current applied to the object, which is itself dependent on the electrode positions. If the third dimension is considered, the number of possible electrode positions and data collection schemes significantly increases. Since the breast is a 3-dimensional malleable organ there is scope for manipulating it into a shape which may promote increased image resolution. For the EIM systems currently in use there are essentially two different approaches for shaping the breast into a form which may be easily imaged. One is to confine the breast in such a way that it may be considered as a set of 2-dimensional stacked disks (fig 5.1). The 3-dimensional volume of the breast may then be imaged as a series of slices with decreasing radius as one moves away from the chest wall towards the nipple.

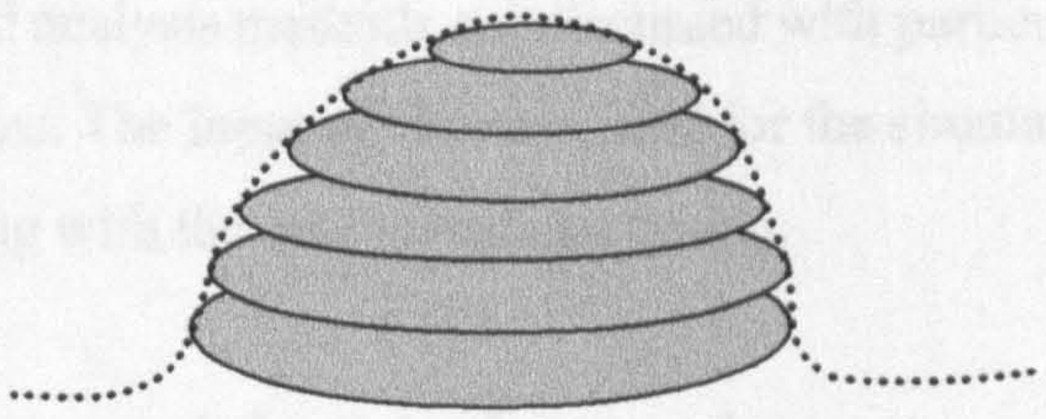

Figure 5.1 – One method for imaging the 3-dimensional breast volume is to treat it as a set of individual 2-dimensional slices, which are subsequently combined into the whole 3D structure.

Since this does not treat the whole volume of the breast at once it is sometimes referred to as 2½-dimensional imaging. The other approach is to press the breast as flat as

possible against the chest wall and image it as a flat surface beneath a 2-dimensional grid of electrodes (figure 5.2).

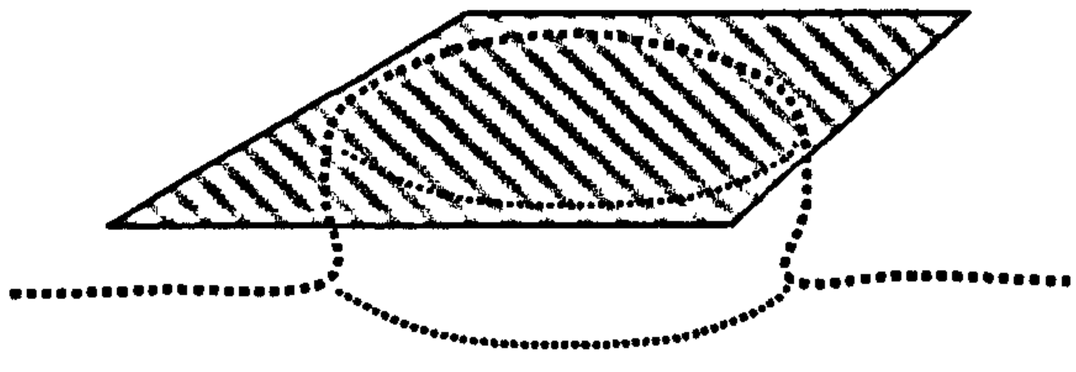

Figure 5.2 – An alternative method used for 3-dimensional EIM is to press the breast flat against the chest wall under a 2-dimensional grid of electrodes.

Both these assumptions simplify the geometry, making the image reconstruction process more straightforward, however, they do not necessarily offer the best electrode arrangement in terms of image resolution. The question which needs answering is:

"*How do the breast shape, 3D electrode distribution and patterns of applied current affect the final image resolution?*"

This chapter aims to develop a simulation procedure for addressing these three issues. It begins by developing a deformable mathematical model to simulate a range of breast shapes in 3D space. An algorithm for simulating 3-dimensional currents and voltages is then presented along with an algorithm for reconstruction of the 3D EIM images. Image display and analysis methods are discussed with particular reference to working in three dimensions. The input parameters used for the simulation are dealt with in the next chapter, along with the results and discussion.

5.2 A software model of the human breast

In this section, a mathematical model for describing the approximate contour of a breast is developed. Particular attention is given to the fact that the breast can be compressed reasonably flat against the chest wall (i.e. if the woman lies in the supine position) or allowed to hang away from the chest wall (if the woman is in the prone position). In addition, a method for tracking the position of a tumour during breast compression is developed.

5.2.1 Modelling the breast shape as a deformable solid

For the purposes of this study, the breast will be considered to be rotationally symmetrical with the axis of rotation passing from the chest wall out through the nipple. Although the breast can assume non-rotationally symmetrical shapes (as used during breast compression for x-ray mammography), it has generally been the case for EIT that the imaged object is assumed to be circular. What is therefore required is a mathematical expression for a cross-sectional profile of the breast which can be deformed in a similar way in which the breast shape changes when it is compressed against the chest wall. This profile can then be rotated about the axis to form the mathematical breast surface. It has been found that an equation of the form:

$$z = \left| r^n \right| \tag{5.1}$$

provides a reasonable model, where z is the distance out from the base of the model (away from the chest wall), r is the radial distance from the rotational axis and n controls the flatness of the curve. By examining a family of these curves for various values of n (figure 5.3) it can be seen that they bear a similar resemblance to the way in which the breast deforms when pressed against the chest wall using a flat surface.

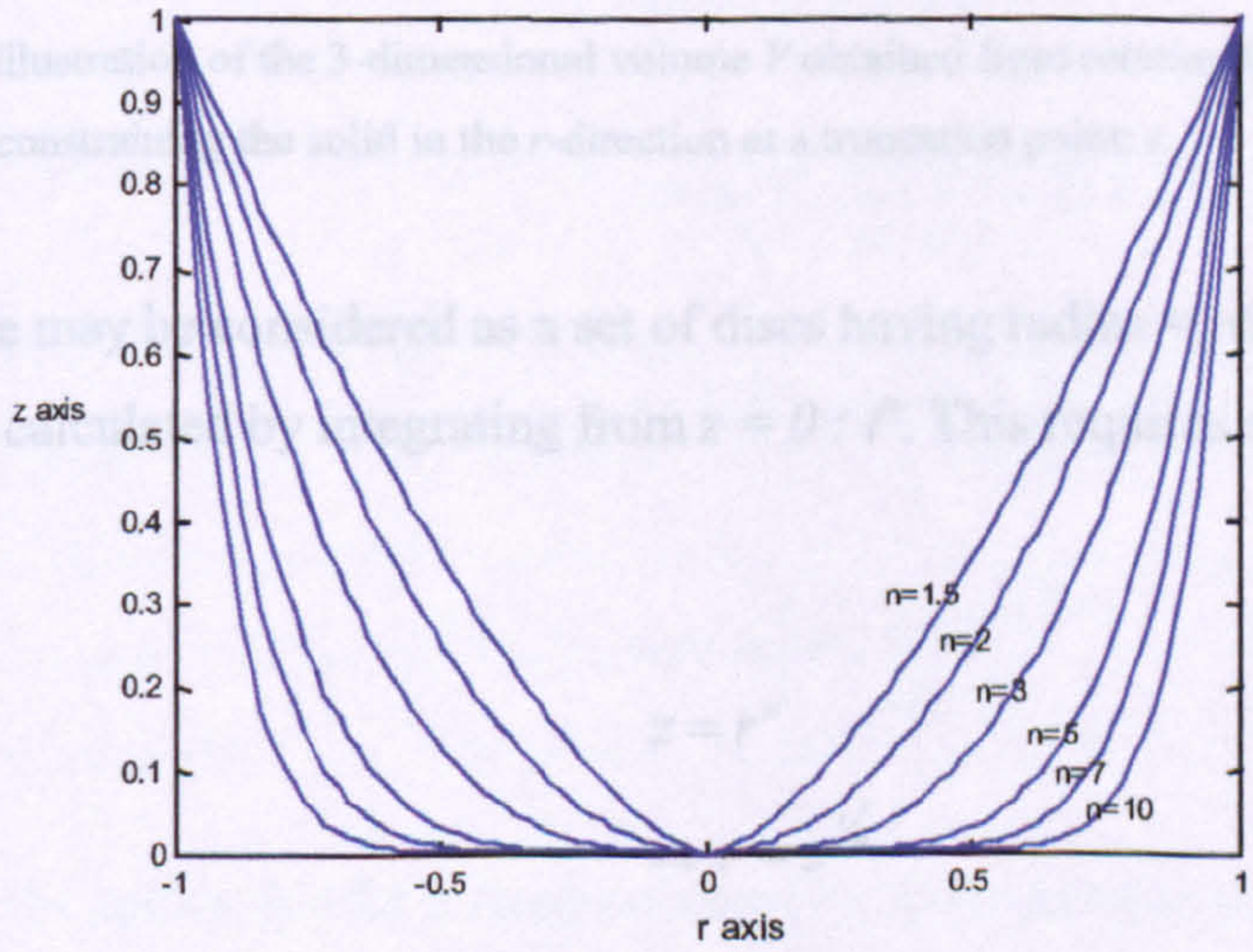

Figure 5.3 – A family of curves based on the equation $z = r^n$ for various values of n.

Lower values of n produce a profile curve similar to a pendant breast whereas higher values of n produce profiles resembling a compressed breast. In order to make use of these curves to provide a sensible breast model it is necessary to constrain the volume enclosed by them since it is reasonable to assume that the volume of any breast remains constant independent of its shape. A simple method for this is to truncate the curve in the $|r|$ direction at a value, say t, which is calculated to preserve the volume. Since this will also control the base diameter of the model, a final check must be performed to ensure that the variation in base diameter as the model is compressed is realistic and preferably minimal. To calculate t an expression must first be derived for the volume enclosed by rotating the curve around the z-axis (figure 5.4).

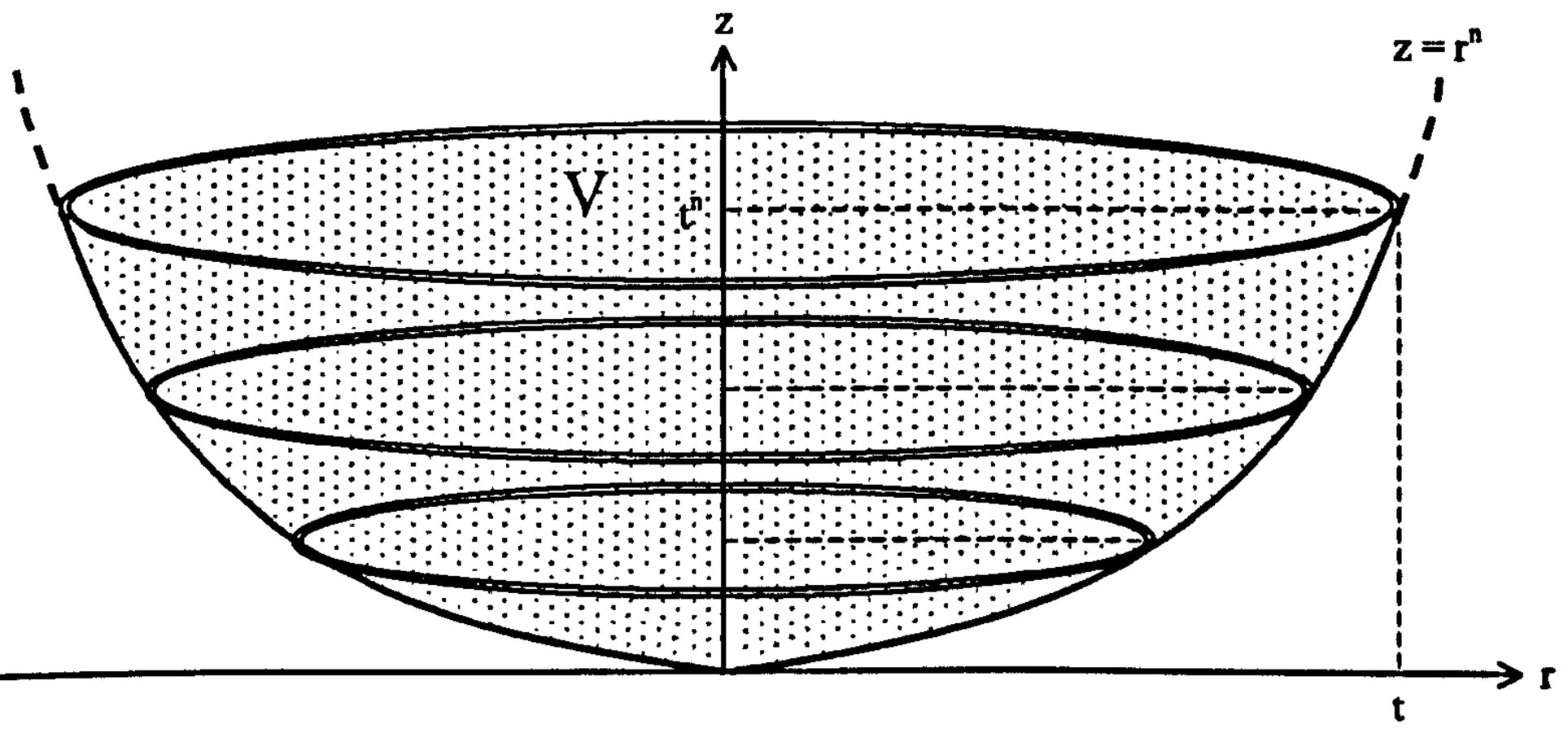

Figure 5.4 – Illustration of the 3-dimensional volume V obtained from rotating the curve $z = r^n$ about the z-axis whilst constraining the solid in the r-direction at a truncation point: t.

The volume may be considered as a set of discs having radius = $r(z)$ and thickness dz, and can be calculated by integrating from $z = 0 : t^n$. This requires an expression for r in terms of z:

$$z = r^n \tag{5.2}$$

$$\Rightarrow r = z^{1/n} \tag{5.3}$$

The area A of each disc is therefore:

$$A = \pi r^2 \tag{5.4}$$

$$= \pi \cdot z^{2/n} \tag{5.5}$$

The volume V is calculated by integrating the areas of all the discs from $z = 0 \rightarrow t^n$:

$$V = \int_0^{t^n} \pi \cdot z^{2/n} dz \tag{5.6}$$

$$= \pi \left[\frac{1}{2/n + 1} z^{2/n+1} \right]_0^{t^n} \tag{5.7}$$

$$= \pi \left[\frac{n}{2+n} z^{\frac{2+n}{n}} \right]_0^{t^n} \tag{5.8}$$

$$= \frac{\pi \cdot n}{2+n} t^{2+n} \tag{5.9}$$

Since the volume is to be constrained by the truncation point t, an expression is required for t in terms of the volume:

$$V = \frac{\pi \cdot n}{2+n} t^{2+n} \tag{5.10}$$

$$\Rightarrow V \cdot \frac{2+n}{\pi \cdot n} = t^{2+n} \tag{5.11}$$

$$\Rightarrow \ln\left(V \cdot \frac{2+n}{\pi \cdot n} \right) = (2+n)\ln(t) \tag{5.12}$$

$$\Rightarrow \ln(t) = \ln\left(V \cdot \left(\frac{2+n}{\pi \cdot n} \right)^{1/2+n} \right) \tag{5.13}$$

$$\Rightarrow t = \left(V \cdot \frac{2+n}{\pi \cdot n} \right)^{1/2+n} \tag{5.14}$$

Equation 5.14 shows that for a fixed volume (V), the truncation point (t) is only dependent on the amount of compression (n). It was specified previously that the relationship between the base diameter (given by $2t$) and compression should be examined to ensure that it is realistic and preferably small. This is easily visualised by

plotting $2t$ as a function of n for various values of V and is shown in figure 5.5. The range of n has been chosen as 1.5 to 12 since these values produce breast shapes which visually correspond to the pendant and compressed positions respectively.

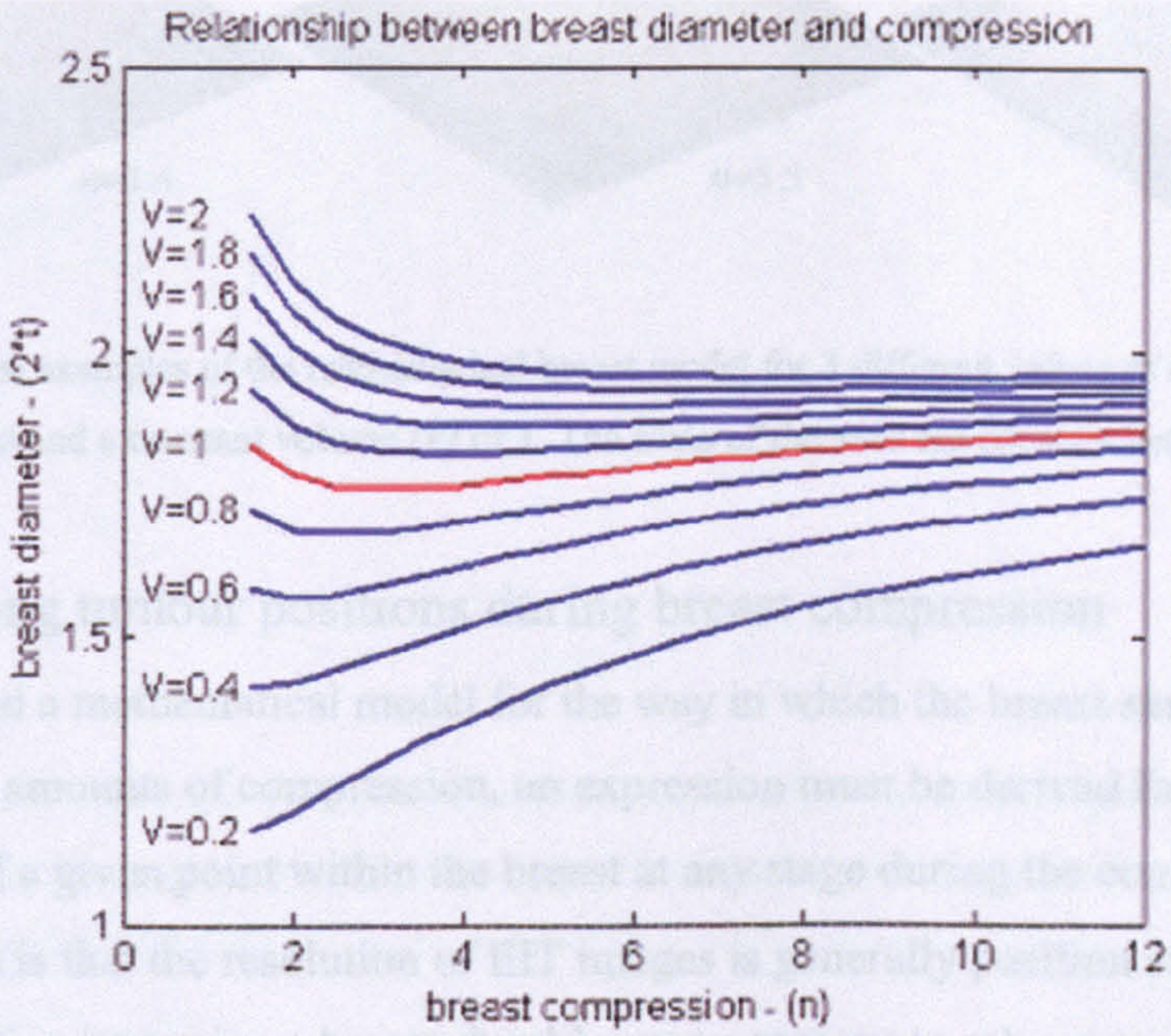

Figure 5.5 – graphical representation of the relationship between the base diameter of the breast model and the amount of compression for a range of different breast volumes. The red corresponds to a volume of 1 for which the variation in breast diameter is smallest.

It can be seen from figure 5.5 that the variation in t is smallest (10%) when V is given a value of 1. Since the variation is small, the model is considered realistic for the purposes of the simulation and will be used throughout the remaining chapters.

Visualisation of the model has been accomplished using the surface rendering functions available in Matlab® (see figure 5.6). To aid visualisation, equation 5.1 has been inverted and translated so that the breast appears to be rising out of the x-y plane rather than resting with the nipple at the origin. This does not affect any of the calculations regarding V or t. The numerical definition of the breast surface is now:

$$\left\{ \begin{array}{ll} z = |t^n - r^n| & \text{for } r <= t^n \\ z = 0 & \text{for } r > t^n \end{array} \right\} \qquad 5.15$$

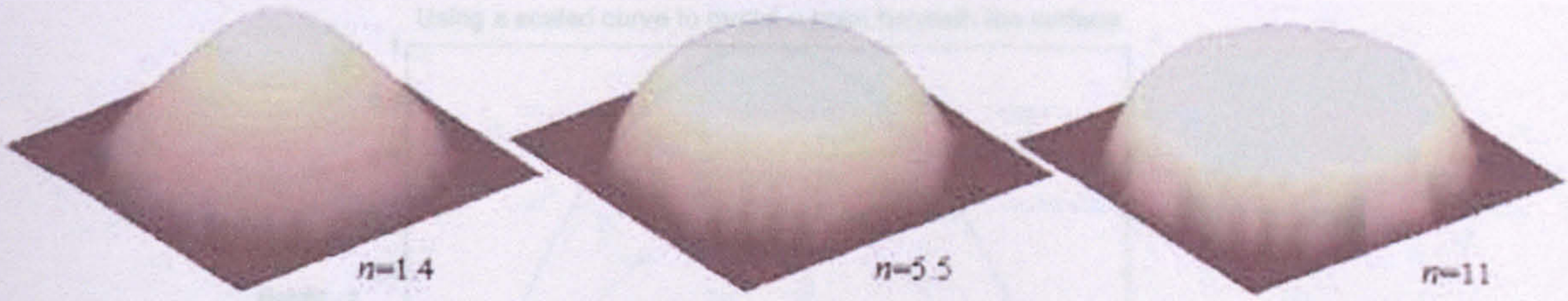

Figure 5.6 – Some examples of the mathematical breast model for 3 different values of n (indicated alongside images) and a constant volume (V) of 1. The scale of the axes are constant between all images.

5.2.2 Tracking tumour positions during breast compression

Having defined a mathematical model for the way in which the breast surface deforms under various amounts of compression, an expression must be derived for calculating the position of a given point within the breast at any stage during the compression. The reason for this is that the resolution of EIT images is generally position sensitive, and if the action of compressing a breast should cause a tumour to relocate relative to the skin surface then this could have a noticeable effect on the ability of the imaging system to detect it. It is therefore essential to know the precise location of a tumour as the breast shape is altered so that the different imaging methods may be accurately simulated and fairly compared.

The first step to solving this problem is to concentrate on the movement of points on the surface of the breast model, since an expression for the surface already exists. Intuitively, any point on the surface of the breast will remain on the surface for any degree of compression. Points located beneath the surface can then be considered to lie on a scaled version of the outer surface. As an example, consider the graph in figure 5.7. The solid line represents the outer surface of the breast and the red circle represents an arbitrary point within the breast. To study the movement of this point inside the breast as the model is compressed, a scaled version of the outer surface which passes through the point (here denoted by a dashed line) is used. In this way the movements of all points inside the model can be found from an understanding of how points move on the surface.

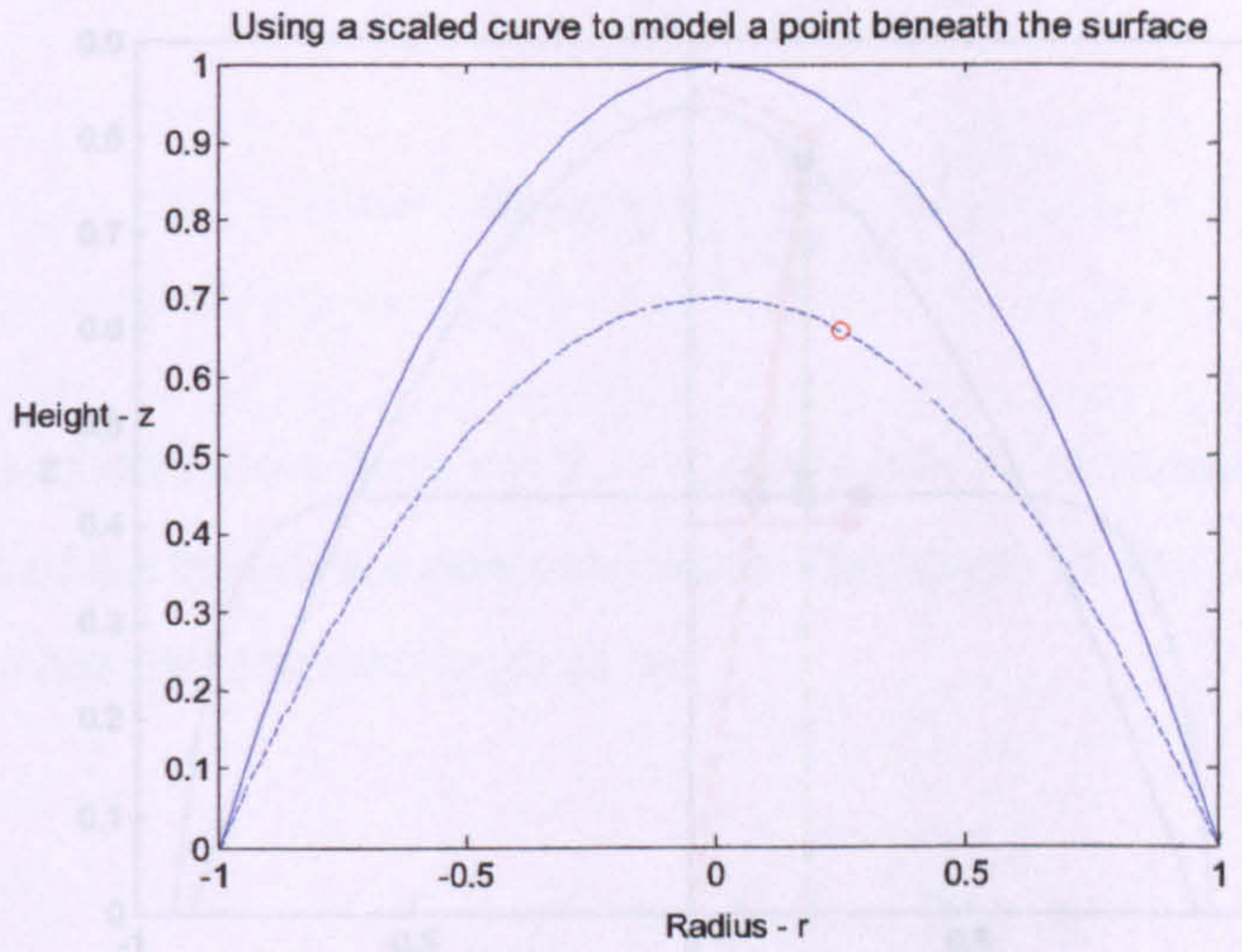

Figure 5.7 – A curve representing the surface profile of the breast model with an arbitrary point (here shown as a red circle) to represent a tumour position. The dotted curve is a scaled version of the outer curve which intersects the point.

As the power value *n* changes, the position of the point also changes along the surface. The way in which the point moves along the surface is a function of the elasticity of the breast tissues, hence a model is required for its behaviour. Three different approaches are considered (see figure 5.8):

1. Translate point in z-direction only
2. Translate point along a line passing through the origin
3. Move point along the surface, preserving the relative distance along the surface from the origin (or nipple) as the surface is altered

To explain the three methods, the black point on the upper curve of figure 5.8 is translated using each of the three methods previously outlined. If the point is translated only in the z-direction it will follow the green arrow. If it is translated on a line passing through the origin it will follow the red arrow. Finally, if the relative distance across the surface in both curves is held constant then the relative distance of the point along the upper curve (i.e. the upper pink arrow) is measured out along the lower curve as shown by the lower pink arrow.

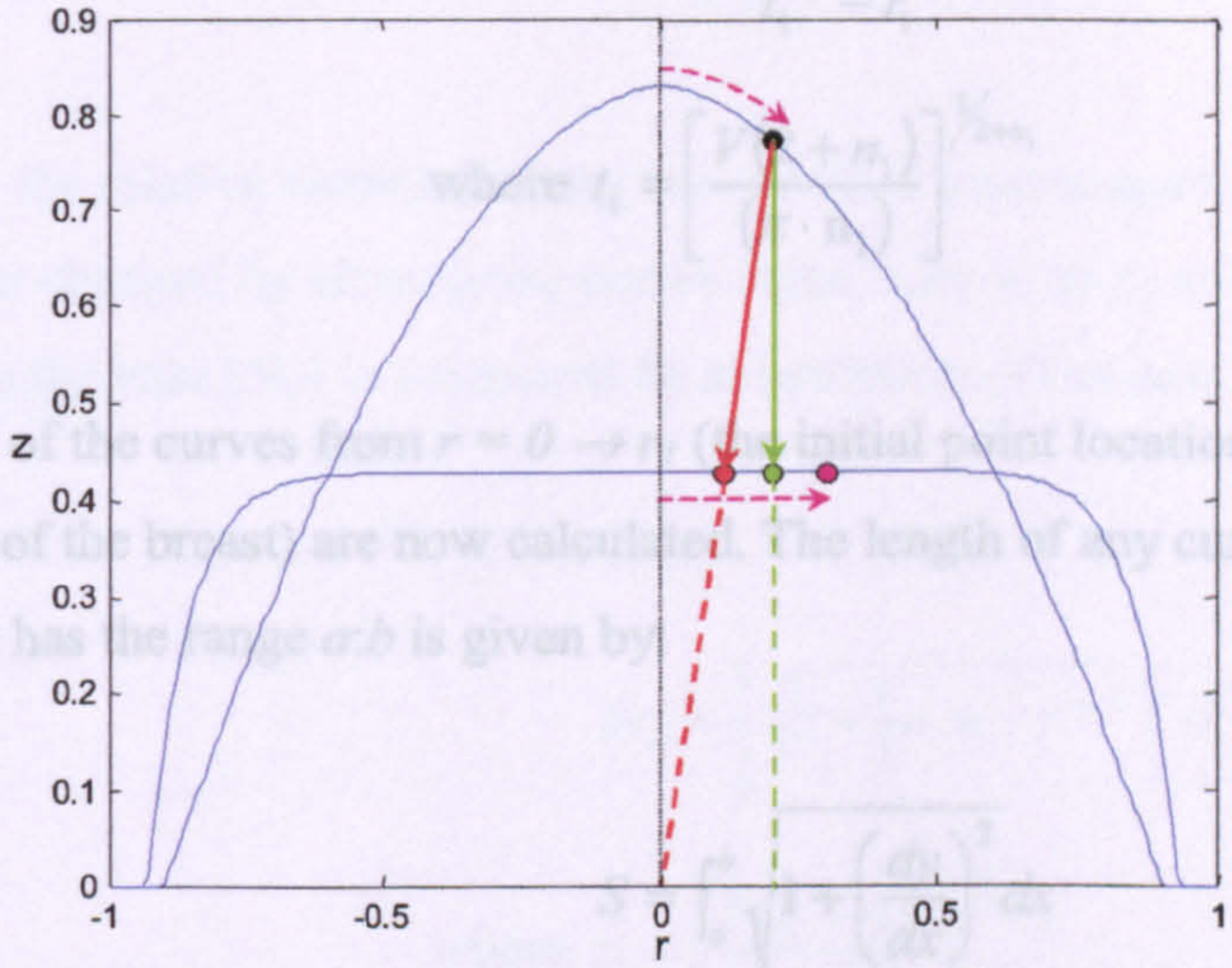

Figure 5.8 – Illustration of the change in tumour position predicted by three different models as the breast is changed from pendant (upper curve) to compressed (lower curve). The original tumour position is represented as a black dot. The green, red and pink dots correspond to the tumour positions predicted by methods 1-3 respectively.

Since human skin has elastic properties, method 3 is intuitively better for modelling the change in tumour position as this aims to preserve the relative distances between all adjacent points in the skin surface as it is compressed into different shapes.

The derivation of a mathematical expression for the change in position of any given point during breast compression now follows:

The initial position of the point is given by $[z_1, r_1, \theta, n_1, V]$ where z_1 is the height from the base of the model, r_1 is the radial distance from the model's axis, θ is the angle made around the X-Y plane, n_1 is the initial power value and V is the breast volume. The compressed breast is then given a power value of n_2, the volume (V) will of course be unchanged, and the resulting point location is described by z_2, r_2 and θ. Note that θ is unchanged, hence is ignored in the derivation. To begin with, the surface (equation 5.15) must be scaled by a factor, a, so that it passes through the point (r_1,z_1):

$$z_1 = a\left(t_1^{n_1} - r_1^{n_1}\right) \tag{5.16}$$

$$\Rightarrow a = \frac{z_1}{t_1^{n_1} - r_1^{n_1}} \tag{5.17}$$

$$\text{where } t_1 = \left[\frac{V(2+n_1)}{(\pi \cdot \mathrm{n}_1)}\right]^{1/2+n_1} \tag{5.18}$$

The lengths of the curves from $r = 0 \rightarrow r_1$ (the initial point location) and from $r = 0 \rightarrow t_1$ (the edge of the breast) are now calculated. The length of any curve of the form $y = f(x)$ where x has the range $a:b$ is given by:

$$S = \int_a^b \sqrt{1 + \left(\frac{dy}{dx}\right)^2}\, dx \tag{5.19}$$

In this case the curve is of the form $z=f(r)$ giving:

$$S = \int_a^b \sqrt{1 + \left(\frac{dz}{dr}\right)^2}\, dr \tag{5.20}$$

$$\text{where } z = a\left(t^{n_1} - r^{n_1}\right) \tag{5.21}$$

$$\Rightarrow \frac{dz}{dr} = -a \cdot n_1 \cdot r^{n_1 - 1} \tag{5.22}$$

$$\Rightarrow S = \int \sqrt{1 + \left(a \cdot n_1 \cdot r^{n_1 - 1}\right)^2}\, dr \tag{5.23}$$

The length of the curve from $r = 0 \rightarrow r_1$ is denoted Sr_1 and the length from $r = 0 \rightarrow t_1$ is denoted St_1. This gives:

$$Sr_1 = \int_0^{r_1} \sqrt{1 + \left(a \cdot n_1 \cdot r^{n_1 - 1}\right)^2}\, dr \tag{5.24}$$

$$St_1 = \int_0^{t_1} \sqrt{1 + \left(a \cdot n_1 \cdot r^{n_1 - 1}\right)^2} \tag{5.25}$$

The proportional distance along the curve of the point (k) is expressed as:

$$k = \frac{Sr_1}{St_1} \qquad 5.26$$

To preserve the relative distances along the curves, k must remain constant. The breast shape is now changed by altering the power value from n_1 to n_2 and the distance from the nipple to the base (St_2) is calculated by substitution of the new values into equation 5.25:

$$St_2 = \int_0^{t_2} \sqrt{1 + \left(a \cdot n_2 \cdot r^{n_2 - 1}\right)^2}\, dr \qquad 5.27$$

$$\text{where } t_2 = \left[\frac{V(2 + n_2)}{(\pi \cdot n_2)}\right]^{1/2 + n_2} \qquad 5.28$$

The new value of Sr_2 may be calculated as a proportion of St_2 using:

$$Sr_2 = k \cdot St_2 \qquad 5.29$$

Finally the new point location (r_2,z_2) is found by solving the equations:

$$Sr_2 = \int_0^{r_2} \sqrt{1 + \left(a \cdot n_2 \cdot r^{n_2 - 1}\right)^2}\, dr \qquad 5.30$$

$$z_2 = a\left(t_2^{\,n_2} - r_2^{\,n_2}\right) \qquad 5.31$$

No analytical solution is found for the integral in equation 5.30, hence an iterative approach involving a numerical approximation is required to obtain r_2. The software listing for the function used to solve these equations is shown in Appendix F. To illustrate the tumour tracking process, a family of curves representing the profiles of a breast at various states of compression, along with a family of points is displayed in figure 5.9.

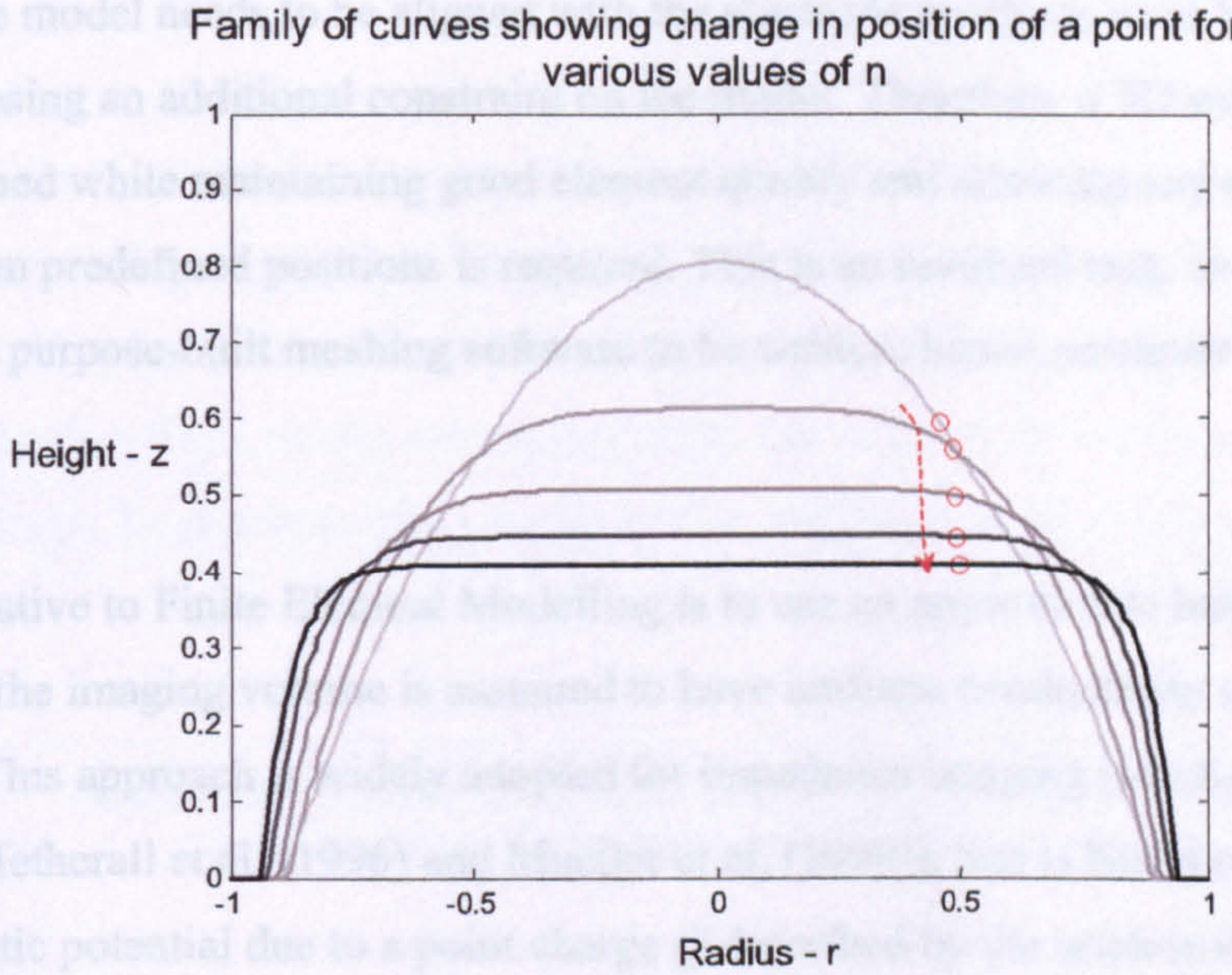

Figure 5.9 – Illustration of a family of breast surface curves in which the positions of a particular point on the breast surface (here represented as a series of red circles) are calculated using the method described by equations 5.30 and 5.31

5.3 Software for simulating 3D EIM systems

Using the breast model described, a simulation framework must be established which is capable of emulating the impedance measurement process, thereby allowing images to be reconstructed from the results.

5.3.1 Simulating currents and voltages within the breast model

For the 2-dimensional simulation, the solution to the forward problem was achieved using a Finite Element approach. Since the image shape and peripheral node positions were kept constant it was possible to design one mesh and use this for all the simulations. In three dimensions however, this is not straight forward. The aim is to study the behaviour of image resolution as a function of breast shape, hence the 3D mesh needs to be deformable. Whilst Finite Element modelling can be used to simulate the mechanical behaviour of an object based on the material properties and external forces, the large degree of deformation possible with the breast will almost certainly lead to large deformations in the 3D element shapes. One of the requirements of Finite Element analysis is that the elements should be even-sided and not become elongated,

hence a difficulty could arise here. Another limitation is that the node distribution within the model needs to be aligned with the electrode positions used for the imaging, thus imposing an additional constraint on the model. Therefore, a 3D mesh which can be deformed while maintaining good element quality and allowing any electrode nodes to be given predefined positions is required. This is an involved task, and requires extensive purpose-built meshing software to be written, hence a simpler approach is sought.

An alternative to Finite Element Modelling is to use an approximate half-plane model in which the imaging volume is assumed to have uniform conductivity and to be semi-infinite. This approach is widely adopted for impedance imaging (see Kotre et al, (1996), Metherall et al, (1996) and Mueller et al, (1999)), and is based on the electrostatic potential due to a point charge Q described by the relationship;

$$V_P = \frac{Q}{4\pi\varepsilon_0}\left(\frac{1}{d_P} - \frac{1}{d_0}\right) \qquad 5.32$$

where V_P is the voltage at a given point P, ε_0 is the permittivity of free space, d_P is the distance from P to the charge Q and d_0 is the distance from Q to a position of zero potential. If it is assumed that the zero potential is at infinity, then the voltage distribution becomes;

$$V_P = \frac{Q}{4\pi\varepsilon_0 d_P} \qquad 5.33$$

In other words, the voltage V_P is inversely proportional to the distance from the point charge Q. A problem with using this model, however, is that when d_P is zero (i.e. when the measurement point P is placed on the charge Q), V_P becomes infinite. In practise this is not true, since a finite voltage can be measured on the current drive electrodes. To work around this, a modification has been made such that if the source voltage V_S applied to a given electrode is known, then the voltage at any point P becomes

$$V_P = V_S \frac{\lambda}{d_P + \lambda} \qquad 5.34$$

where λ is the 'half-distance', or the distance at which the measured voltage V_P is half of the source voltage V_S and can be thought of as representing the conductivity of the half-plane. Varying the λ parameter produces a family of voltage curves but in all cases, when $d_P = 0$ (i.e. on the source electrode) the value of V_P will be equal to V_S, the source voltage. To illustrate this a family of the voltage/distance profiles is shown in figure 5.10.

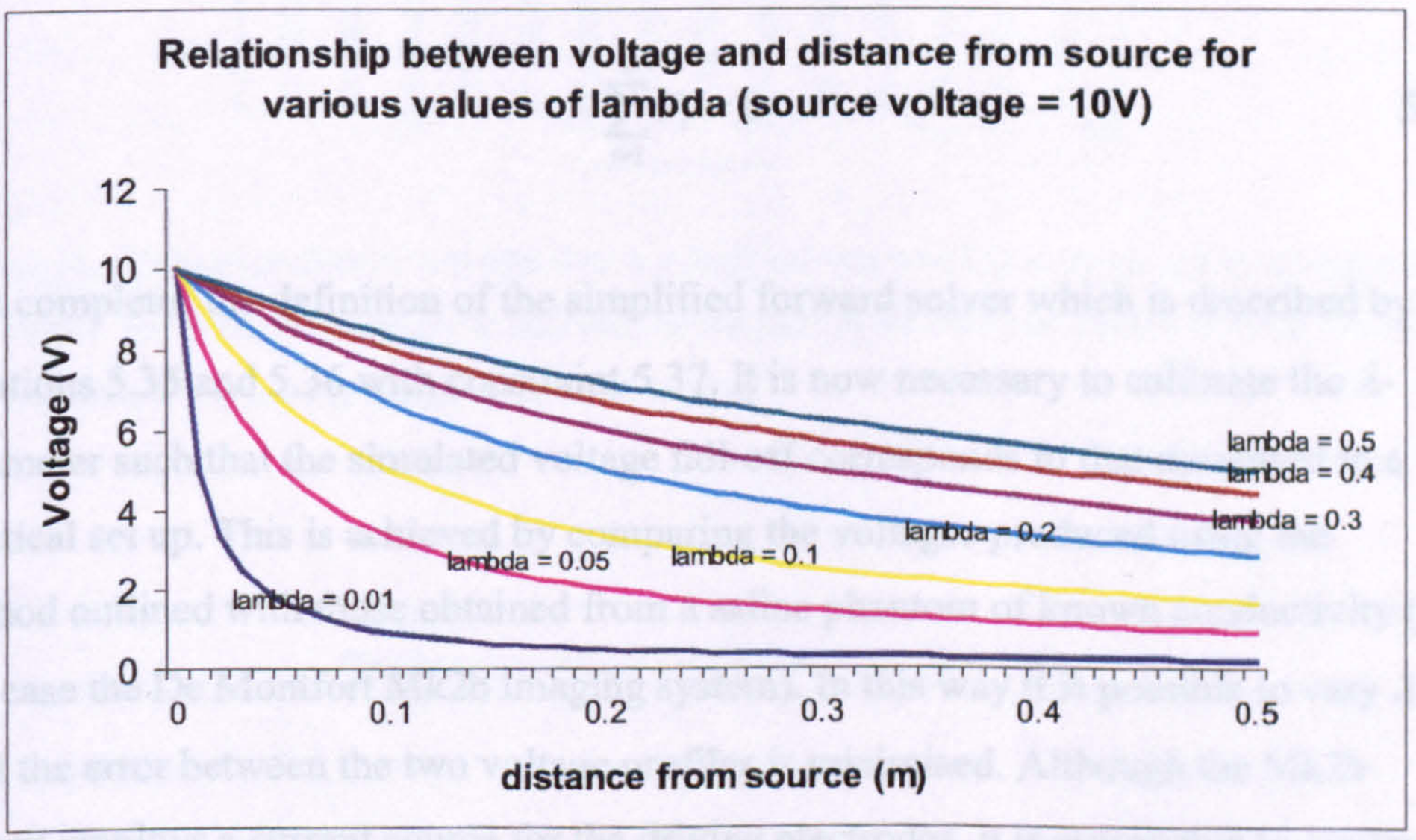

Figure 5.10 – A family of Voltage/distance curves obtained using equation 5.34 based on a source voltage of 10V and λ ranging from 1cm to 50cm. The important properties of these curves is that they all pass through 10V when d_P is zero, and they are all inversely proportional to d_P.

To complete the model it must be extended to allow for multiple source electrodes since in EIT there are at least two current-driving electrodes. This is easily implemented by making use of the superposition theory which states that for a linear system, each element of the system may be treated independently, and their outputs summed to produce the overall response. This is summarised in the formula:

$$V_P = \sum_{i=1}^{n} V_i \frac{\lambda}{\lambda + d_i} \qquad 5.35$$

where n is the number of voltage sources, V_i is the voltage on the i^{th} electrode and d_i is the distance from the measurement point P to the i^{th} electrode and is calculated as:

$$d_i = \sqrt{(x_P - x_i)^2 + (y_P - y_i)^2 + (z_P - z_i)^2} \qquad 5.36$$

where (x_P, y_P, z_P) are the co-ordinates of P and (x_i, y_i, z_i) are the co-ordinates of the i^{th} electrode. In order to uphold Kirchoff's 2nd law, an additional constraint is applied such that:

$$\sum_{i=1}^{n} V_i = 0 \qquad 5.37$$

This completes the definition of the simplified forward solver which is described by equations 5.35 and 5.36 with constraint 5.37. It is now necessary to calibrate the λ-parameter such that the simulated voltage fall-off corresponds to that measured in a practical set up. This is achieved by comparing the voltages produced using the method outlined with those obtained from a saline phantom of known conductivity (in this case the De Montfort Mk2b imaging system). In this way it is possible to vary λ until the error between the two voltage profiles is minimised. Although the Mk2b system employs a current source for the driving electrodes, it is reasonable to assume that the voltages applied to the drive pairs will all be the same as long as the saline has uniform conductivity and that the electrodes are evenly spaced. In this case the Mk2b system can be considered to be operating in a voltage-source mode and the measured profile should be compatible with the forward solver outlined. The graphs in figure 5.11 show the calculated and simulated voltage profiles superimposed on one another.

In order to correlate the voltage profiles, the DC component is removed from both of them and the simulated profile scaled to match the amplitude of the measured profile. By repeating this for several values of λ and calculating the RMS error between the measured and simulated data (see figure 5.12) it is possible to find a value for λ at which the error is minimised. For the saline phantom described, the optimum value of λ is found to be 0.01468m.

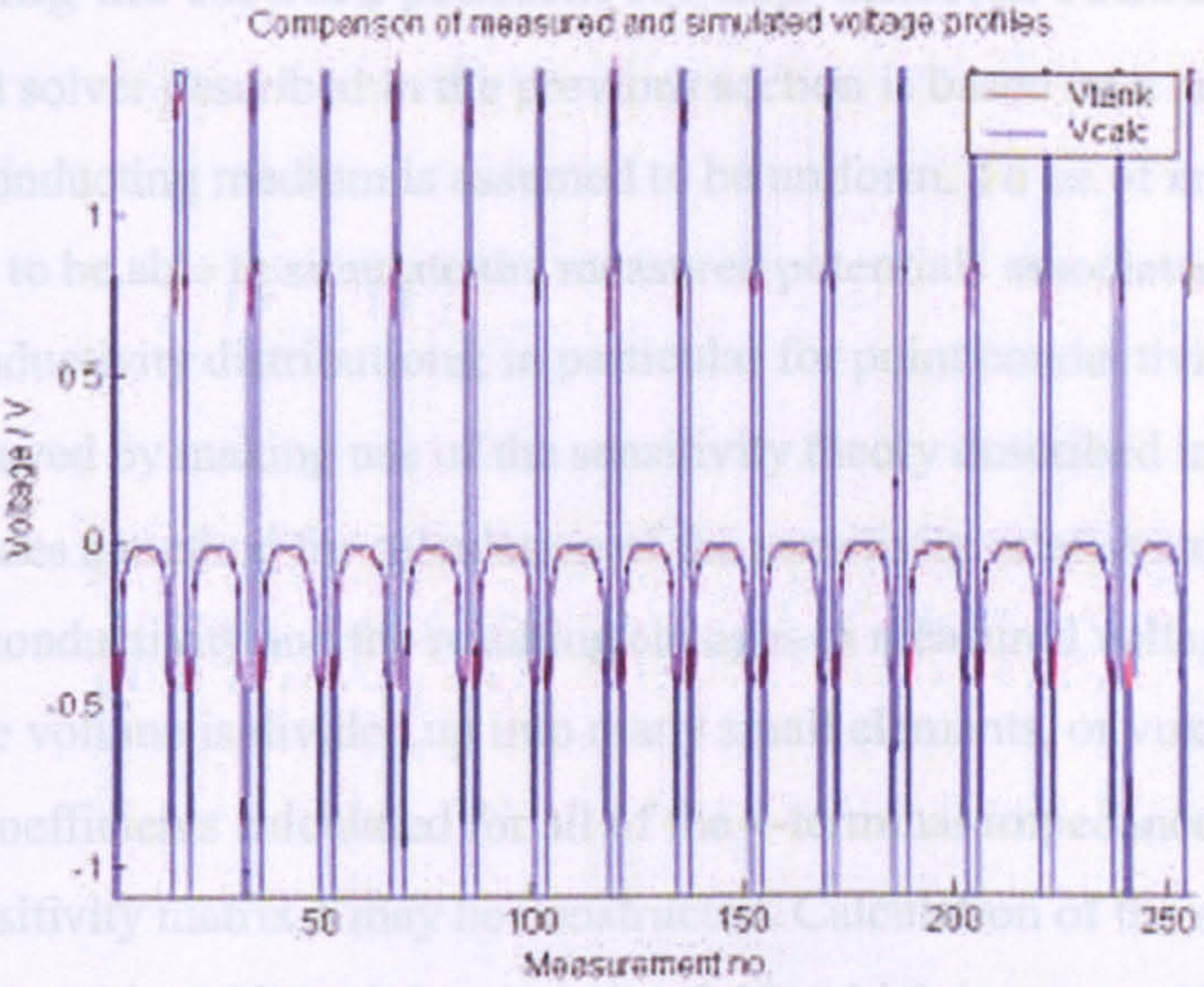

Figure 5.11 – Voltage profiles of real data from a cylindrical saline tank (red curve) and simulated data (blue curve). The saline conductivity is 2mS and the diameter of the electrode array is 0.094m. For the simulated data, λ is given a preliminary value of 0.014m.

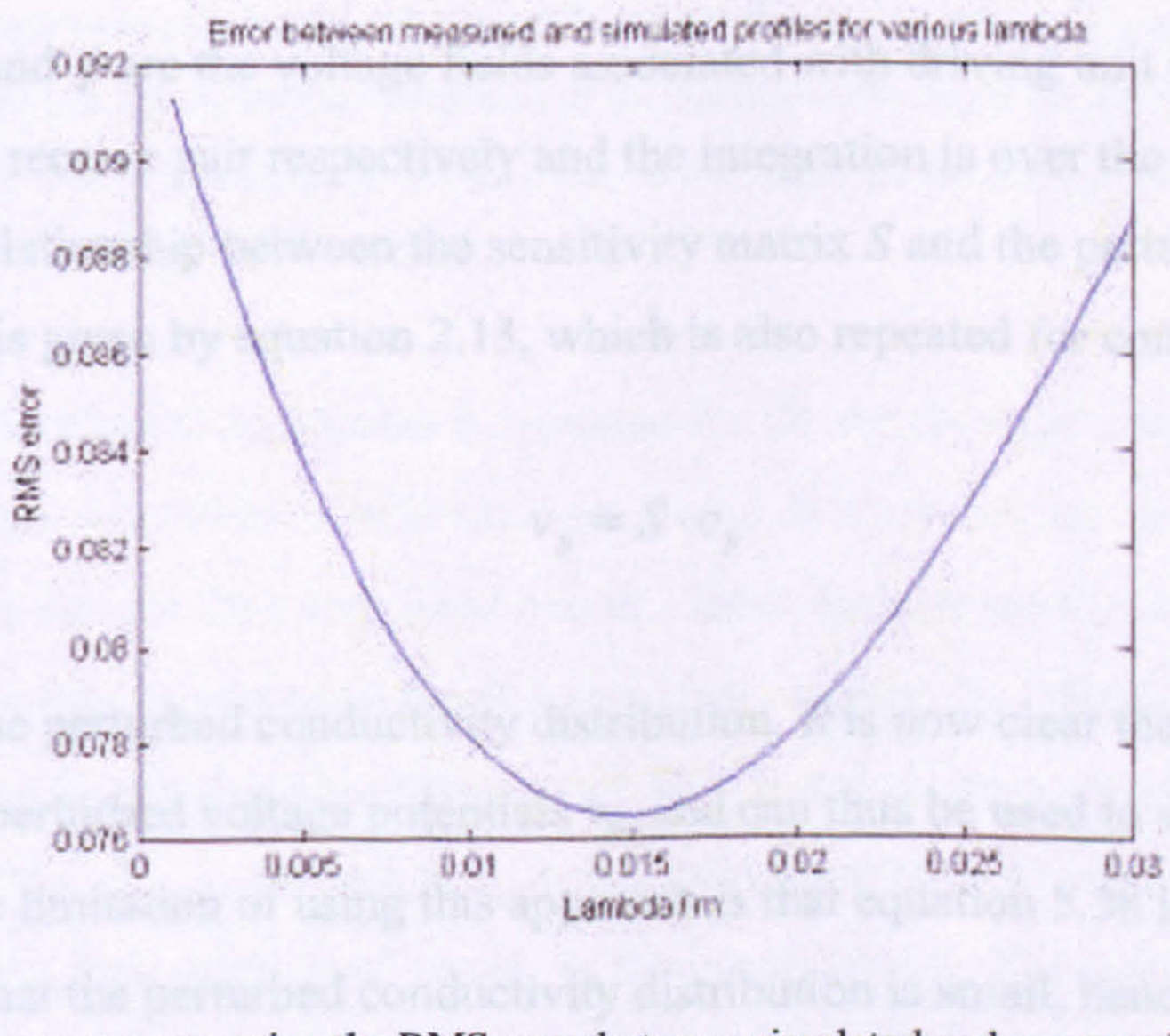

Figure 5.12 – A curve representing the RMS error between simulated and measured data for various values of λ. By finding the minimum of this curve it is possible to choose a value of λ which effectively optimises the voltage relationship described by equation 5.34 for the saline phantom.

5.3.2 Solving the forward problem for non-uniform conductivity

The forward solver described in the previous section is based on a half-plane model in which the conducting medium is assumed to be uniform. To be of any practical value it is necessary to be able to simulate the measured potentials associated with non-uniform conductivity distributions; in particular for point conductivity sources. This may be achieved by making use of the sensitivity theory described in section 2.3.3, which provides a method for calculation of the sensitivity relationship between small changes in conductivity and the resulting changes in measured voltages. For the breast model, if the volume is divided up into many small elements, or voxels, and the sensitivity coefficients calculated for all of the 4-terminal impedance measurements, then the sensitivity matrix S may be constructed. Calculation of the sensitivity coefficients is achieved by solving equation 2.12, which is repeated here for convenience:

$$S_{i,j} = -\int \nabla\phi \cdot \nabla\psi dv \qquad 5.38$$

where $S_{i,j}$ represents the sensitivity coefficient for drive/receive pair i and image element j, ϕ and ψ are the voltage fields associated with driving unit current through the drive and receive pair respectively and the integration is over the volume of the voxel. The relationship between the sensitivity matrix S and the perturbed surface potentials v_p is given by equation 2.13, which is also repeated for convenience:

$$v_p = S \cdot c_p \qquad 5.39$$

where c_p is the perturbed conductivity distribution. It is now clear that S can be used to arrive at the perturbed voltage potentials v_p, and can thus be used to solve the forward problem. The limitation of using this approach is that equation 5.38 is based on the assumption that the perturbed conductivity distribution is small, hence the calculated voltages are only an approximation.

So far, the shape of the voxels used for calculating the sensitivity coefficients has not been defined. Since equation 5.38 involves calculating the voltage field gradients, it

was chosen to discretise the breast model into small even-sided cubic regions. An added benefit of this approach is that it also simplifies the subsequent image display. Implementation of the gradient operator (∇) in equation 5.38 is illustrated in figure 5.13. For a given cubic voxel of side l centred on co-ordinates (x_v,y_v,z_v) there are 8 defined corner nodes. The voltages on each of these is calculated using the voltage model described in section 5.3.1. The ∂x component may then be extracted by averaging the 4 voltage vectors pointing in the x-direction. The ∂y and ∂z components are extracted using the same method applied in their respective directions.

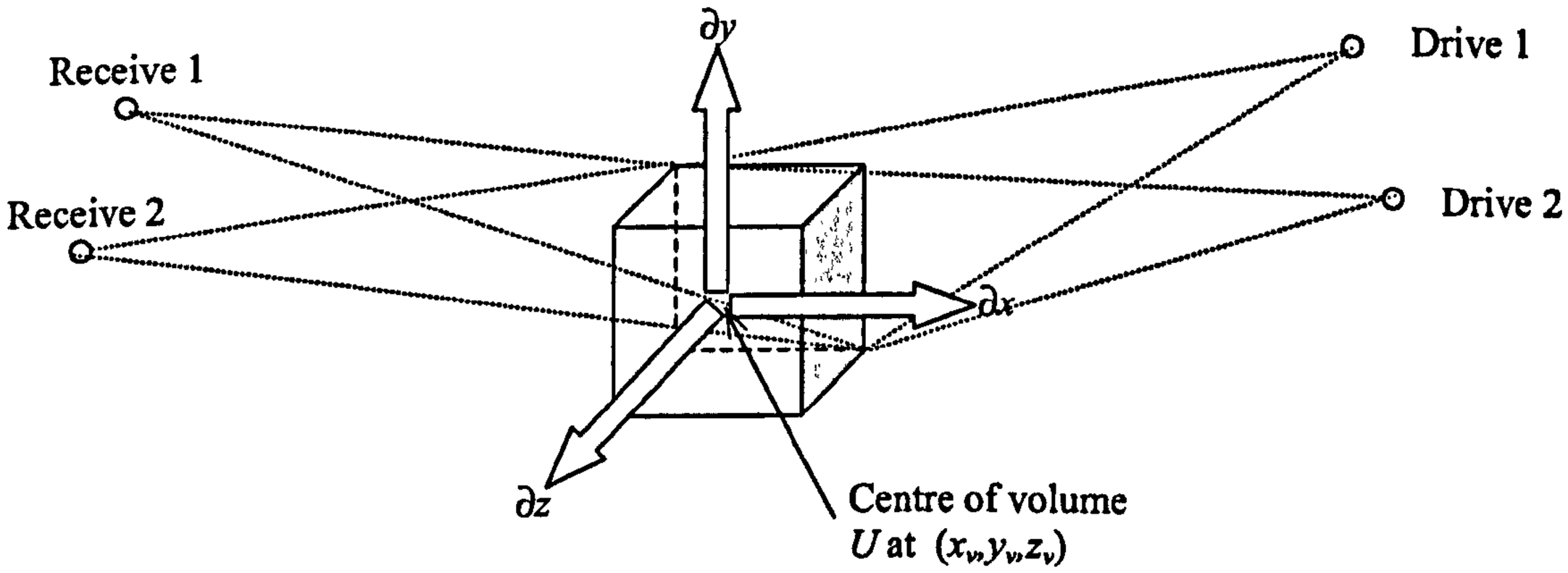

Figure 5.13 – Illustration of a single cubic voxel for which the sensitivity coefficients are to be calculated. By calculating the voltage potentials at the corners of the voxel (using the forward solver in section 5.3.1) the voltage gradients ∂x, ∂y, & ∂z can be calculated as the average of the four voltage vectors pointing in the respective directions.

The sensitivity calculation process is repeated for all voxels within the imaging volume and the resultant sensitivity coefficients are stored as a row vector. The subsequent drive-receive pairs are then simulated one at a time, and the sensitivity coefficients calculated in the same way until the full sensitivity matrix has been built up. This matrix contains the relationship between all voxels and all drive-receive measurements and has size $[N_{pairs},N_{voxels}]$ where N_{pairs} is the total number of drive-receive pairs used and N_{voxels} is the total number of voxels in the breast model. The software used to implement this is listed in Appendix G.

5.3.3 Defining the 3D voxel structure using the breast model

Having specified that the target imaging volume should be discretised into cubic voxels, this process is now considered. The proposed simulation for modelling 3D breast imaging involves reconstructing a number of images based on a range of breast shapes ranging from compressed to pendant. In choosing a scheme for quantising the different shapes into cubic structures, it is important to ensure that the volume of the voxels from one shape to the next remains constant. The reason for this is that in each simulation, a single voxel is used to represent a point change in conductivity, hence for consistency in the measured resolution there should be a consistency in the applied conductivity perturbations.

The chosen method for calculating the voxel structure is to initially define a cuboid imaging block that encloses the breast model (figure 5.14a). At this stage the breast model is given a unit base radius that can later be scaled to represent various breast sizes. Based on the desired voxel size, evenly spaced node positions are generated which fill the entire cuboid block. (figure 5.14b). In order to maintain consistency between different breast shapes, the central node is always positioned at (0,0,0). A check is then carried out on all node co-ordinates, and any which are outside the breast surface (i.e. their z-coordinate is greater than that predicted by the breast model – equation 5.15) are discarded. The data now consists of a list of nodes which evenly fill the breast volume (figure 5.14c). These nodes are used to define the voxel corners, but to specify which nodes belong to which voxels, the positions of all possible voxel centres are generated. This is accomplished by taking each node position and adding an offset of half the voxel width to the x, y and z coordinates (This process adds some positions which are outside the breast model but they are easily discarded). For each voxel centre, the distances to all other nodes are calculated and those which are less than one voxel-width are listed. This list contains all nodes which surround the voxel, however for voxels near the surface (or voxels with high x, y or z values) there may not be a complete set of 8 nodes. Therefore if there are 8 nodes in the list, the voxel centre is valid and the voxel can be stored as a set of 8 indices into the node coordinate arrays, otherwise that voxel is discarded. The final voxel block may be displayed by 'patching' the 6 surfaces of each voxel onto a 3-dimensional coordinate display (figure 5.13d). The software for implementing this process is given in Appendix H.

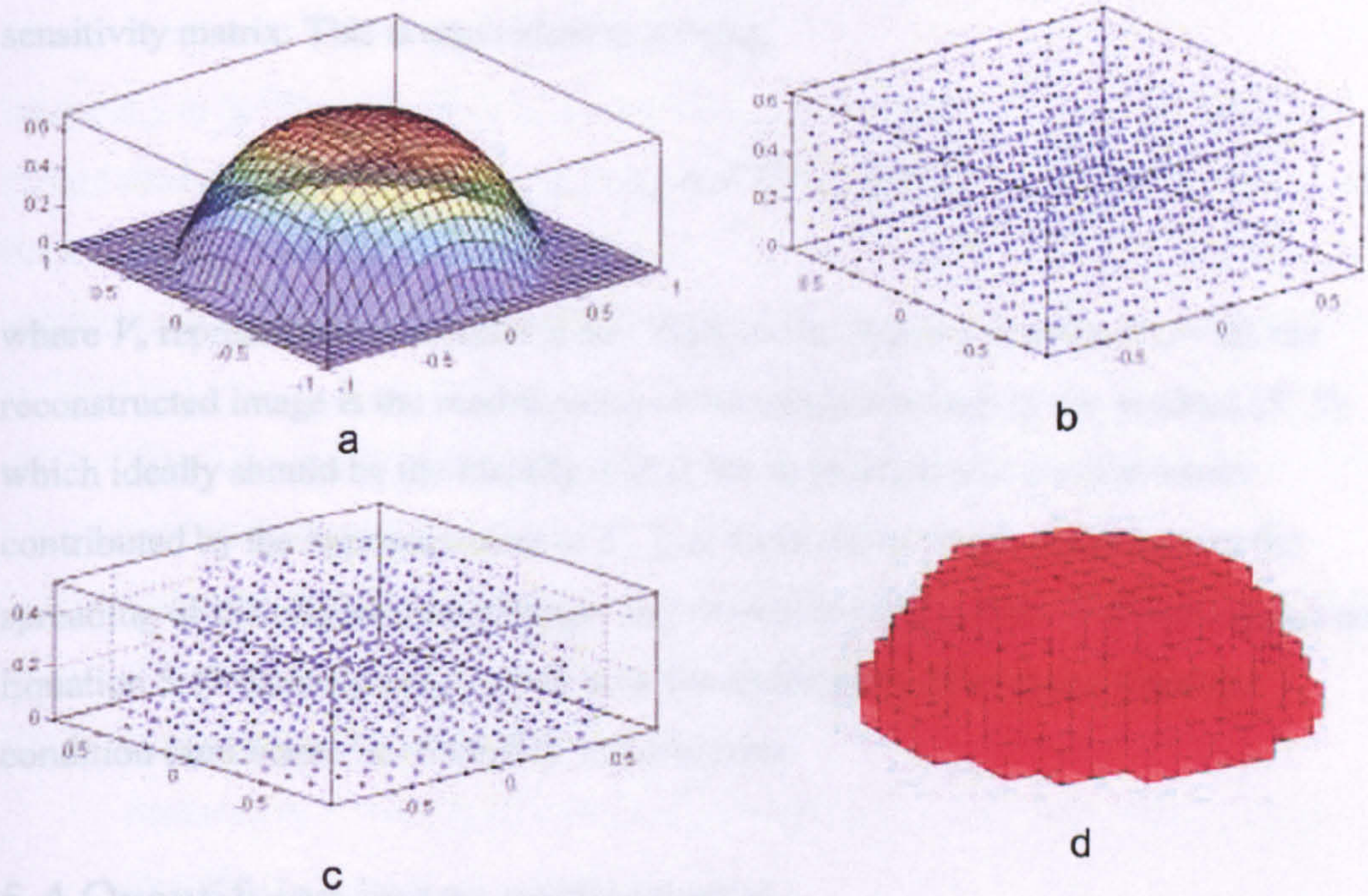

Figure 5.14 – Illustration of the method for defining the cubic voxel structure for any given breast shape. Diagram (a) shows the breast surface enclosed by a cuboid region. Here the model is scaled to have a unit base radius. Diagram (b) shows all the node positions generated for a spacing of 0.15. In diagram (c) the nodes which are outside the breast model surface have been discarded. Finally in (d) the groups of 8 nodes which form the vertices of each voxel are calculated based on their proximity to the voxel centres.

5.3.4 The image reconstruction algorithm

In order to maintain consistency with the 2-dimensional simulation study, the sensitivity method has been chosen for reconstructing 3-dimensional images. This is also the logical choice since the sensitivity matrix is already calculated for solving the forward problem. Practical implementation of the sensitivity method in three dimensions is exactly the same as described in section 4.2.2 for the two dimensional case, that is the relationship:

$$c_p = S^+ v_p \qquad 5.40$$

is solved, where v_p is the vector of perturbed voltages calculated by equation 5.39, c_p is the vector of perturbed conductivity values and S^+ is the pseudo-inverse of the sensitivity matrix. This is equivalent to solving:

$$c_p = S^+\left(S \cdot c_p + V_n\right) \qquad 5.41$$

where V_n represents the artificial noise. Thus in the absence of noise ($V_n = 0$), the reconstructed image is the modification of the original image by the product ($S^+.S$), which ideally should be the identity matrix but in practise will contain errors contributed by the approximation of S^+. It is these errors which contribute to the spreading of the original point image, and the subsequent notion of image resolution. Equation 5.41 demonstrates clearly how the resolution suffers more when the condition (and hence 'invertability') of S is poor.

5.4 Quantifying image performance

Measuring the image performance in three dimensions introduces some problems that were not encountered in the two dimensional simulation, particularly in the area of quantifying spatial variance. The resolution profiles used in an attempt at quantifying spatial variance in 2-dimensional images are based on having a constant image radius. In three dimensional imaging this requires a hemispherical image. Since this simulation is aimed at investigating various breast shapes it is unreasonable to assume they are all roughly hemispherical, hence a different concept for handling spatial variance is required. This is now considered along with measurement of resolution and the effects of signal noise on image quality.

5.4.1 Measuring the spatial resolution in 3-dimensions

For 2-dimensional images it is found that the resolution can be adequately calculated as the square root of the relative area of the Point Spread Function (PSF), since it is not dependent on the shape of the PSF. In 3-dimensional imaging this concept may be extended such that the resolution is represented as the cube root of the relative volume of the PSF. The formula is:

$$R_{vol} = \sqrt[3]{\frac{V_{PSF}}{V_{tot}}} \qquad 5.42$$

where R_{vol} is the (volume-based) resolution value, V_{PSF} is the volume of the point spread function (defined as the region of the image with an amplitude greater than half the maximum) and V_{tot} is the total volume of the object. Calculation of V_{PSF} / V_{tot} needs some consideration as there are several methods, three of which are considered here:

1. Count the number of voxels within the PSF and divide by the total number of voxels in the image.
2. Calculate the sum of the volumes of all the voxels within the PSF and divide by the mathematical volume of the breast model (which is preset to 1)
3. Generate an isosurface that surrounds the PSF and calculate the volume enclosed by it. Divide this result by the mathematical volume of the breast model

The problem with method 1 is that when the breast model is compressed, the total number of voxels within the model does not remain constant, hence an error is introduced into the calculation. This effect is synonymous to quantization error and is brought about by representing a continuous volume with smaller finite volumes. Method 2 offers an improvement upon this by calculating V_{PSF} as the sum of volumes of the voxels within the PSF and setting V_{tot} to 1 (which is the chosen volume for the model – see section 5.2.1). Method 3 involves calculation of an isosurface which surrounds the PSF, from which the volume of the PSF can be calculated. This helps to smooth out the quantization effect of voxel-counting. Whilst an isosurface function is available in MATLAB®, no function for calculating the volume within an isosurface could be found. Method 2 is therefore chosen with the additional benefit that since V_{tot} is unity, the resolution is simply the cube-root of the combined volumes of the voxels within the PSF.

5.4.2 The spatial variance of 3D image resolution

For 2-dimensional circular images, the spatial variance of the resolution was calculated by generating resolution profiles along the image radius and modelling the curves

using two different functions from which the central resolution and spatial variance were extracted (section 4.3.1.3). The accuracy of the spatial variance parameters was determined by comparing them with the standard deviation of all the resolution values collected for one profile. Although the original intention was to provide a method for validating the two proposed models, it was realised that the model itself is perhaps unneseccary since the standard deviation of a representative cross section of resolution values provides a reasonable measure of the spatial variance. An added bonus of the standard deviation approach is that it is less dependent on the geometry of the imaging target, hence is considered ideal for the 3D breast model. To work successfully, the important issue is to ensure that the resolution measurements made are representative of the entire volume. Since the model has rotational symmetry it is reasonable to assume that point sources only need to be simulated within a coronal quadrant of the model (see figure 5.15).

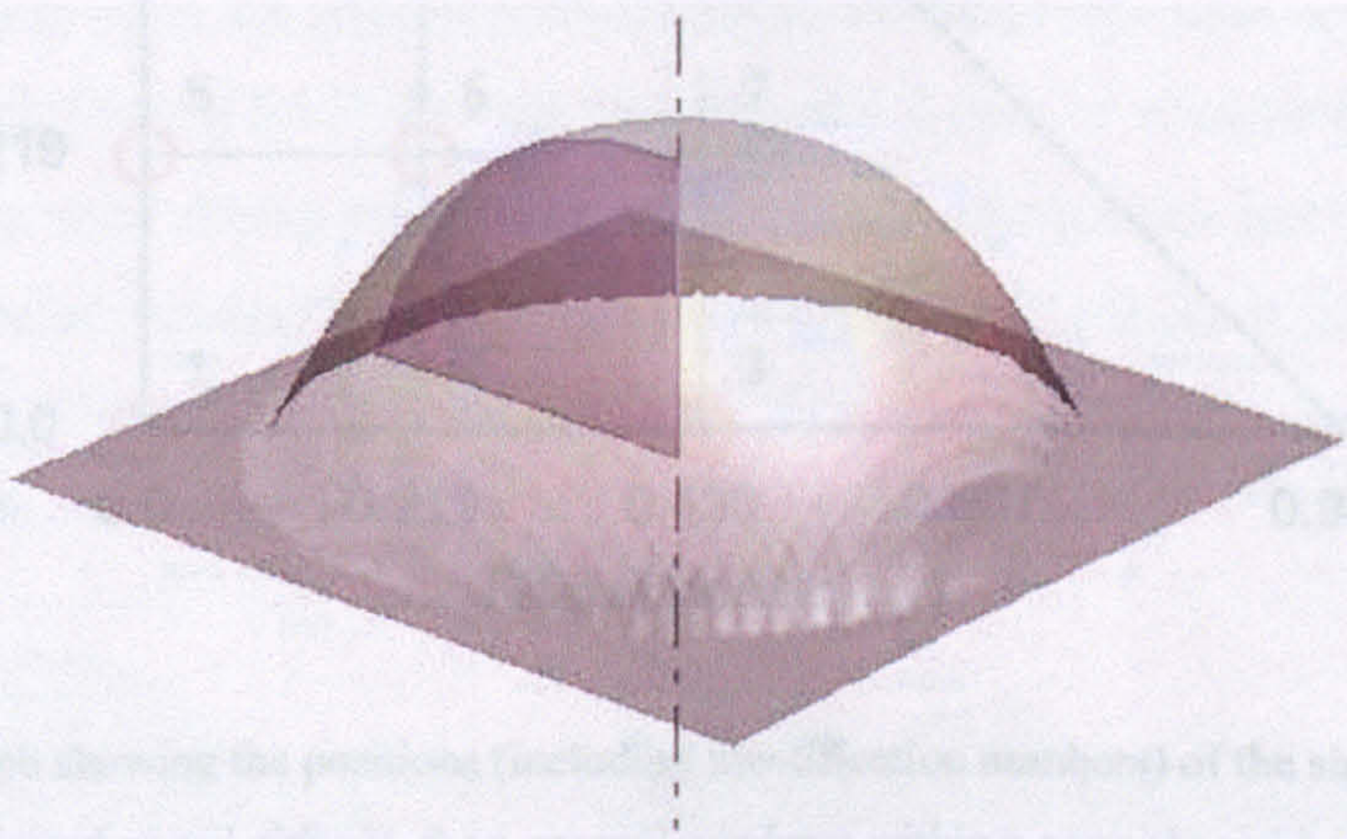

Figure 5.15 – Illustration of a coronal quadrant within the breast model (here shown in pink). Due to rotational symmetry of the model, resolution measurements only need to be made within this quadrant, since they are representative of measurements made by rotating the point sources about the axis (here shown as a dashed line).

For the simulation ten evenly spaced point sources within such a quadrant are chosen. Since the locations of these ten points change with breast shape as it is compressed, the point locations for one particular breast shape must be defined after which the tumour-tracking algorithm can be used to calculate their positions. The approach chosen here is to define the tumour positions with the breast model set as a cone ($n = 1$), for which the coronal quadrant (as illustrated in figure 5.15) becomes triangular. It is then

straightforward to define the ten evenly spaced points. Preliminary trials revealed that the points should not be allowed to come too close to the surface of the model, since the voxel structure does not always fill the entire volume. The final point locations used in the simulation study are shown in figure 5.16.

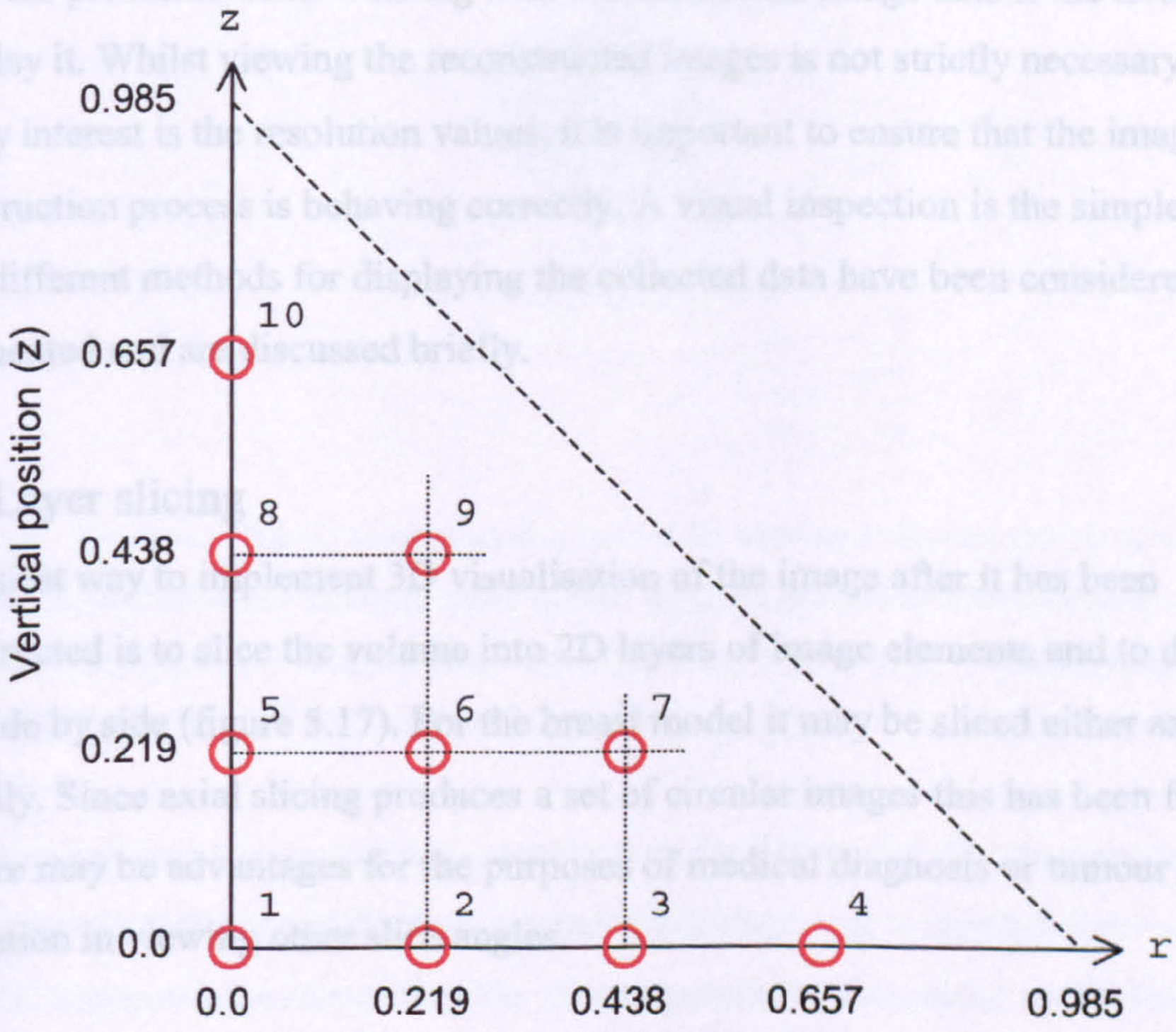

Figure 5.16 – Graph showing the positions (including identification numbers) of the simulated point sources, (here indicated as red cirlces), for a coronal quadrant within a cone shaped breast. The positions are located well beneath the surface of the model (denoted by the dashed diagonal line) in order to prevent them extending beyond the limit of the voxel structure. The positions are recalculated for each breast shape using the tumour tracking algorithm developed in section 5.2.2

Since each point source is to be simulated by increasing the conductivity of one of the voxels, the final location is chosen as the voxel which surrounds the (x,y,z) point source co-ordinates as defined above.

5.4.3 Quantifying the sensitivity of the image to data noise

For 2-dimensional imaging, the noise sensitivity of the reconstructed images was calculated by subtracting a noise-free image from a noise-contaminated image, and

quoting the standard deviation of the resulting pixel intensities (see section 4.3.2). This process is used in exactly the same way for the 3-dimensional simulation.

5.5 Visualisation of the 3D image volume

One of the problems when working with 3-dimensional image data is the issue of how to display it. Whilst viewing the reconstructed images is not strictly necessary since the primary interest is the resolution values, it is important to ensure that the image reconstruction process is behaving correctly. A visual inspection is the simplest check. Three different methods for displaying the collected data have been considered and implemented and are discussed briefly.

5.5.1 Layer slicing

The easiest way to implement 3D visualisation of the image after it has been reconstructed is to slice the volume into 2D layers of image elements and to display them side by side (figure 5.17). For the breast model it may be sliced either axially or coronally. Since axial slicing produces a set of circular images this has been favoured but there may be advantages for the purposes of medical diagnosis or tumour localisation in viewing other slice angles.

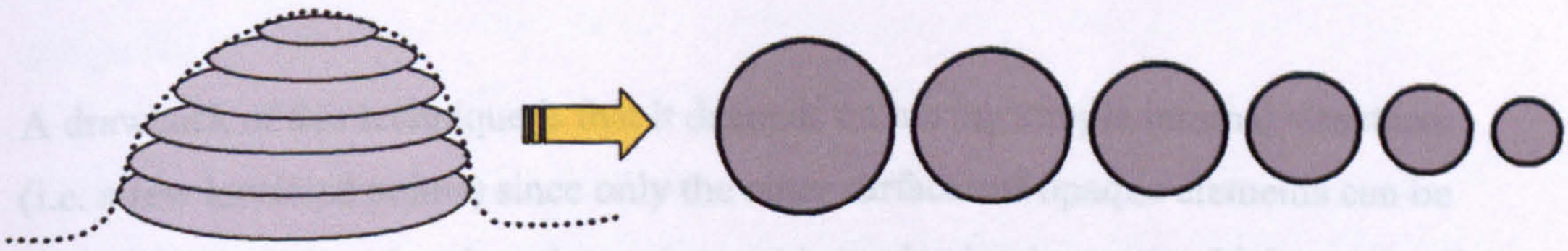

Figure 5.17 – Illustration of the layer slicing concept for visualising 3-dimensional breast data. The 3D volume is sliced axially in this example, resulting in a set of circular images.

5.5.2 3D voxel rendering with transparency

An improvement upon the layer slicing method is to render the 6 faces of each voxel using a 3D rendering algorithm and to use a colour scale with transparency in order to make interesting features stand out against the normal background values (figure 5.18). The surface outline of the image can be superimposed either as a wire-frame or a series

of concentric rings (shown here) in order to present the viewer with an idea of the shape of the breast.

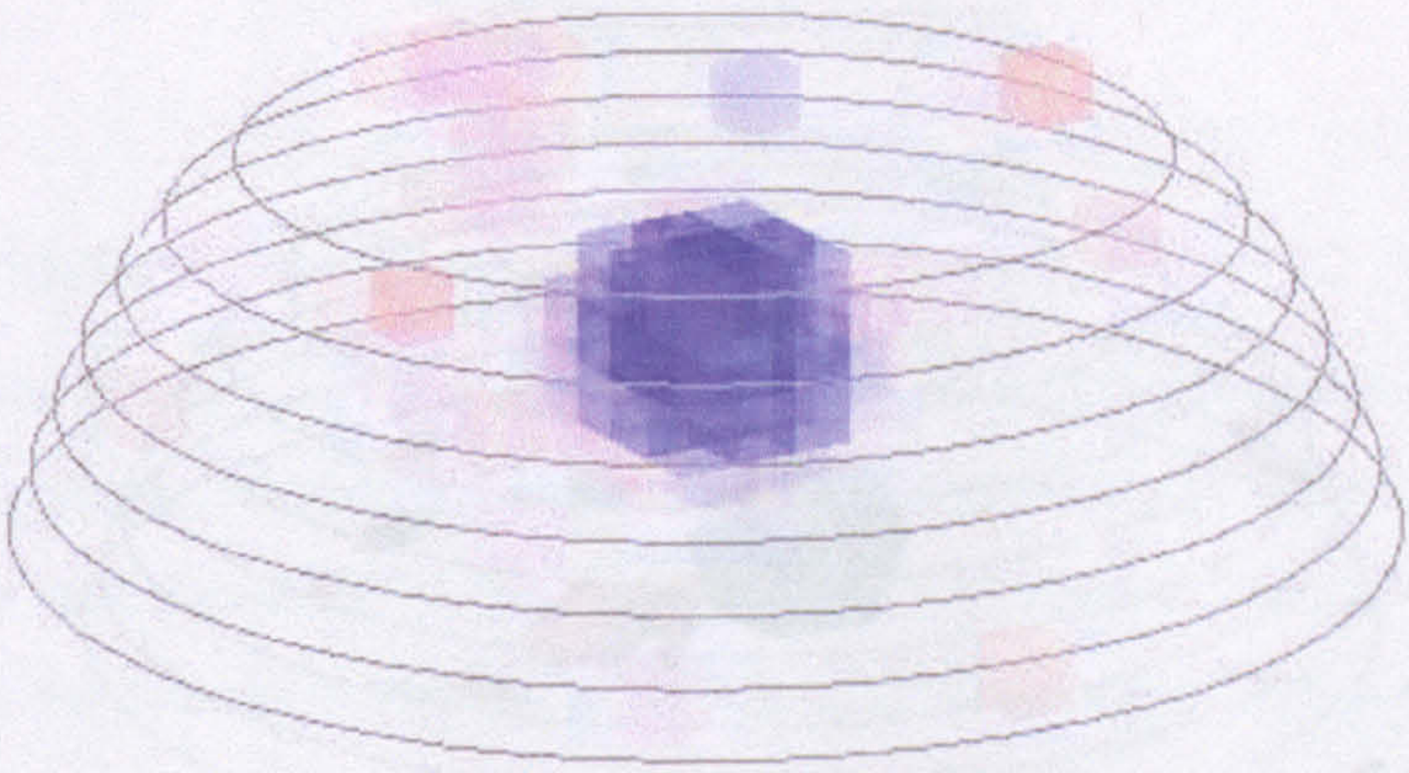

Figure 5.18 – Example of the 3D voxel rendering method for viewing 3-dimensional breast data. Using this technique, each of the six faces that make up each voxel are patched onto the computer screen. The colour scale is chosen so that the interesting features (in this case point source images) are given a solid colour, whilst the background voxels are made transparent.

In order to enhance the viewer's appreciation of the 3D spatial distribution further, it is possible to rotate the image through several small steps and to display these as a cinematic sequence, thereby giving the viewer parallax information as the internal structures pass in front of and behind one another.

A drawback of this technique is that it depends on having simple internal structures (i.e. a few localised points) since only the outer surfaces of opaque elements can be seen. For breast imaging the primary interest is in viewing tumours which are usually confined to localised volumes so this method of viewing is realistic. Also for the simulation work carried out the aim is to reconstruct images of point sources against a constant conductivity background. Consequently the 3D rendering technique with transparency is well suited to the type of images expected.

5.5.3 Isosurface rendering

If it is known that the reconstructed image consists of constrained volumes of localised conductivity change, then a useful way of displaying it as a 3D structure is to create an isosurface which passes through all points in the volume having a particular value

(figure 5.19). For example, consider a localised region having conductivity 3mS against an otherwise uniform background conductivity of 1mS. An isosurface passing through all points at 1.5mS would effectively contain the region of interest.

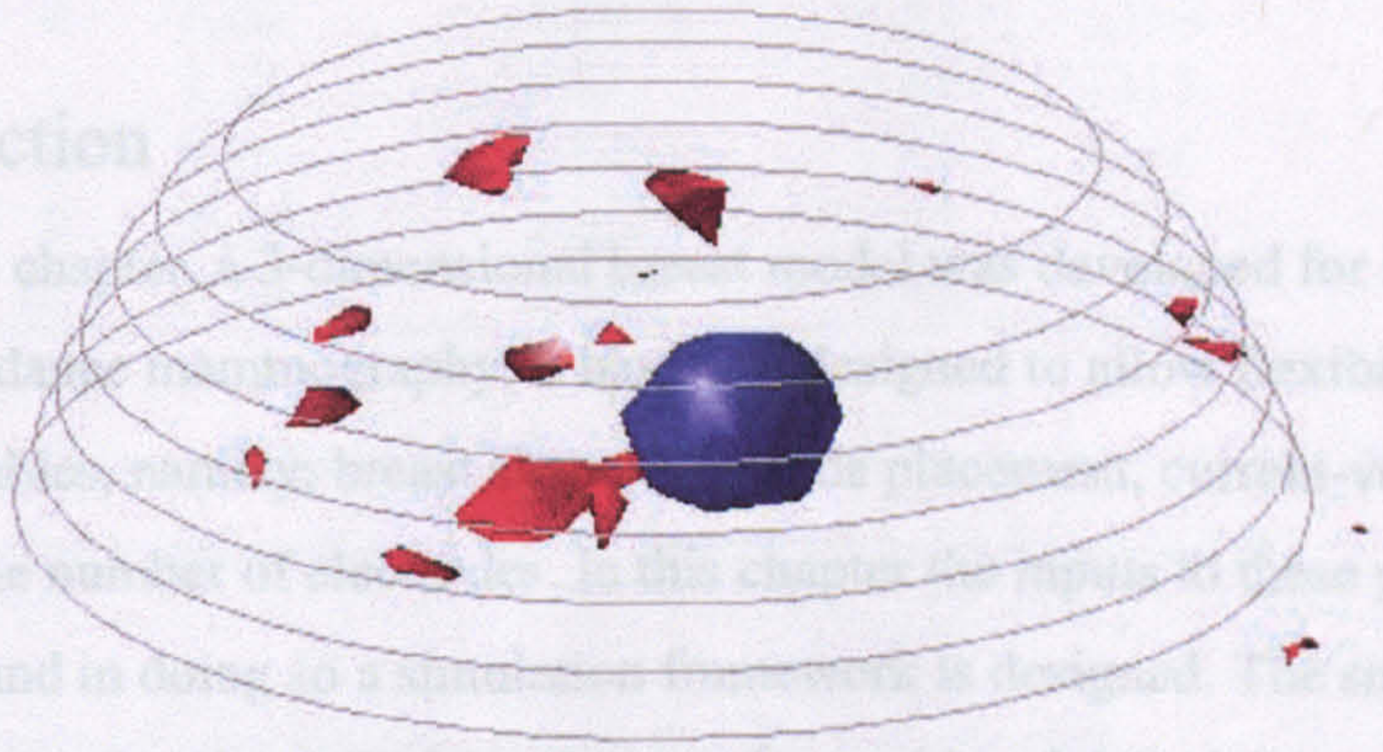

Figure 5.19 – Example of a point source image (blue) which has been rendered using the isosurface method. With this approach, a surface is calculated that passes through all regions of the image at a predefined intensity. This approach is more suited to viewing regions of interest (ROIs) than the entire 3D image (NB – the red regions in the image are caused by image noise).

The surface can be rendered using 3D software rendering techniques and the outline of the breast shape added as a wire-frame structure. It should be noted that this technique is only of use in isolating regions of interest (ROIs) and not for displaying the full image data.

Of the three methods outlined, method 2 (3D voxel rendering) has been chosen for examining each image. In the next chapter, four key input parameters for the 3-dimensional resolution performance simulation are defined. These parameters are breast shape, electrode placement, current-voltage patterns and the number of electrodes. Results of the simulation work are presented and discussed at the end of the chapter.

CHAPTER SIX

SIMULATING THE TUMOUR DETECTION PERFORMANCE USING THE 3D BREAST MODEL

6.1 Introduction

In the previous chapter, a 3-dimensional breast model was developed for simulating electrical impedance mammography. It has been designed to allow flexibility over four important variables, namely; breast shape, electrode placement, current-voltage patterns, and the number of electrodes. In this chapter the inputs to these parameters are addressed and in doing so a simulation framework is designed. The simulation results are presented at the end of the chapter along with a detailed discussion.

6.2 Choosing parameters for the 3D simulation

6.2.1 Breast shape

For the simulation study, ten different breast shapes are used to model the change in shape of a breast from the prone (pendant) position to the supine (flattened) position. The range of *n*-values used to control the shapes has been chosen empirically based on the visual appearances of the computer-rendered images. The dimensions of the models are based on achieving a volume of unity, but are scalable since the image reconstruction process is not concerned with absolute dimensions. Calculation of the resolution, however, is more straightforward if the model has unit volume. The voxels were specified to have a side length of 0.085 units. This is an empirical decision based on achieving a reasonable number of voxels within the model whilst avoiding computational overloads. The spatial resolution based on a voxel of this size is 8.5%, hence this is the resolution limit for the reconstructed images. Table 6.1 lists the ten breast shapes along with some of the parameters associated with them. 3D rendered images of all ten shapes can be found in Appendix I.

Shape	n-factor	Base diameter	Height	voxels
1	1.44	1.85	0.89	1372
2	2.10	1.78	0.78	1368
3	2.89	1.76	0.69	1328
4	3.80	1.77	0.62	1308
5	4.84	1.78	0.57	1376
6	6.00	1.80	0.53	1256
7	7.29	1.81	0.49	1312
8	8.70	1.83	0.47	1156
9	10.24	1.85	0.45	1172
10	11.90	1.86	0.43	1216

Table 6.1 – Details of the ten different models used to represent the ten breast shapes. The dimensions are based on achieving a volume of unity, and the voxels have a side length of 0.085.

6.2.2 Placement of electrodes using the breast model

As discussed in section 5.1, the two principal methods of electrode placement currently in use for breast EIM are:

1. A circular array of 16 or 32 electrodes which has variable diameter and height and is used to reconstruct one or more 2-dimensional images. For multiple images they can theoretically be stacked to form a 3D image volume (Osterman *et al.* 2000).
2. A flat grid of 256 breast electrodes in conjunction with two fixed wrist electrodes from which several image slices are reconstructed. (Korjenevsky *et al.* 2001).

These electrode arrangements tackle the extremes of breast shape, namely *pendant* (hanging away from the chest wall) and *flat* (pressed against the chest wall). However, the simulations in this study aim to investigate electrode positions distributed on the 3D surface of the breast for a number of different breast shapes ranging from pendant to flat. To achieve this, two additional methods of electrode placement are proposed:

3. A grid array having electrodes positioned at fixed x,y co-ordinates whilst allowing the electrode to translate in the z-direction so that it can accommodate a wide range of breast shapes (See figure 6.1).

4. A set of concentric rings of electrodes which are all centred on (x=0,y=0) but are allowed to move independently in the z-direction so as to fit any given breast shape (See figure 6.2).

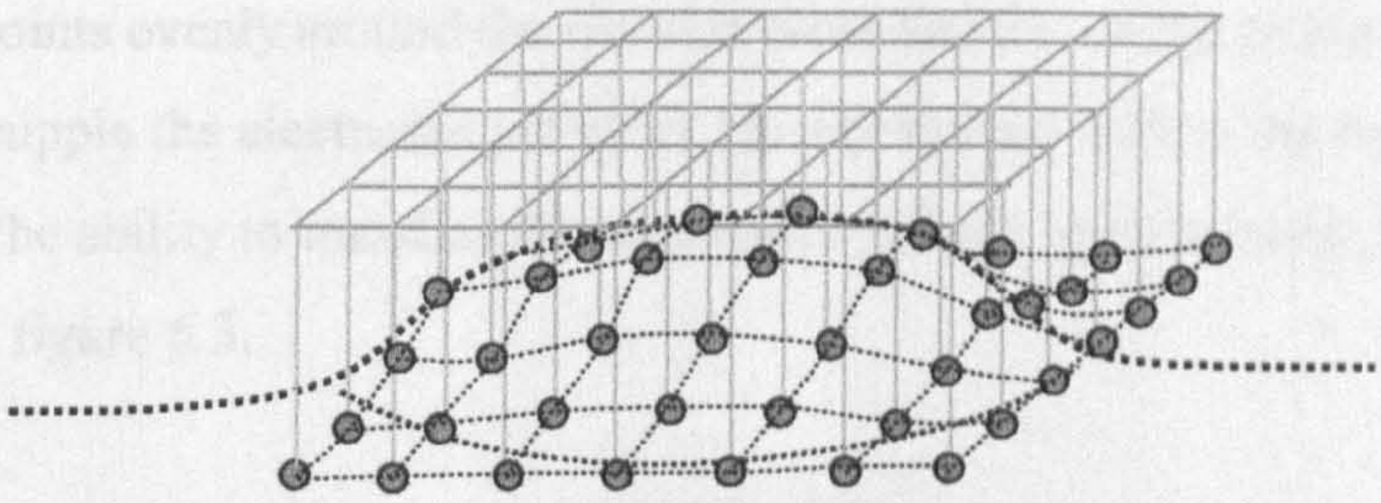

Figure 6.1 – Illustration of a grid electrode array in which the heights of the electrodes are allowed to adapt to the profile of the breast (here represented with a dotted line).

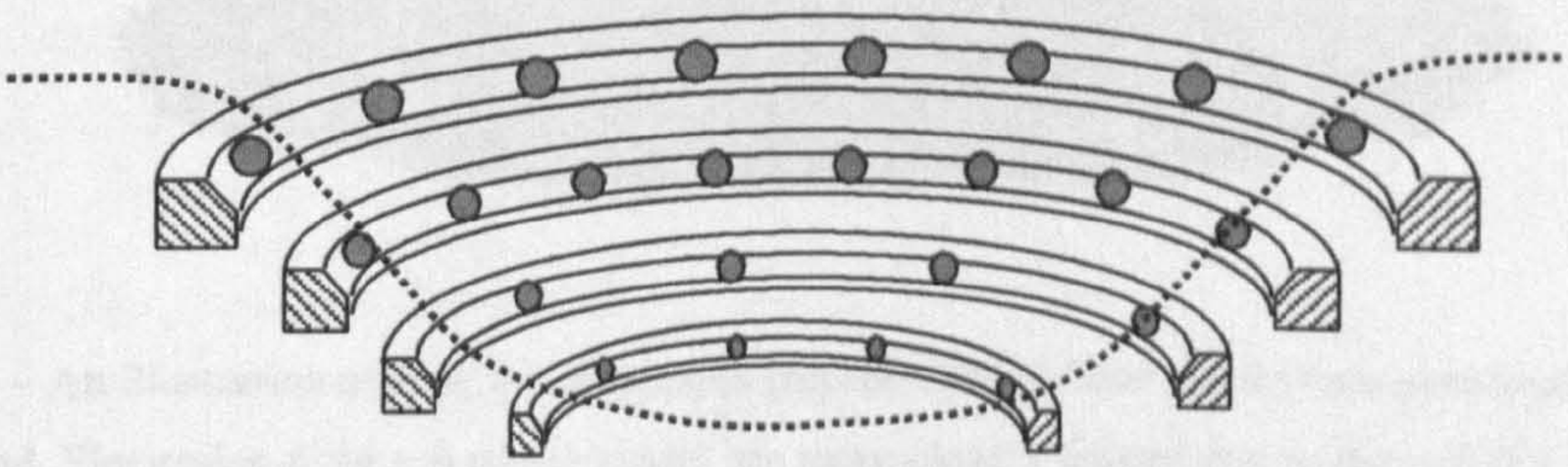

Figure 6.2 – Cross-sectional illustration of an electrode array in which four concentric rings of electrodes are allowed to translate vertically so as to follow the breast surface (here illustrated with a dotted line).

Thus four electrode placement strategies are tested in the simulation study. The precise calculations used to arrive at the electrode positions are outlined below for each of the four strategies. The headings used for each method are the names used to refer to them throughout the remainder of the thesis.

6.2.2.1 *2D-Ring* electrode placement

This is the application of the standard 2D circular imaging technique to the breast. Since this method only allows one slice to be collected at a time, the process is simulated with the electrode ring positioned at several locations in the z-direction.

These locations are chosen such that they correspond with the layers of voxels into which the image is reconstructed. As the breast model is compressed, the number of layers of voxels reduces, hence the number of ring positions depends on the amount of breast compression. The *x*,*y* co-ordinates for a given *z*-position are calculated by spacing 32 points evenly around the circular cross-section of the breast surface, thus towards the nipple the electrodes are more closely spaced than at the base of the breast. In this way, the ability to translate the electrodes radially is simulated. This is illustrated in figure 6.3.

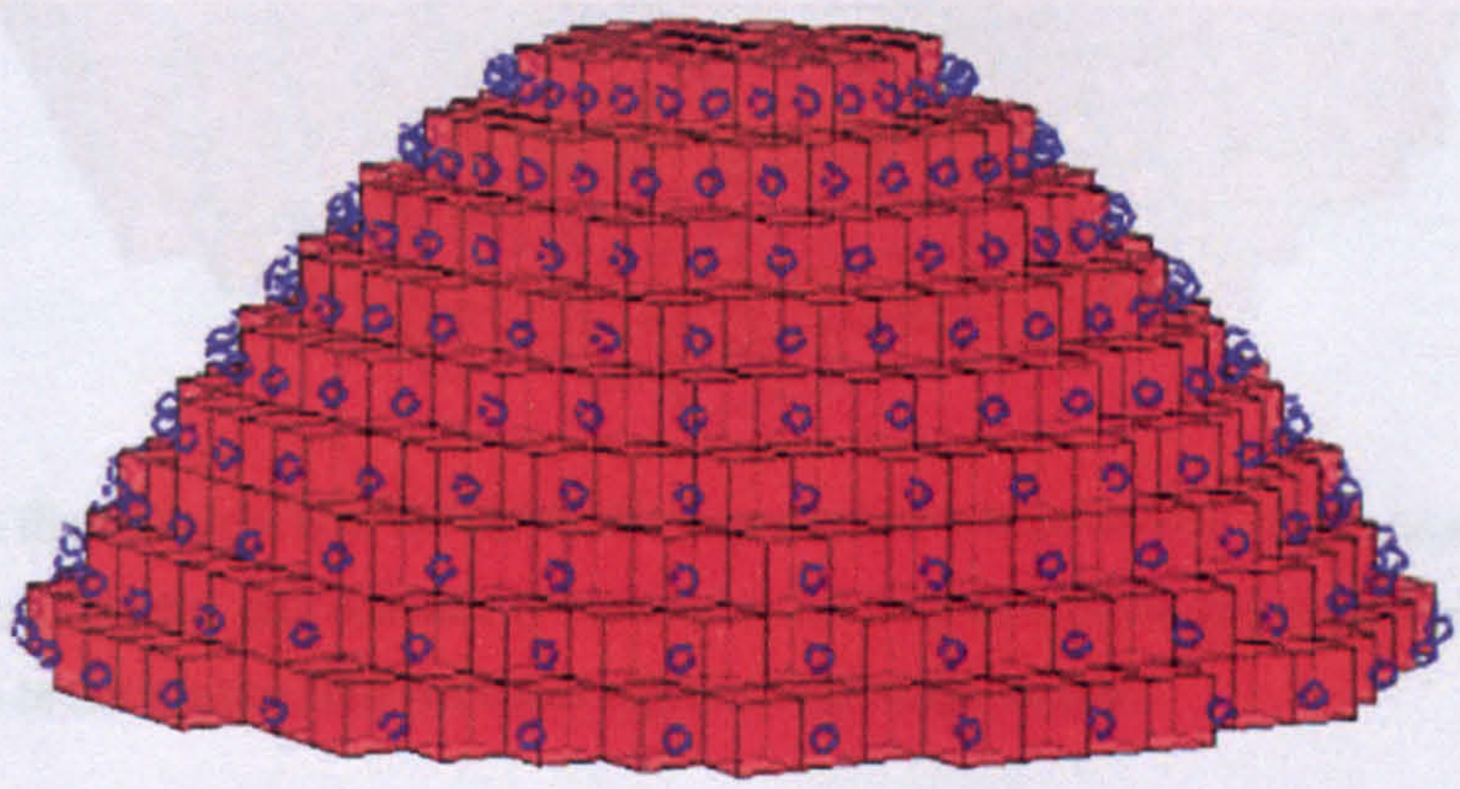

Figure 6.3 – An illustration of how the electrodes (represented as blue circles) are positioned for the *2D-ring* method. Electrodes at the top of the model are more closely spaced due to the radially translating placement method being simulated. The red cubes represent the image voxels and are used to determine the heights of each electrode ring.

6.2.2.2 *Flat-Grid* electrode placement

The *Flat-Grid* method has electrodes arranged on a rigid flat grid format, which is pressed onto the surface of the breast. The spacing of the grid is defined by the required number of electrodes and the overall diameter of the breast model. In order to maximise the use of the electrodes, the grid is defined to be a circular shape with a diameter 80% of the base diameter of the breast model. Although the *Flat-Grid* electrode array is only designed for compressed breasts (thereby ensuring the maximum number of electrodes come into contact with the skin), simulations are still performed with the full range of breast shapes from pendant to compressed. This is for completeness of the resulting measurements. In order to determine which electrodes are in contact with the skin, the radius of all points within 5% of the maximum breast

height is calculated, and all electrodes within this radius are allowed. Figure 6.4 shows an example of the *Flat-Grid* array applied to a compressed breast.

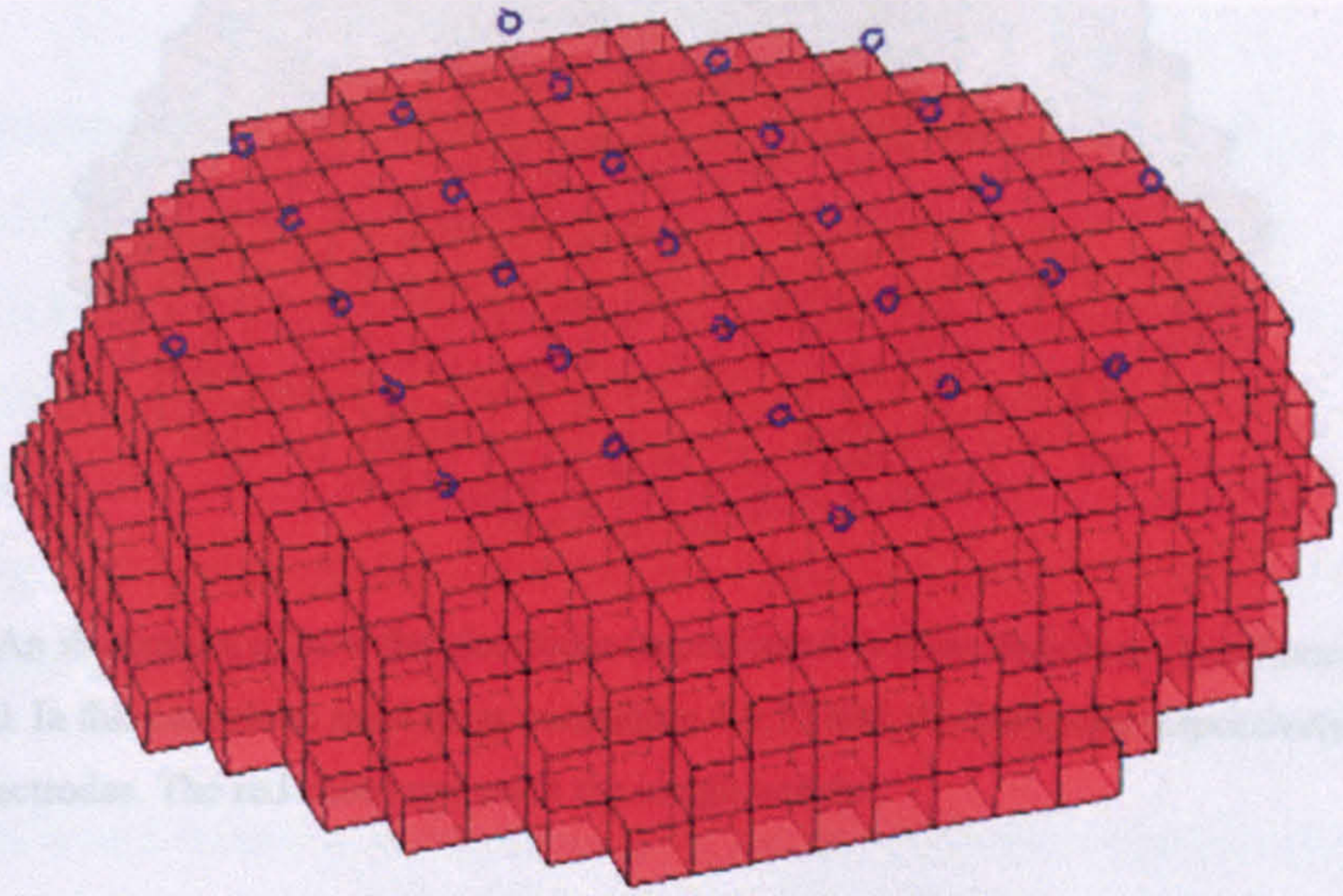

Figure 6.4 – An illustration of how the electrodes (represented as blue circles) are positioned for the *Flat-Grid* method. The full grid contains 37 electrodes, but only 29 of these are considered to be in contact with the breast surface. The red cubes represent the image voxels.

6.2.2.3 *3D-Rings* electrode placement

The *3D-Rings* electrode placement method is an adaptation of the *2D-Ring* method whereby several concentric electrode rings are defined in the *x*-*y* plane. Each ring, however, can assume any position in the *z*-direction, thus allowing it to adapt to the shape of the breast. An additional advantage of this method over the *2D-Ring* method is that all of the electrodes are available for driving current, not just those in the same ring. In order to maintain an approximately even spacing of electrodes, the smaller rings require fewer electrodes than the larger rings. For this simulation the number of electrodes on each successive ring follow the sequence 4,8,12,16,… This was an arbitrary decision, and there is no reason why other evenly increasing electrode numbers could not be used. For the ring diameters the outer ring is given a diameter 95% of the base diameter of the breast model and the remaining rings have evenly decreasing diameters. The *z*-coordinates are calculated such that each ring rests on the breast surface as defined by the breast model equation. An example of the electrode distribution using the *3D-Rings* method can be seen in figure 6.5.

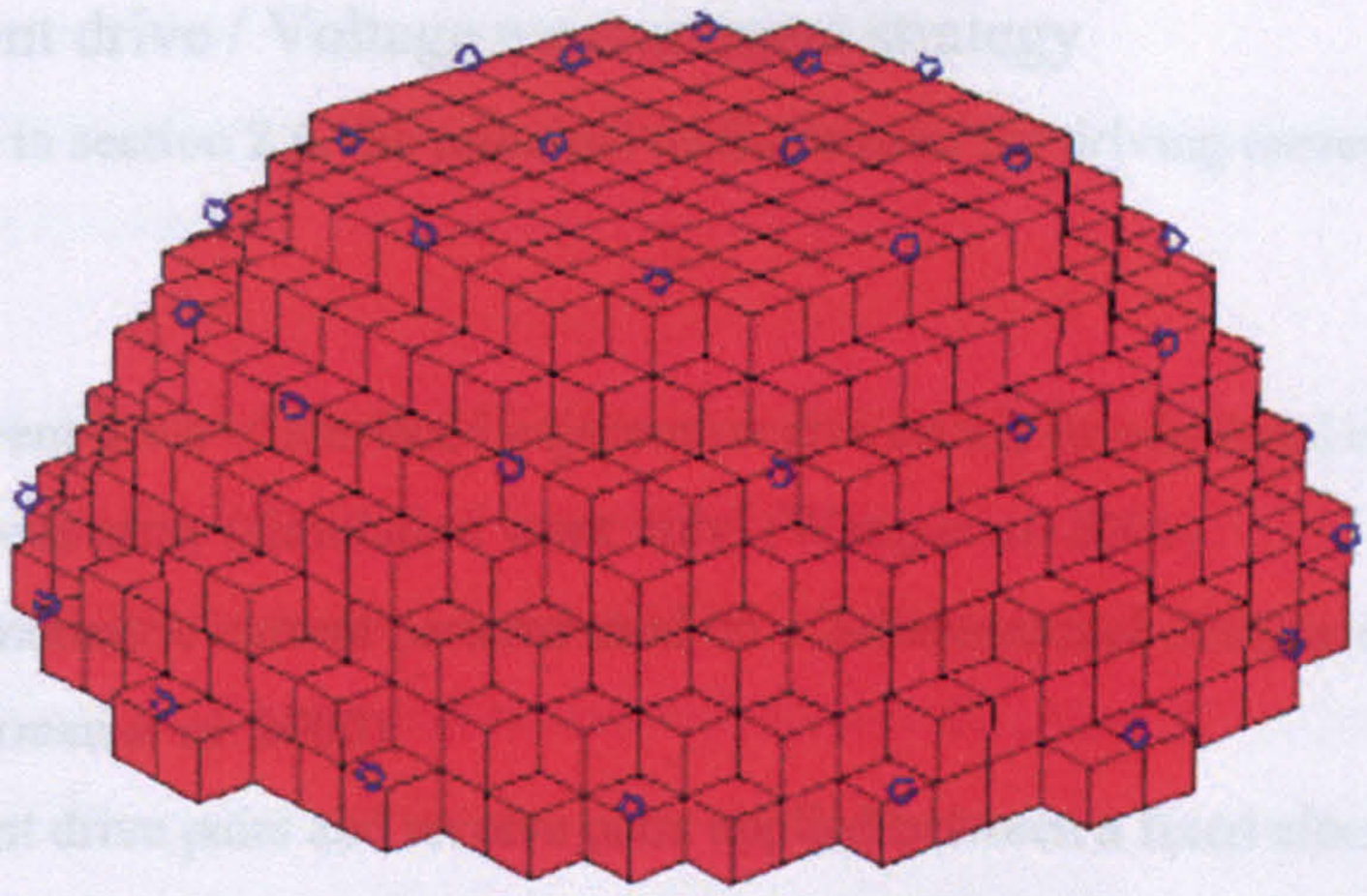

Figure 6.5 – An illustration of how the electrodes (represented as blue circles) are positioned for the *3D-Rings* method. In this case there are 4 rings containing 4,8,12 and 16 electrodes respectively giving a total of 40 electrodes. The red cubes represent the image voxels.

6.2.2.4 *Curved-Grid* electrode placement

The *Curved-Grid* electrode placement method is an adaptation of the *Flat-Grid* method in which the *x*,*y* co-ordinates are calculated in the same manner, but the *z*-positions are allowed to translate so that all electrodes can come into contact with the breast surface. In this way none of the electrodes are excluded from the simulation as can happen with the *Flat-Grid* method. An example of electrode positioning using the *Curved-Grid* method can be seen in figure 6.6.

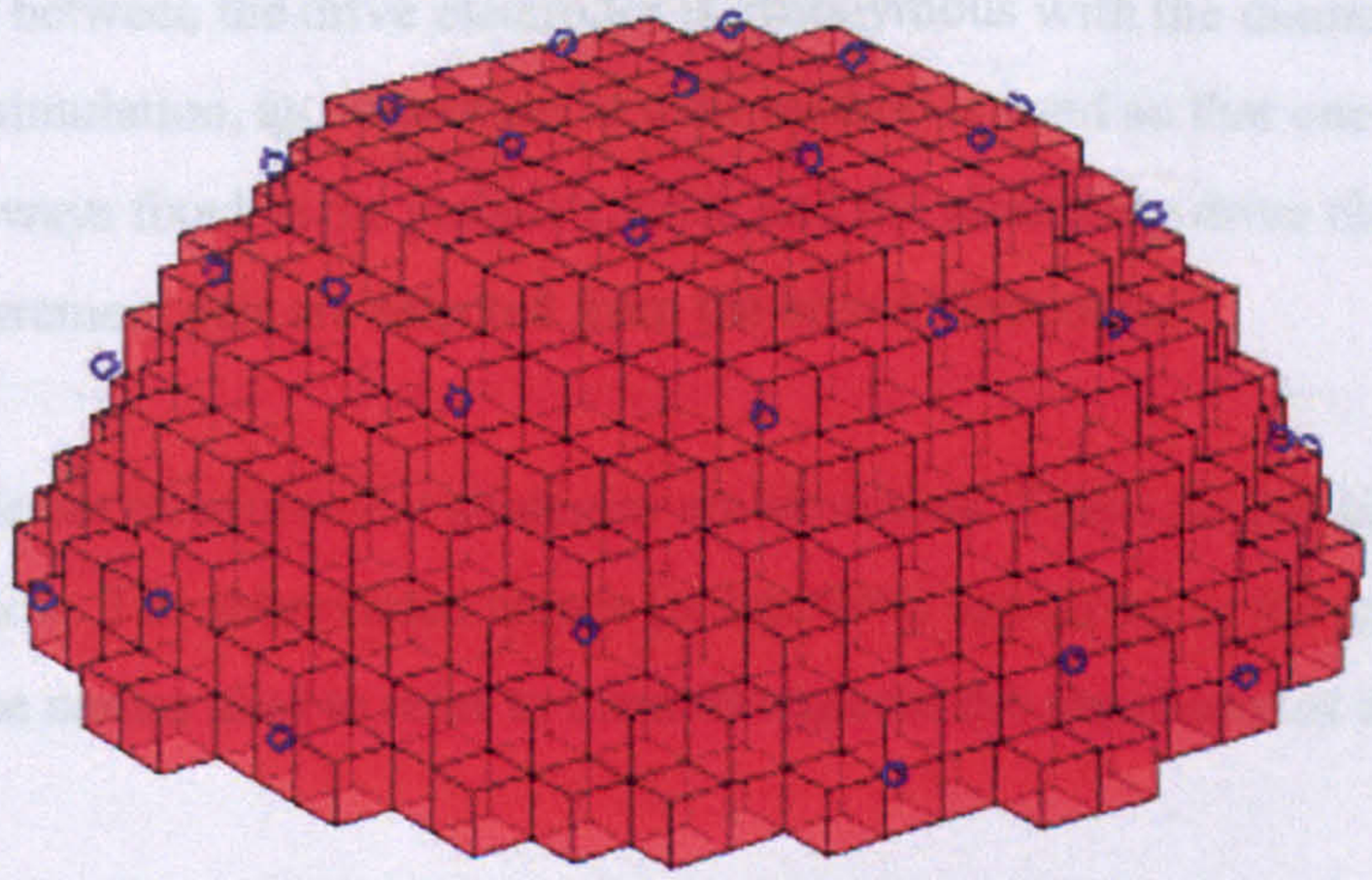

Figure 6.6 – An illustration of how the electrodes (represented as blue circles) are positioned for the *Curved-Grid* method. In this case there are a total of 37 electrodes. The red cubes represent the image voxels.

6.2.3 Current drive / Voltage measurement strategy

As discussed in section 2.6, the principal methods used for driving currents in breast imaging are:

1. Adjacent drive – interlaced adjacent receive on a 2-dimensional circular electrode array (simulation work only) (Wang *et al.* 2001).
2. Trigonometric current patterns used on a 2-dimensional circular electrode array (Osterman *et al.* 2000).
3. Distant drive pairs and receive pairs applied between a fixed electrode(s) on the wrist and a grid electrode array on the breast. (Korjenevsky *et al.* 2001, Assenheimer et. al. 2001).

Method 2 is based on using multiple current sources rather than bipolar currents, therefore it will not be considered further since the work presented here is primarily concerned with optimising the bipolar current drive method. Methods 1 and 3 both use bipolar current sources, but represent opposing ideologies. For this reason they are both simulated in order to resolve which (if any) is most suited to breast imaging.

An alternative method originally proposed for imaging of the head is to place the current drive electrodes as far apart as possible but to use adjacent electrodes for the voltage measurement (Gibson *et al.* 2001). In this case there is no fixed electrode used so the distance between the drive electrodes is synonymous with the diameter of the head. For this simulation, an adaptation of their method is used so that one of the drive electrodes is always fixed to the patient's wrist, and the remaining drive electrode and adjacent measurement pair are selected from the breast electrodes.

Thus three different measurement strategies are simulated. These are explained in more detail below. The abbreviated names (in brackets) appearing in the subsection headings are the names used to refer to them throughout the remainder of the simulation.

6.2.3.1 Adjacent drive / adjacent receive (*Adj-Adj*)

This is the adjacent drive – adjacent receive method. It is applied in two slightly different ways as follows:

For simulating electrodes arranged in the *2D-Ring* positions, the *16 electrode adjacent interlaced* method (as described in the 2-dimensional simulation study) is used. This simulation therefore represents a 3-dimensional application of the De Montfort Mk2b EIM system. Since no fixed electrode is available it is the only appropriate current-voltage pattern that may be used.

For the three remaining electrode distribution patterns a different approach is taken. Since the electrodes are not always arranged in neat rows, a definition of what constitutes 'adjacent electrodes' is required. For this study the term 'adjacent' refers to any electrode that is within 120% of the straight-line distance from a given electrode to its closest neighbouring electrodes. For the *Flat-Grid* method this includes the four electrodes at 0,90,180 and 270° relative to the reference point, but not the diagonally adjacent electrodes (See figure 6.6).

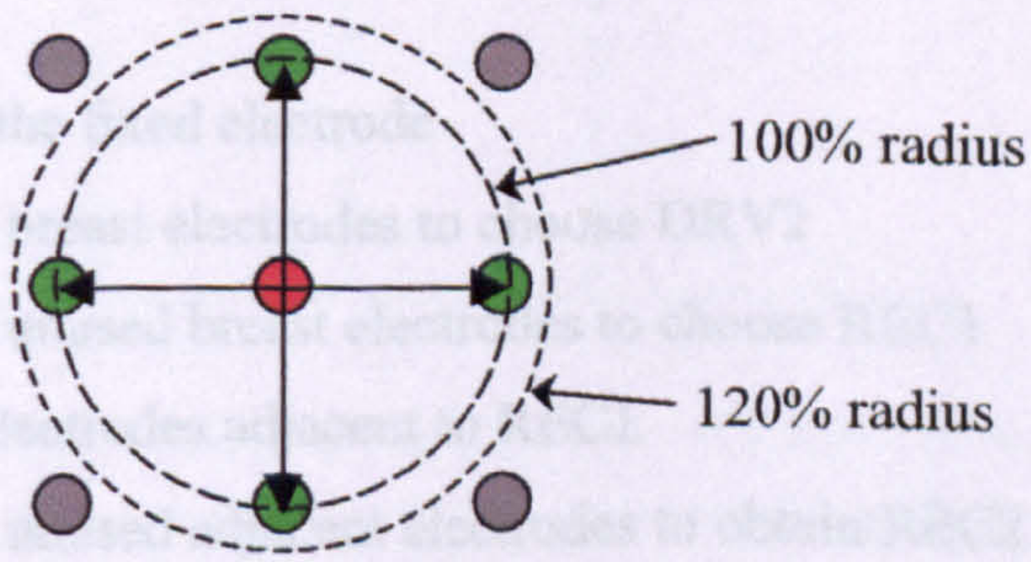

Figure 6.6 – An Illustration of how 'adjacent electrodes' are defined. The red circle represents an electrode for which the 'adjacent neighbours' are to be found. The green circles represent the closest electrodes and are circumscribed by the 100% radius line. The 120% radius line represents the allowed locus in which any other electrodes can be termed 'adjacent'. In this case the next closest electrodes (grey circles) are too far away.

For the *Curved-Grid* and *3D-Rings* methods it depends on the breast shape as to which electrodes are deemed to be adjacent. Based on the above definition of 'adjacent', the procedure for selecting the drive and receive pairs is as follows:

1. Loop through all breast electrodes to choose DRV1
2. Obtain list of electrodes adjacent to DRV1
3. Loop through adjacent electrodes to obtain DRV2
4. Loop through all remaining breast electrodes to choose REC1
5. Obtain list of electrodes adjacent to REC1
6. Loop through unused adjacent electrodes to obtain REC2

6.2.3.2 Fixed drive / adjacent receive (*Fix-Adj*)

For this method one of the drive electrodes is fixed to the wrist and the receive pair are selected as adjacent pairs from the breast electrodes. For the simulation, the wrist electrode is modelled by placing it at a sufficient distance beneath the electrode array such that the current can be considered to be travelling in parallel lines through the breast. To achieve this the x and y coordinates are set to zero (thus placing the electrode on the z-axis of the breast model) and the z coordinate is set to a negative value ten times larger than the base diameter of the breast model. With the fixed electrode included, and adjacent electrodes defined as before, the drive and receive pairs are selected as follows:

1. Set DRV1 to be the fixed electrode
2. Loop around the breast electrodes to choose DRV2
3. Loop around the unused breast electrodes to choose REC1
4. Obtain a list of electrodes adjacent to REC1
5. Loop around the unused adjacent electrodes to obtain REC2

6.2.3.3 Fixed drive / fixed receive (*Fix-Fix*)

The final current/voltage pattern utilises fixed electrodes for both the drive and receive pairs. For *in-vivo* imaging it is preferable to use both wrists so that the measurements are made using the 4-terminal principle (i.e. the drive and receive circuitry are never forced to share an electrode). For the simulation presented here, electrode-to-skin contact is not modelled, so it is acceptable to use the same fixed electrode for both the drive and receive pairs. In this case it is defined as in section 6.2.3.2. The procedure for selecting drive and receive pairs is:

1. Set DRV1 to be the fixed electrode
2. Loop through all breast electrodes to obtain DRV2
3. Set REC1 to be the fixed electrode
4. Loop through all unused breast electrodes to obtain REC2

6.2.3.4 Removing non-independent electrode pairs

The three procedures outlined above have no checks built into them to detect reverse polarity and reciprocal measurements. For example, if electrodes 1 and 2 are adjacent and also electrodes 5 and 6 are adjacent, then the *Adj-Adj* method selects them in up to seven other permutations, as listed in Table 6.2. However, all of them represent the same 4-terminal impedance measurement. In order to prevent lengthy and unnecessary computations, an algorithm has been written to check through each list of drive-receive pairs and remove any such permutations.

DRV 1	DRV 2	REC 1	REC 2
1	2	5	6
2	1	5	6
1	2	6	5
2	1	6	5
5	6	1	2
5	6	2	1
6	5	1	2
6	5	2	1

Table 6.2 – The possible permutations for selecting electrodes 1,2,5 and 6. In this case 1 & 2 are adjacent and 5 & 6 are adjacent, and the *Adj-Adj* drive-receive selection method is applied.

6.2.4 Number of electrodes

The final variable to be defined is the number of electrodes used in the simulation. This is an important variable because in one sense the simulation is aimed at evaluating the performance of existing hardware but in another sense the intention is to evaluate the concepts of existing hardware. For example, the De Montfort Mk2b system employs 32 electrodes whereas the grid method described by Korjenevsky *et al.* (2001) uses 256 electrodes. If the results from both of these systems is comparable then the De Montfort Mk2b system would be preferred since it requires fewer electrodes. On the other hand, if the grid method is shown to perform better using 32

electrodes then it would emerge as superior. Another factor to be taken into consideration is the computational loads required. A 256-electrode grid can generate up to 65536 fixed electrode drive-receive pairs. This combined with a typical image structure containing ~1200 voxels means that the sensitivity matrix would have 65536 x 1200 entries. At 4 bytes per entry the memory requirements are ~315Mbytes which is beyond the physical size of RAM in the computer to be used for this simulation. A more realistic approach therefore is to use around 32 electrodes for the 3D electrode placement methods.

For the simulation, electrode array sizes of 24 and 40 are used since they fall either side of the 32 electrodes used in the De Montfort Mk2b system, thus symbolising both diminished and improved performance. Since the 2-dimensional performance of the *2D-Ring* method with up to 128 electrodes is already understood from Chapter 4, it is not considered necessary to simulate more than 40 electrodes in 3 dimensions.

6.3 Outline of 3D EIM simulation

The principle aim of this study is to evaluate the resolution performance of a number of 3D EIM imaging methods, two of which have been described in literature, and the remainder of which have been proposed as new alternatives. There are a total of 4 variables, namely; number of electrodes, data collection strategy, point source position and breast shape. The number of electrodes used depends on the electrode placement strategy; for the *2D-Ring* method 32 electrodes are used, and for the 3D electrode placement methods, arrays of 24 and 40 electrodes are simulated. (Note – due to their geometry, the *Flat-Grid* and *Curved-Grid* methods use 37 electrodes rather than 40). The data collection strategy is governed by the combination of electrode placement method and current/voltage patterns. There are ten possible combinations using the chosen methods as outlined above. A comprehensive list of the measurement strategies is shown in Table 6.2. For the point source positions it is chosen to use ten different locations as explained in section 5.4.2. The breast shape is also varied according to one of ten different shapes ranging from pendant to flat. By implementing all possibilities of these variables a total of 2000 different resolution measurements are made, which are presented as profiles based on the amount of breast compression. The profiles are grouped under headings relating to both the number of electrodes used and data

measurement strategy, and in each group there are ten profiles for each of the ten different point sources.

Placement	rive – receive	lectrodes
2D-Ring	Adj-Adj	32
Flat-Grid	Adj-Adj	24 37
	Fix-Adj	24 37
	Fix-Fix	24 37
Curved-Grid	Adj-Adj	24 40
	Fix-Adj	24 40
	Fix-Fix	24 40
3D-Rings	Adj-Adj	24 40
	Fix-Adj	24 40
	Fix-Fix	24 40

Table 6.2. A list of all the measurement strategies used for the 3D simulation study grouped in terms of electrode placement, drive-receive method and the number of electrodes used.

6.4 Results of the 3D EIM simulation

The 3D resolution profiles for each of the 10 data collection methods, the 10 breast shapes and the 10 point source positions are presented. They are grouped in terms of the data collection method used, beginning with the *2D-Ring* method followed by the *Flat-Grid* method, the *3D-Rings* method and finally the *Curved-Grid* method. A discussion of all the results can be found at the end of the chapter in section 6.5.

The data collection method used to produce the curves shown in figure 6.7 is the *2D-Ring Adj-Adj* method applied to a 32-electrode array. This is equivalent to using the De Montfort Mk2b system. It can be seen from the curves that the best resolution is achieved for pendant breast shapes (towards the left of the horizontal axis). However, not all point source locations are affected by breast shape; for example, PSF locations 1,2 and 5 (towards the centre of the breast model) remain imaged with a resolution of ~27% whatever the shape of the breast, whereas PSF locations 7-10 (towards the nipple region) are imaged much better when the breast is pendant.

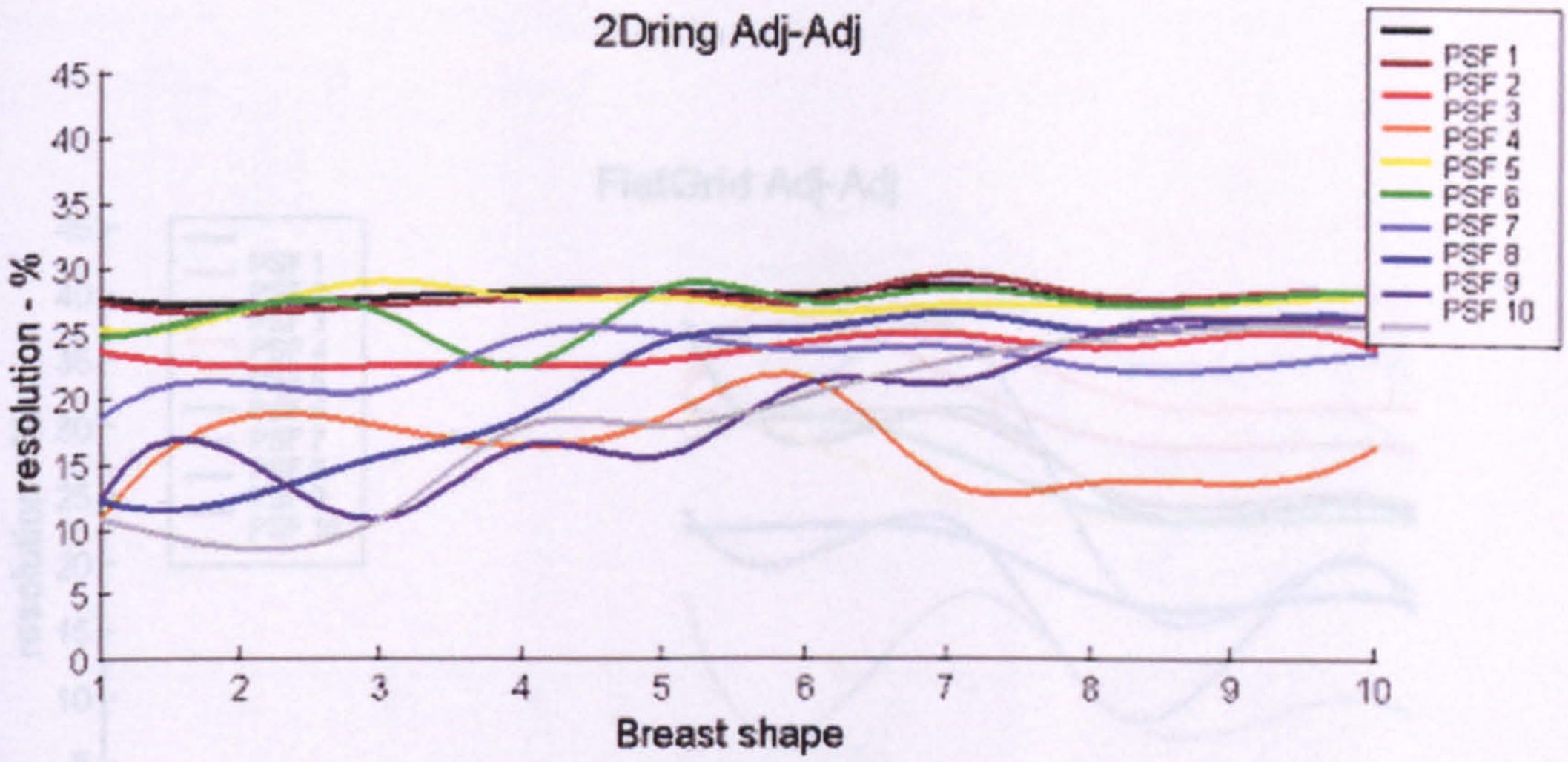

Figure 6.7 – Resolution profiles of the 10 different point source positions as a function of breast shape. The measurement strategy used is: *2D-Ring Adj-Adj* with 32-electrodes.

The graphs in figure 6.8 are produced by the *Flat-Grid Adj-Adj* method. The curves in figure a) represent results obtained from a 24-electrode array and the curves in figure b) represent those from a 40-electrode array. A prominent feature of these graphs is that they have no data for the pendant end of the breast shape axis. The reason for this is that when the *Flat-Grid* electrode array is brought into contact with the breast model in its pendant form, only a few of the electrodes touch the skin surface. For impedance measurements to be successfully simulated at least four electrodes must be in contact, hence a certain degree of breast compression is required before the simulation can be performed properly. In comparison with the *2D-Ring* data collection method (figure 6.7), the resolution is generally much worse, having range of ~10-40% for both sizes of electrode array. The spread of resolution values (and hence spatial variance) is greater, with a tendency to image the surface regions (PSF numbers 4,8,9 & 10) more accurately. The overall negative gradient of the curves indicates that this technique is better suited to compressed breast shapes. The graphs in figure 6.9 correspond to the same data collection method with the exception that one of the drive electrodes is fixed.

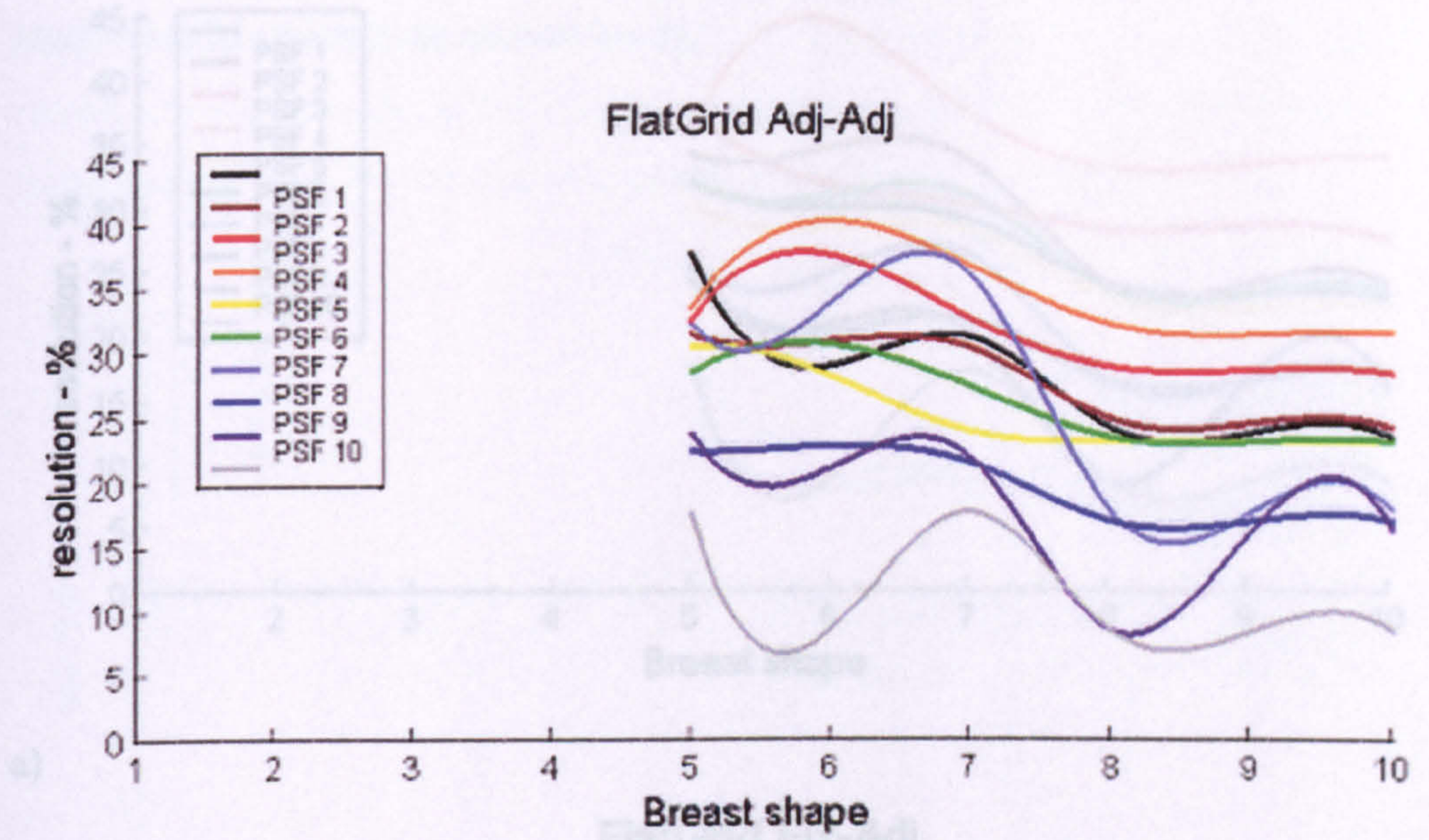

a)

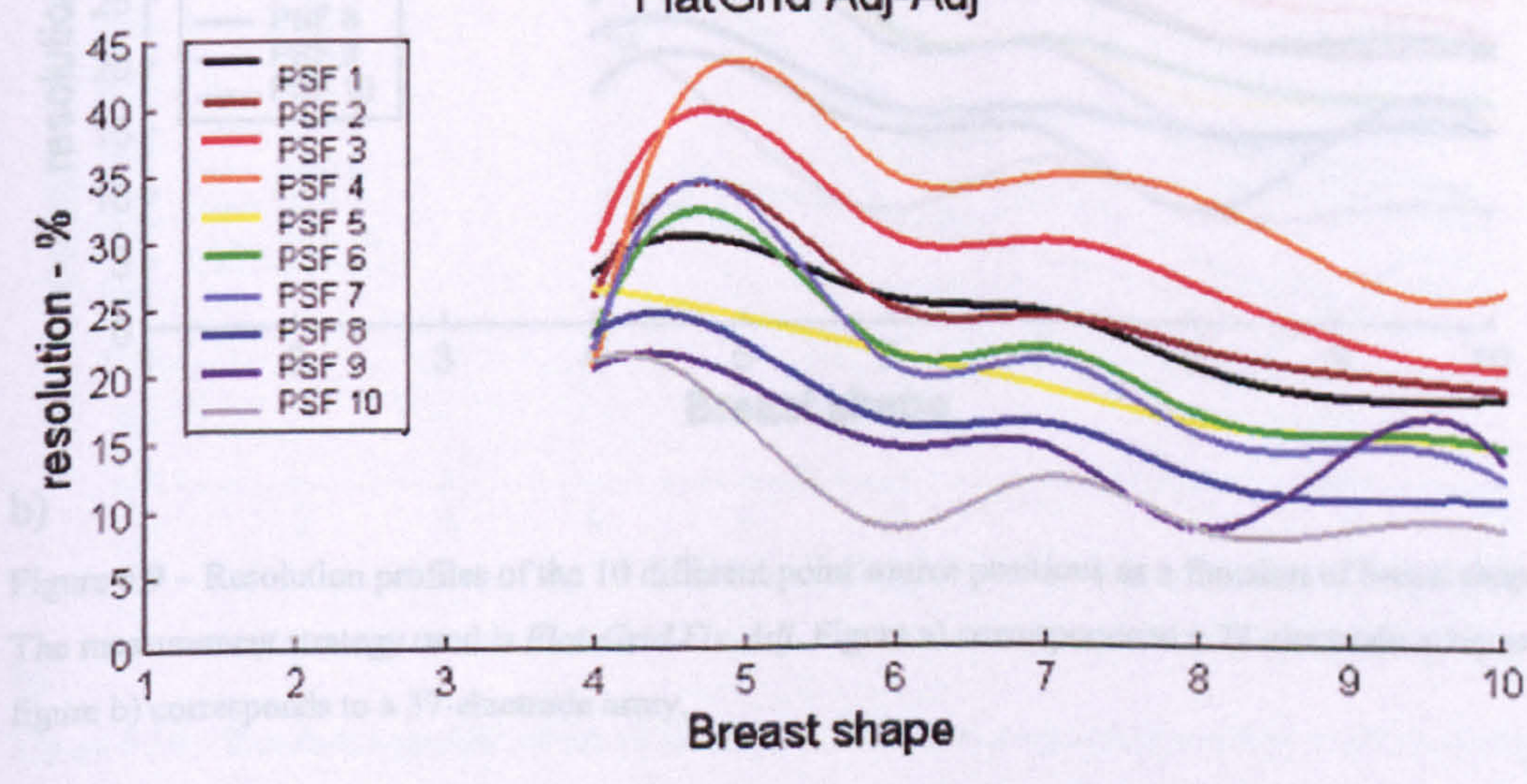

b)

Figure 6.8 – Resolution profiles of the 10 different point source positions as a function of breast shape. The measurement strategy used is *Flat-Grid Adj-Adj*. Figure a) corresponds to a 24-electrode array and figure b) corresponds to a 37-electrode array.

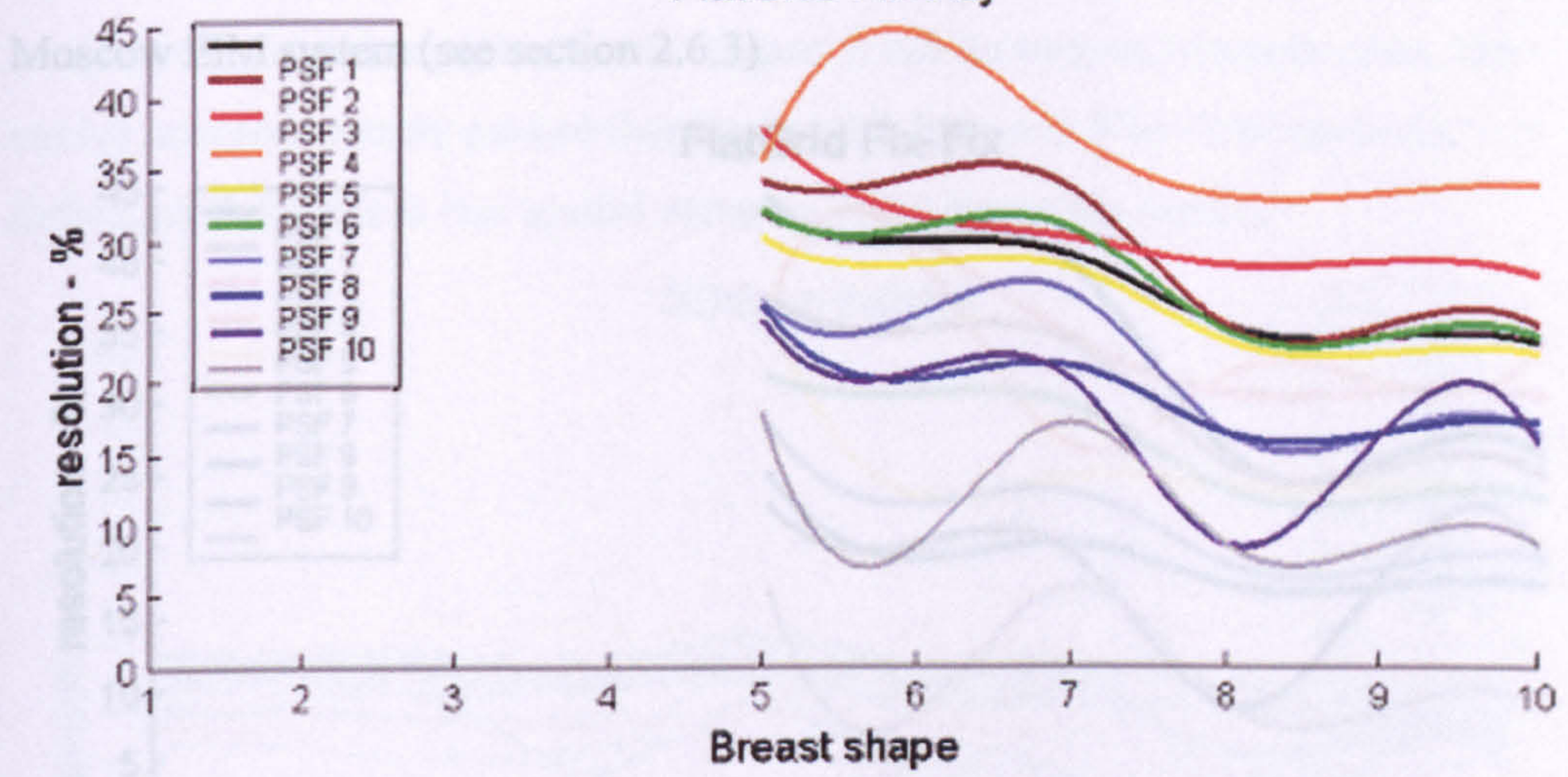

a)

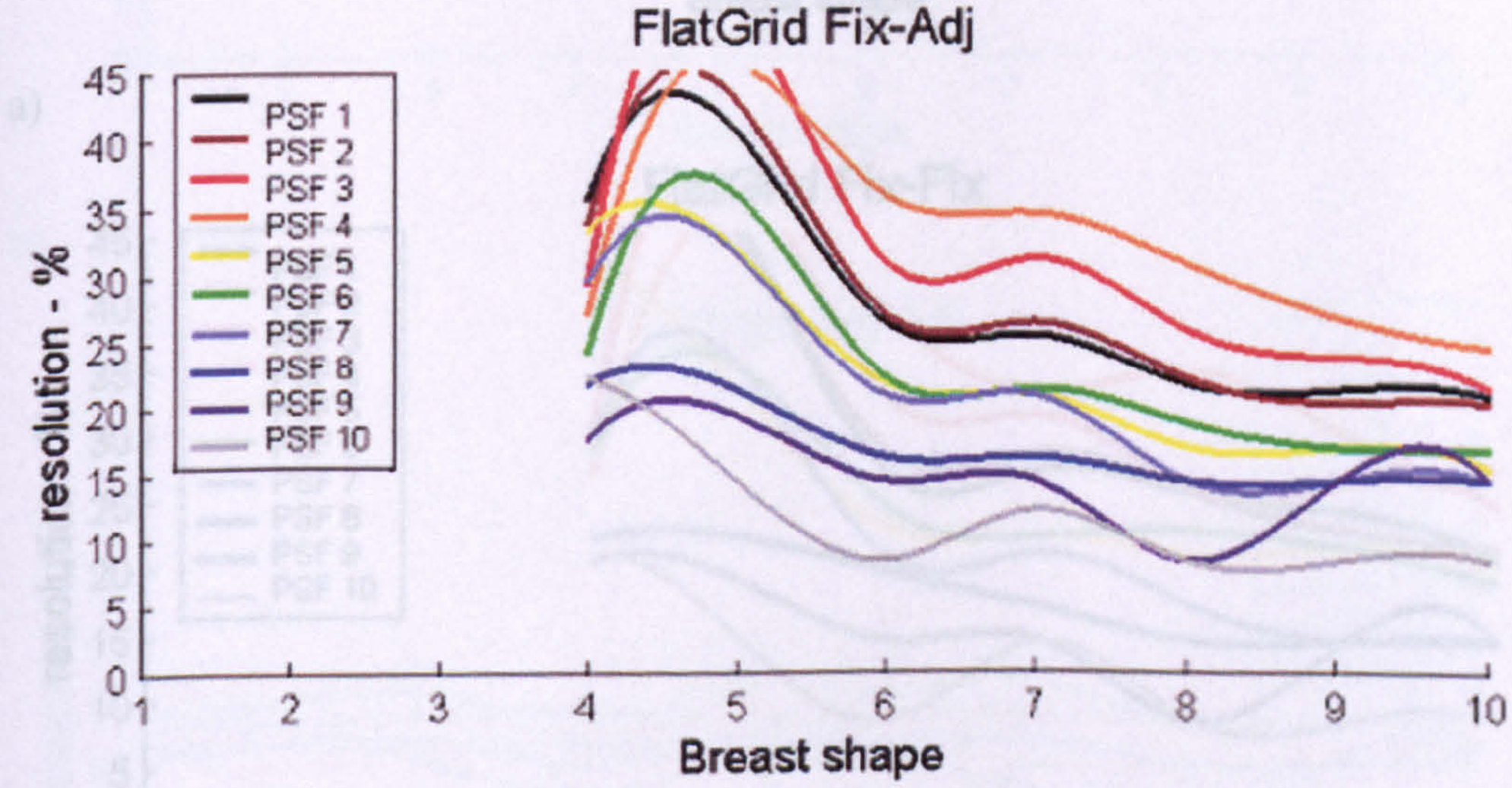

b)

Figure 6.9 – Resolution profiles of the 10 different point source positions as a function of breast shape. The measurement strategy used is *Flat-Grid Fix-Adj*. Figure a) corresponds to a 24-electrode array and figure b) corresponds to a 37-electrode array.

The results are essentially the same except that for the 37-electrode array (figure 6.9b) the resolution for breast shape number 5 is significantly worse, in some cases exceeding 45%. However, when the breast model is fully compressed (right hand end of breast shape axis) there appears to be no notable difference between the resolution values of figures 6.8 and 6.9. The graphs in figure 6.10 are as a result of fixing one

electrode from the drive and the receive pair and is the same as the method used for the Moscow EIM system (see section 2.6.3).

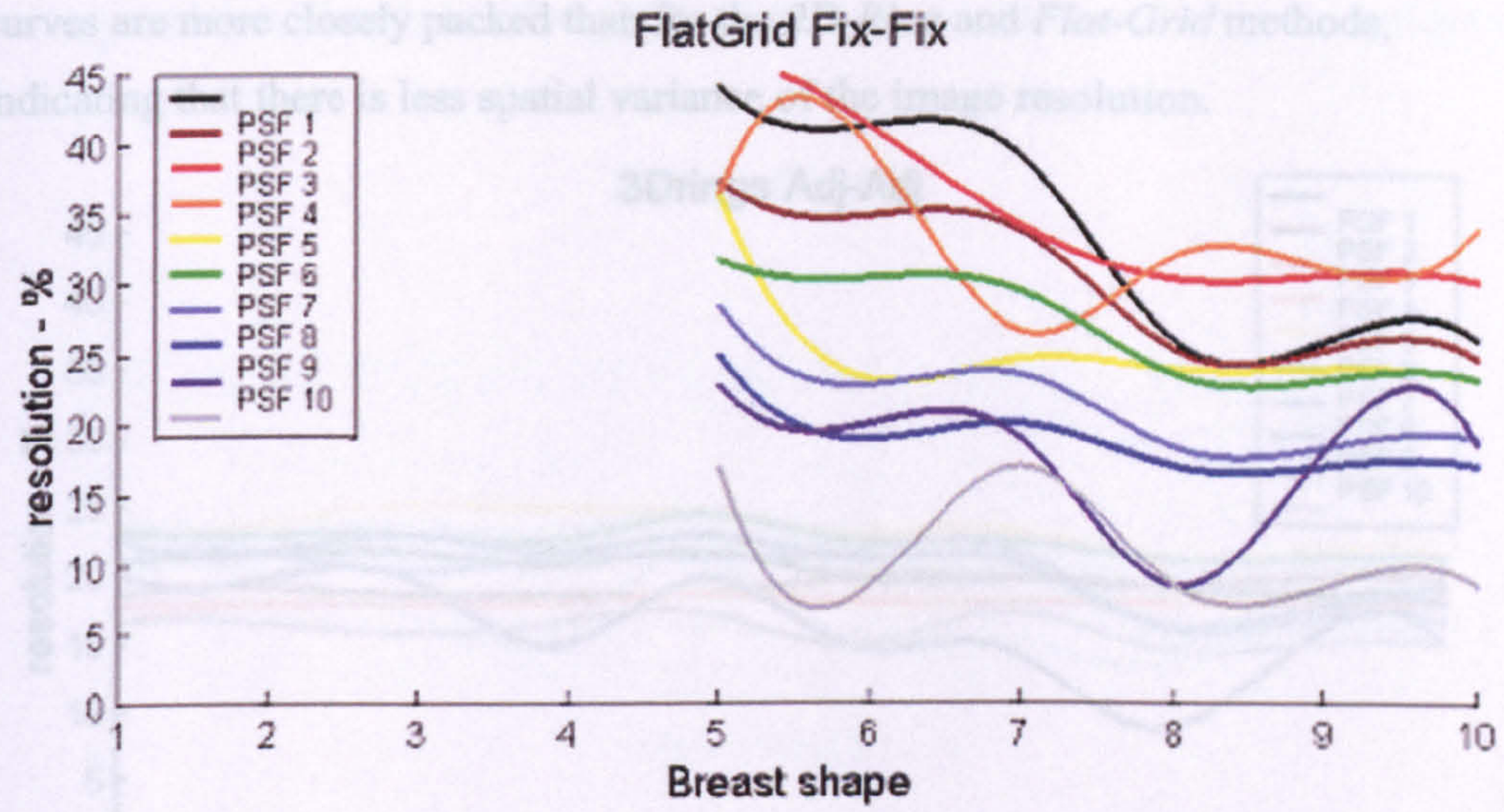

a)

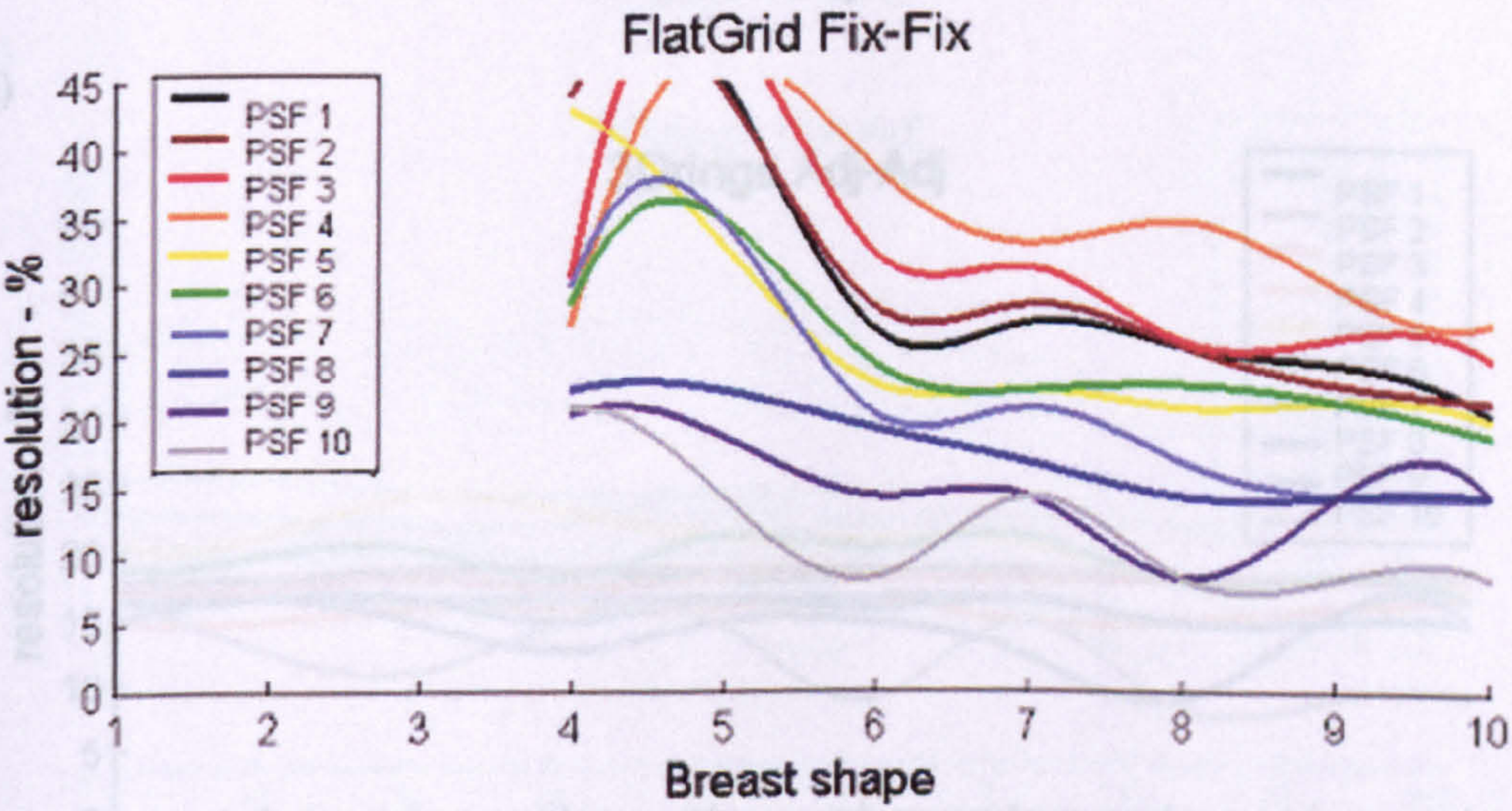

b)

Figure 6.10 – Resolution profiles of the 10 different point source positions as a function of breast shape. The measurement strategy used is *Flat-Grid Fix-Fix*. Figure a) corresponds to a 24-electrode array and figure b) corresponds to a 37-electrode array.

There are no obvious changes in the observed resolution performance, suggesting that the choice of drive-receive method has little effect on image quality for the *Flat-Grid* electrode array. The graphs in figure 6.11 are produced by the *3D-Rings Adj-Adj* method. The *3D-Rings* electrode placement scheme is an original approach to

electrode placement in that it allows a more successful implementation of 3D breast imaging over a wide range of breast shapes. It can be seen that in both cases, the curves are more closely packed than for the *2D-Ring* and *Flat-Grid* methods, indicating that there is less spatial variance of the image resolution.

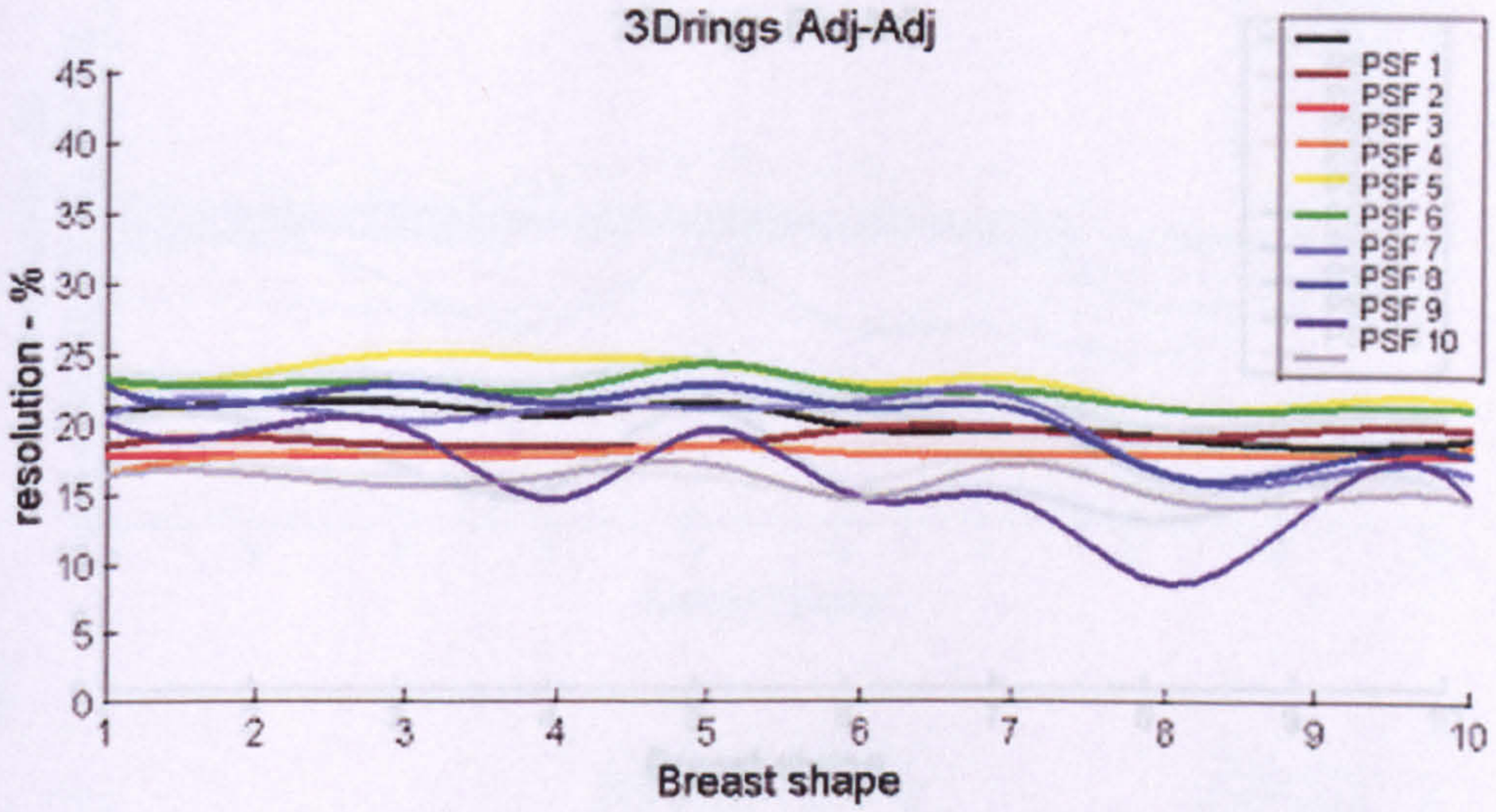

a)

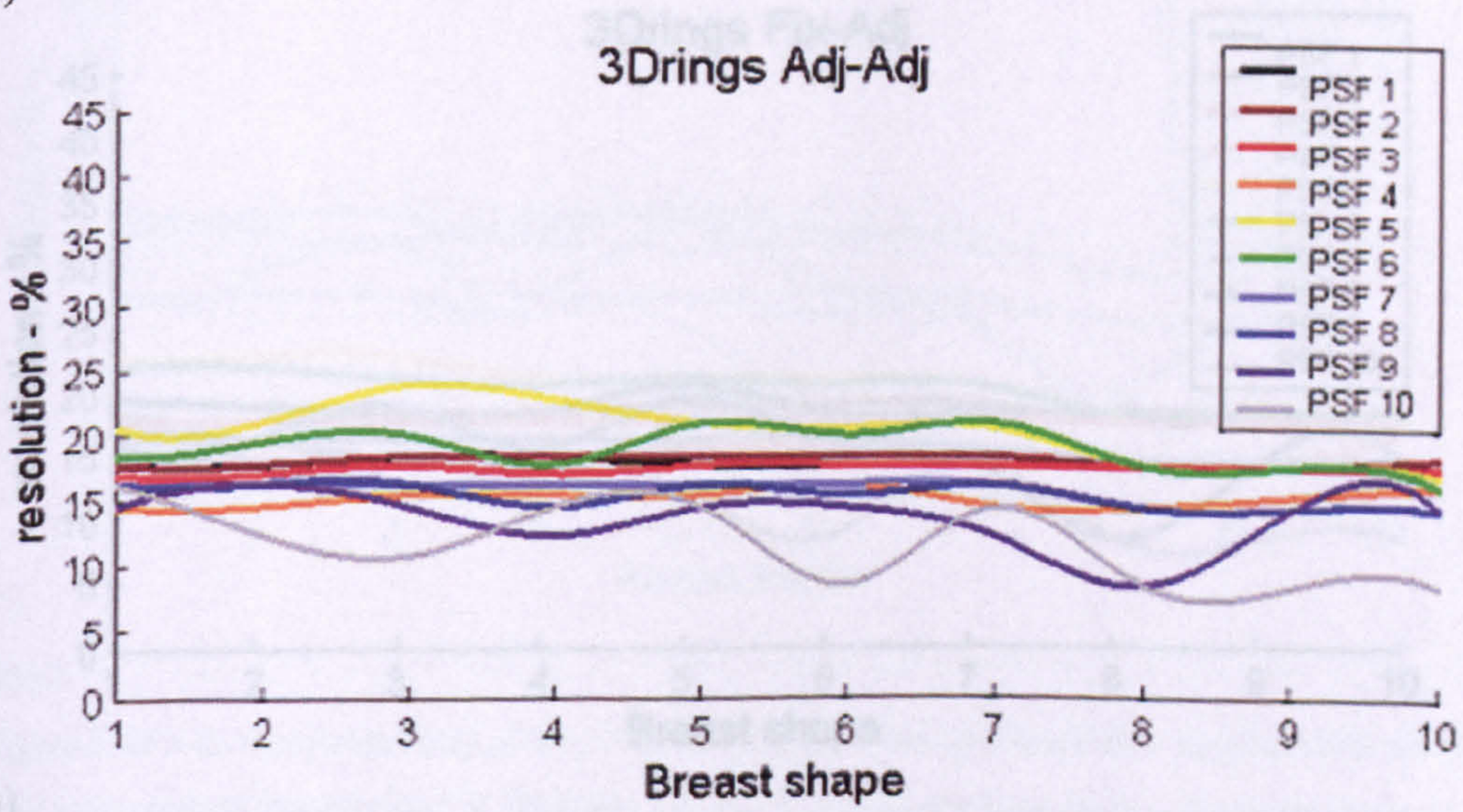

b)

Figure 6.11 – Resolution profiles of the 10 different point source positions as a function of breast shape. The measurement strategy used is *3D-Rings Adj-Adj*. Figure a) corresponds to a 24-electrode array and figure b) corresponds to a 40-electrode array.

The range of resolution values is ~16-24% for the 24-electrode array and ~15-21% for the 40-electrode array, indicating that the use of more electrodes improves the image resolution. Unlike the *2D-Ring* and *Flat-Grid* methods there is no overall gradient to

the curves, demonstrating that this data collection method is not biased towards any particular breast shape. The graphs in figure 6.12 show the results for a data collection strategy which is identical to that of figure 6.11 except that the drive pair employs one fixed electrode.

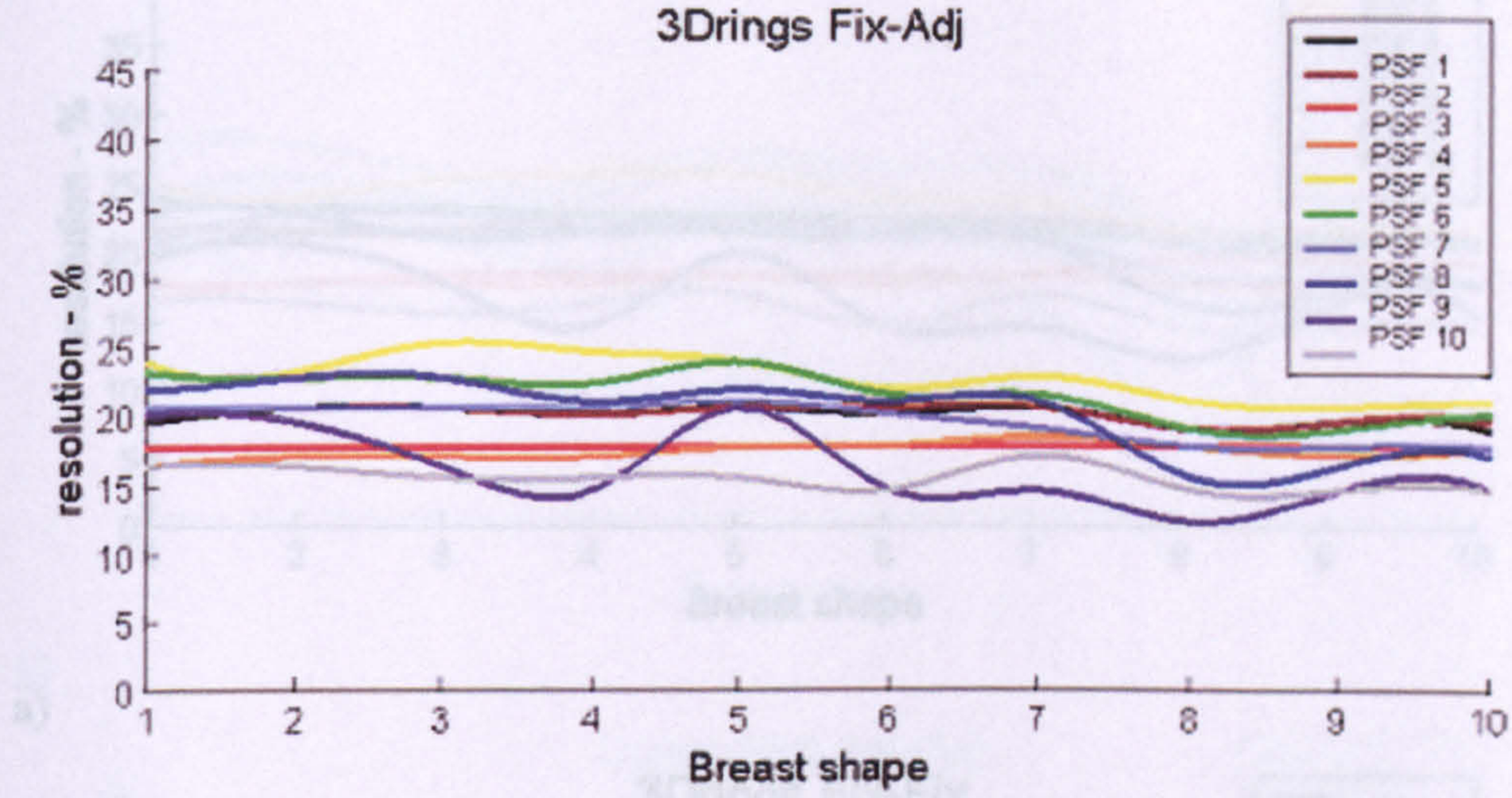

a)

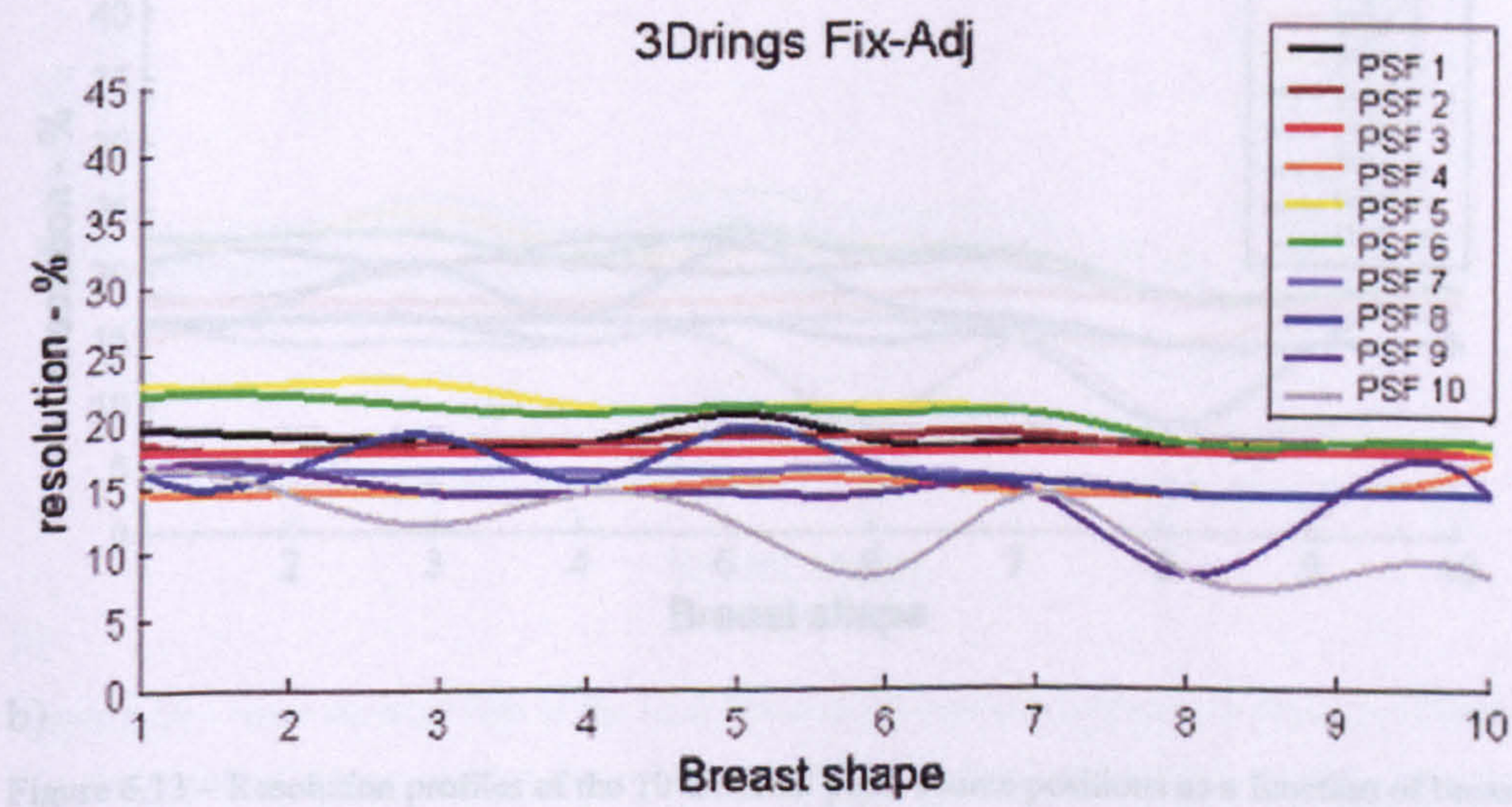

b)

Figure 6.12 – Resolution profiles of the 10 different point source positions as a function of breast shape. The measurement strategy used is *3D-Rings Fix-Adj*. Figure a) corresponds to a 24-electrode array and figure b) corresponds to a 40-electrode array.

Visually there is little difference to be observed from a comparison of the results of figures 6.11 and 6.12, so all the comments for the *3D-Rings Adj-Adj* method also apply. Subtle differences will be highlighted in the Discussion where the results are numerically analysed. The curves shown in figure 6.13 are for the *3D-Rings Fix-Fix*

method. Once again there is little notable difference to be detected from a visual inspection of the curves.

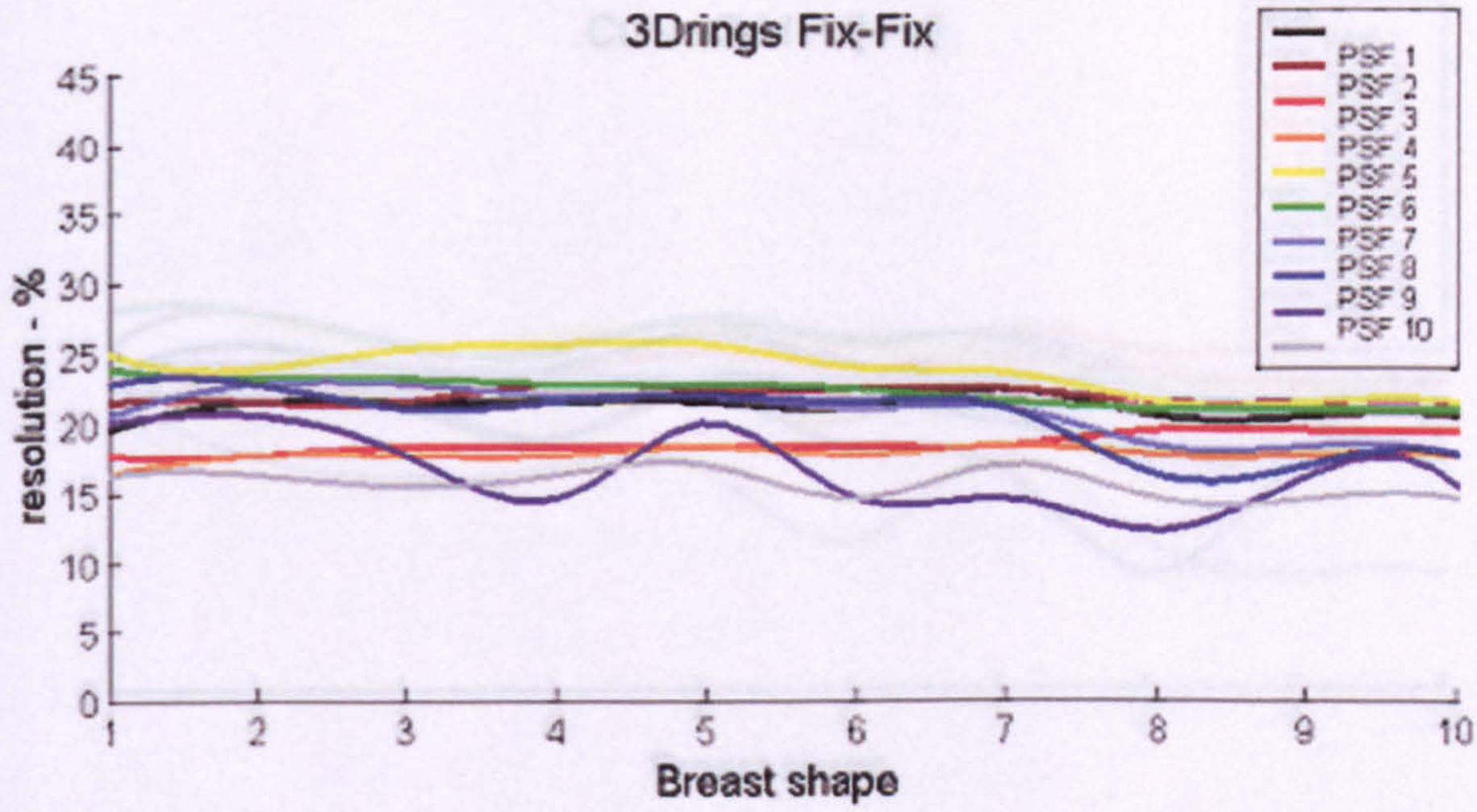

a)

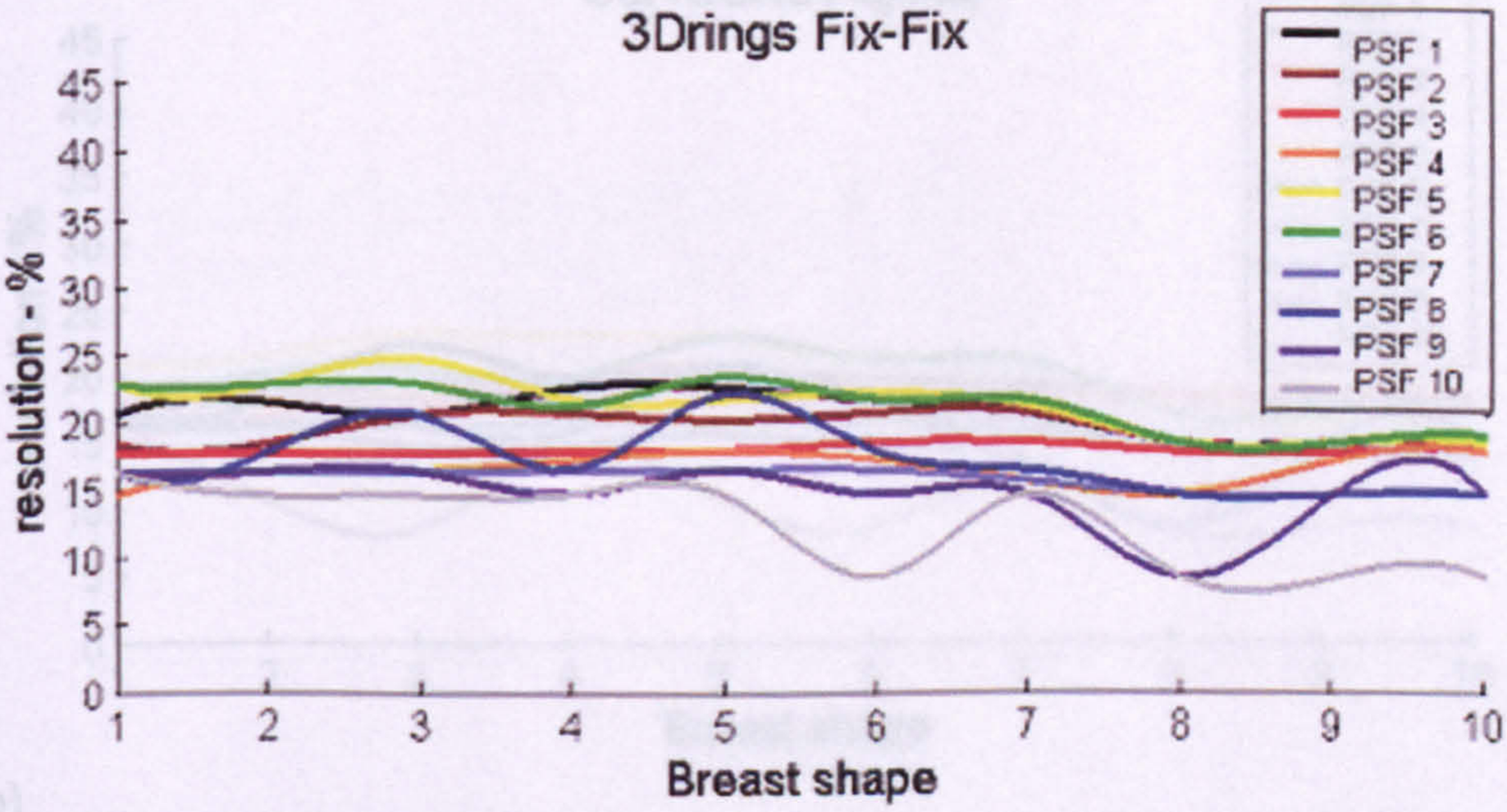

b)

Figure 6.13 – Resolution profiles of the 10 different point source positions as a function of breast shape. The measurement strategy used is *3D-Rings Fix-Fix*. Figure a) corresponds to a 24-electrode array and figure b) corresponds to a 40-electrode array.

The data collection method used to produce the results shown in figure 6.14 is the *Curved-Grid Adj-Adj* method. The *Curved-Grid* electrode placement scheme is proposed as an improvement over the *Flat-Grid* and is therefore an original approach. By comparing the results in figure 6.14 with the equivalent results of the *Flat-Grid* method (figure 6.8) it is immediately obvious that the *Curved-Grid* method performs

better. Since all electrodes are able to come into contact with the breast at all times it is possible to image pendant breasts successfully.

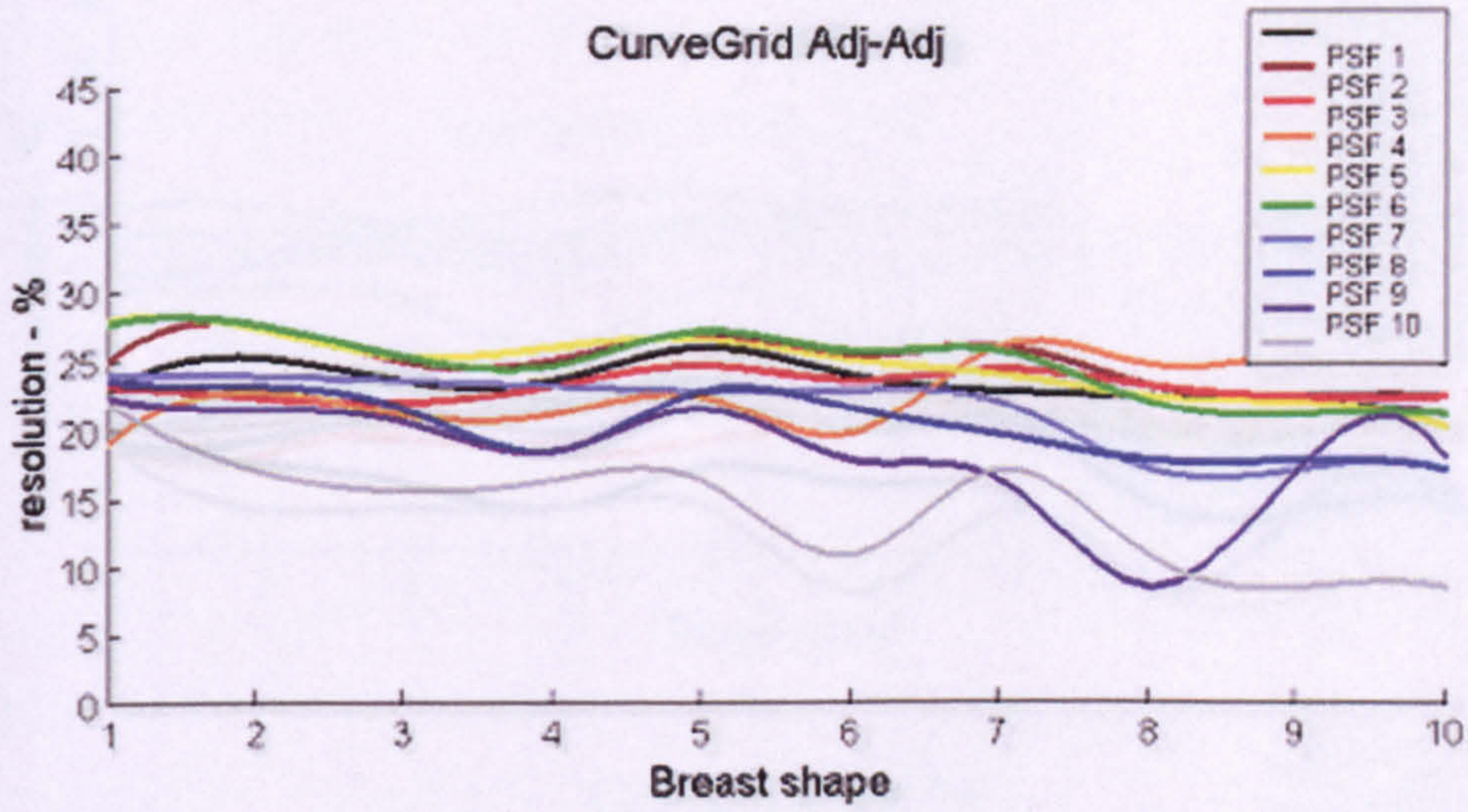

a)

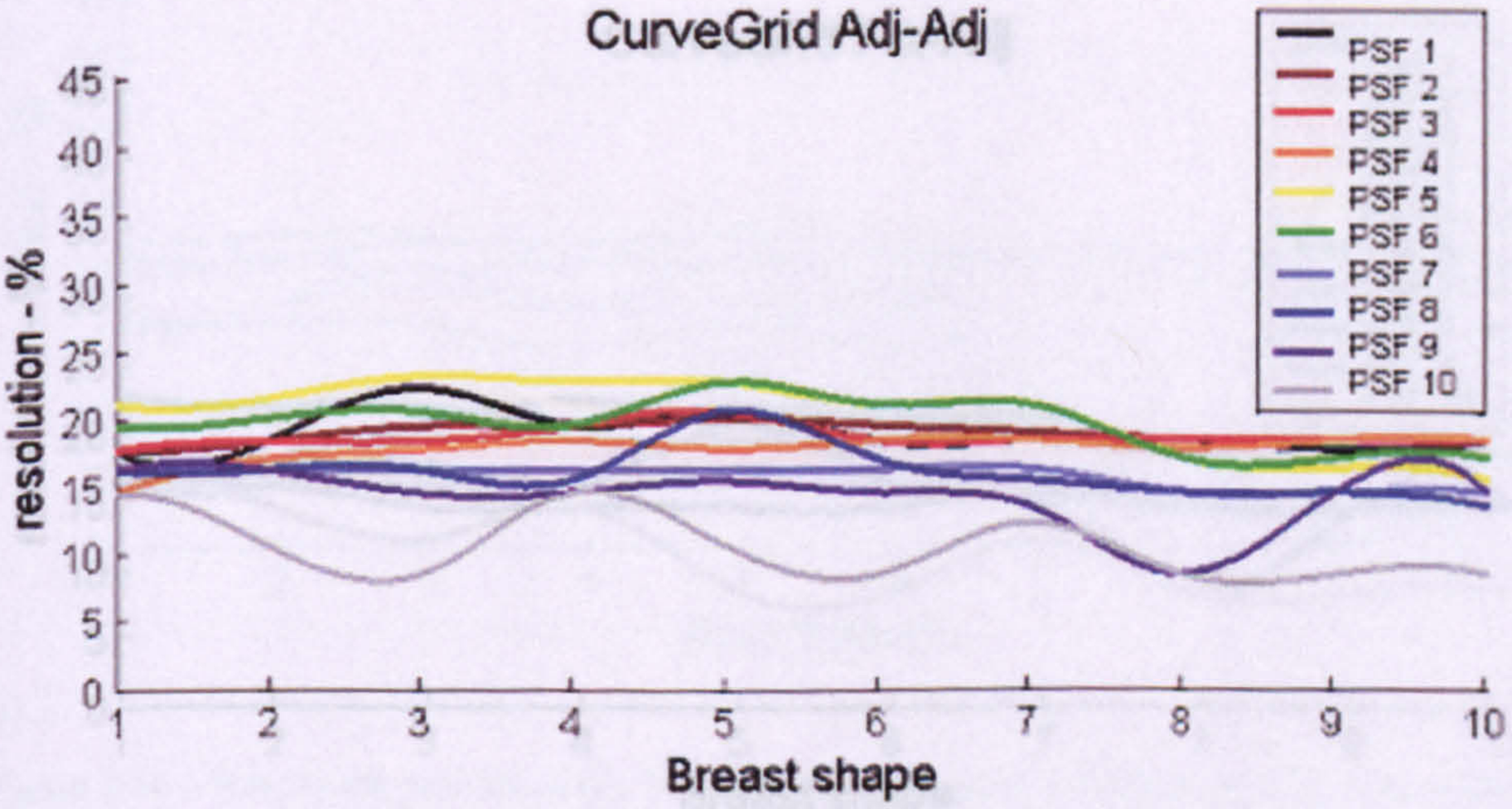

b)

Figure 6.14 – Resolution profiles of the 10 different point source positions as a function of breast shape. The measurement strategy used is *Curved-Grid Adj-Adj*. Figure a) corresponds to a 24-electrode array and figure b) corresponds to a 37-electrode array.

The typical range of resolution values for the *Flat-Grid* method is 10-40% whereas for the *Curved-Grid* method it is significantly better at ~15-27% for a 24-electrode array and ~14-23% for a 37-electrode array. There is little gradient to the resolution profiles, indicating that the new method is not biased towards any particular breast shape. An additional benefit of the *Curved-Grid* approach is that the spatial variance is low, seen

in figure 6.14 from the closely packed resolution profiles. The curves in figure 6.15 correspond to the *Curved-Grid* method with a fixed drive electrode.

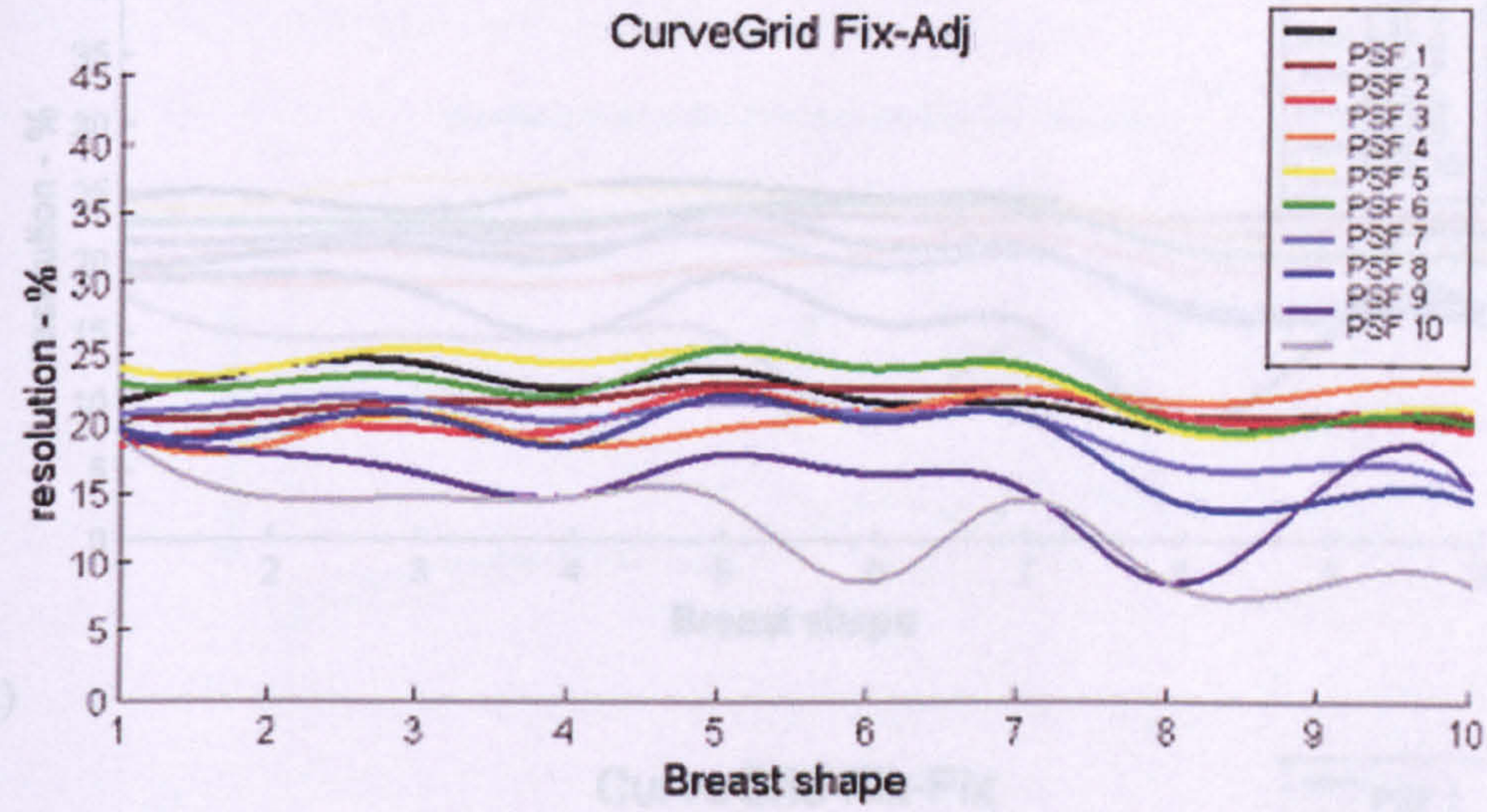

a)

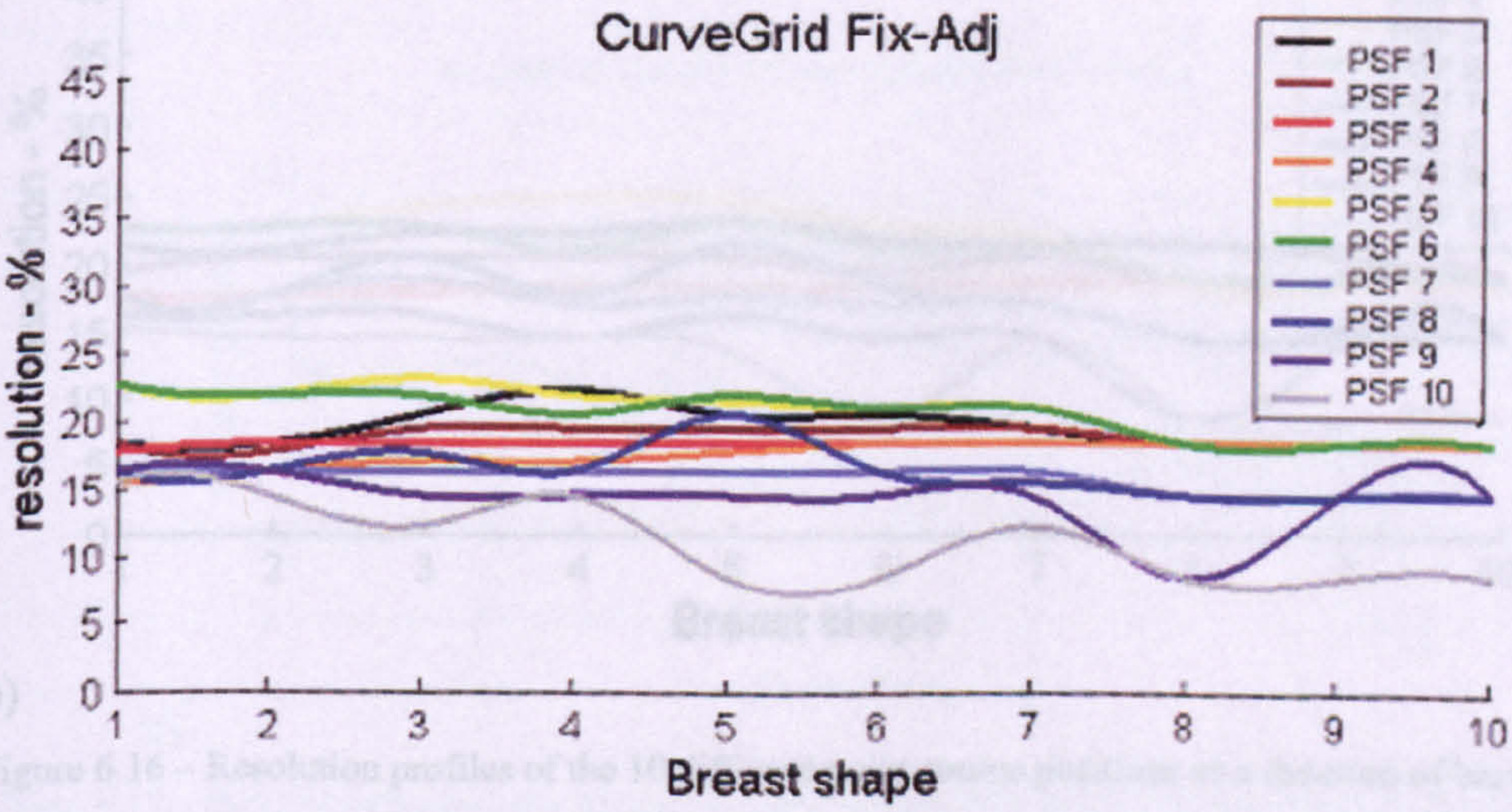

b)

Figure 6.15 – Resolution profiles of the 10 different point source positions as a function of breast shape. The measurement strategy used is *Curved-Grid Fix-Adj*. Figure a) corresponds to a 24-electrode array and figure b) corresponds to a 37-electrode array.

In comparison with the graphs of figure 6.14 there is little change, suggesting that the choice of drive currents is less significant than the electrode positions. This is also the case for figure 6.16 in which a fixed electrode was used for both the drive pair and the receive pair.

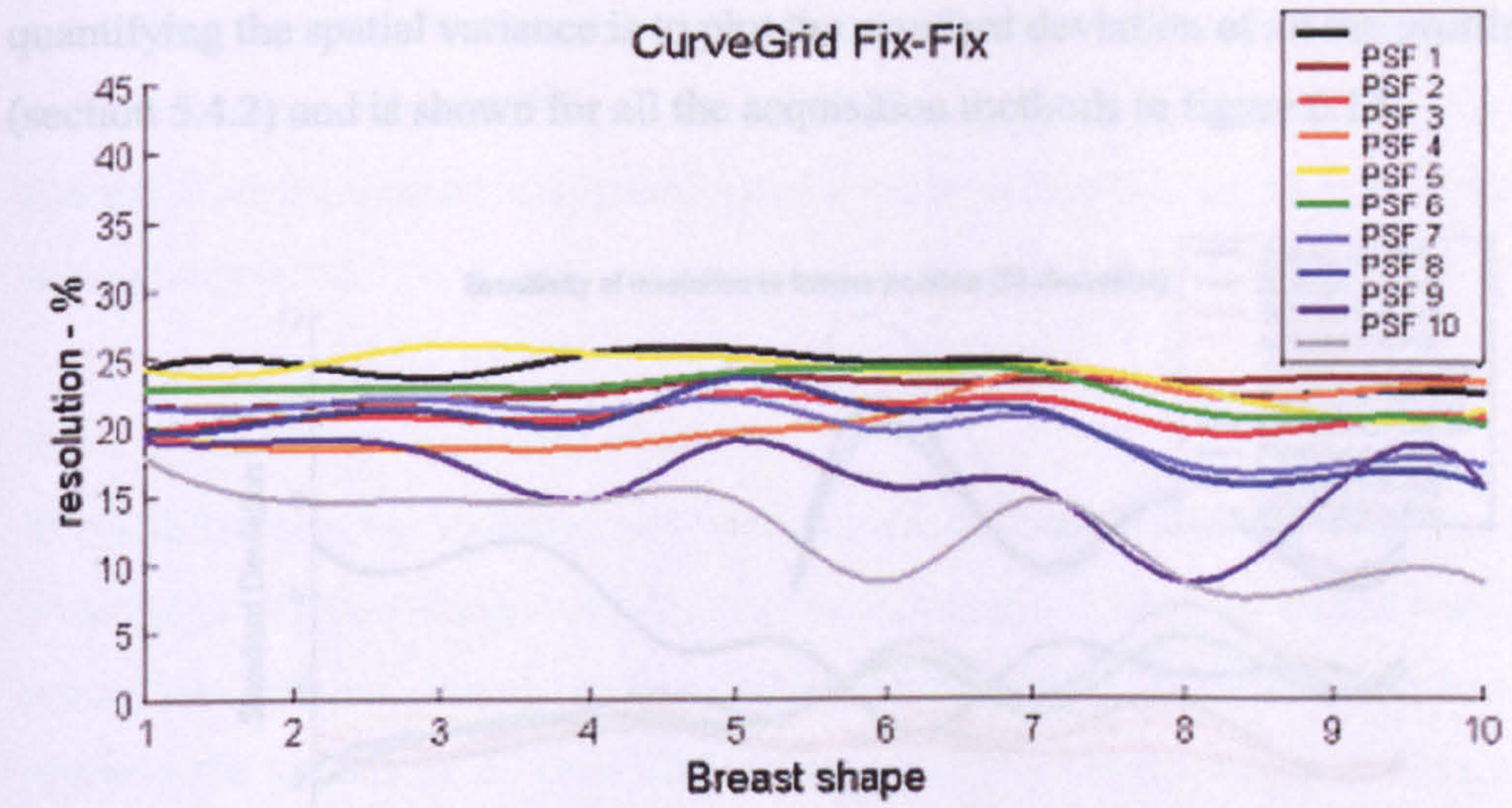

a)

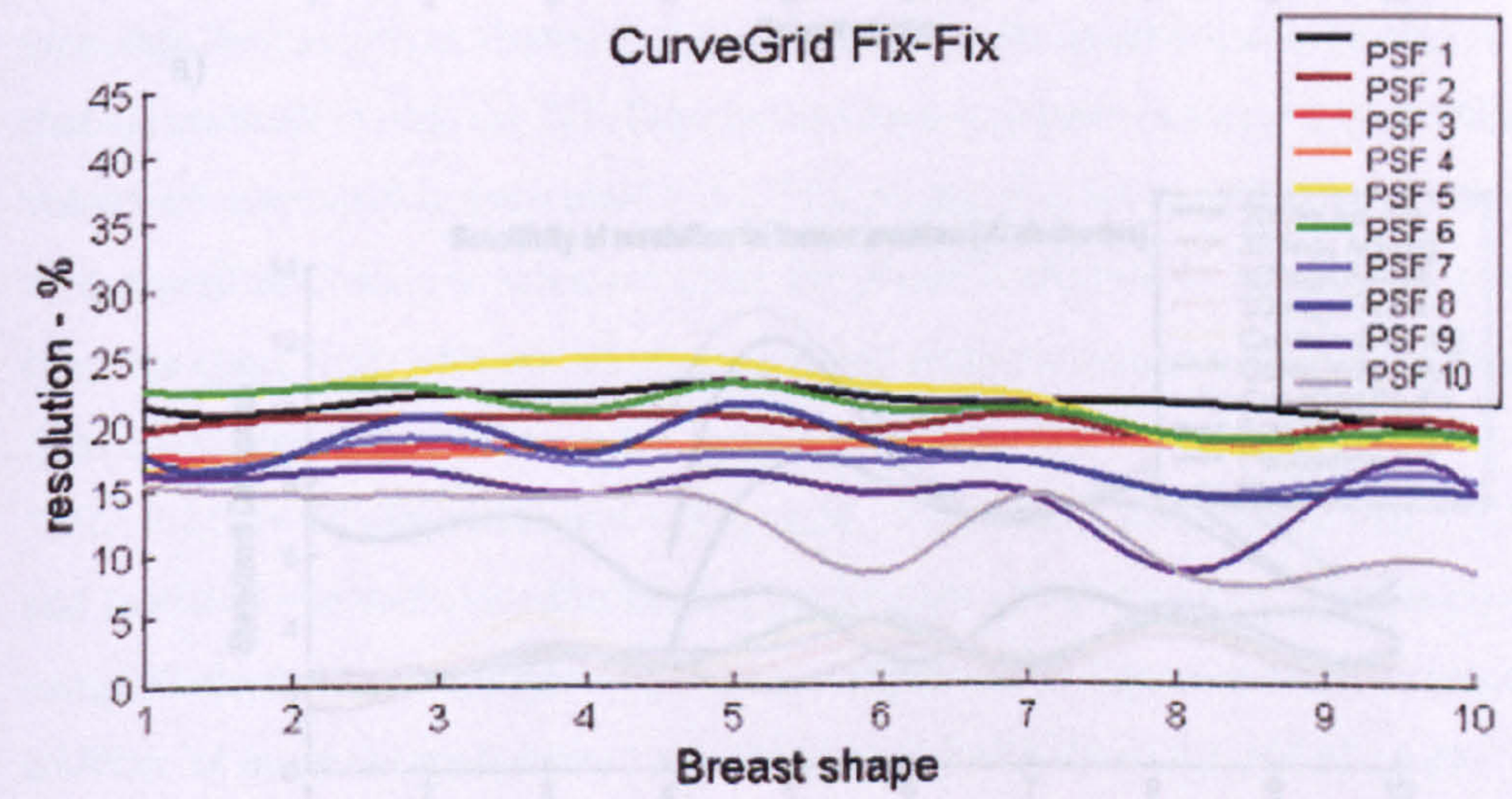

b)

Figure 6.16 – Resolution profiles of the 10 different point source positions as a function of breast shape. The measurement strategy used is *Curved-Grid Fix-Fix*. Figure a) corresponds to a 24-electrode array and figure b) corresponds to a 37-electrode array.

6.5 Discussion

6.5.1 Spatial variance of the resolution

For each acquisition method there are ten resolution profiles representing the ten different point source positions within the breast model. An ideal acquisition method would detect all areas of the breast with equal sensitivity. In practise this does not happen due to the spatial variance of the resolution. The chosen method for

quantifying the spatial variance is to plot the standard deviation of all the profiles (section 5.4.2) and is shown for all the acquisition methods in figure 6.17.

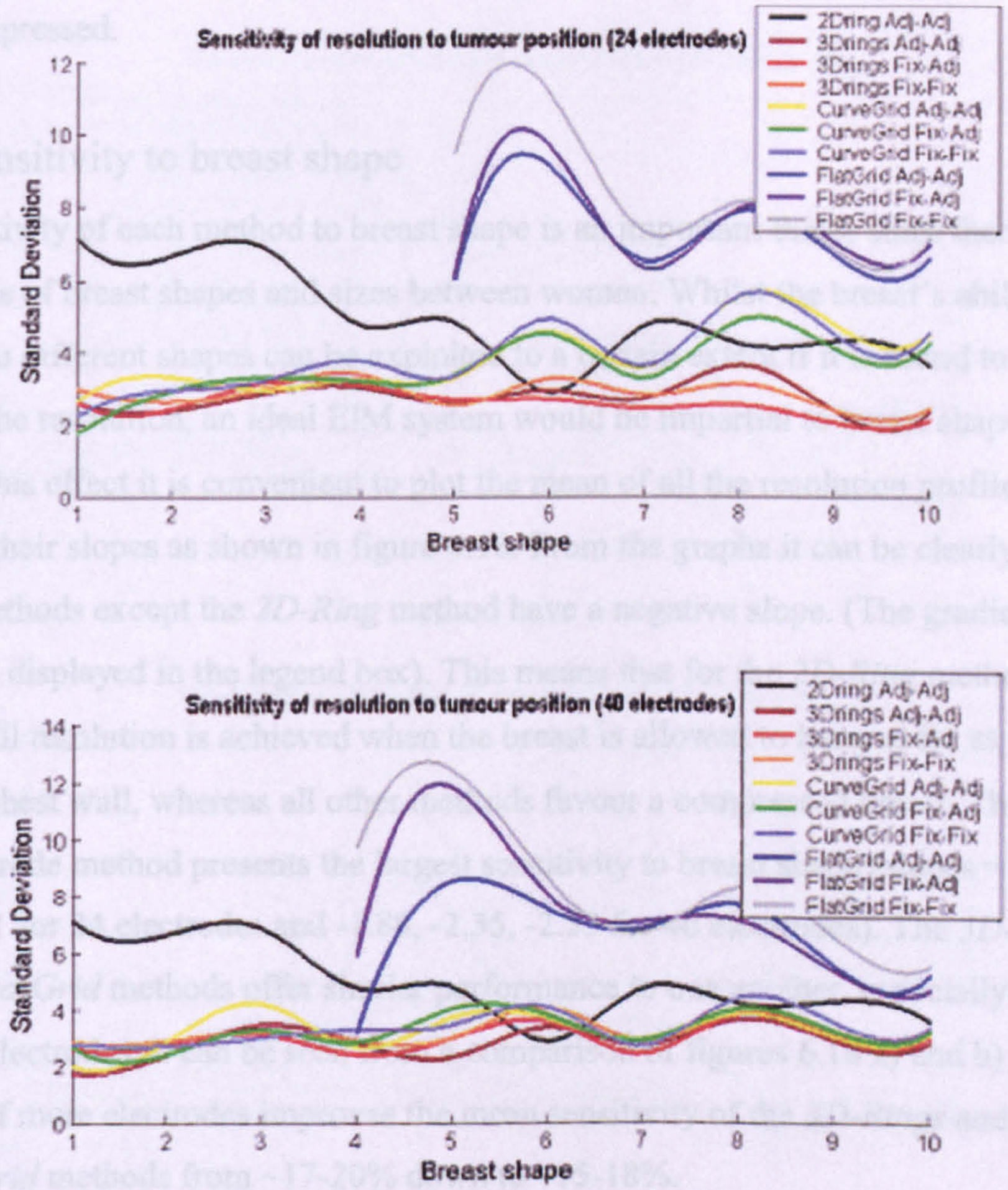

Figure 6.17 – Profiles indicating the spatial variance of each data collection strategy as a function of breast shape. The vertical axes correspond to the standard deviation of the resolution values of the 10 point sources. Figure a) contains results from the 24-electrode array, and figure b) has results from the 40-electrode array.

It can be clearly seen from the standard deviation profiles that there are large differences between some of the acquisition methods. In all cases the *Flat-Grid* electrode arrangement exhibits more sensitivity to tumour position than the other methods. For 24-electrode arrays, the *3D-Rings* method has the minimum spatial variance (2%), especially when the breast is more compressed. With 40-electrode arrays, the *3D-Rings* and *Curved-Grid* methods are almost indistinguishable in their spatial variance which varies between 2% and 4% across the range of breast sizes. It is

interesting that the addition of more electrodes has the effect of slightly increasing the spatial variance of the *3D-Rings* method, particularly when the breast is compressed. For the *2D-Ring* method, the spatial variance is at its best (~4%) when the breast is more compressed.

6.5.2 Sensitivity to breast shape

The sensitivity of each method to breast shape is an important factor since there are a wide range of breast shapes and sizes between women. Whilst the breast's ability to mould into different shapes can be exploited to a certain extent if it is found to help improve the resolution, an ideal EIM system would be impartial to breast shape. To measure this effect it is convenient to plot the mean of all the resolution profiles and to calculate their slopes as shown in figure 6.18. From the graphs it can be clearly seen that all methods except the *2D-Ring* method have a negative slope. (The gradient values are displayed in the legend box). This means that for the *2D-Ring* method, the best overall resolution is achieved when the breast is allowed to hang as far as possible from the chest wall, whereas all other methods favour a compressed breast. The *Flat-Grid* electrode method presents the largest sensitivity to breast shape (slopes = -1.87, -1.92, -2.11 for 24 electrodes and -1.88, -2.35, -2.53 for 40 electrodes). The *3D-Rings* and *Curved-Grid* methods offer similar performance to one another, especially when using 40 electrodes. It can be seen from a comparison of figures 6.18 a) and b) that the addition of more electrodes improves the mean sensitivity of the *3D-Rings* and *Curved-Grid* methods from ~17-20% down to ~15-18%.

6.5.3 Sensitivity to noise

Each of the resolution profile measurements shown in figures 6.7 to 6.16 are as a result of pure data with no added noise. However, the same profile measurements were also carried out using simulated noise at RMS amplitudes of 1, 3 and 5μV in order to evaluate the sensitivity of each method to noise. For this the chosen procedure is to subtract *pure-data* images from the *noisy-data* images to produce *pure-noise* images, and to calculate the standard deviation of the pixel intensities (see section 4.3.2). For any given data collection method and noise level there are 100 noise measurements (arising from 10 breast shapes and 10 point source locations), thus calculating the mean of these values produces a figure which should be representative of the overall

noise sensitivity for that data collection method. The final values obtained are therefore three noise figures for simulated noise of 1,3 and 5μV respectively. These are summarised in the charts shown in figure 6.19.

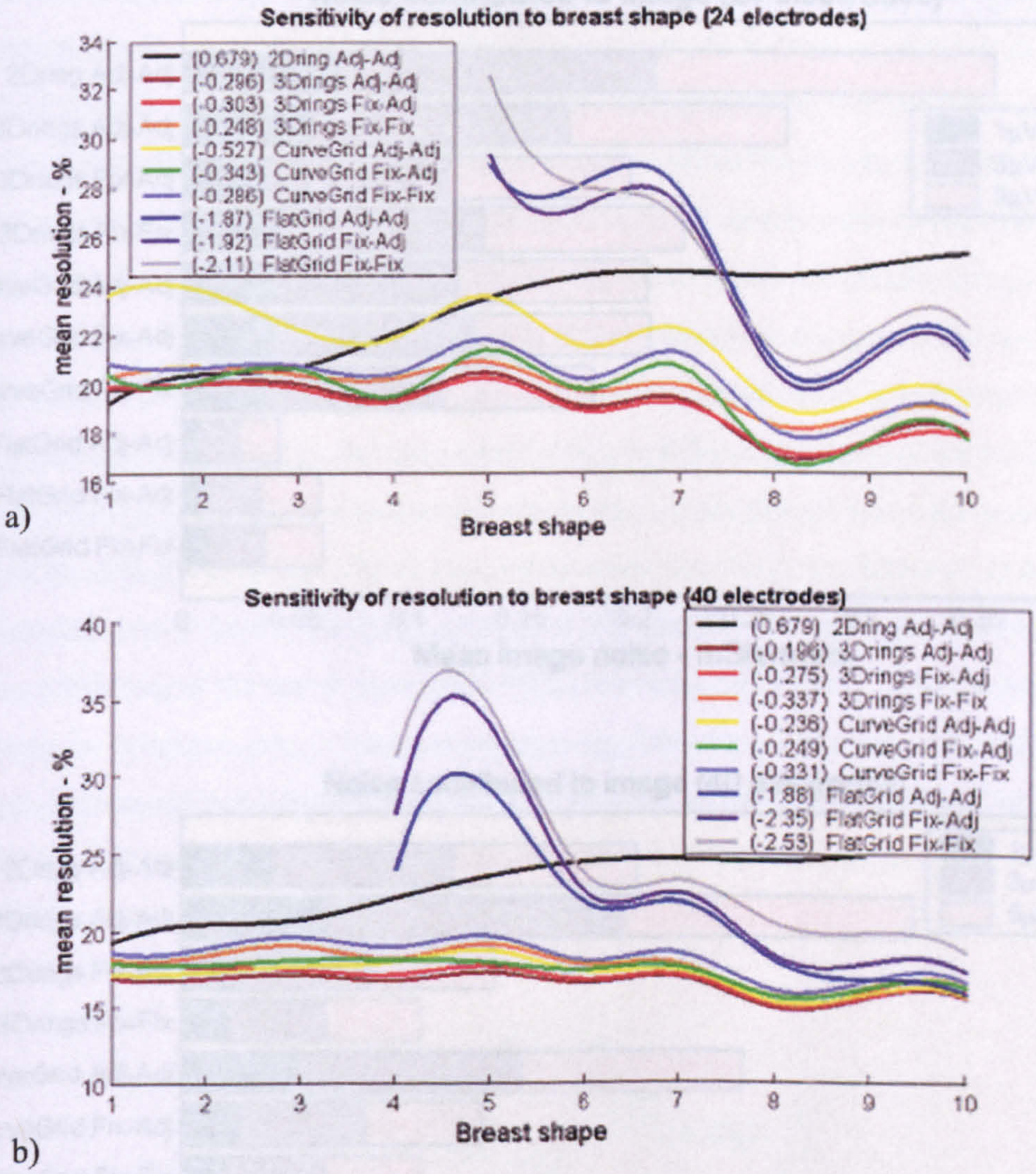

Figure 6.18 – Profiles indicating how the mean resolution for each of the 10 tumour positions varies with breast shape. The gradient of the profiles (shown in the legends) provides an indication of the variation with (and hence sensitivity to) breast shape. Figure a) corresponds with the 24-electrode arrays and figure b) with the 40 electrode arrays.

The first point of interest is that for the 40-electrode arrays, the noise sensitivity values are roughly twice those of the 24-electrode arrays. It is possible that the extra measurements achieved as a result of using more electrodes means that extra noise is

added into the overall image formation process (a feature also observed for the 2D simulations).

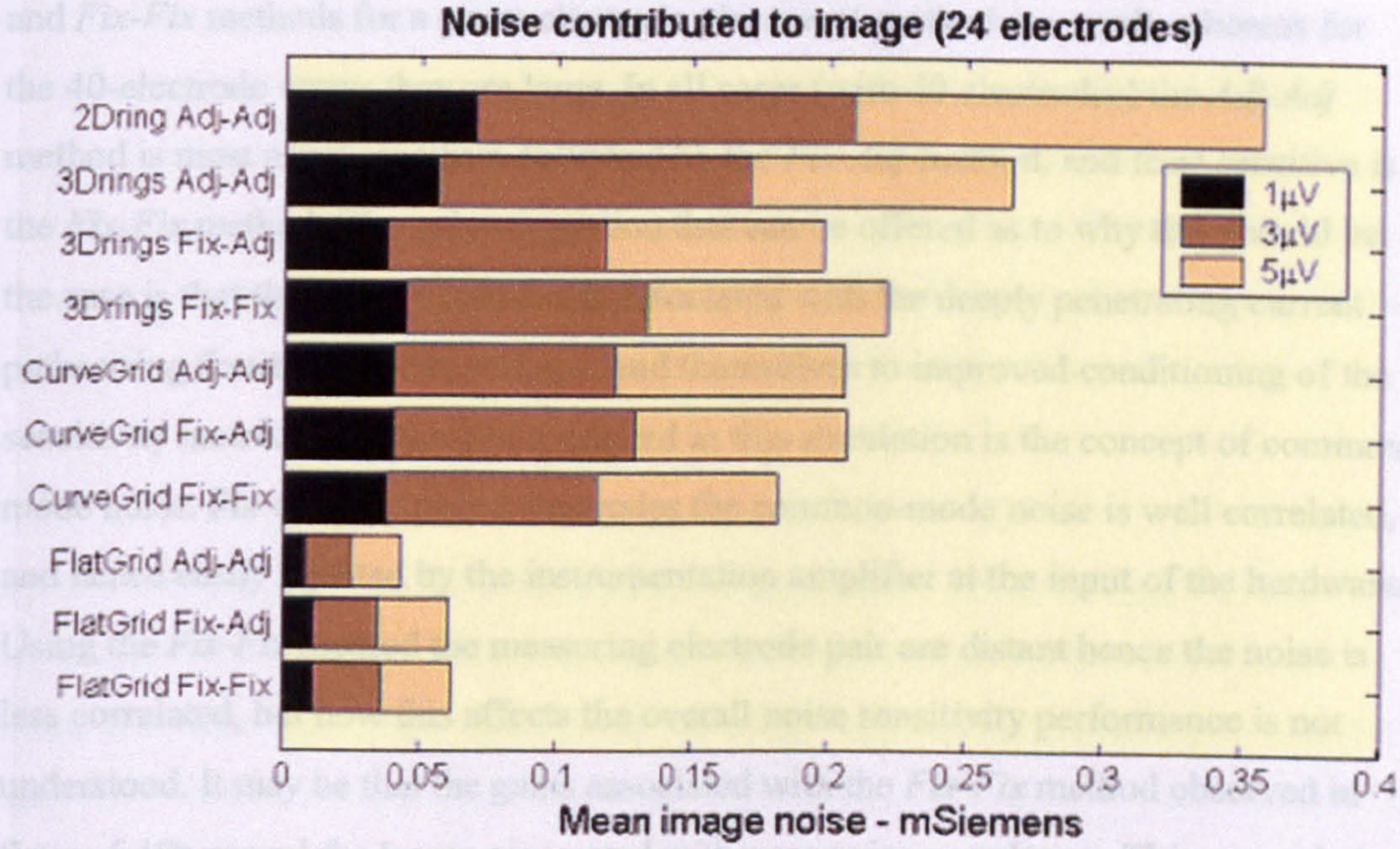

a)

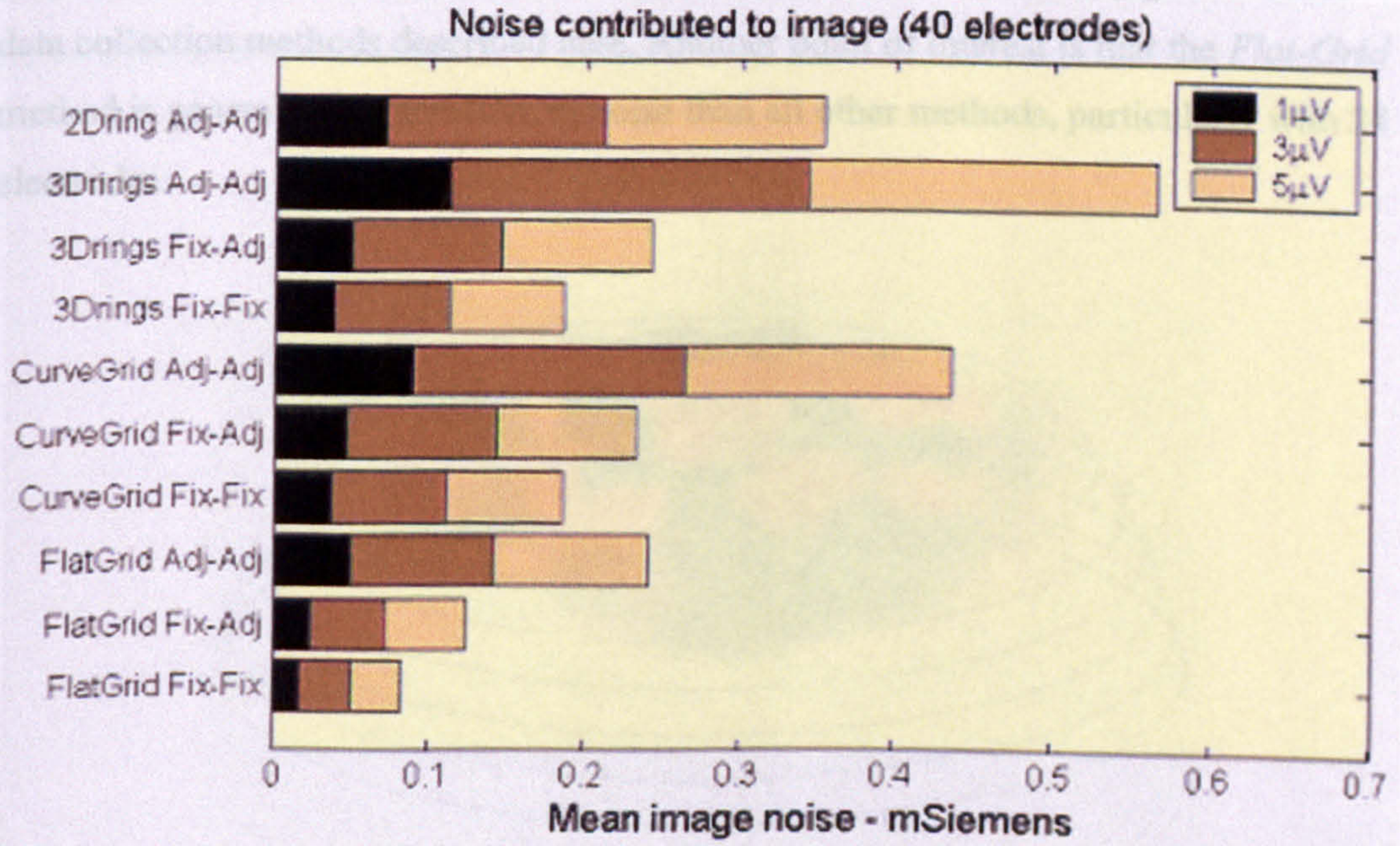

b)

Figure 6.19 – Graphical representation of the mean variation in image noise (measured in milli-Siemens) as a function of the amount of absolute noise present in the measured data. The results are grouped by measurement strategy. Figure a) refers to 24 electrode arrays and figure b) refers to 40-electrode arrays.

Now turning to the individual data collection methods, a striking observation is that for 24-electrode arrays, the differences in noise sensitivity between the *Adj-Adj*, *Fix-Adj* and *Fix-Fix* methods for a given electrode placement method are small, whereas for the 40-electrode arrays they are large. In all cases (with 40 electrodes) the *Adj-Adj* method is most noise sensitive, followed by the *Fix-Adj* method, and least sensitive is the *Fix-Fix* method. The only suggestion that can be offered as to why this should be the case is that the voltage lead fields associated with the deeply penetrating current paths using fixed electrodes perhaps lend themselves to improved conditioning of the sensitivity matrix. A feature not modelled in this simulation is the concept of common-mode noise. For closely spaced electrodes the common-mode noise is well correlated, and hence easily rejected by the instrumentation amplifier at the input of the hardware. Using the *Fix-Fix* method the measuring electrode pair are distant hence the noise is less correlated, but how this affects the overall noise sensitivity performance is not understood. It may be that the gains associated with the *Fix-Fix* method observed in figure 6.19b cancel the losses associated with poor noise correlation. This can only be properly investigated using a hardware system capable of implementing the various data collection methods described here. Another point of interest is that the *Flat-Grid* method is generally less sensitive to noise than all other methods, particularly with 24 electrodes.

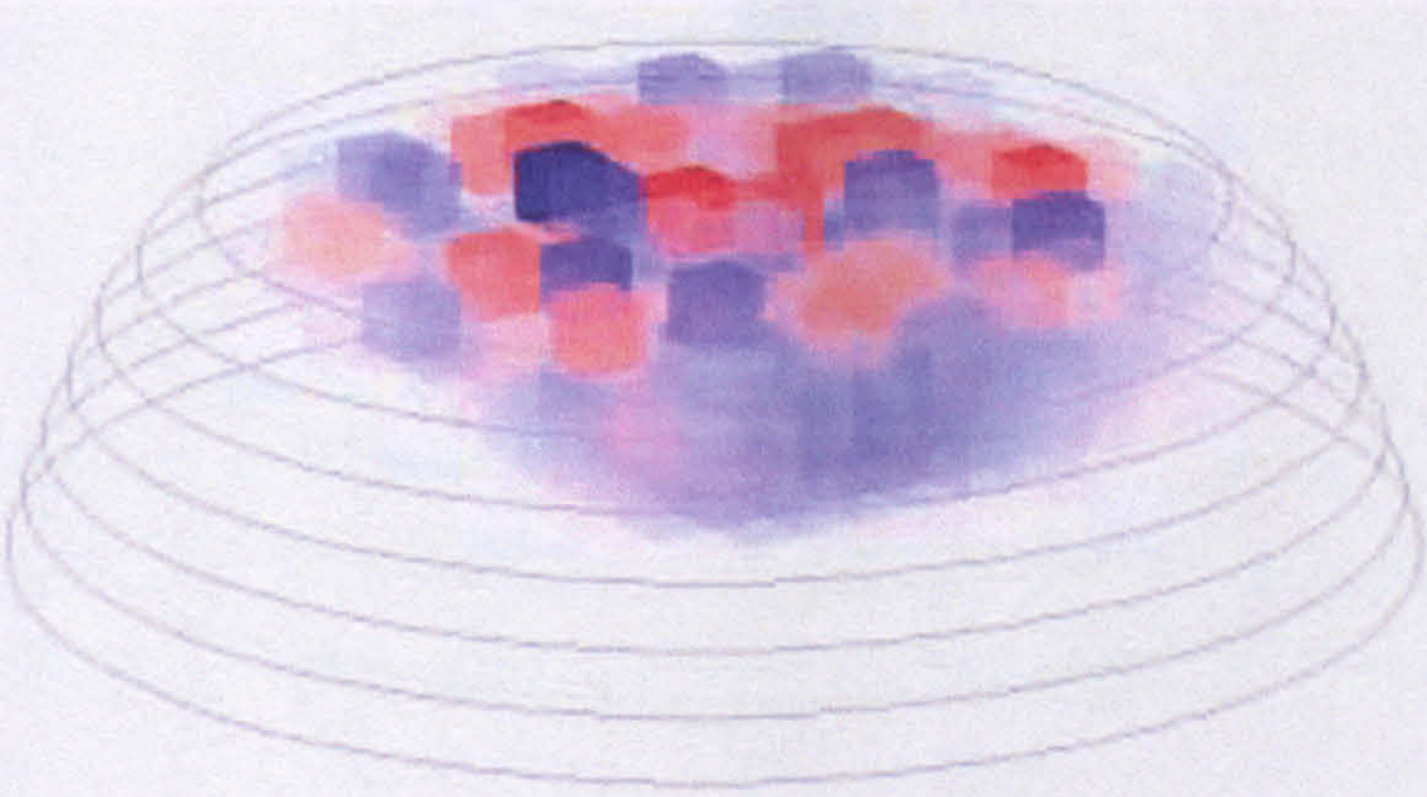

Figure 6.20 – An example of an image reconstructed using the 24 electrode *Flat-Grid* Adj-Adj with no noise. The point source is at position 3 and the breast shape is number 6. Since point source number 3 is located on the base of the model (roughly ¾ along the radius), the speckled voxels at the top of the image can only come from noise within the reconstruction process.

On closer inspection of the actual images formed it has been found that many of the images from the *Flat-Grid* array are in fact inherently noisy even when there is no noise added to the measured data (figure 6.20). This is particularly true for the less compressed breast shapes and is thought to be due to having only a few electrodes in contact with the breast under these conditions. This would explain how the large values of resolution are obtained even for zero added noise. It is still not clear why the noise sensitivity of the *Flat-Grid* method is notably less than the other methods, but its generally poor image quality offsets any gains made in noise robustness.

6.5.4 Overall image performance

From a comparison of all the results the *2D-Ring* method clearly struggles to offer a competitive contribution to breast imaging. One of its limitations is that the breast shape for which it performs best in terms of image resolution (i.e. pendant) is also the shape for which it performs worst in terms of its sensitivity to tumour position. One of the reasons for this is that the vertical resolution of the *2D-Ring* method is very poor (see figure 6.21), presumably because the arrangement of the electrode drive and receive pairs (and hence spatial information) excludes the vertical direction.

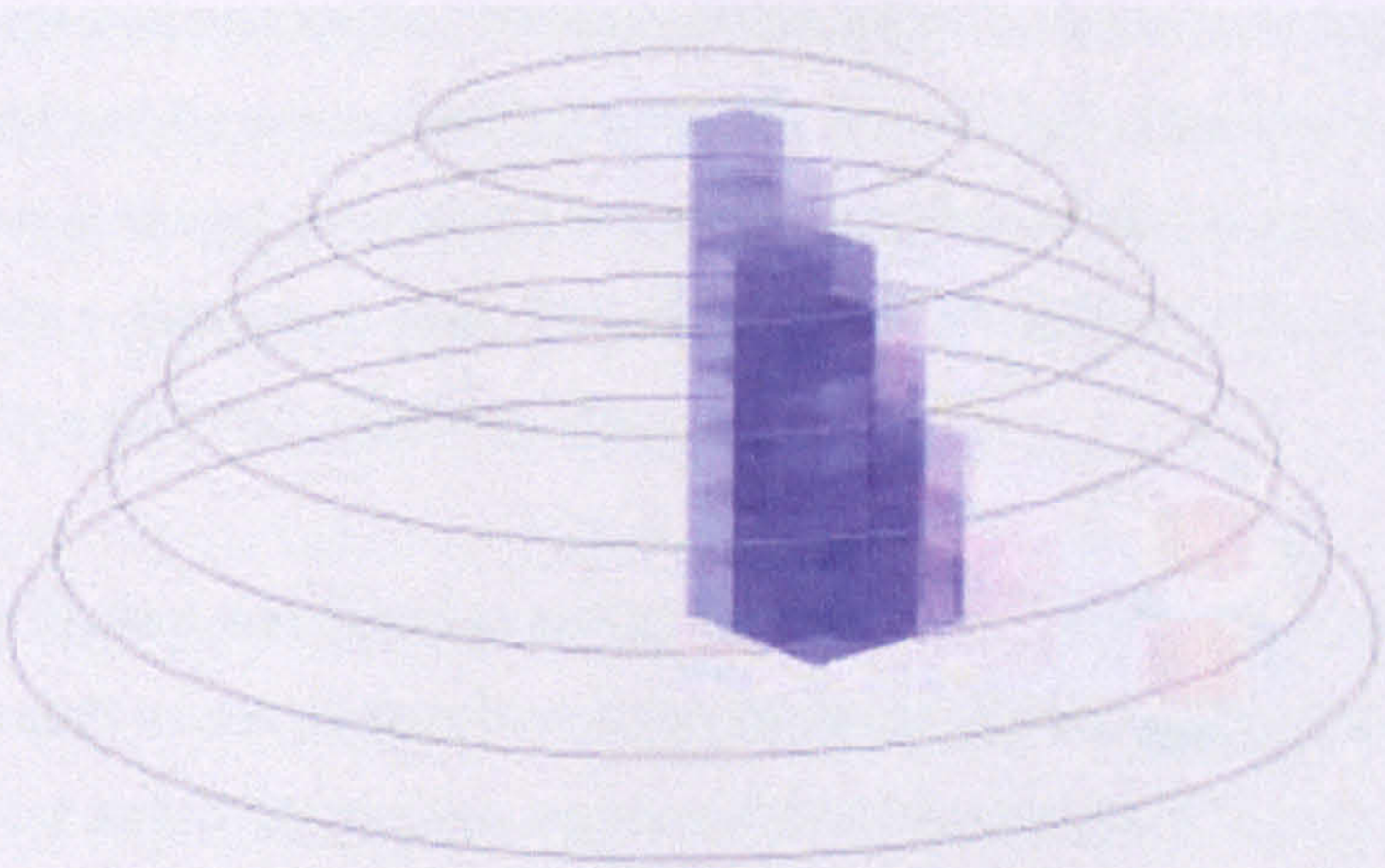

Figure 6.21 – An image reconstructed using the 32 electrode *2D-Ring Adj-Adj* method with zero noise. The breast shape is number 2 and the point source is at position 2 which is located on the base of the breast model. The PSF shows reasonable transaxial resolution but very poor vertical resolving power.

Of the 3D electrode placement methods the *Flat-Grid* is the worst since it only really performs well when the breast is pressed as flat as possible, but even under these conditions it is still more affected by point source location than the *3D-Rings* and *Curved-Grid* methods (see figure 6.17). The *3D-Rings* and *Curved-Grid* methods have been found superior in all respects except for noise performance. There is little quantifiable difference between their reconstructed images. Since they are both based on treating the breast volume as a whole and not assuming the breast should take on one particular shape it is reasonable to conclude that this is why they emerge as being better.

CHAPTER SEVEN

CONCLUSIONS AND RECOMMENDATIONS FOR FURTHER RESEARCH

7.1 Introduction

In this final chapter, all of the conclusions from both the 2D and 3D simulations are presented. The chapter closes with a list of recommendations for further research.

7.2 Conclusions

7.2.1 Placement of electrodes

Four different electrode placement strategies have been investigated in this work, two of which are already reported in literature (*2D-Ring* and *Flat-Grid*) and two of which are original (*3D-Rings* and *Curved-Grid*). It has been found that they exert a strong influence on the image quality, and therefore electrode placement must be regarded as an important factor in the design of an EIM system.

The *2D-Ring* method was applied throughout the entire 2-dimensional simulation but was also considered for use in building up layers to form 3-dimensional images. Since injected current is always constrained to a single x-y plane with this method, the resolution in the z-direction is poor. This effect manifests itself as PSFs that are elongated in the z-direction (figure 6.21).

The *Flat-Grid* method was found to perform poorly in all but the most compressed breasts. This result was expected since it was designed for use with a flattened imaging target. The noise sensitivity analysis suggested that this method offers good noise robustness, but this was considered to be offset by the generally poor resolution values and intolerance to different breast shapes. From a mechanical point of view this method is the easiest to implement. However, even when simulated with very compressed breasts, the resolution performance is still inferior to other electrode placement strategies.

The newly proposed *3D-Ring* and *Curved-Grid* methods were both designed to offer a more flexible interface with different breast shapes. Their resolution performance was found to be similar when compared against one another, but alongside the *2D-Ring* and *Flat-Grid* methods they offer superior resolution performance in both their sensitivity to breast shape and tumour position. From a practical point of view, the *Curved-Grid* method involves greater mechanical complexity since each individual electrode must be allowed to translate in the *z*-direction, whereas the *3D-Rings* method groups the electrodes in such a way that all the electrodes on each ring can translate together, thus reducing the mechanical complexity.

An area in which these two methods may not be optimised is for extremely large breasts where the electrode spacing in the *z*-direction could become significantly larger than the spacing in the *x-y* plane, thus preventing even electrode spacing. The only way to overcome this would be to allow the electrodes to move in all three dimensions such as would be achieved if all the electrodes were attached on a thin sheet of rubber that was stretched around the breast. In this case, however, it would be very difficult to know the precise locations of all the electrodes, leading to a possible source of errors in the reconstruction process.

7.2.2 Number of electrodes

The issue of electrode quantity was dealt with more thoroughly for 2-dimensional imaging, for which it was found that whilst increasing the number of electrodes can produce slight improvements in image quality, the added circuit complexity which would be required does not justify it. In 3-dimensional imaging using Flat-Grid, 3D-Rings and Curved-Grid electrode positions, only two different electrode quantities were assessed, namely 24-electrode systems and 40-electrode systems. For the *2D-Ring* method, 32 electrodes were used throughout. Using the *Flat-Grid* method, no change in mean resolution was observed, however, for the *3D-Rings* and *Curved-Grid* arrays, use of 40 electrodes gave rise to a 3% improvement in resolution over 24 electrodes. It is not possible to determine an optimum number of electrodes from these results since simulations involving a number of different array sizes would be required. However, based on the conclusion that 16 electrode arrays as applied to 2D imaging provide adequate images, it can be suggested that a similar electrode spacing applied

evenly over the three dimensions of the breast (i.e. ~2cm for a 10cm diameter breast) could provide a realistic guideline to the useful maximum number of electrodes.

7.2.3 Breast shape

The development of the 3-dimensional breast model has allowed for an interesting and original insight into the effects of breast shape on EIM. It was found that the optimum shape depends on the electrode placement method used. For the *2D-Ring* method the breast should be allowed to hang away from the body (i.e. pendant) but for the *Flat-Grid* electrode array the breast must be pressed as flat as possible against the chest wall. For the *Curved-Grid* and *3D-Rings* electrode placement methods, the breast shape has very little effect, but their performance is slightly better when the breast is flattened. It can therefore be concluded that whilst breast shape can affect resolution, it is possible to minimise the effect if the electrode placement strategy is carefully designed.

7.2.4 Current drive patterns

For 2-dimensional imaging, the current patterns were found to have a strong influence on the image resolution and noise sensitivity, with the *Adjacent* and *Cross* methods generally performing significantly better than the *Polar* method. For 3-dimensional imaging the issue of drive current patterns was divided into either *Adjacent drive* where the electrode separation is never more than one electrode spacing, or *Fixed drive* where one of the electrodes is always placed on the patient's wrist and the other chosen from any of the breast electrodes. No significant difference in resolution performance was found between the two methods, but the noise sensitivity is improved when using the *Fixed drive* technique with the larger electrode arrays. This is an important result as the *Fixed drive* method requires only one multiplexer, thus offering a simplification in circuitry over the two multiplexers required by the *Adjacent drive* method.

7.2.5 Voltage measurement patterns

For 2-dimensional imaging three different voltage measuring patterns were investigated, namely *standard, interleaved* and the newly proposed *interpolated* method. The *interleaved receive* method was found to improve the image resolution in most cases compared with the *standard receive* technique, but the downside is that in

all cases the images become much more susceptible to corruption by system noise. The *interpolated receive* technique was found to offer a slight improvement in resolution performance whilst maintaining similar levels of noise robustness, however, the improvement in resolution is not significant enough to justify the added circuit complexity of multiplexing out to the additional electrodes.

For 3-dimensional imaging, two different measurement strategies were investigated; namely *Adjacent* and *Fixed*. There is no marked difference in image resolution between them, although for the 40-electrode array the noise robustness is slightly improved for the *3D-Rings* and *Flat-Grid* method with the *Fixed* receive technique. This suggests that the measuring circuitry can be simplified by fixing one electrode, thus only requiring one multiplexer. An effect that was not simulated, however, was that of common mode noise cancellation. For the *Adjacent* receive patterns, the measuring electrodes are close together with the result that common mode noise is well correlated and can therefore be easily removed if the input stage of the preamplifier has a good common-mode rejection ratio. For the *Fixed* receive however, common mode noise may not be so well correlated due to the large distance between the breast and the wrist. It may be possible to reduce this effect slightly by placing fixed electrodes on the back of the patient in line with each breast, but this could introduce other problems as a result of the shoulder blades and ribs interfering with the current paths. The concept of fixed electrode measurements therefore needs further investigation to provide a more comprehensive answer as to whether it is useful to EIM.

7.2.6 Resolution measurement methods

The methods used for measuring resolution are the *square root relative area* of the PSF for 2-dimensional imaging, and the *cube root relative volume* of the PSF for 3-dimensional imaging. These were found to be reliable and allow a degree of comparison between two- and three-dimensional images.

The concept of quantifying the spatial variance of resolution is entirely original, and was introduced in order to arrive at a more comprehensive measure of resolution performance in impedance imaging. Three different approaches have been explored.

For 2-dimensional imaging, two different models of the spatial behaviour of resolution were assessed, (the *r-squared* and *quadratic* models), from which a spatial variance parameter can be calculated. The *r-squared* method was found to be superior in terms of accurately representing the central resolution and spatial variance. However, in the course of analysing them it was discovered that simply calculating the standard deviation of a representative sample of resolution values produces an equally useful measure of spatial variance. This third approach has also been applied to 3-dimensional images with great success. The standard deviation technique is therefore considered valuable, since it is appropriate both for 2- and 3-dimensional imaging and does not rely on any particular model of the spatial variance in order to produce a valid result.

7.3 Recommendations for further work

7.3.1 Design of a 3D Finite Element Model of the breast

The forward solver and image reconstruction algorithm for the 3D breast model is based on a crude model of the behaviour of voltage fields in a uniform semi-infinite conducting medium. A much better solution is to use the Finite Element Method since it allows modelling of bounded solids for which the conductivity distribution (or better still admittivity) can be specified explicitly. In addition it allows for modelling of surface effects such as current shunting and electrode-to-skin modelling. The problem encountered in this work is that the breast shape is required to be deformable whilst the electrode positions are to be defined by the various electrode placement techniques. As a consequence the algorithm for generating the mesh needs to allow some of the surface nodes to be forced into defined positions. The ideal solution is to develop some dedicated FEM software which models both the mechanical and electrical properties of the breast, since this allows accurate modelling of the breast shape under various amounts of compression as well as the conductivity distribution of the breast tissues.

7.3.2 Development of image reconstruction based on 3D breast model

If a comprehensive breast model is developed as described above, then the next logical step is to form an image reconstruction algorithm based on it. An additional requirement is to develop a convenient method for displaying the 3D images based on

the preferences of clinicians working in mammography. This would serve to steer EIM towards a commercially viable position.

7.3.3 FEM Simulation of optimal current patterns with 3D breast model

The current-drive methods investigated in this study are all bipolar in that they have one source and one sink electrode. It has been shown by Isaacson *et al*, (1986) that the best current patterns in terms of distinguishability of small conducting regions involve using multiple currents applied to all available electrodes simultaneously. There are considerable costs involved in designing and building circuitry capable of achieving this, hence it would be particularly useful to simulate the resolution performance in order to decide whether the benefits justify the electronics required.

7.3.4 Design of an adaptable '3D rings' patient interface

It is found in this study that the *3D-Rings* electrode placement method offers superior resolution performance in that it copes well with different breast shapes and is not dependent on the tumour position. A practical realisation of this design is therefore very desirable. This requires the positions in the *z*-direction of each ring to be recorded so that they can be passed on to the image reconstruction algorithm. An initial suggestion is to mount the rings on springs so that they can mould themselves naturally around the breast, then to employ linear encoders to record the *z*-coordinates of each ring.

REFERENCES

1. Adler A and Guardo R 1996 Electrical impedance tomography: regularized imaging and contrast detection *IEEE Transactions on Biomedical Imaging* **15** 170-179

2. Assenheimer M, Laver-Moskovitz O, Malonek D, Manor D, Nahaliel U, Nitzan R and Saad A 2001 The T-SCAN^{TM} technology: electrical impedance as a diagnostic tool for breast cancer detection *Physiological Measurement* **22** 1-8

3. Avis N J 1993 Image reconstruction in electrical impedance tomography *PhD Thesis, Dept. Medical Physics and Clinical Engineering, University of Sheffield.*

4. Avis N J and Barber D C 1994 Image reconstruction using non-adjacent drive configurations *Physiological Measurement* **15** A153-A160

5. Barber D C, Brown B H and Freeston I L 1983 Imaging spatial distributions of resistivity using applied potential tomography *Electronics Letters* **19** 933-935

6. Brown B H and Seagar A D 1985 Applied Potential Tomography – data collection problems *Proc. IEE Conf. Electric Magn. Fields Med. B Applied Potential Tomography* 79-82

7. BS5724, British Standards 5724

8. Cancer Research UK, 2002 Breast cancer factsheet

9. Cherepenin V, Karpov A, Korjenevsky A, Kornienko V, Mazaletskaya A, Mazourov D and Meister D 2001 A 3D electrical impedance tomography (EIT) system for breast cancer detection *Physiological Measurement* **22** 9-18

10. Cheyney M and Isaacson D 1995 Issues in Electrical Impedance Imaging *IEEE Computational Science and Engineering* **2** 53-62

11. Cole K S 1940 Permeability and impermeability of cell membranes for ions *Cold Spring Harbor Symp. Quant. Biol.* **8** 110-22

12. Cole K S and Cole R H 1941 Dispersion and absorption in dielectrics. I. Alternating current characteristics *J. Chem Phys* **9** 341-51

13. Cook R D, Sauliner G J, Gisser D G, Goble J C, Newell J C and Isaacson D 1994 ACT3: A high-speed, high-precision electrical impedance tomograph *IEEE Transactions on Biomedical Engineering* **41(8)** 713-722

14. Cutrone J A, Khalkhali I, Yospur L S, Diggles L, Weinburg I, Pong E M, Tolmos J, Vargas M P and Vargas H I 1999 Tc-99m Setstamibi scintimammography for the evaluation of breast masses in patients with radiographically dense breasts *The Breast Journal* **5(6)** 383-388

15. De Wolf D A 2001 Essentials of electromagnetics for engineering, *Cambridge University Press*

16. Dobson D C and Santosa F 1994 An image-enhancement technique for electrical impedance tomography *Inverse Problems* **10** 317-334

17. Durfee S M, Selland D G, Smith D N, Lester S C, Kaelin C M and Meyer J E 2000 Sonographic evaluation of clinically palpable breast cancers invisible on mammography *The Breast Journal* **6(4)** 247-251

18. Editorial 1999 Breast MRI: ready for general use? *The Breast Journal* **5(4)** 219-220

19. Entrekin R, Jackson P, Lago J R and Porter B A 1999 Real time spatial compound imaging in breast ultrasound: technology and early clinical experience *Medicamundi* **43(3)** 35-43

20. FDA 1999, *Food and Drug Administration*, FDA Approval P970033

21. Geddes L A and Baker L E 1967 The specific resistance of biological material – a compendium of data for the biomedical engineer and physiologist *Medical and Biological Engineering* **5** 271-93

22. Geselowitz D B 1971 An application of electrocardiographic lead theory to impedance plethysmography *IEEE Transactions on Biomedical Engineering* **18(1)** 38-41

23. Gibson A, Eadie L, Bayford R H, Holder D S 2001 Optimum four terminal impedance measurements from the surface of a sphere *Scientific Abstracts, 3rd EPSRC Engineering Network Meeting, Biomedical Applications of EIT*

24. Griffiths H 1995 A Cole phantom for EIT *Physiological Measurement* **16** A29-A38

25. Hartov A, Mazzarese R A, Reiss F R, Kerner T E, Ostermann K S, Williams D B and Paulsen K D 2000 A multichannel continuously selectable multifrequency electrical impedance spectroscopy measurement system *IEEE Transactions on Biomedical Engineering* **47(1)** 49-58

26. Hua P, Webster J G and Tompkins W J 1987 Effect of the measurement method on noise handling and image quality of EIT imaging *Proceedings of the Ninth Annual Internation IEEE Conference of the Engineering in Medicine and Biology Society* **9** 1429-1430

27. Hua P, Woo E J, Webster J G and Tompkins W J 1991 Iterative reconstruction methods using regularization and optimal current patterns in electrical impedance Tomography *IEEE Transactions on medical imaging* **10(4)** 621-628

28. Isaacson D 1986 Distinguishability of conductivities by electric current computed tomography *IEEE Transactions on Medical Imaging* **MI-5** 92-95

29. Joshi M, Duva-Frissora A, Padmanabhan R, Greeley J, Ranjan A, Ferrucci F, Kwon J and Khettry U 2001 Atypical ductal hyperplasia in stereotactic breast biopsies: enhanced accuracy of diagnosis with the mammotome *The Breast Journal* **7(4)** 207-213

30. Kerner T, Hartov A, Soho S, Poplack S and Paulsen K 2001a Using Electrical Impedance Spectroscopy to image human breast: practical considerations which influence exam consistency *Scientific Abstracts, 3rd EPSRC Engineering Network Meeting, Biomedical Applications of EIT*

31. Kerner T E, Hartov A, Osterman K S, DeLorenzo C and Paulsen K D 2001b An improved data acquisition method for electrical impedance tomography *Physiological Measurement* **22** 31-38

32. Kerner T E, Hartov A, Soho S K, Poplack S P and Paulsen K D 2002 Imaging the breast with EIS: an initial study of exam consistency *Physiological Measurement* **23** 221-236

33. Kim Y, Webster J G and Tompkins W J 1983 Electrical Impedance imaging of the thorax *Journal of Microwave Power* **18(3)** 245-257

34. Kleinermann F, Avis N J, Judah S K and Barber D C 1996 Three-dimensional image reconstruction for electrical impedance tomography *Physiological Measurement* **17** A77-A83

35. Korjenevsky A V, Cherepenin V A, Karpov A Yu, Kornienko V N and Kultiasov Yu S 2001 An Electrical Impedance Tomography system for 3-D breast tissues imaging *Proc. XIth Int. Conf. on Electrical Bio-Impedance* 403-407

36. Kotre C J 1994 EIT image reconstruction using sensitivity weighted filtered back projection *Physiological Measurement* **15** A125-A136

37. Kotre C J 1996 Subsurface electrical impedance imaging: measurement strategy, image reconstruction and *in vivo* results *Physiological Measurement* **17** A197-A204

38. Malur S, Wurdinger S, Moritz A, Michels W and Schneider A 2001 Comparison of written reports of mammography, sonography and magnetic resonance mammography for preoperative evaluation of breast lesions, with special emphasis on magnetic resonance mammography *Breast Cancer Research* **3** 55-60

39. Metherall P, Barber D C, Smallwood R H and Brown B H 1996 Three-dimensional electrical impedance tomography *Nature* **780** 509-512

40. Metherall P 1998 Three dimensional electrical impedance tomography of the human thorax *PhD thesis, University of Sheffield, UK*

41. Moore K L 1992 Clinically Oriented Anatomy (3rd Ed) *Lippincott, Williams and Wilkins* ISBN: 0-683-06133-X

42. Moffat D B 1993 Lecture Notes on Anatomy (2nd Ed) *Blackwell Scientific Publications* ISBN: 0-632-03696-6

43. Mueller J L, Isaacson D and Newell J C 1999 A reconstruction algorithm for electrical impedance tomography data collected on rectangular electrode arrays *IEEE Transactions on Biomedical Engineering* **46(11)** 1379-1386

44. Murai T and Kagawa Y 1985 Electrical Impedance Computed Tomography based on a Finite Element Model *IEEE Transactions on Biomedical Engineering* **32(3)** 177-184

45. Newell J C, Blue R S, Isaacson D, Sauliner G J and Ross A S 2001 Phasic three-dimensional impedance imaging of cardiac activity *Scientific Abstracts, 3rd EPSRC Engineering Network Meeting, Biomedical Applications of EIT*

46. Osterman K S, Kerner T E, Williams D B, Hartov A, Poplack S P and Paulsen K D 2000 Multifrequency electrical impedance imaging: preliminary in vivo experience in breast *Physiological Measurement* **21** 99-109

47. Pappo I, Horne T, Weissburg D, Wasserman I and Orda R 2000 The usefulness of MIBI scanning to detect underlying carcinoma in women with acute mastitis *The Breast Journal* **6(2)** 126-129

48. Powell H M, Barber D C and Freeston I L 1987 Impedance imaging using linear electrode arrays *Clinical Physics and Physiological Measurement* **8 Suppl. A** 109-118

49. Rigaud B, Hamzaoui L, Frikha M R, Chauveau N and Morucci J-P 1995 In vitro tissue characterization and modelling using electrical impedance measurements in the 100 Hz-10 MHz frequency range *Physiological Measurement* **16** A15-A28

50. Smith R W M, Freeston I L and Brown B H 1995 A real-time electrical impedance tomography system for clinical use – design and preliminary results *IEEE Transactions on Biomedical Engineering* **42(2)** 133-140

51. (SEER) Surveillance, Epidemiology and End Results Program 1995-1997 *National Cancer Institute*

52. Surowiec A J, Stuchly S S, Barr J R and Swarup A 1988 Dielectric properties of breast carcinoma and the surrounding tissues *IEEE Transactions on Biomedical Engineering* **35(4)** 257-263

53. Tartter P I, Weiss S, Ahmed S, Kamath S, Hermann G and Drossman S 1999 Mammographically occult breast cancers *The Breast Journal* **5(1)** 22-25

54. Tortora G J and Grabowski S R 1993 Principles of Anatomy and Physiology (7^{th} Ed) *Harper Collins* ISBN: 0-060-46702-9

55. Trokhanova O, Karpov A, Cherepenin V, Korjenevsky A, Kornienko V, Kultyasov Y and Marushkov V 2001 Electro-impedance mammography testing at some physiological woman's periods *Scientific Abstracts, 3rd EPSRC Engineering Network Meeting, Biomedical Applications of EIT*

56. Tsourlos P I and Ogilvy R D 1999 An algorithm for the 3-D inversion of tomographic resistivity and induced polarisation data: Preliminary results *Journal of the Balkan Geophysical Society* **2(2)** 30-45

57. Tunstall B G 2000 An investigation into the use and limitations of electrical impedance mammography as a clinical diagnostic tool *PhD Thesis, De Montfort University, Leicester, UK*

58. Underwood J C E (Editor) 2000 General and Systematic Pathology 3rd ed. *Churchill Livingstone*

59. Wang W, Tunstall B, Chauhan D and McCormick M 1998 The Design of De Montfort Mk2 Electrical Impedance Mammography System *Proc. IEEE EMBS 20th Annual International Conference*

60. Wang W, Tang M, McCormick M and Dong X 2001 Preliminary results from an EIT breast imaging system *Physiological Measurement* **22** 39-48

61. Webb S (Ed) 1988 The Physics of Medical Imaging *Institute of Physics Publishing* ISBN 0-85274-349-1

62. Wexler A, Fry B and Neuman M R 1985 Impedance Computed Tomography algorithm and systems *Applied Optics* **24** 3985-3992

63. Wheeler J L 1996 Linear electrode array for impedance imaging of bone fractures *M.Sc. Thesis, Dept. of Bio-medical Physics and Bio-engineering, University of Aberdeen, UK*

64. Wheeler J L, Wang W and Tang M 2002 A comparison of methods for measurement of spatial resolution in two-dimensional circular EIT images *Physiological Measurement* **23** 169-176

65. Woo E J, Hua P, Webster J G and Tompkins W J 1993 A robust image reconstruction algorithm and its parallel implementation in electrical impedance tomography *IEEE Transactions on Medical Imaging* **12** 137-46

66. Yorkey T J, Webster J G and Tompkins W J 1987 Comparing reconstruction algorithms for electrical impedance tomography *IEEE Transactions on Biomedical Engineering* **34(11)** 843-852

APPENDIX A – LISTING OF THE 2D FORWARD SOLVER SOFTWARE

The two programs listed here contain the code used for solving the 2-dimensional forward problem based on a Finite Element Method approach. The first program, *FEM.m* is written in MATLAB script language and the second, *forward.c* is a C++ routine, compiled as a '.dll' file to run in the MATLAB environment.

```
% ------------- Finite Element Solver ------------------
%
% Function for interfacing with the 'forward.c' routine for
% the purposes of solving the forward voltages for a given
% mesh and drive/receive pattern. There are 4 valid methods
% of calling this function:
%
% 1 - V_out = FEM()
% 2 - V_out = FEM('mesh_name','IV_name')
% 3 - V_out = FEM(Z_el,element_nodes,nodes_XY)
% 4 - V_out = FEM(Z_el,element_nodes,nodes_XY,'IV_name')


function [Vprofile] = FEM(arg1,arg2,arg3,arg4)

global RootDir                                          % import the global variable RootDir
                                                        % check input arguments
if nargin == 0                                          % if no arguments, need to prompt for data sources
   [fname pname] = uigetfile([RootDir '2Dsimulation\mesh_database\*.mat']); % get mesh filename
   if fname, load([pname fname])                        % load mesh data
   else error('Mesh name not recognised');end
   [fname pname] = uigetfile([RootDir '2Dsimulation\IV_patterns\*.mat']);   % get data collection filename
   if fname, load([pname fname])                        % load data collection variables
         else error('IV Pattern not recognised');end
elseif nargin == 2                                      % if 2 arguments, assume mesh and data collection filenames
   load(arg1)                                           % load mesh data
   load(arg2)                                           % load data collection variables
elseif nargin == 3                                      % if 3 arguments...
   Z_el = arg1;                                         % argument 1 must be Z_el
   element_nodes = arg2;                                % argument 2 must be element_nodes
   node_XY = arg3;                                      % argument 3 must be node_XY
   [fname pname] = uigetfile([RootDir 'simulation\IV_patterns\*.mat']); % get data collection filename
   if fname, load([pname fname])                        % load data collection variables
         else error('IV Pattern not recognised');end
elseif nargin == 4                                      % if 4 arguments...
   Z_el = arg1;                                         % argument 1 must be Z_el
   element_nodes = arg2;                                % argument 2 must be element_nodes
   node_XY = arg3;                                      % argument 3 must be node_XY
   load(arg4)                                           % argument 4 must be data collection filename -> load it
else error('Wrong number of input arguments');end

no_nds = size(node_XY,1);                               % get number of nodes
no_drv = size(I,2);                                     % get number of drive positions
no_rec = size(V,2);                                     % get number of receive positions

if ~isequal(size(element_nodes,1),size(Z_el,1))         % check mesh geometry matches conductivity distribution
   error('Mesh design does not match conductivity array')
end

% Calculate number of boundary nodes from X,Y co-ordinates
radii = sqrt(node_XY(:,1).^2 + node_XY(:,2).^2);        % calculate radial positions of all nodes
max_radius = radii(no_nds);                             % get maximum radial position (i.e. radius of mesh)
bound_nds = length(find(radii < max_radius+1e-6 & radii > max_radius-1e-6));    % get number of boundary nodes
scale = 256/bound_nds;                                  % calculate factor for scaling mesh to I and V
if scale ~= round(scale), error('Boundary nodes do not fit evenly into 256');end

% Rescale voltage vector to fit mesh
Vglobal = zeros(no_nds,no_rec);                         % set global V matrix
for rec = 1:no_rec                                      % loop around receive positions
   Vglobal(no_nds-bound_nds+1 : no_nds,rec) = V(1:scale:256,rec);   % scale receive positions to 256 boundary nodes
      if sum(Vglobal(:,rec)) ~= 0                       % check for + and - positions on mesh
      error('Some of the measurement nodes are misaligned with the mesh');
   end
end

% Rescale current vector to fit mesh
Iglobal = zeros(no_nds,no_drv);                         % set global I matrix
for drv = 1:no_drv                                      % loop around all drive positions
   if sum(I(:,drv)) > 1e-16, error('Drive currents must sum to zero');end   % check drive currents sum to zero
   Iglobal(no_nds-bound_nds+1 : no_nds,drv) = I(1:scale:256,drv);     % scale drive positions to 256 boundary nodes
   if sum(Iglobal) > 1e-16                              % check currents still sum to zero
      error('Some of the input currents are misaligned with the mesh');
   end
end

forward(element_nodes,node_XY,Z_el,Iglobal)             % call the forward solver
Vprofile = reshape(Vglobal'*Iglobal,1,no_drv*no_rec);   % extract required voltages
```

```
// -------------- FORWARD --------------------
//
// MATLAB dll file for solving the forward problem based on the Finite
// Element Method. The mesh geometry, conductivity distribution and
// current source positions are supplied to the function.
//
// forward(element_nodes,node_XY,Z_el,drive_nodes)
//
// where: element_nodes = array of 3 nodes for each element
//        node_XY       = (X,Y) co-ordinates of each node
//        Z_el          = conductivitiy of each element
//        drive_nodes   = vector of drive nodes (global numbering)
//
//        Result is placed into 'drive_nodes' matrix
//
// NB, this code was adapted from an original routine supplied by MengXing Tang,
// a research student also at De Montfort University, hence comments are only
// available where the code has been modified, or where they already existed
// in the original source code.

#include "mex.h"
#include<math.h>
#include"matrix.h"
#include<stdlib.h>

void forward(double *element_nodes, double *node_XY, double *Z_el, int no_nds,
             int no_els, int no_drv, double *voltage)

{
    int md,i0,j0,i,j,e0,e1,e2, *max_length;
    double x0,y0,x1,y1,x2,y2;
    double b0,b1,b2,c0,c1,c2;
    double s,r,Resis;
    double *max_coeff,*max_coeff2,*Resist1,*Node1;
    int length;

    int ii,jj;
    int l,l1,Electrod_in,Electrod_out;
    double current, min_current, force_vol;

    int force_node;
    int iig,mi,mj,mij,igp,jjg,k,kk;

    max_length = mxMalloc(sizeof(int)*no_nds);

//                  *** Matlab calls with Nodes starting from 1, not 0! ***

    for(i=0; i<3*no_els; i++)
        element_nodes[i]=element_nodes[i]-1;

//                  *** calculate the length of the 1-dimension matrix ***

    for(i=0;i<no_nds;i++)
    {
        md=0;
        for(j=0;j<no_els;j++)
        {
            if(element_nodes[j]==i || element_nodes[j+no_els]==i || element_nodes[j+2*no_els]==i)
            {
                i0 = (int)element_nodes[j];
                if(element_nodes[j+no_els]<i0)   i0 = (int)element_nodes[j+no_els];
                if(element_nodes[j+2*no_els]<i0) i0 = (int)element_nodes[j+2*no_els];
                j0 = i-i0;
                if(j0>md) md = j0;
            }
        }
        if(i>0)  max_length[i] = max_length[i-1]+md+1;
        else  max_length[i] = 0;
        md = 0;
    }

//                  *** compose the coefficient matrix ***

    length = max_length[no_nds-1]+1;
    max_coeff  = mxMalloc(sizeof(double)*(length+1));
    max_coeff2 = mxMalloc(sizeof(double)*(length+1));

    for(i=0; i<length; i++)  max_coeff[i]=.0;

    for(i=0; i<no_els; i++)
    {
        e0 = (int)element_nodes[i];
        e1 = (int)element_nodes[i+no_els];
        e2 = (int)element_nodes[i+2*no_els];
        x0 = node_XY[e0];
        y0 = node_XY[e0+no_nds];
        x1 = node_XY[e1];
        y1 = node_XY[e1+no_nds];
        x2 = node_XY[e2];
        y2 = node_XY[e2+no_nds];
//      a0 = x1*y2-x2*y1; a1 = x2*y0-x0*y2; a2 = x0*y1-x1*y0;
        b0 = y1-y2; b1 = y2-y0; b2 = y0-y1;
        c0 = x2-x1; c1 = x0-x2; c2 = x1-x0;

        s = (b0*c1-b1*c0)/2.0;
        Resis = Z_el[i];

        // Admitivity

        r = Resis/2.0/s;

        j0 = max_length[e0];
        max_coeff[j0] = max_coeff[j0]+r*(b0*b0+c0*c0);
        j0 = max_length[e1];
        max_coeff[j0] = max_coeff[j0]+r*(b1*b1+c1*c1);
        j0 = max_length[e2];
        max_coeff[j0] = max_coeff[j0]+r*(b2*b2+c2*c2);

        if ((e0-e1)>=0) j0 = max_length[e0]-(e0-e1);
        else j0 = max_length[e1]-(e1-e0);
        max_coeff[j0] = max_coeff[j0]+r*(b0*b1+c0*c1);
```

```
        if (e0>=e2) j0 = max_length[e0]-(e0-e2);
        else j0 = max_length[e2]-(e2-e0);
        max_coeff[j0] = max_coeff[j0]+r*(b0*b2+c0*c2);
        if(e1>=e2) j0 = max_length[e1]-(e1-e2);
        else j0 = max_length[e2]-(e2-e1);
        max_coeff[j0] = max_coeff[j0]+r*(b1*b2+c1*c2);
    }

    for(i=0;i<length;i++)
        max_coeff2[i]=max_coeff[i];


//          *** form the right side and solve the equation ***

    for(l=0; l<no_drv; l++)                         // Loop around the drive pairs
    {
        min_current = 0;                            // force boundary condition....
        for(i=0; i<no_nds; i++)                     // Choose minimum-current node as 'force_node'
        {
            if (voltage[i+l*no_nds] < min_current)
            {
                min_current = voltage[i+l*no_nds];
                force_node = i;
            }
        }
        force_vol = 0;


        for(i=0; i<length; i++)
            max_coeff[i]=max_coeff2[i];
        i = force_node;
        if (i == 0)
        {
            iig = -1;
            mi=1;
        }
        else
        {
            iig = max_length[i]-i-1;
            mi  = max_length[i-1]-iig+1;
        }
        for(j=mi-1; j<=i-1; j++)
        {
            igp = iig+j+1;
            voltage[j] = voltage[j]-force_vol*max_coeff[igp];
            max_coeff[igp] = 0;
        }

        max_coeff[max_length[i]] = 1;
        voltage[i+l*no_nds] = force_vol;

        for(j=i+1; j<no_nds; j++)
        {
            jjg = max_length[j]-j-1;
            igp = i+jjg+1;
            mj  = max_length[j-1]-jjg+1;
            if (i+1 >= mj)
            {
                voltage[j+l*no_nds] = voltage[j+l*no_nds] - max_coeff[igp]*force_vol;
                max_coeff[igp] = 0;
            }
        }
        // solve the equation group

        for(i=0; i<no_nds; i++)
        {
            ii = i+l*no_nds;
            if (i != 0)
            {
                iig = max_length[i]-i-1;
                mi  = max_length[i-1]-iig+1;
            }
            else
            {
                iig = -1;
                mi  = 1;
            }
            for(j=mi-1; j<=i; j++)
            {
                jj  = j+l*no_nds;
                igp = iig+j+1;
                if (j != 0)
                {
                    jjg = max_length[j]-(j+1);
                    mj  = max_length[j-1]-jjg+1;
                }
                else
                {
                    jjg = -1;
                    mj  = 1;
                }
                mij = max(mi,mj);
                for(k=mij; k<=j; k++)
                    max_coeff[igp] = max_coeff[igp]-max_coeff[iig+k]*max_coeff[max_length[k-1]]*max_coeff[jjg+k];

                if(j<i)
                {
                    max_coeff[igp] = max_coeff[igp]/max_coeff[max_length[j]];
                    voltage[ii] = voltage[ii]-max_coeff[igp]*max_coeff[max_length[j]]*voltage[jj];
                }
                else voltage[ii] = voltage[ii]/max_coeff[max_length[i]];
            }
        }

        for(i=no_nds-1; i>=0; i--)
        {
            ii = i+l*no_nds;
            if (i != 0)
            {
                iig = max_length[i]-(i+1);
                mi  = max_length[i-1]-iig+1;
            }
            else
```

```
            {
                iig = -1;
                mi=1;
            }
            for(k=mi-1; k<=i-1; k++)
            {
                kk = k+1*no_nds;
                voltage[kk] = voltage[kk]-max_coeff[iig+k+1]*voltage[ii];
            }
        }
        i = 0;
    }

    mxFree(max_length);
    mxFree(max_coeff);
    mxFree(max_coeff2);
//        *** Restore the element_nodes() array ***
    for(i=0; i<3*no_els; i++)
        element_nodes[i]=element_nodes[i]+1;
}

// MATLAB interfacing code
void mexFunction(int nlhs, mxArray* plhs[], int nrhs, const mxArray* prhs[])
{
    double *element_nodes, *node_XY, *Z_el, *voltage;
    int    no_els, no_nds, no_drv;

    element_nodes  = mxGetPr(prhs[0]);
    node_XY        = mxGetPr(prhs[1]);
    Z_el           = mxGetPr(prhs[2]);
    Voltage        = mxGetPr(prhs[3]);

    no_els         = mxGetM(prhs[0]);
    no_nds         = mxGetM(prhs[1]);
    no_drv         = mxGetN(prhs[3]);

    forward(element_nodes,node_XY,Z_el,no_nds,no_els,no_drv,voltage);
}
```

APPENDIX B – LISTING OF THE IMAGE RECONSTRUCTION SOFTWARE

The functions listed here contain the code used for reconstructing simulated EIT images. The Finite Element Method is used to solved the forward problem using the code in Appendix A and the image reconstruction method involves inversion of the sensitivity matrix using the Generalised Matrix Inverse (GMI). The first function, *reconstruct.m* is called by the user and all subsequent functions are called by *reconstruct.m* to gather the required data. All programs are written in MATLAB script language.

```
% ------------------------- reconstruct ----------------------
%
% Reconstructs simulated EIT images based on selecting a background and
% foreground mesh along with a data collection strategy. Noise can be
% added to the simulated voltage data by supplying the absolute RMS value.
% The reconstruction algorithm is based on the sensitivity method for
% which the sensitivity matrix is inverted using the Generalised Matrix
% Inverse (GMI) using Truncated Singular Value Decomposition (TSVD). As
% such the truncation level (expressed in dB) can be supplied.
%
% Function called using:
%
% [pic] = reconstruct(Vn,tr);
%
% where     pic = reconstructed image
%            Vn = simulated noise amplitude (RMS)
%            tr = truncation level for matrix inverse (dB)

function[pic] = reconstruct(Vn,tr)
global RootDir                                  % get root directory for matlab user data
[Fname Pname] = uigetfile([RootDir '2Dsimulation\mesh_database\2048_x_128\'],'Select background mesh');
back_mesh = [Pname Fname];                      % get name of backgrouns mesh
[Fname Pname] = uigetfile(Pname,'Select foreground mesh');
fore_mesh = [Pname Fname];                      % get name of foreground mesh
[Fname Pname] = uigetfile([RootDir '2Dsimulation\IV_patterns\'],'Select data collection method');
IV_name = [Pname Fname];                        % get name of data collection method

Vback = FEM(back_mesh,IV_name);                 % simulate background voltage profile
Vfore = FEM(fore_mesh,IV_name);                 % simulate foreground voltage profile

Vback = Vback + Vn*randn(size(Vback));          % add simulated noise to background voltage profile
Vfore = Vfore + Vn*randn(size(Vfore));          % add simulated noise to foreground voltage profile

Sinv = invertSENS(back_mesh,IV_name,tr);        % get inverted sensitivity matrix
pic = (Vfore(:)-Vback(:))'*Sinv;                % reconstruct image
load(back_mesh)                                 % load background mesh to get geometry
draw_mesh(pic,0,element_nodes,node_XY)          % draw reconstructed image
```

```
% ------------------------- invertSENS -----------------------------
%
% Used for inverting the sensitivity matrix to a required truncation level.
% The required mesh and data collection strategy are supplied as a string
% containing the full path and filenames. The truncation level for the
% Generalised Matrix Inverse (GMI) is supplied as a dB level
%
% Called using:
%
% function[Sinv,ti] = invertSENS(mesh_name,IV_name,tr)
%
% Where:
%
%              Sinv = inverted sensitivity matrix
%                ti = truncation level in terms of the number of singular values used
%         mesh_name = string containing full path and filename of mesh
%           IV_name = string containing full path and filename of data collection strategy
%                tr = truncation level (in dB) for the generalised matrix inversion
%
% Note 1: if tr=0, the function searches for the first steep drop in the singular value
%         profile and uses that instead. This is not always guarenteed to work though
%
% Note 2: The invertSENS function can also be called with a single argument representing
%         the truncation level, in which case the user is prompted for the mesh and data
%         collection names.

function[Sinv,ti] = invertSENS(mesh_name,IV_name,tr)
```

```
global RootDir
if nargin < 3                       % alternative calling of function where only tr is specified
    tr = mesh_name;                 % prompts user for mesh and IV patterns
    [mesh_name mesh_path] = uigetfile([RootDir '2Dsimulation\mesh_database\*.mat']);
    if mesh_name, mesh_name = [mesh_path mesh_name];
    else error('Mesh name not recognised');end
    [IV_name IV_path] = uigetfile([RootDir '2Dsimulation\IV_patterns\*.mat']);
    if IV_name, IV_name = [IV_path IV_name];
    else error('IV Pattern not recognised');end
end


[U,S,V] = calc_svd(mesh_name,IV_name);  % get SVD matrices for specified mesh and IV pattern

sv = diag(S);                       % extract diagonal components from S matrix
sv_norm = sv/sv(1);                 % normalise the singular value profile
sv_norm = sv_norm(find(sv_norm));   % remove any zero-values from the singular value profile
sv_log = 20*log10(sv_norm);         % form the logarithmic sv profile

if tr==0
    SVgrad = diff(diff(sv_log));    % form double differential of profile of singular values
    ti = min(find(SVgrad > 3*std(SVgrad)));     % look for first sharp drop in the gradient (change > 3 standard
deviations)
else
    ti = max(find(sv_log > tr));
end

sv_tr = sv_log(ti);                 % calculate actual dB at truncation point
disp(['Truncating at ' num2str(sv_tr) ' dB     (singular value: ' int2str(ti) ')'])
if sv_tr > -20 | isempty(tr), pic = []; return; end % return empty array if truncation point is invalid

s = diag(ones(ti-1,1)./sv(1:ti-1));     % compute the truncated singular value matrix
Sinv = V(:,1:ti-1)*s*U(:,1:ti-1)';      % invert the SENS matrix from the SVD matrices



% ------------------------- calc_svd ----------------------------
%
% Used to calculate the three Singular Value Deconposition (SVD) matrices
% used for inversion of the sensitivity matrix. The function is called
% with the mesh and data collection strategy names rather than the sensitivity
% matrix itself.
%
% function called using:
%
% [U,S,V] = calc_svd(mesh_name,IV_name)
%
% where:
%
%         [U,S,V] = the three singular value decomposition matrices
%       mesh_name = string containing full path and filename of mesh
%       IV_name = string containing full path and filename of data collection strategy
%
% Note: if function is called with no input arguments, the user is prompted for
%       the required filenames

function[U,S,V] = calc_svd(mesh_name,IV_name)

global RootDir                                  % get root directory for matlab user data

SVDpath = [RootDir '2Dsimulation\SVD\'];        % set path for SVD data files

if nargin == 0                                  % check to see if no input arguments were supplied
    [mesh_name mesh_path] = uigetfile([RootDir '2Dsimulation\mesh_database\*.mat']);
    if mesh_name, mesh_name = [mesh_path mesh_name];
    else error('Mesh name not recognised');end
    [IV_name IV_path] = uigetfile([RootDir '2Dsimulation\IV_patterns\*.mat']);
    if IV_name, IV_name = [IV_path IV_name];
    else error('IV Pattern not recognised');end
end

% The following code is used to generate an identification string for the filename of the
% SVD matrices. If the matrices have already been calculated they are stored on the hard
% disk to speed up future image reconstruction otherwise they are calculated the long way.

index = find(mesh_name == '\');                 % get indices of all backslashes
ind1 = index(length(index)-1);                  % get index of penultimate '\'
ind2 = max(index);                              % get index of last '\'
meshID = mesh_name(ind1+1 : ind2-1);            % extract mesh type

ind1 = max(find(IV_name == '\'));               % get index of last backslash
ind2 = find(IV_name == '.');                    % get index of '.'
IVID = IV_name(ind1+1 : ind2-1);                % extract IV_pattern name

SVDname = [meshID '_' IVID '.mat'];             % generate SVD identifier
if exist([SVDpath SVDname])                     % check if the file already exists
    load([SVDpath SVDname])                     % if so load it...
    return                                      % and return to the calling function
end

S = calc_s_fem(mesh_name,IV_name);              % if file doesn't exists, need to load up the SENS matrix
[U,S,V] = svd(S,0);                             % get singular value decomposition of it
save([SVDpath SVDname],'U','S','V');            % save results to disk



% ------------------------- calc_s_fem ------------------------------
%
% Used for calculation of the sensitivity matrix based on a Finite Element
% mesh structure and a given data collection strategy. The technique used
```

```
% is the perturbation technique, where each conductivity element within the
% mesh is perturbed in turn, and the resulting perturbations in the surface
% voltages recorded. It is slow, but works well. Once calculated the file is
% stored on the hard disk so it can be retrieved quickly if the same mesh/IV
% combination is requested at a later time.
%
% Called using:
%
% [S] = calc_s_fem(mesh_name,IV_name)
%
% where:
%
%            S = sensitivity matrix
%    mesh_name = string containing full path and filename of mesh
%      IV_name = string containing full path and filename of data collection strategy
%
% Note: if function is called with no input arguments, the user is prompted for
%       the required filenames

function [S] = calc_s_fem(mesh_name,IV_name)

global RootDir                                          % get root directory for matlab user data

Spath = [RootDir '2Dsimulation\sensitivity\'];          % set path of sensitivity matrix data files

if nargin == 0                                          % check to see if no input arguments were supplied
    [mesh_name mesh_path] = uigetfile([RootDir '2Dsimulation\mesh_database\*.mat']);
    if mesh_name, mesh_name = [mesh_path mesh_name];
    else error('Mesh name not recognised');end
    [IV_name IV_path] = uigetfile([RootDir '2Dsimulation\IV_patterns\*.mat']);
    if IV_name, IV_name = [IV_path IV_name];
    else error('IV Pattern not recognised');end
end

% The following code is used to generate an identification string for the filename of the
% sensitivity matrices. If the matrices have already been calculated they are stored on the hard
% disk to speed up future image reconstruction otherwise they are calculated the long way.

index = find(mesh_name == '\');                         % get indices of all backslashes
ind1 = index(length(index)-1);                          % get index of penultimate '\'
ind2 = max(index);                                      % get index of last '\'
meshID = mesh_name(ind1+1 : ind2-1);                    % extract mesh type

ind1 = max(find(IV_name == '\'));                       % get index of last backslash
ind2 = find(IV_name == '.');                            % get index of '.'
IVID = IV_name(ind1+1 : ind2-1);                        % extract IV_pattern name

Sname = [meshID '_' IVID '.mat'];                       % generate sensitivity identifier
if exist([Spath Sname])                                 % check if the file already exists
    load([Spath Sname])                                 % if so load it...
    return                                              % and return to the calling function
end

load(mesh_name)                                         % load mesh to get conductivity values
no_els = size(Z_el,1);                                  % get number of elements in the mesh

Vback = FEM(Z_el,element_nodes,node_XY,IV_name);        % solve for background voltages
for el=1:no_els                                         % loop round each element in turn
    Zback = Z_el(el);                                   % get conductivity of element
    Z_el(el) = Z_el(el) * 1.01;                         % change conductivity by 1%
    disp(['element ' int2str(el) ' out of ' int2str(no_els)]);
    Vfore = FEM(Z_el,element_nodes,node_XY,IV_name);    % solve forward problem for this element
    Vdiff = Vfore - Vback;                              % calculate perturbed voltage profile
    S(el,:) = Vdiff;                                    % update corresponding row of S matrix
    Z_el(el) = Zback;                                   % return element to original conductivity
end

save([Spath Sname],'S');                                % save matrix for future retrieval
```

APPENDIX C – LISTING OF THE SOFTWARE FOR CALCULATION OF THE SPATIAL RESOLUTION

The function listed here contains MATLAB script the code used for generating a point source within a chosen Finite Element mesh and reconstructing its image. Simulated noise can be added to the simulated voltage data and the truncation level for inversion of the sensitivity matrix can be specified. The resolution of the resulting image is calculated using the method described in section 4.3.1.2.

```
% ---------------------- simulatePSF --------------------------
%
% used for simulating a point source having a 10% increase in
% conductivity from the background value. The resolution of the
% resultant image is calculated from the area of the PSF. A special
% algorithm is used to ensure that only elements within a given
% radius of the known PSF centre are used for calculation of the
% resolution in order to prevent errors caused by large artefacts
% which can sometimes occur in EIT images, particularly when noise
% is added to the simulated data.
%
% called using:
%
% [resolution] = simulatePSF(PSFel,Vn,tr)
%
% where:   resolution = calculated resolution value
%             PSFel = conducting element to be used as a point source
%                tr = truncation level for the matrix inversion (in dB)


function [resolution] = simulatePSF(PSFel,Vn,tr)

global RootDir                                  % get root directory for matlab user data
[Fname Pname] = uigetfile([RootDir '2Dsimulation\mesh_database\2048_x_128\'],'Select background mesh');
back_mesh = [Pname Fname];                      % get name of background mesh
load(back_mesh)                                 % load background mesh
[Fname Pname] = uigetfile([RootDir '2Dsimulation\IV_patterns\'],'Select data collection method');
IV_name = [Pname Fname];                        % get name of data collection method

Vback = FEM(Z_el,element_nodes,node_XY,IV_name);  % get background voltage profile
Vback = Vback + Vn*randn(size(Vback));          % add simulated noise to background voltage profile

Zfore = Z_el;                                   % make a copy of the background conductivity distribution
Zfore(PSFel) = Zfore(PSFel)*1.1;                % increase conductivity of PSF element by 10%
Vfore = FEM(Zfore,element_nodes,node_XY,IV_name); % get foreground voltage profile
Vfore = Vfore + Vn*randn(size(Vfore));          % add simulated noise to foreground voltage profile

Sinv = invertSENS(back_mesh,IV_name,tr);        % get inverted sensitivity matrix
pic = (Vfore(:)-Vback(:))'*Sinv;                % reconstruct image

[el_centre,el_area] = meshstat(element_nodes,node_XY); % get element information from mesh geometry
mesh_rad = range(node_XY(:,1));                 % calculate mesh radius
search_rad = .25 * mesh_rad;                    % set PSF search radius to 25% of mesh radius
dist = get_radii(PSFel,el_centre);              % get distances from PSFel to all other elements
PSFmax = max(pic(find(dist < search_rad)));     % get peak PSF value within search radius
PSFind = find(dist < search_rad & pic' > .5*PSFmax); % get indices of valid PSF elements
pic2 = zeros(size(pic));                        % initialise masked image
pic2(PSFind) = pic(PSFind);                     % make image of only PSF pixels
resolution = 100*sqrt(sum(el_area(PSFind)) / sum(el_area)); % get area resolution of PSF from picture


figure(1);                                      % draw the final images
subplot(1,2,1), draw_mesh(pic,0,element_nodes,node_XY);
subplot(1,2,2), draw_mesh(pic2,0,element_nodes,node_XY);
title(['Resolution - ' num2str(resolution) ' %'])
```

```
function[el_centre,el_area] = meshstat(element_nodes,node_XY)
no_els = length(element_nodes);
for el=1:no_els
    x1 = node_XY(element_nodes(el,1),1);
    y1 = node_XY(element_nodes(el,1),2);
    x2 = node_XY(element_nodes(el,2),1);
    y2 = node_XY(element_nodes(el,2),2);
    x3 = node_XY(element_nodes(el,3),1);
    y3 = node_XY(element_nodes(el,3),2);
    el_area(el) = triangle(x1,y1,x2,y2,x3,y3);
    el_centre(el,:) = [mean([x1 x2 x3]) mean([y1 y2 y3])];
end

function[dist] = get_radii(PSFel,el_centre)
Xpsf = el_centre(PSFel,1);
Ypsf = el_centre(PSFel,2);
dist = sqrt((Xpsf-el_centre(:,1)).^2 + (Ypsf-el_centre(:,2)).^2);
```

APPENDIX D – LISTING OF THE SOFTWARE FOR IMPLEMENTING THE RESOLUTION PROFILE CURVE-FITTING ALGORITHMS

The functions listed here contain MATLAB script code used for implementing the *r-squared* and *quadratic* curve fitting models described in section 4.3.1.2. Both functions are supplied with two vectors; one (*radii*) containing the radial positions of the point sources and the other (*Rprof*) containing the resolution values for each of the point sources. The values returned from the functions are the central resolution (R_c), the spatial variance (α) and the regression coefficient (R^2).

```
% ------------------- rsquared_fit ---------------------
%
% function for fitting a profile of resolution data to the formula:
%
%         R = Rc.(1-alpha.r²)
%
% called by:      [Rc,alpha,R²] = rsquared_fit(radii,Rprof)
%
% where:          Rc = central resolution value
%              alpha = spatial invariance coefficient
%                 R² = regression coeffient
%              radii = radial positions of PSFs
%              Rprof = resolution profile values

function [Rc,alpha,R2] = rsquared_fit(radii,Rprof)

Rprof = Rprof(:);                                   % Ensure vectors are column
radii = radii(:);

Rc(1)     = Rprof(1);                               % Initialise Rc to 1st value in resolution profile
alpha(1)  = 0;                                      % Initialise alpha to zero (ideal case)
add_alpha = 1;
add_Rc    = 1;

iter = 1;                                           % initialise iteration counter
while (abs(add_alpha) > .00001 | abs(add_Rc) > .01 & iter<100)   % check for convergence requirements
   [add_alpha,add_Rc] = grad_R2(radii,Rprof,Rc(1),alpha(1));    % get updated alpha and Rc values
   alpha(1) = alpha(1) + add_alpha;                 % update alpha
   Rc(1) = Rc(1) + add_Rc;                          % update Rc
   iter=iter+1;                                     % increment iteration counter
end

Rfit = Rc(1)*(1-alpha(1)*radii.^2);                 % calculate fitted curve
SSE = sum((Rprof - Rfit).^2);                       % Sum of square errors
SST = sum((Rprof - mean(Rprof)).^2);                % Total sum of squares
R2(1) = 1-(SSE/SST);                                % Square of the multiple correlation coefficient

function [out1,out2] = grad_R2(radii,Rprof,Rc,alpha);   % function to calculate the alpha and Rc updates
out1 = .1*(mean(Rprof - Rc*(1-alpha*radii.^2))^2 - mean(Rprof - Rc*(1-(alpha+.01)*radii.^2))^2);
out2 = .1*(mean(Rprof - Rc*(1-alpha*radii.^2))^2 - mean(Rprof - (Rc+.01)*(1-alpha*radii.^2))^2);
```

```
% ------------------- quadratic_fit ---------------------
%
% function for fitting a profile of resolution data to the quadratic
% model expressed using the formulae:
%
%          Rfit = Rc.(1 + alpha1.r + alpha2.r²)
%         alpha = sqrt(alpha1² + alpha2²)
%
% called by:      [Rc,alpha,R²] = quadratic_fit(radii,Rprof)
%
% where:          Rc = central resolution value
%              alpha = spatial variance coefficient
%                 R² = regression coeffient
%              radii = radial positions of PSFs
%              Rprof = resolution profile values

function [Rc,alpha,R2] = quadratic_fit(radii,Rprof)

P = polyfit(radii,Rprof,2);                 % get 2nd order polynomial coefficients
Rfit = polyval(P,radii);                    % create fitted curve based on coefficients

SSE = sum((Rprof - Rfit).^2);               % Sum of square errors
SST = sum((Rprof - mean(Rprof)).^2);        % Total sum of squares
R2 = 1-(SSE/SST);                           % Square of the multiple correlation coefficient
```

```
Rc = P(3);                              % get Rc
alpha1 = P(2)/P(3);                     % calculate alpha1
alpha2 = P(1)/P(3);                     % calculate alpha2
alpha = sqrt(alpha1^2+alpha2^2);        % calculate geometric mean to form alpha
```

APPENDIX E – IMAGES RECONSTRUCTED FROM THE 2D SIMULATION (ZERO ADDED NOISE)

Adjacent: 16-drv 16-rec

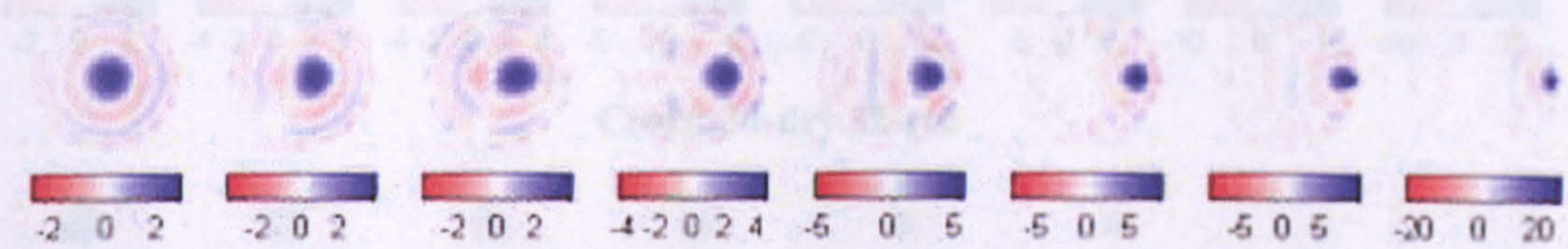

Adjacent: 32-drv 32-rec

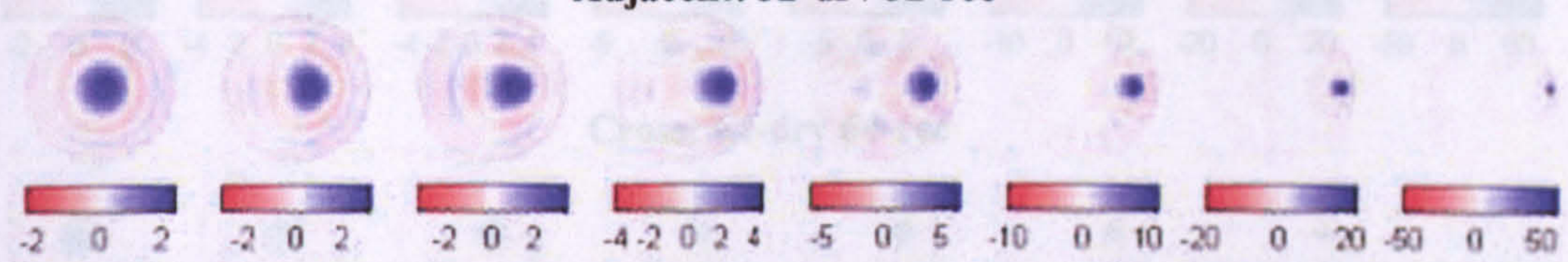

Adjacent: 64-drv 64-rec

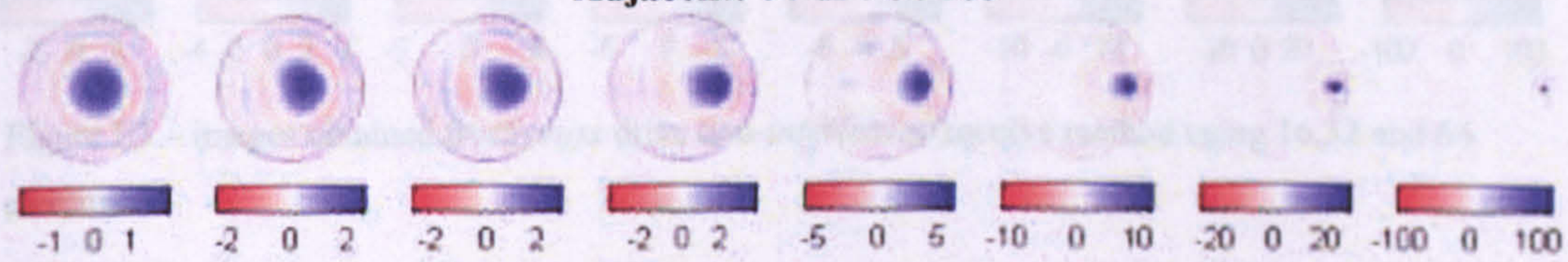

Figure E1 – images obtained from *adjacent* drive non-*interleaved* receive method using 16,32 and 64 electrodes.

Adjacent: 16-drv 16-rec(int)

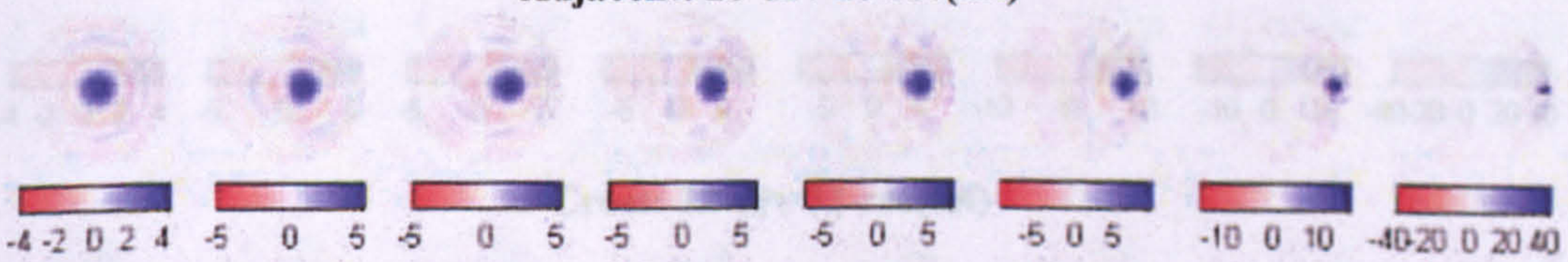

Adjacent: 32-drv 32-rec(int)

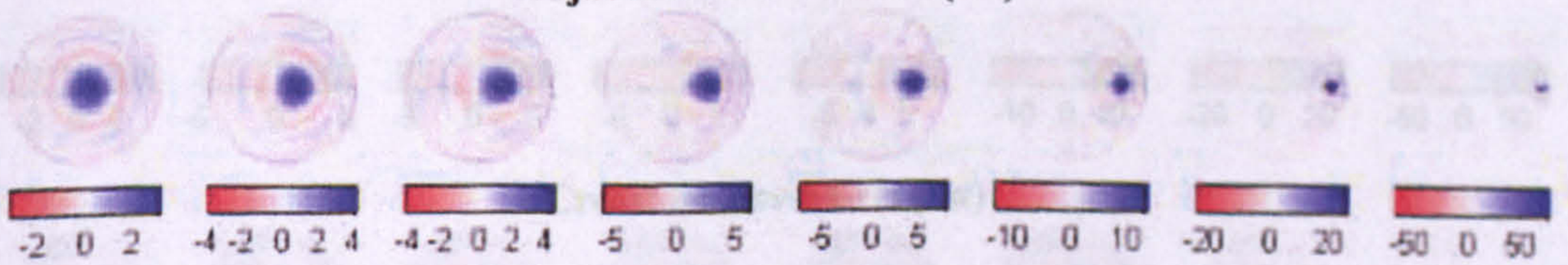

Adjacent: 64-drv 64-rec(int)

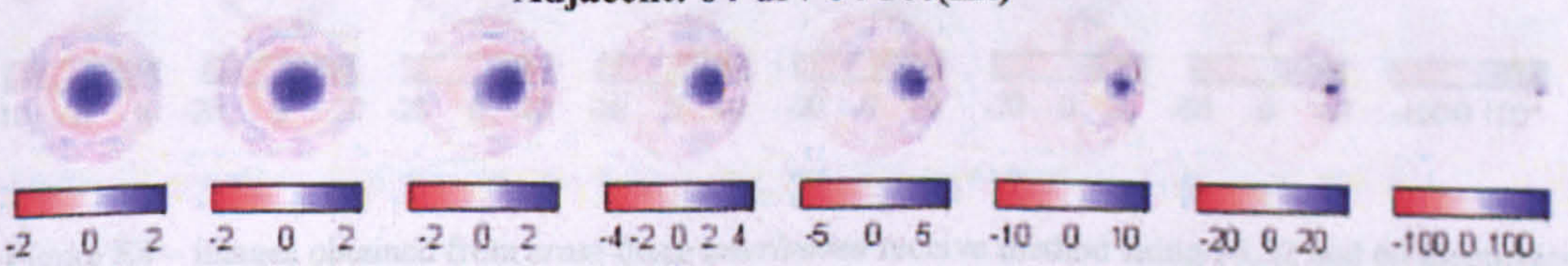

Figure E2 – images obtained from *adjacent* drive *interleaved* receive method using 16,32 and 64 electrodes.

Cross: 16-drv 16-rec

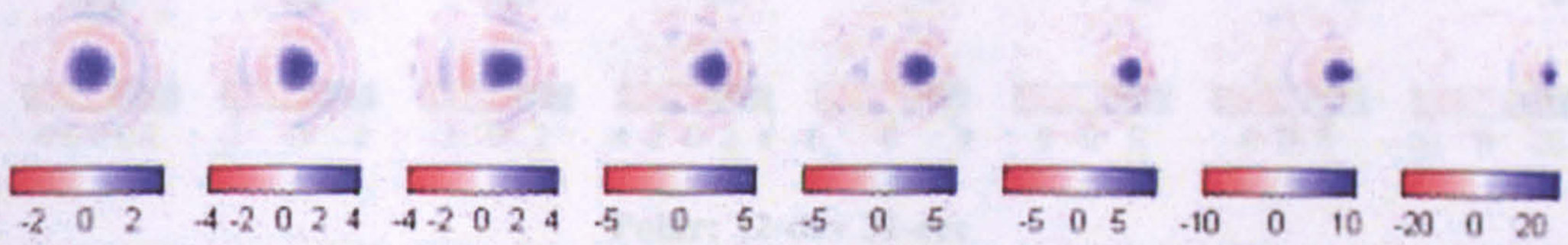

Cross: 32-drv 32-rec

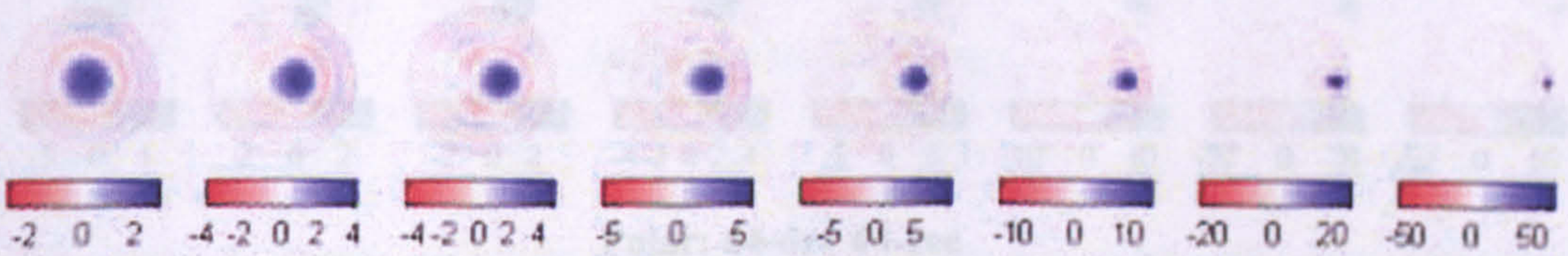

Cross: 64-drv 64-rec

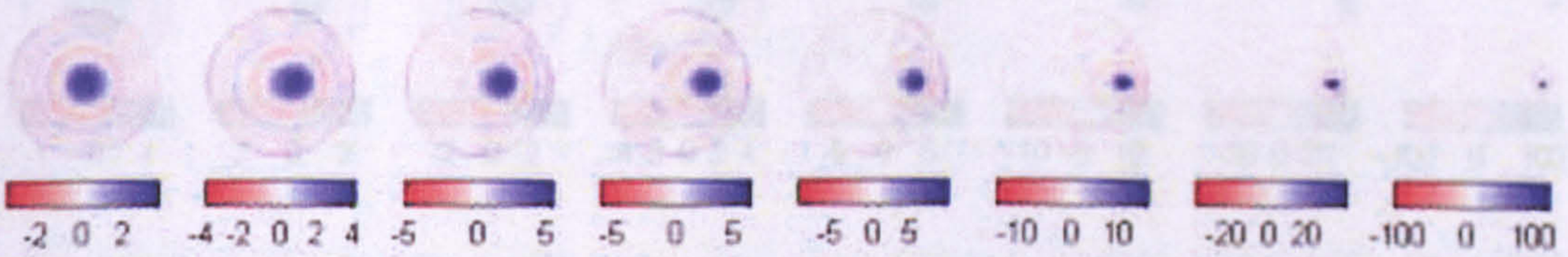

Figure E3 – images obtained from *cross* drive non-*interleaved* receive method using 16,32 and 64 electrodes.

Cross: 16-drv 16-rec(int)

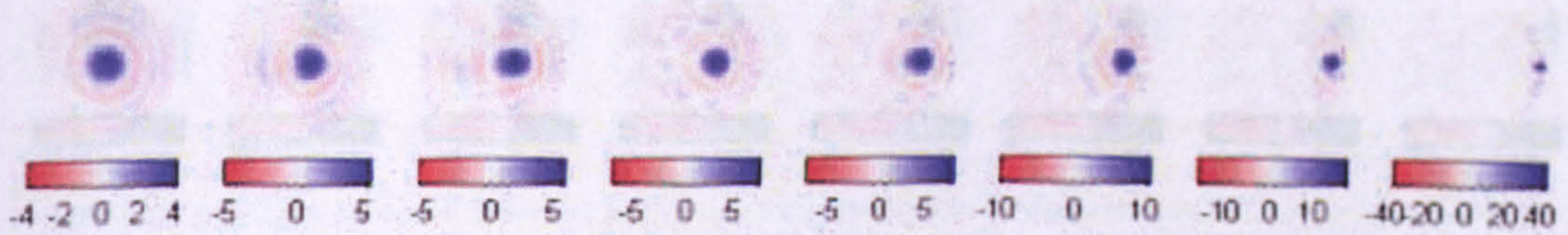

Cross: 32-drv 32-rec(int)

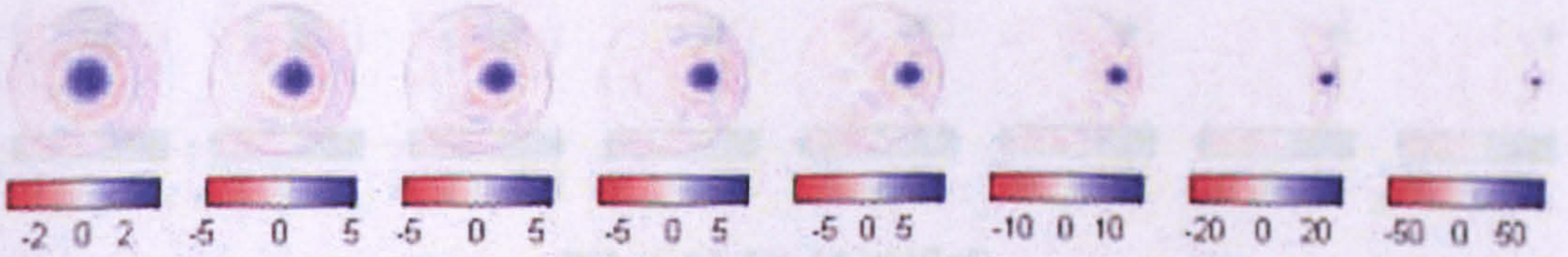

Cross: 64-drv 64-rec(int)

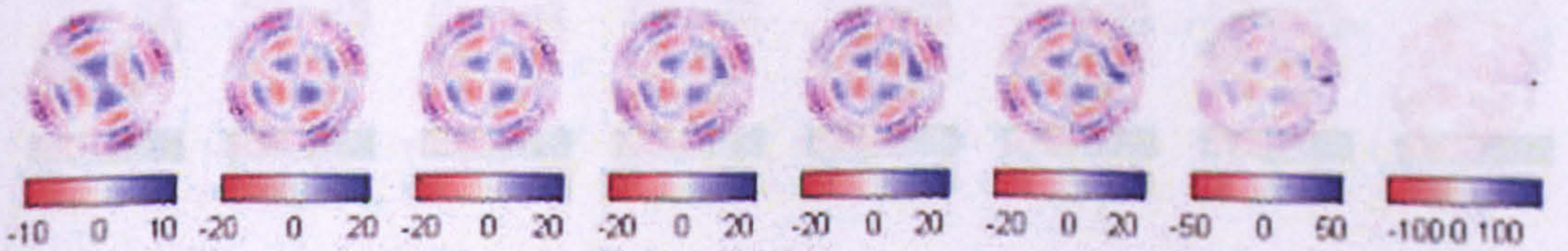

Figure E4 – images obtained from *cross* drive *interleaved* receive method using 16,32 and 64 electrodes.

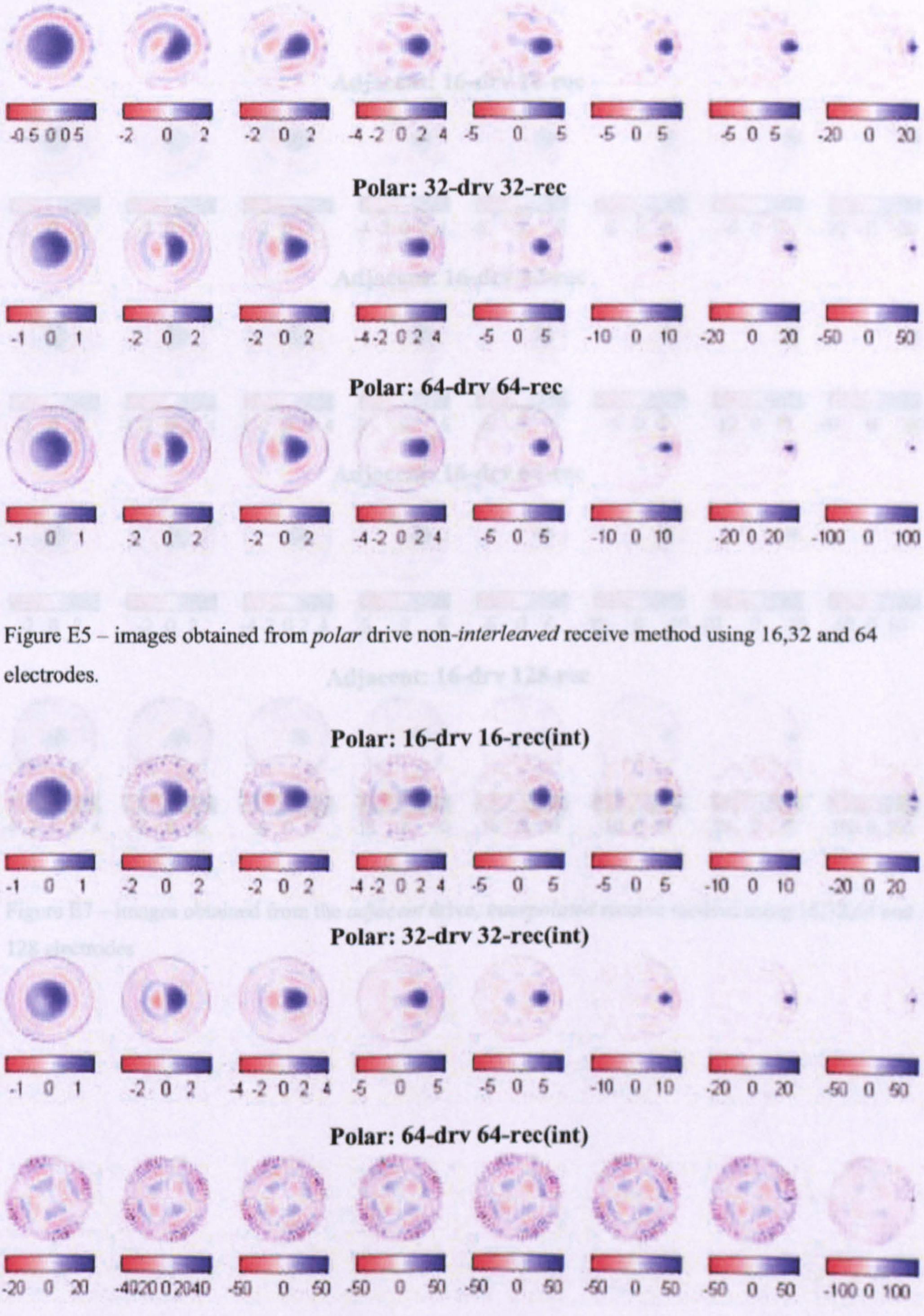

Figure E5 – images obtained from *polar* drive non-*interleaved* receive method using 16,32 and 64 electrodes.

Figure E6 – images obtained from *polar* drive *interleaved* receive method using 16,32 and 64 electrodes.

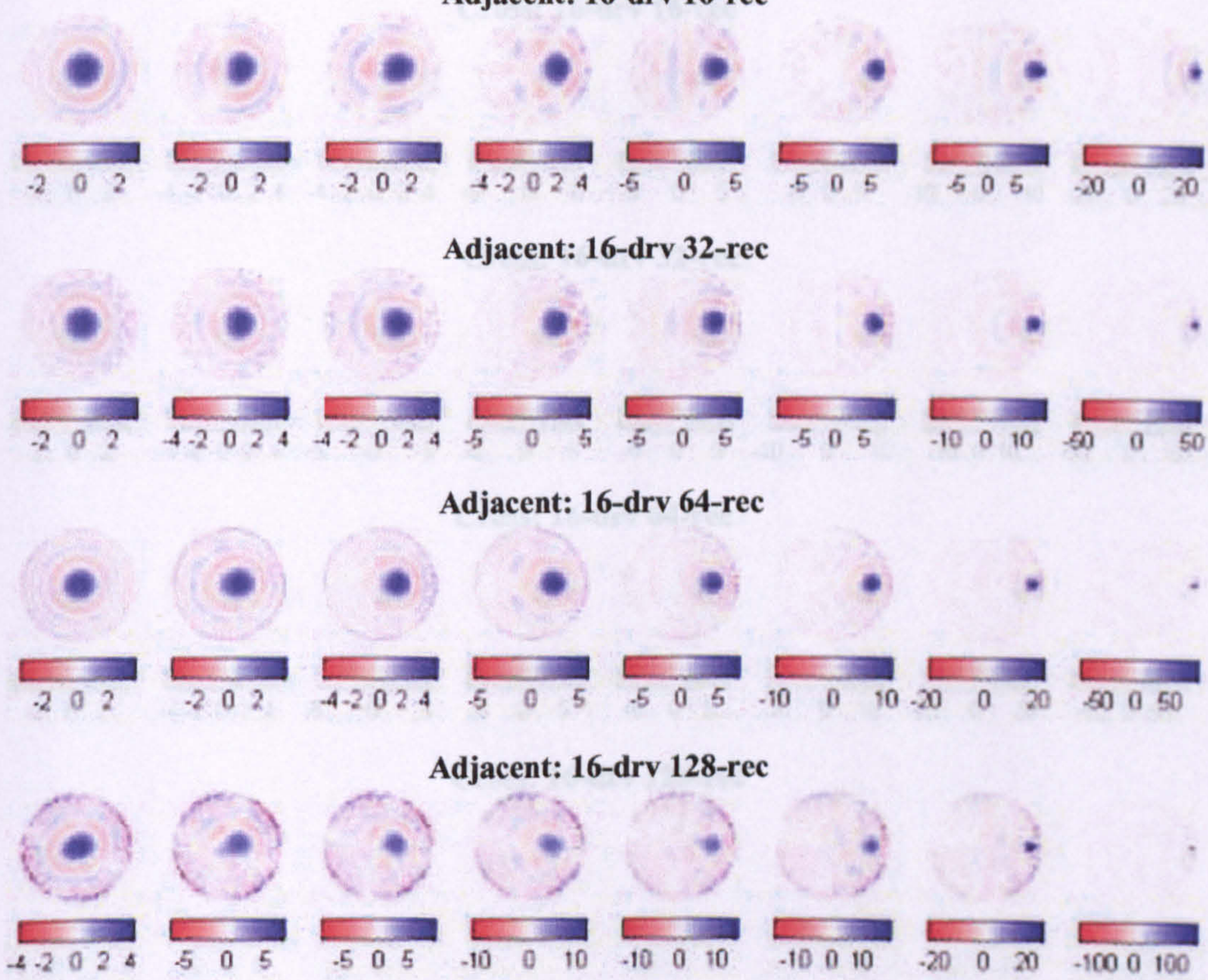

Figure E7 – images obtained from the *adjacent* drive, *interpolated* receive method using 16,32,64 and 128 electrodes

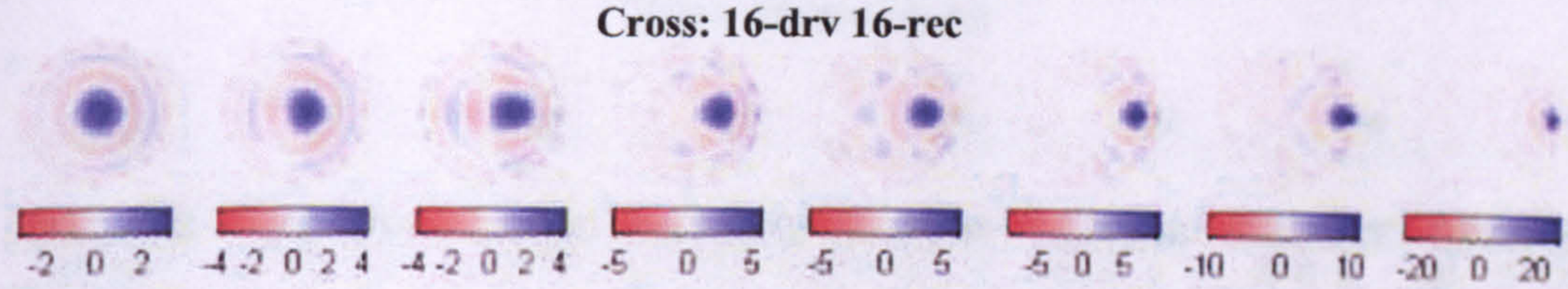

Figure E8 – images obtained from the *cross* drive, *interpolated* receive method using 16,32,64 and 128 electrodes

Polar: 16-drv 16-rec

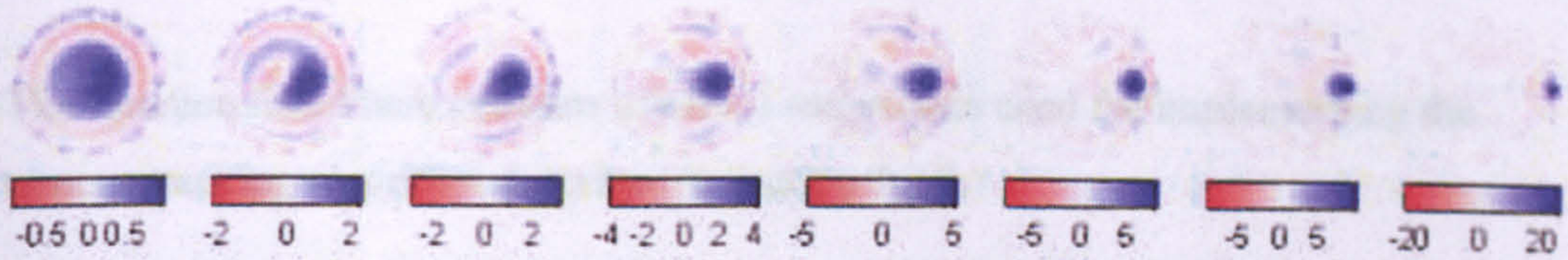

Polar: 16-drv 32-rec

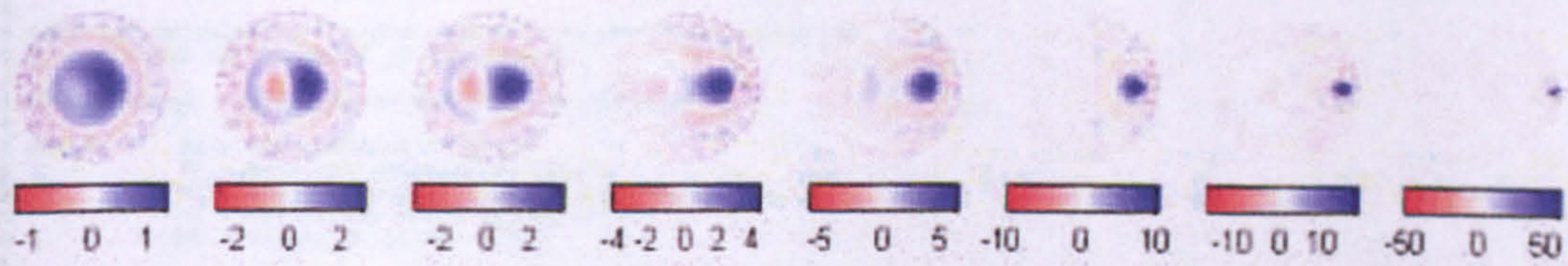

Polar: 16-drv 64-rec

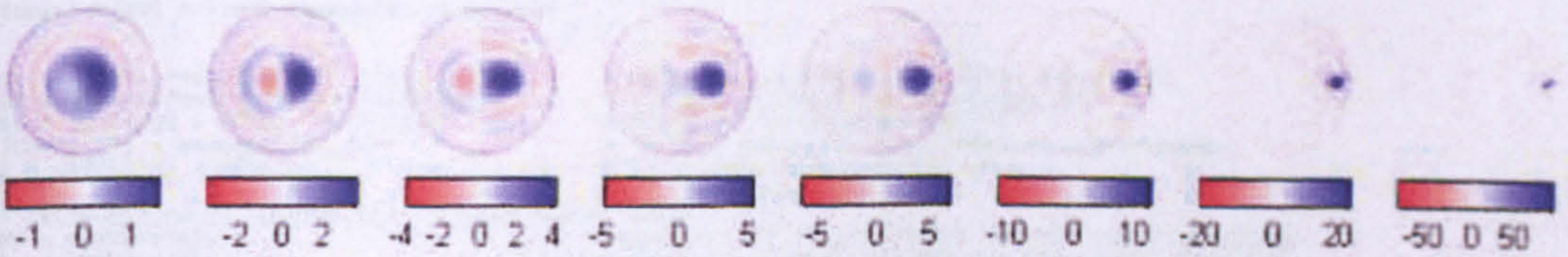

Polar: 16-drv 128-rec

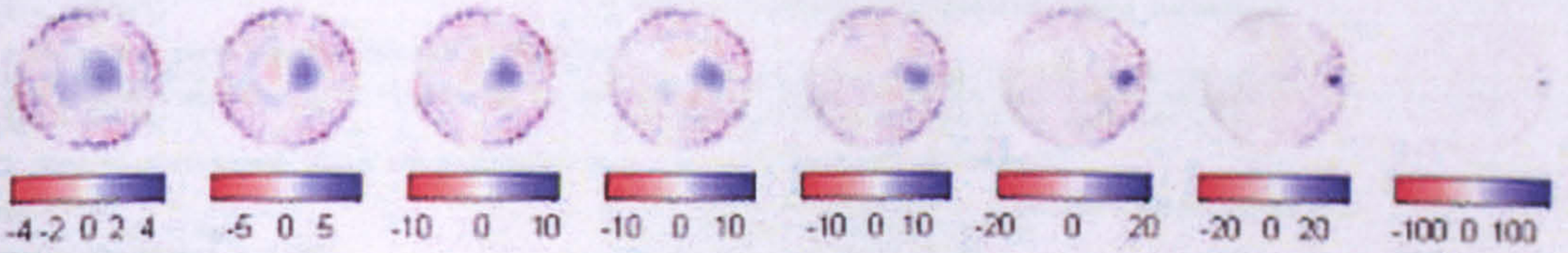

Figure E9 – images obtained from the *polar* drive, *interpolated* receive method using 16,32,64 and 128 electrodes

APPENDIX F – LISTING OF THE SOFTWARE FOR IMPLEMENTING THE TUMOUR TRACKING ALGORITHM

The function listed here contains MATLAB script code used for implementing the tumour tracking algorithm described in section 5.2.2.

```
% ------------------ track_tumour ----------------------
%
% used for calculating the position of a given point within the
% breast model as the model is compressed.
%
% called using:  [P2] = track_tumour(P1,n1,n2,vol)
%
% where:      P2 = new position of point
%             P1 = original position of point
%             n1 = original breast shape (power value)
%             n2 = new breast shape (power value)
%            vol = volume of breast model
%
% Note: P1 and P2 are vectors containing the x,y & z co-ordinates
%       e.g. P1 = [x1 y1 z1]

function[P2] = track_tumour(P1,n1,n2,vol)


t1 = ((2+n1)*vol/(pi*n1))^(1/(2+n1));          % truncation point for original shape (n1)
t2 = ((2+n2)*vol/(pi*n2))^(1/(2+n2));          % truncation point for new shape (n2)
x1 = P1(1);y1 = P1(2); z1 = P1(3);             % get x,y,z co-ordinates of P1
[theta,r1] = cart2pol(x1,y1);                  % Convert point P1 to cylindrical coordinates
a = z1/(t1^n1 - r1^n1);                        % Calculate scaling factor: a

% Calculate curve lengths for original breast shape
N1 = num2str(n1);                              % get 'n1' in string format for the 'quad' function
A  = num2str(a);                               % get 'a' in string format for the 'quad' function
if r1, Sp1 = quad(['sqrt(1 + (' A '*' N1 '*x.^(' N1 '-1)).^2)'],0,r1); % length from nipple to point P1
else Sp1 = 0; end
St1 = quad(['sqrt(1 + (' A '*' N1 '*x.^(' N1 '-1)).^2)'],0,t1); % length from nipple to base
k = Sp1/St1;                                   % Calculate proportional position along surface: k

% Calculate curve lengths for new breast shape
N2 = num2str(n2);                              % get 'n2' in string format for the 'quad' function
St2 = quad(['sqrt(1 + (' A '*' N2 '*x.^(' N2 '-1)).^2)'],0,t2); % length from nipple to base
Sp2 = k*St2;                                   % length from nipple to new point position (P2)

% Need to iteratively solve for new radius (r2) until curve length matches Sp2

r2 = t2;                                       % Set radius to outer limit (i.e. the truncation point)
error = St2 - Sp2;                             % Make initial error calculation
while abs(error) > 0.001                       % while error is still large
   r2 = r2 - error/5;                          % reduce radius
   error = quad(['sqrt(1 + (' A '*' N2 '*x.^(' N2 '-1)).^2)'],0,r2) - Sp2; % recalculate error
end                                            % keep going until r2 is found

z2 = a*(t2^n2 - r2^n2);                        % calculate new z position
x2 = r2*cos(theta);                            % calculate new x position
y2 = r2*sin(theta);                            % calculate new y position
P2 = [x2 y2 z2];                               % form new point location vector (P2)
```

APPENDIX G – LISTING OF THE SOFTWARE FOR CALCULATION OF THE 3D SENSITIVITY MATRICES

The two functions used for calculation of the 3D sensitivity matrices (as described in section 5.3.2) consist of a MATLAB function; *calc_S.m* which calls a C++ routine; *calc_Sprof.dll*. This approach is used in order to speed up the process.

```
% function[S] = calc_S(drv,rec,elec_xyz,voxel_nodes,node_xyz,lambda,Vdrv)
%
% Used for calculating the sensitivity matrix of a specified voxel volume
% using the 'best n pairs' from the specified electrode array
%
% ---------------------------------------------------------------------
%
%           S : Sensitivity matrix. Dimensions: (voxels , D/R pairs)
% ---------------------------------------------------------------------
%         drv : list of drive pair numbers
%         rec : list of receive pair numbers
%    elec_xyz : (x,y,z) coordinates of electrode positions
% voxel_nodes : indices of the 8 nodes surrounding each voxel
%    node_xyz : (x,y,z) coordinates of the node positions
%      lambda : voltage fall-off with distancce
%        Vdrv : magnitude of differential voltage applied to drive pair


function[S,drv,rec] = calc_S(drv,rec,elec_xyz,voxel_nodes,node_xyz,lambda,Vdrv)

no_vox = size(voxel_nodes,1);                                % get number of voxels in breast model
disp('Calculating S-matrix.....')
for voxel = 1:no_vox                                         % loop around each voxel in turn
    voxel_xyz = node_xyz(voxel_nodes(voxel,:),:);            % get [x,y,z] coordinates of current voxel
    S_prof = calc_Sprof(drv,rec,Vdrv,elec_xyz,voxel_xyz,lambda); % calculate sensitivity profile
    S(voxel,:) = S_prof;                                     % Assign whole S-profile to final S matrix
End
```

```
#include "mex.h"
#include <math.h>
#include <stdlib.h>
#include <string.h>
#include <conio.h>

void calc_grad(double *G, double *drv_V, double *drv_xyz, int no_drv,
               double *voxel_xyz, double lambda)
{
    int node, drv;
    double drv_x, drv_y, drv_z, node_x, node_y, node_z;
    double dist, V[8];
    double Xmean, Ymean, Zmean, Vxpos, Vxneg, Vypos, Vyneg, Vzpos, Vzneg;

    for(node=0; node<8; node++)                    // Loop around the 8 corner nodes
    {
        node_x = voxel_xyz[node];                  // get x position of node
        node_y = voxel_xyz[node+8];                // get y position of node
        node_z = voxel_xyz[node+16];               // get z position of node
        V[node] = 0;                               // initialise node voltage to 0

        for(drv=0; drv<no_drv; drv++)              // loop around drive electrodes
        {
            drv_x = drv_xyz[drv];                  // get x position of drive
            drv_y = drv_xyz[drv+no_drv];           // get y position of drive
            drv_z = drv_xyz[drv+2*no_drv];         // get z position of drive
            // calculate distance between node and drive
            dist = sqrt((drv_x-node_x)*(drv_x-node_x) + (drv_y-node_y)*(drv_y-node_y) + (drv_z-node_z)*(drv_z-
node_z));
            V[node] += (drv_V[drv] * alpha) / (dist + lambda);   // update node voltage
    }
}

// From the 8 nodes, find dx,dy & dz components
// First compile lists of indices representing vector locations

Xmean = 0; Ymean = 0; Zmean = 0;
for(node=0; node<8; node++)          // loop around 8 corner nodes
{
    Xmean += voxel_xyz[node];
    Ymean += voxel_xyz[node+8];
    Zmean += voxel_xyz[node+16];
}
Xmean /= 8; Ymean /= 8; Zmean /= 8; // calculate centre position of voxel

Vxpos = 0; Vxneg = 0;
Vypos = 0; Vyneg = 0;
Vzpos = 0; Vzneg = 0;
for(node=0; node<8; node++)          // loop around 8 corner nodes
{
    node_x = voxel_xyz[node];        // get x position of node
    node_y = voxel_xyz[node+8];      // get y position of node
    node_z = voxel_xyz[node+16];     // get z position of node
```

```
        if (node_x > Xmean) Vxpos += V[node];    // positive x-vector node
        else Vxneg += V[node];                   // negative x-vector node

        if (node_y > Ymean) Vypos += V[node];    // positive y-vector node
        else Vyneg += V[node];                   // negative y-vector node

        if (node_z > Zmean) Vzpos += V[node];    // positive z-vector node
        else Vzneg += V[node];                   // negative z-vector node
    }

    G[0] = (Vxpos - Vxneg)/4;                // Voltage gradient in x-direction
    G[1] = (Vypos - Vyneg)/4;                // Voltage gradient in y-direction
    G[2] = (Vzpos - Vzneg)/4;                // Voltage gradient in z-direction
}


double calc_sens(int no_drv, double *drv_V, double *drv_xyz,
                 int no_rec, double *rec_V, double *rec_xyz,
                 double *voxel_xyz, double lambda)
{
    double Gdrv[3], Grec[3], S;

    calc_grad(&Gdrv[0], drv_V, drv_xyz, no_drv, voxel_xyz, lambda); // get gradient field for DRV pair
    calc_grad(&Grec[0], rec_V, rec_xyz, no_rec, voxel_xyz, lambda); // get gradient field for REC pair

    S = Gdrv[0]*Grec[0] + Gdrv[1]*Grec[1] + Gdrv[2]*Grec[2];        // calculate sensitivity value
                                                                    // (dot product of gradients)
    return S;
}


void calc_Sprof(const mxArray *Sprof, double *DRV, double *REC, double Vdrv, int no_pairs,
                double *elec_xyz, double *voxel_xyz, int no_elec, double lambda)
{
    const int no_drv = 2, no_rec = 2;                   // set number of drive and receive electrodes to 2
    int pair;
    double drv_V[2] = {Vdrv, -Vdrv};
    double rec_V[2] = {Vdrv, -Vdrv};
    double drv_xyz[6], rec_xyz[6];
    double *S_prof;

    S_prof = mxGetPr(Sprof);                            // get pointer to output array

    for(pair=0; pair<no_pairs; pair++)                  // loop around all drive/receive pairs
    {
        drv_xyz[0] = elec_xyz[((int)DRV[pair]-1)];                          // DRV1 - x position
        drv_xyz[2] = elec_xyz[((int)DRV[pair]-1) + no_elec];                // DRV1 - y position
        drv_xyz[4] = elec_xyz[((int)DRV[pair]-1) + 2*no_elec];              // DRV1 - z position
        drv_xyz[1] = elec_xyz[((int)DRV[pair + no_pairs]-1)];               // DRV2 - x position
        drv_xyz[3] = elec_xyz[((int)DRV[pair + no_pairs]-1) + no_elec];     // DRV2 - y position
        drv_xyz[5] = elec_xyz[((int)DRV[pair + no_pairs]-1) + 2*no_elec];   // DRV2 - z position
        rec_xyz[0] = elec_xyz[((int)REC[pair]-1)];                          // REC1 - x position
        rec_xyz[2] = elec_xyz[((int)REC[pair]-1) + no_elec];                // REC1 - y position
        rec_xyz[4] = elec_xyz[((int)REC[pair]-1) + 2*no_elec];              // REC1 - z position
        rec_xyz[1] = elec_xyz[((int)REC[pair + no_pairs]-1)];               // REC2 - x position
        rec_xyz[3] = elec_xyz[((int)REC[pair + no_pairs]-1) + no_elec];     // REC2 - y position
        rec_xyz[5] = elec_xyz[((int)REC[pair + no_pairs]-1) + 2*no_elec];   // REC2 - z position

        S_prof[pair] = calc_sens(no_drv, drv_V, drv_xyz, no_rec, rec_V, rec_xyz, voxel_xyz, lambda);
    }
}


// ------------------------------------------------------------------


void mexFunction(int nlhs, mxArray* plhs[], int nrhs, const mxArray* prhs[])
{
    int    no_pairs, no_elec;
    double *DRV, *REC, *elec_xyz, *voxel_xyz;
    double Vdrv, lambda;
    const  mxArray *Sprof;

    no_pairs  = mxGetM(prhs[0]);        // get number of drive/receive pairs
    no_elec   = mxGetM(prhs[3]);        // get number of electrodes

    DRV       = mxGetPr(prhs[0]);       // get pointer to DRV array
    REC       = mxGetPr(prhs[1]);       // get pointer to REC array
    Vdrv      = mxGetScalar(prhs[2]);   // get value of Vdrv
    elec_xyz  = mxGetPr(prhs[3]);       // get pointer to elec_xyz array
    voxel_xyz = mxGetPr(prhs[4]);       // get pointer to voxel_xyz array
    lambda    = mxGetScalar(prhs[5]);   // get value of lambda

    plhs[0] = mxCreateDoubleMatrix(1,no_pairs,mxREAL); // make pointer to output array
    Sprof = plhs[0];                                   // assign pointer to output variable

//    mexPrintf("number of pairs: %d\n",no_pairs);
//    mexPrintf("number of electrodes: %d\n",no_elec);

    calc_Sprof(Sprof, DRV, REC, Vdrv, no_pairs, elec_xyz, voxel_xyz, no_elec, lambda);
}
```

APPENDIX H – LISTING OF THE SOFTWARE FOR CALCULATION OF THE VOXEL STRUCTURE OF THE 3D BREAST MODEL

The function listed here contains MATLAB script code used for calculation of the voxel structure of the breast model as described in section 5.3.3.

```
% function[voxel_nodes,node_xyz] = SetVoxels(n,vol,side)
%
% Used to calculate the voxel positions within the defined breast
% model (n,vol). The 'side' parameter determines the side length of
% each voxel cube.
% ------------------------------------------------------
%
% voxel_nodes : indices into node_xyz array for the 8 nodes around each voxel
%    node_xyz : (x,y,z) coordinates of the nodes
% ------------------------------------------------------
%           n : power value to determine breast shape
%         vol : volume of breast
%        side : side length of each voxel

function[voxel_nodes,node_xyz] = SetVoxels(n,vol,side)

Sc = 1;                                  % overall scale of model: 1=full size, <1 shrinks voxel structure
tol = .5 * side;                         % tolerance value - allows voxel edges to be just outside breast model
t = Sc*((2+n)*vol/(pi*n))^(1/(2+n)); % truncation point to preserve volume

maxXY = max(0:side:t);                   % get max XY value which still fits within truncation limit
posXY = -maxXY:side:maxXY;               % define range of node x,y-values
posZ  = 0:side:t^n+tol;                  % define range of node z-values

[node_x,node_y,node_z] = meshgrid(posXY,posXY,posZ);    % define all node x,y,z values
node_xyz = [node_x(:) node_y(:) node_z(:)];             % combine node coordinates into a single output vector

radii = sqrt(node_xyz(:,1).^2 + node_xyz(:,2).^2);      % calculate radii of all node positions
idx = find(radii-t <= tol);                             % find indices of all nodes within XY radial limit
node_xyz = node_xyz(idx,:);                             % discard all nodes outside XY radial limits
radii  = radii(idx);                                    % update radii vector

maxZ = t^n - radii.^n;                                  % calculate max height for each XY position
idx = find(maxZ-node_xyz(:,3) >= -tol);                 % find indices of all nodes within Z limit of model
node_xyz = node_xyz(idx,:);                             % discard all nodes outside height limit

if length(find(node_xyz(:,3) == max(node_xyz(:,3)))) < 9% check number of top nodes
    idx = find(node_xyz(:,3) < max(node_xyz(:,3)));     % remove them if there are less than 9 since they
    node_xyz = node_xyz(idx,:);                         % cannot contribute to voxel structure
end

% The following code finds which nodes surround each voxel:

no_nodes = size(node_xyz,1);             % get number of nodes
i = 0;                                   % counter for indexing voxel array
for nd=1:no_nodes                        % loop around each node in turn
    x = node_xyz(nd,1);                  % Get node x-coordinate
    y = node_xyz(nd,2);                  % Get node y-coordinate
    z = node_xyz(nd,3);                  % Get node z-coordinate

    Xvox = x + side/2;                   % Calculate voxel centre coordinates
    Yvox = y + side/2;                   % as +ve offset from the 3 node coordinates
    Zvox = z + side/2;

    d = sqrt((Xvox-node_xyz(:,1)).^2 + (Yvox-node_xyz(:,2)).^2 + (Zvox-node_xyz(:,3)).^2); % distances to all nodes
    Vn = find(d < side);                 % Find all nodes closer than node spacing
    if length(Vn) == 8                   % Must have 8 surrounding nodes to be valid voxel
        i = i+1;                         % increment index counter
        voxel_nodes(i,1:8) = (Vn(:))';   % Add voxel nodes to list
    end
end
```

APPENDIX I – THE TEN BREAST SHAPES USED THROUGHOUT THE 3D SIMULATION

Shape 1
n = 1.44

Shape 2
n = 2.10

Shape 3
n = 2.89

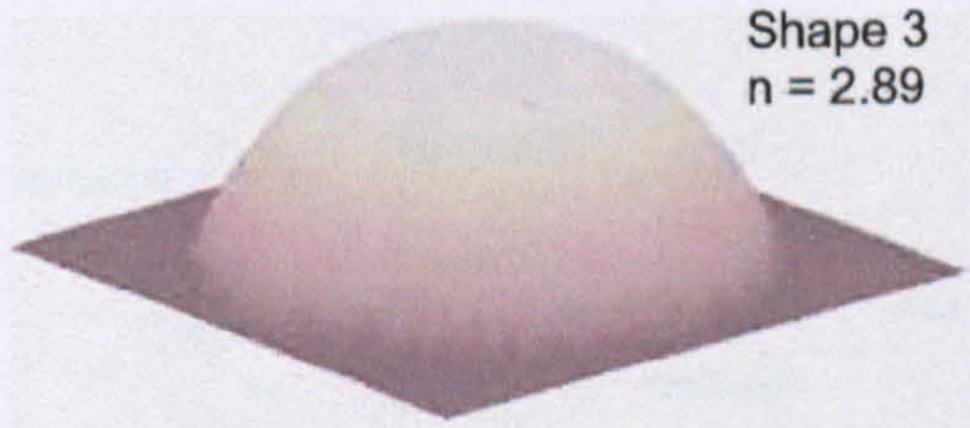

Shape 4
n = 3.80

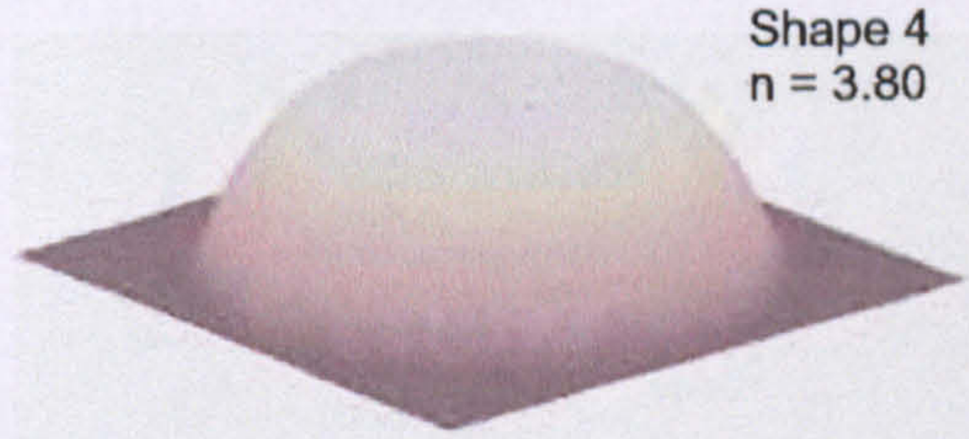

Shape 5
n = 4.84

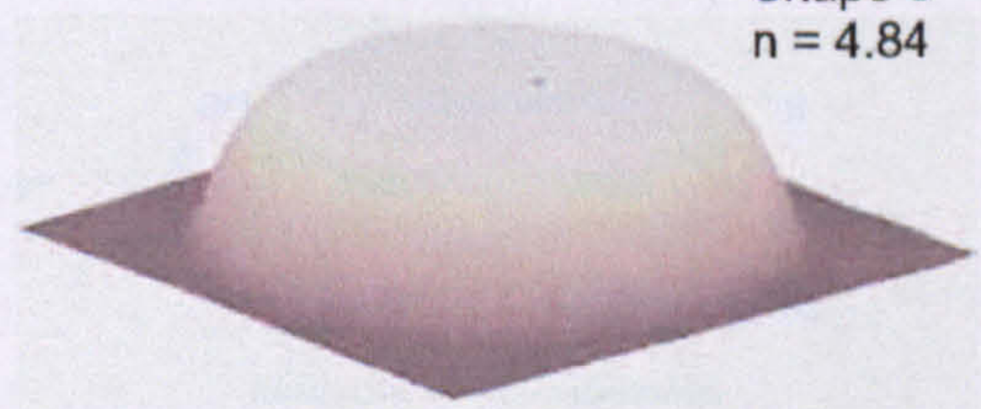

Shape 6
n = 6.00

Shape 7
n = 7.29

Shape 8
n = 8.70

Shape 9
n = 10.24

Shape 10
n = 11.90